Dissertation
submitted to the
Combined Faculties of the Natural Sciences and for Mathematics
of the Ruperto-Carola University of Heidelberg, Germany
for the degree of
Doctor of Natural Sciences

Put forward by
Dipl.-Phys. Christian Angrick
born in Northeim
Oral examination: July 6th, 2011

**On the derivation of an X-ray temperature function without reference to mass and the prediction of weak-lensing number counts from the statistics of Gaussian random fields**

Referees: Prof. Dr. Matthias Bartelmann
Prof. Dr. Luca Amendola

"*Logic is the beginning of wisdom; not the end.*"
– Spock

## Über die Ableitung einer Röntgentemperaturfunktion ohne Massenbezug und die Vorhersage der Anzahl von Detektionen beim schwachen Gravitationslinseneffekt mithilfe der Statistik von Gauß'schen Zufallsfeldern

***Zusammenfassung:*** Wir präsentieren einen neuen Ansatz für die Ableitung der Röntgentemperaturfunktion von Galaxienhaufen, der auf der Statistik von Gauß'schen Zufallsfeldern basiert, wobei letztere auf das kosmische Gravitationspotential angewendet wird. Er beruht nur auf lokal definierten Größen, sodass kein Bezug zur Masse eines Haufens hergestellt werden muss. Um das lineare und das nicht-lineare Potential ins Verhältnis zu setzen und um nur bereits kollabierte Strukturen zu zählen, berücksichtigen wir entweder sphärischen oder ellipsoiden Kollaps und vergleichen beide daraus resultierenden Modelle mit Temperaturfunktionen, die aus einer numerischen Simulation gewonnen wurden. Da in der Simulation für hohe Rotverschiebungen Abweichungen von der theoretischen Vorhersage gefunden werden, entwickeln wir ein analytisches Modell zur Berücksichtigung von Effekten, die durch das Verschmelzen von Galaxienhaufen zustande kommen. Wir bestimmen gemeinsam die kosmologischen Parameter $\Omega_{\mathrm{m0}}$ und $\sigma_8$ mit Hilfe von zwei verschiedenen Haufenkatalogen für unterschiedliche Temperaturdefinitionen und finden eine gute Übereinstimmung mit Beschränkungen, die von WMAP5 abgeleitet wurden. Indem wir, basierend auf dem *upcrossing* Kriterium, definieren, was wir theoretisch unter einer Detektion verstehen, fassen wir unseren analytischen Ansatz in zwei Dimensionen neu und benutzen ihn, um die Anzahldichte von unechten Detektionen, die von großskaliger Struktur und Schrotrauschen verursacht werden, in gefilterten Karten der Konvergenz des schwachen Gravitationslinseneffekts vorherzusagen. Übereinstimmungen mit einer numerischen Simulation entsprechen dem erwarteten Niveau.

## On the derivation of an X-ray temperature function without reference to mass and the prediction of weak-lensing number counts from the statistics of Gaussian random fields

***Abstract:*** We present a novel approach for the derivation of the X-ray temperature function for galaxy clusters, which is based on the statistics of Gaussian random fields applied to the cosmic gravitational potential. It invokes only locally defined quantities so that no reference to the cluster's mass is made. To relate linear and non-linear potential and to take into account only structures that have collapsed, we include either spherical- or ellipsoidal-collapse dynamics and compare both resulting models to temperature functions derived from a numerical simulation. Since deviations from the theoretical prediction are found in the simulation for high redshifts, we develop an analytic model to include the effects of mergers in our formalism. We jointly determine the cosmological parameters $\Omega_{\mathrm{m0}}$ and $\sigma_8$ from two different cluster samples for different temperature definitions and find good agreement with constraints from WMAP5. Introducing theoretically a refined detection definition based on the upcrossing criterion, we reformulate our analytic approach for 2D and use it to predict the number density of spurious detections caused by large-scale structure and shot noise in filtered weak-lensing convergence maps. Agreement with a numerical simulation is found at the expected level.

# Contents

# List of Figures

# List of Tables

# Introduction

Over the past decade, measurements of various cosmological probes have merged consistently to a picture of our Universe that is often called *the standard model of cosmology*. It is capable of explaining with only few parameters the overall evolution of the Universe which, according to that model, originated from an initial singularity, the *Big Bang*, approximately 13.7 billion years ago. Due to its main constituents, the cosmological constant $\Lambda$, originally introduced by Einstein into his General Theory of Relativity to allow for static world models, and a non-relativistic and non-interacting (or possibly mildly weakly interacting) unknown form of matter dubbed *cold dark matter*, it is called the $\Lambda$CDM model.

Despite its enormous success in understanding the expansion history of the Universe and the growth of structures from small initial perturbations to large objects like galaxies or galaxy clusters, the latter with a size of order 1 Mpc, the model also clearly states that the baryonic matter that we know from the standard model of particle physics, only contributes 4–5% to the total energy density of the Universe, whereas the rest is not fundamentally understood. Additionally, an epoch of accelerated expansion, called *inflation*, is needed in order to explain why the Universe that we observe today seems to be very close to spatially flat, and why the cosmic microwave background is almost perfectly isotropic with deviations of order $10^{-5}$. The easiest explanation is a scalar field slowly rolling down its potential. Yet, also the physical nature of this scalar field is unknown.

This implies several questions: What is the nature of the dark matter responsible for flat rotation curves measured in the outskirts of galaxies and needed to give galaxy clusters a mass large enough to explain lensing phenomena observed in the sky? What is the physical origin of the cosmological constant in the field equations of General Relativity, and why is it so small compared to estimates for the vacuum energy that arises from quantum field theory? Is it really the cosmological constant, or does a symmetry, which is still unknown to us, lead to the cancellation of the vacuum term so that $\Lambda = 0$? Then, another source must be found to be responsible for the observed accelerated expansion of the Universe, dubbed *dark energy*. It follows the notion of "dark matter", where again the word "dark" should express our ignorance of the deeper physical understanding. Various suggestions are discussed in the astronomical community, e.g. quintessence, k-essence, and chameleon fields. Most of them also involve a scalar field and most importantly, do vary with time, whereas a cosmological constant has always the same value. Could there be a relation to the field that led to the inflationary period or even to dark matter? Or do we simply rely on the wrong theory of gravity, and there are deviations from General Relativity on large cosmological scales?

The preceding list is surely not complete. In order to find deviations from the simple $\Lambda$CDM model, one has to compare theoretical predictions to observations carefully and to understand systematics well enough so that results are not biased towards wrong parameter values and deviations from the model predictions are not due to an incomplete or erroneous analysis of observational data. The even better alternative is to avoid systematics from the start. Although it is sometimes relatively easy to make theoretical predictions for some quantity, it turns out, however, that it is difficult or even impossible to compare these predictions to observational data since this quantity is in practice either difficult to measure observationally or even worse, it is even not an observable. In these two cases, it is then necessary to find a relation between the quantity used in the theoretical framework and another quantity that can be measured without any greater problems. If it is not possible to establish a relation theoretically, e.g. due to complex physics, one often has to rely on empirical relations introducing a large scatter in the relation and finally also in cosmological conclusions drawn from them.

Using the halo mass function of galaxy clusters in this context exactly reflects the aforementioned

issue. Although it can be relatively easily derived from the theory of structure formation, it requires the mass of a galaxy cluster to be measured, a quantity to which hardly any precise meaning can be given since it is a *global* quantity, requiring an integral over a volume. A galaxy cluster, however, does not have a sharp boundary and consequently, its mass is not an observable. Several definitions exist in the literature, based on spheres that include on average a certain multiple of the cosmic background density. If the overdensity is chosen too large, however, the resulting masses are core masses rather than cluster masses, if it is chosen too low, one needs to measure the halo's density profile in its outskirts, where it is only hardly measurable if not at all. A second problem is to fix the cluster's centre. Also here, different choices are possible, e.g. the minimum of the local gravitational potential or the maximum of the density. Both possibilities, however, do generally not coincide.

Determining a cluster's mass from numerical simulations reflects this problem in a different way. There, haloes are often defined by particles which are separated by a distance smaller than a certain linking length. This procedure is called the *friend-of-friend algorithm*. The choice of the linking length, however, is again only empirically motivated without any defendable physical motivation behind. The results are often highly irregularly shaped objects contradicting the usual assumptions of hydrostatical and thermal equilibrium. Two recent works deal with the discrepancies of halo mass definitions and underline the aforementioned problems. While More et al. (2011) find that the overdensity which can be associated with the value for the linking length wildly used in the literature is much lower than any of the overdensity thresholds typically chosen in the theoretical prescriptions, Anderhalden & Diemand (2011) argue that a non-negligible amount of particles participating in the gravitational collapse of a halo are usually not taken into account by the friend-of-friend algorithm so that the masses of haloes inferred from numerical simulations should be significantly higher.

In the present work, we propose a different approach. Instead of making the detour via the mass, we suggest to work directly with the cosmic gravitational potential, which is a *local* quantity. Assuming that the main contribution to the X-ray luminosity is due to thermal bremsstrahlung, and presuming virial equilibrium, the X-ray temperature in the centre of a galaxy cluster can be directly related to a minimum in the potential without invoking the cluster's mass. The statistics of Gaussian random field based on the formalism by Bardeen et al. (1986) are used to derive the number density of potential minima. In order to count small haloes correctly and to give satisfying results, a proper high-pass filter has to be introduced, removing perturbing large potential modes and large-scale potential gradients, so that first, the potential depth of a cluster is defined with respect to its direct vicinity and second, the constraint that the potential's gradient vanish is fulfilled also for smaller haloes.

The formalism used in the derivation of the X-ray temperature function is based on the spherical-collapse model to relate the linear and the non-linear evolution of potential depths. Inspired by the Sheth-Tormen mass function, which is built on ellipsoidal-collapse dynamics and in better agreement with numerical simulations than the classical Press-Schechter mass function, based on spherical collapse, we refine the ellipsoidal-collapse model of Bond & Myers (1996) by physically better motivated initial conditions for the ellipticity and prolaticity, an improved model for the contribution of the external gravitational shear, and by adding proper virialisation conditions for the individual axes. The results are then included in our derivation of the cluster temperature function. A comparison to a numerical simulation reveals that the latter version is in good agreement with a temperature function based on the so-called mass-based temperature definition at low redshift, while the spherical-collapse version is in good agreement with a temperature function based on the emission-weighted temperature, which is in better agreement with observationally inferred temperatures.

For high redshifts, however, the numerical temperature function starts deviating from our theoretical prediction based on the statistics of Gaussian random fields. We argue that the observed increase of objects for a given temperature with respect to our original theoretical prediction based on virial equilibrium is due to the influence of merger events and develop a simple analytic model that quantifies successfully the temperature boost caused by infalling clumps. Including merger effects in the theoretical prescription, we then find good agreement between our model and the results of the numerical

simulation. We quantify the influence of mergers on the joint determination of the two cosmological parameters $\Omega_{\mathrm{m0}}$ and $\sigma_8$ from two different cluster samples and conclude that their presence introduces a non-negligible bias, which is in qualitative agreement with a study by Randall et al. (2002), based on a numerical simulation. Thus, our analytic model of the temperature function including merger effects is a competitive alternative to computationally costly $N$-body studies.

A similar situation can be found in weak-lensing studies. Also here, numerical simulations are often necessary to make theoretical predictions that can then be compared to observations, e.g. to quantify the influence of by-chance projections of the large-scale structure and shot noise on halo number counts from filtered weak-lensing convergence maps. Using a refined definition of the so-called up-crossing criterion, originally proposed by Bardeen et al. (1986), we are able to predict analytically the number of contours at a given signal-to-noise ratio as a function of cosmological and survey parameters, again based on the statistics of Gaussian random fields, but now in two instead of three dimensions in contrast to the derivation of the temperature function. A comparison to results from a numerical simulation is in good agreement for different filters and scales typically used in the literature. Additionally, we are able to show that a filter proposed by Maturi et al. (2005) yields the smallest amount of contaminations from large-scale structure and shot noise.

This thesis is structured as follows. First, we introduce the basics of the ΛCDM model and non-relativistic structure formation in Chaps. 1 and 2, respectively, to provide the background knowledge needed for the derivation of the X-ray temperature function from the statistics of Gaussian random fields in Chap. 3. In Chap. 4, we present our refined ellipsoidal-collapse model and embed it into the theoretical description of the X-ray temperature function in Chap. 5, where we also present our model for the influence of mergers on the cluster temperature function and the joint analysis of $\Omega_{\mathrm{m0}}$ and $\sigma_8$. Chapter 6 is dedicated to the basics of weak gravitational lensing that are required for deriving the analytic model of weak-lensing number counts, which is then described in Chap. 7. Appendices A to C include supplementary material for the work presented in the chapters before, and App. D lists astronomical units and physical constants that are needed for the calculations presented in this thesis.

We write three- and higher-dimensional vectors with an arrow (e.g. $\vec{x}$, $\vec{r}$) while two-dimensional vectors, as needed for gravitational lensing, are written in boldface (e.g. $\boldsymbol{\theta}$, $\boldsymbol{\xi}$).

For a further introduction to the standard model of cosmology as well as a list of cosmological probes which led to our picture of the Universe and its enormous success, we refer to Bartelmann (2010a).

Parts of this work were published in the following papers:

- **Angrick, C.** & Bartelmann, M. (2009): *Statistics of gravitational potential perturbations: A novel approach to deriving the X-ray temperature function*. A&A, 494, 461.
- **Angrick, C.** & Bartelmann, M. (2010): *Triaxial collapse and virialisation of dark-matter haloes*. A&A, 518, A38+.
- Maturi, M., **Angrick, C.**, Pace, F., & Bartelmann, M. (2010): *An analytic approach to number counts of weak-lensing peak detections*. A&A, 519, A23+.
- **Angrick, C.** & Bartelmann, M. (2011): *The influence of mergers on the cluster temperature function and cosmological parameters derived from it*. A&A, submitted, `arXiv:1102.0458`.

# Chapter 1

# Cosmological background evolution

In the following chapter, we want to present the basic principles of the cosmological standard model based on Einstein's Theory of General Relativity and discuss relevant quantities that are necessary to better understand the following work and to put it into an overall context.

## 1.1 The Friedmann-Lemaître-Robertson-Walker model

On large cosmological scales, gravity is the most important force dictating the dynamical behaviour and the ultimate fate of the Universe. Since deviations from classical Newtonian dynamics on such large distances are non-negligible, a world model has to rely naturally on General Relativity (Einstein, 1915, 1916), the only model of gravity that has passed successfully all solar-system tests. Like in Special Relativity (Einstein, 1905), space and time are no longer separate but form a four-dimensional manifold called *space-time*. Its line element is given by

$$\mathrm{d}s^2 = g_{\mu\nu}\,\mathrm{d}x^\mu \mathrm{d}x^\nu \,, \tag{1.1}$$

where $g_{\mu\nu}$ is the metric and $0 \leq \mu, \nu \leq 3$. Due to the symmetry of $g_{\mu\nu}$, only ten of the sixteen components are independent.

General relativity establishes a connection between the properties of space-time with the energy content via the *field equations*

$$R_{\mu\nu} - \frac{1}{2} g_{\mu\nu} R - \Lambda g_{\mu\nu} = \frac{8\pi G}{c^4} T_{\mu\nu} \,, \tag{1.2}$$

where $R_{\mu\nu}$ is the *Ricci tensor*, which is constructed from the curvature tensor $R_{\mu\nu\kappa\lambda}$ by contraction $R_{\mu\nu} \equiv R^\lambda_{\ \mu\lambda\nu}$. Here and in the following, we adopt Einstein's summation convention so that we sum over an index that appears twice, once in an upper and once in a lower position. The *Ricci scalar* $R$ is constructed from the Ricci tensor by $R \equiv R^\lambda_{\ \lambda}$. $\Lambda$ is the *cosmological constant*, originally introduced by Einstein to allow static world models, $G$ is *Newtons's constant*, $c$ the speed of light, and $T_{\mu\nu}$ the *energy-momentrum tensor*. Equation (1.2) implies that matter (or more generally speaking, all forms of energy) directly influences space-time's geometry, which reversely dictates the motion of matter.

To simplify Eq. (1.2) and the metric $g_{\mu\nu}$, we make the following two assumptions:

(1) *The Universe is isotropic.*

Thinking of the *cosmic microwave background* (CMB), which originates from the time when radiation decoupled from matter and the Universe was ~380,000 years old, and its temperature fluctuations of order $\Delta T/T = 10^{-5}$ around $T = 2.73$ K and galaxy distributions at early times, we can say that at least in early cosmic history, this assumption was almost perfectly fulfilled. Although the galaxy distribution became more and more clumpy over the time due to gravitational attraction and therefore, the assumption is clearly violated, isotropy is restored again if averaged over scales of about 100 Mpc.

(2) *The Universe is homogeneous.*

This assumption is directly related to the Copernican Principle stating that we are at an average position in the Universe[1]. Since then it appears isotropic to any average observer at an arbitrary position, the Universe has to be also homogeneous, and its general properties do not depend on the space coordinates $x_i$ with $1 \leq i \leq 3$.

The only metric that is fully compatible with the aforementioned assumptions is the *Robertson-Walker* (RW) *metric*. Introducing the time coordinate $t$ and the spherical coordinates $(r, \theta, \phi)$, the line element can be written as

$$\mathrm{d}s^2 = c^2\mathrm{d}t^2 - a^2(t)\left[\frac{\mathrm{d}r^2}{1-Kr^2} + r^2(\mathrm{d}\theta^2 + \sin^2\theta\,\mathrm{d}\phi^2)\right] \tag{1.3}$$

(Robertson, 1935; Walker, 1935), where $a(t)$ is the *cosmological scale factor* taking into account a possible expansion or contraction of space without violating the assumptions of homogeneity and isotropy[2]. The coordinates $(r, \theta, \phi)$ do not depend on time and are thus *comoving* with freely falling observers (see Fig. 1.1 for an illustration).

The parameter $K$ accounts for the curvature of the three-dimensional space. Depending on the value of $K$, the following cases are possible:

(1) $K < 0$: open universe,

(2) $K = 0$: flat universe,

(3) $K > 0$: closed universe.

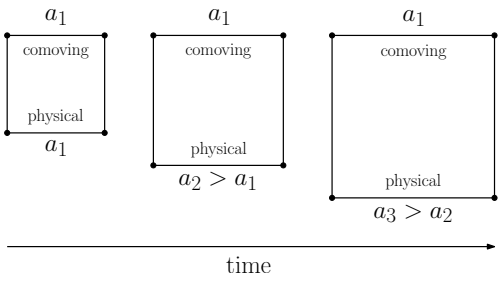


**Figure 1.1:** Comoving vs. physical coordinates. While in comoving coordinates, the distance between two objects with vanishing peculiar velocities is fixed at an arbitrary scale factor and stays constant over time, it increases in physical coordinates due to the expansion of the Universe.

In Fig. 1.2, we show a two-dimensional illustration of the three different curvature cases. Only in the flat case, the angles of a triangle add up to 180°, whereas the sum is > 180° in the closed case and < 180° in the open case.

Using the RW metric (1.3) and assuming additionally that the energy-momentum tensor $T_{\mu\nu}$ is that of a perfect fluid with the components $T_{00} = \rho c^2$, $T_{ii} = -p$, and all other entries are zero, the field equations (1.2) can be simplified a lot yielding the two *Friedmann equations* for the scale factor $a$,

$$\left(\frac{\dot{a}}{a}\right)^2 = \frac{8\pi G}{3}\rho - \frac{Kc^2}{a^2} + \frac{\Lambda}{3}\,, \tag{1.4}$$

$$\frac{\ddot{a}}{a} = -\frac{4\pi G}{3}\left(\rho + \frac{3p}{c^2}\right) + \frac{\Lambda}{3} \tag{1.5}$$

(Friedmann, 1922, 1924; Lemaître, 1927). Note that we have the freedom to normalise the scale factor such that we set it to unity today, $a(t_0) = 1$. Often, only the first equation (1.4) is called *the* Friedmann equation.

A RW metric that also fulfills Eqs. (1.4) and (1.5) is called a *Friedmann-Lemaître-Robertson-Walker* (FLRW) metric and the corresponding cosmological model a FLRW model.

[1] Strictly speaking, this is only true if one subtracts the motion of the Milky Way and hence Earth with respect to the CMB, which acts as a rest frame. This motion imprints a large dipole signal in the temperature anisotropies due to the Doppler effect, increasing the temperature in one direction and decreasing it in the other.

[2] Observational input is needed to distinguish if the Universe is expanding or contracting. This cannot be predicted inherently by theory. Since galaxies that are far away from us are redshifted instead of blueshifted, we can infer that the Universe is in fact expanding.

## 1.2 Cosmological redshift

The expansion of the Universe, parametrised by the scale factor $a(t)$, induces a redshift $z$ of light that reaches us from objects far away. Its dependence on $a$ can be derived from the FLRW metric as follows. We reparametrise the radial coordinate $r$ depending on the curvature,

$$r(\chi) = \begin{cases} K^{-1/2}\sin(K^{1/2}\chi) & (K>0) \\ \chi & (K=0) \\ (-K)^{-1/2}\sinh\left[(-K)^{1/2}\chi\right] & (K<0)\,. \end{cases} \tag{1.6}$$

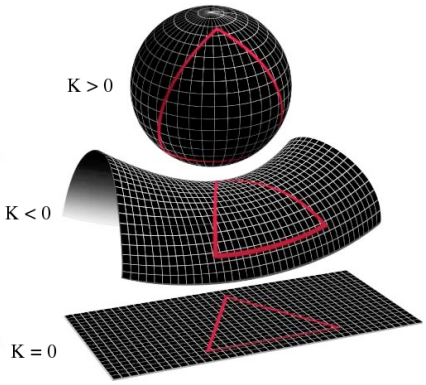


**Figure 1.2:** Two-dimensional illustration of the different curvature cases.[3]

In this way, the metric (1.3) can be rewritten as

$$\mathrm{d}s^2 = c^2\mathrm{d}t^2 - a^2(t)\left[\mathrm{d}\chi^2 + r^2(\chi)(\mathrm{d}\theta^2 + \sin^2\theta\,\mathrm{d}\phi^2)\right]. \tag{1.7}$$

Since light moves on geodesics with constant $\theta$ and $\phi$ and $\mathrm{d}s^2 = 0$, we have $c\,\mathrm{d}t = a(t)\,\mathrm{d}\chi$ or

$$\chi = \int_{t_{\mathrm{em}}}^{t_0} \frac{c\,\mathrm{d}t}{a(t)}\,, \tag{1.8}$$

where $t_{\mathrm{em}}$ is the time of emission. Consider now two consecutive maxima of a light wave that moves from the source to us,

$$\chi = \int_{t_{\mathrm{em}}}^{t_0} \frac{c\,\mathrm{d}t}{a(t)} = \int_{t_{\mathrm{em}}+\Delta t_{\mathrm{em}}}^{t_0+\Delta t_0} \frac{c\,\mathrm{d}t}{a(t)} = \int_{t_{\mathrm{em}}}^{t_0} \frac{c\,\mathrm{d}t}{a(t)} + \frac{c\Delta t_0}{a(t_0)} - \frac{c\Delta t_{\mathrm{em}}}{a(t_{\mathrm{em}})} \quad\Rightarrow\quad \frac{\Delta t_{\mathrm{em}}}{a(t_{\mathrm{em}})} = \frac{\Delta t_0}{a(t_0)}\,. \tag{1.9}$$

Since the time difference between the two maxima is proportional to the wave length $\lambda$, we get

$$\frac{\Delta t_0}{\Delta t_{\mathrm{em}}} = \frac{\lambda_0}{\lambda_{\mathrm{em}}} = 1 + \frac{\lambda_0 - \lambda_{\mathrm{em}}}{\lambda_{\mathrm{em}}} \equiv 1 + z = \frac{a(t_0)}{a(t_{\mathrm{em}})} \quad\Rightarrow\quad a(t_{\mathrm{em}}) = \frac{1}{1+z}\,, \tag{1.10}$$

where we have used that $a(t_0) = 1$ in the last step.

## 1.3 Dimensionless density parameters

We can rewrite Eq. (1.4) by taking into account different matter contributions to $\rho$ and $p$ and rephrase the cosmological-constant and the curvature term.

At first, we introduce the *Hubble function*

$$H(t) \equiv \frac{\dot{a}}{a}\,. \tag{1.11}$$

It is a time-dependent quantity, whose value today is the *Hubble constant* $H_0 \equiv H(t_0)$. For historical reasons, the Hubble constant is often given as $h$, defined as $H_0$ in units of 100 km s$^{-1}$ Mpc$^{-1}$.

Introducing the *equation-of-state parameter*

$$w \equiv \frac{p}{\rho c^2}\,, \tag{1.12}$$

we account for two different matter contributions, namely non-relativistic matter $\rho_{\mathrm{m}}$ with $w = 0$ and relativistic matter in form of radiation (and neutrinos) $\rho_{\mathrm{r}}$ with $w = 1/3$. The matter density itself

[3] http://www.talkorigins.org/faqs/astronomy/bigbang.html, slightly modified version.

consists again of two different contributions: $\rho_\mathrm{m} = \rho_\mathrm{bar} + \rho_\mathrm{CDM}$, where $\rho_\mathrm{bar}$ is the contribution from baryons and $\rho_\mathrm{CDM}$ the contribution of *cold dark matter*, which is an unknown form of non-luminous matter that seems to act only gravitationally. The word *cold* refers to the fact that this form of matter needs to be slow in order to be consistent with observations and is therefore non-relativistic. The existence of dark matter is primarily inferred from observations of the CMB and rotation curves of galaxies that flatten at large distances from their galactic centres.

In order to infer the dependence of the individual densities on the scale factor, we can combine Eqs. (1.4) and (1.5) to the *adiabatic equation*

$$\frac{\mathrm{d}}{\mathrm{d}t}\left(a^3\rho c^2\right) + w\rho c^2 \frac{\mathrm{d}}{\mathrm{d}t}\left(a^3\right) = 0 \,. \tag{1.13}$$

Inserting the equation-of-state parameter for relativistic and non-relativistic matter, respectively, we can conclude that $\rho_\mathrm{m} \propto a^{-3}$ and $\rho_\mathrm{r} \propto a^{-4}$. This can be understood intuitively since the matter density is diluted due to the expansion of the Universe and the photons, however, are redshifted additionally to the dilution, adding another factor $a^{-1}$ (see Sect. 1.2).

Using the Hubble function $H(t)$, we can define the *critical density*

$$\rho_\mathrm{c}(t) \equiv \frac{3H(t)}{8\pi G} \,, \tag{1.14}$$

which allows us to introduce the dimensionless *density parameters*

$$\Omega_\mathrm{m} \equiv \frac{\rho_\mathrm{m}}{\rho_\mathrm{c}} \quad \text{and} \quad \Omega_\mathrm{r} \equiv \frac{\rho_\mathrm{r}}{\rho_\mathrm{c}} \,, \tag{1.15}$$

while the contributions from the cosmological constant and the curvature can be expressed by

$$\Omega_\Lambda \equiv \frac{\Lambda}{3H^2} \quad \text{and} \quad \Omega_\mathrm{K} \equiv -\frac{Kc^2}{H^2} \,. \tag{1.16}$$

Denoting quantities *today* with the additional subscript '0', we can rewrite the Friedmann equation (1.4) as

$$H^2(a) = H_0^2 E^2(a) \equiv H_0^2\left(\Omega_{\mathrm{r}0}a^{-4} + \Omega_{\mathrm{m}0}a^{-3} + \Omega_{\mathrm{K}0}a^{-2} + \Omega_{\Lambda 0}\right) \,, \tag{1.17}$$

where we have also defined the *expansion function* of the Universe $E(a)$. All contributions scale with different powers of the scale factor. Dividing Eq. (1.4) by $H^2$ and using the definition of the density parameters, Eq. (1.15), one can easily see that the sum of all four density parameters has to fulfill $\Omega_\mathrm{m} + \Omega_\mathrm{r} + \Omega_\mathrm{K} + \Omega_\Lambda = 1$ for any $a$ .

Eq. (1.17) has some interesting implications:

- Since the radiation density scales with the largest negative power, there was a time in the early Universe when it was the dominant component.
- For very large $a$, the cosmological constant will finally take over so that $\dot{a} \approx H_0\sqrt{\Omega_{\Lambda 0}}\,a$. This will lead to a scale factor which behaves like $a \propto \exp(H_0\sqrt{\Omega_{\Lambda 0}}\,t)$, i.e. the Universe will ultimately expand exponentially.
- A Universe for which $\Omega_\mathrm{m} + \Omega_\mathrm{r} + \Omega_\Lambda = 1$ is spatially Euclidian.
- If the content of the Universe was only made of matter, the critical density would have another illustrative meaning. For $\rho_\mathrm{m} < \rho_\mathrm{c}$, the Universe would expand forever, for $\rho_\mathrm{m} > \rho_\mathrm{c}$ the Universe would collapse in a finite time, and for $\rho_\mathrm{m} = \rho_\mathrm{c}$, the expansion would slow down continuously but only stop in the limit $a \to \infty$.

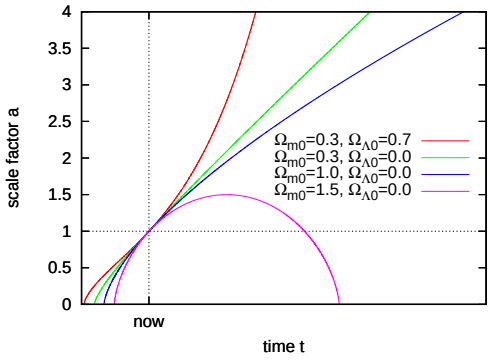


**Figure 1.3:** The scale factor as a function of time for various cosmological models.

| parameter | value | comments |
|---|---|---|
| $h$ | $0.704^{+0.013}_{-0.014}$ | assuming $\Omega_{K0} = 0$ |
| $\Omega_{bar0}$ | $0.0456 \pm 0.0016$ | |
| $\Omega_{CDM0}$ | $0.227 \pm 0.014$ | |
| $\Omega_{m0}$ | $0.272^{+0.016}_{-0.015}$ | |
| $\Omega_{\Lambda 0}$ | $0.728^{+0.015}_{-0.016}$ | |
| $t_0$ | $13.75 \pm 0.11$ Gyr | |
| $\Omega_{r0}$ | $\left(8.375^{+0.309}_{-0.333}\right) \times 10^{-5}$ | from CMB temperature (including neutrinos) |
| $\Omega_{K0}$ | $-0.0023^{+0.0054}_{-0.0056}$ | assuming $\Omega_{K0} \neq 0$ |
| $\Omega_{tot0}$ | $1.0023^{+0.0056}_{-0.0054}$ | |

**Table 1.1:** WMAP7+BAO+$H_0$ best fit values. We also included the contribution by neutrinos, which add a factor 1.68 to $\Omega_r$.

We illustrate these points for 4 different cosmological models in Fig. 1.3. Note also that the inferred age of the Universe varies depending on the cosmological parameters.

In Tab. 1.1, we list the cosmological parameters introduced so far and the age of the Universe $t_0$ as inferred from a joint analysis of the 7-year data release of the *Wilkinson microwave anisotropy probe* (WMAP7) together with data from *baryonic acoustic oscillations* (BAO)[4] and measurements of the Hubble constant $H_0$ (Komatsu et al., 2011 and WMAP's web page[5]). The evolution of the density parameters for this model with scale factor $a$ is shown in Fig. 1.4.

These findings leave us with a picture of the Universe which is rather disturbing since they indicate towards a spatially flat, Euclidian Universe in which the cosmological constant $\Lambda$ contributes ~73% to the total energy, whereas normal baryons contribute only ~4-5%, and the rest (~23%) is dark matter. The contribution from radiation is only of order $10^{-5}$ and therefore negligible today. Although ~95% of the energy content of our Universe is due to unknown dark components, the $\Lambda$CDM model, that we have sketched so far, is in remarkable agreement with other cosmological probes and became the *standard model of cosmology*.

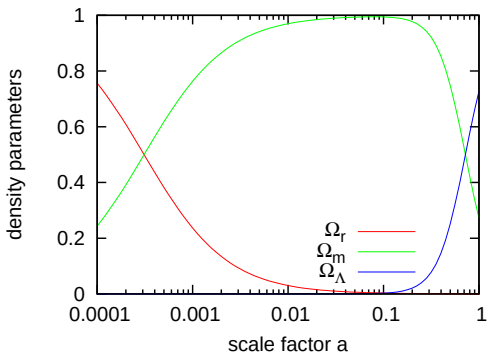


**Figure 1.4:** Evolution of the density parameters as a function of the scale factor for the cosmological model with WMAP7+BAO+$H_0$ best fit values.

One of the key goals of modern cosmology is to understand the physical nature of dark matter and the cosmological constant. While a possible dark-matter particle could be explained by extentions of the standard model of particle physics, like e.g. supersymmetry or axions, the origin of the $\Lambda$ term is more controversial. Basic calculations from quantum field theory suggest that the source of the cosmological constant could be found in the vacuum energy that contributes to the energy density of the Universe and hence acts as an additional source of gravity. But then, the term should be $\sim 10^{120}$ (!) times larger than observed. This enormous discrepancy is one of the reasons to think about other possible explanations of the $\Lambda$ term, which is in this much more general context named *dark energy*. Various concepts are discussed in the cosmological community.

[4] BAOs are oscillations in the primordial plasma as a result of the counter-acting forces of gravity pointing inwards and pressure in the baryonic part of the matter which is pointed outwards.

[5] http://lambda.gsfc.nasa.gov/product/map/current/

One suggests that the source of the dark energy is not the vacuum energy but an additional dynamical scalar field that acts, differently from a cosmological constant, on the right-hand side of Eq. (1.2). The most prominent representative of this class of models is the so-called *quintessence*. Following this approach, the influence of the vacuum energy on the curvature of space-time would need to vanish due to a yet unknown symmetry in quantum field theory. The only way to distinguish this scenario from a cosmological constant is to observe differences from the expectations of a flat ΛCDM model. Being able to make precise predictions as a function of the cosmological parameters is therefore very important to find slight deviations from the cosmological standard model that could point towards an explanation of the poorly understood nature of dark matter and dark energy.

## 1.4 Distance definitions

In an expanding and curved space-time, distance measurements are no longer uniquely defined. Care has to be taken that, depending on the cosmological probe, the correct distance definition of the following four is used for its theoretical description.

(1) The *proper distance* $D_{\mathrm{prop}}$.

The time that light needs to travel from one point to another defines $\mathrm{d}D_{\mathrm{prop}} \equiv -c\,\mathrm{d}t = -c\,\mathrm{d}a/\dot{a}$. Since both $a$ and $t$ are decreasing away from the observer while the distance should increase, the additional minus sign is introduced. Making use of the Friedmann equation (1.17), the proper distance between the redshifts $z_1$ and $z_2$ is given by

$$D_{\mathrm{prop}}(z_1, z_2) = -c \int_{a(z_1)}^{a(z_2)} \frac{\mathrm{d}a'}{\dot{a}'} = \frac{c}{H_0} \int_{a(z_2)}^{a(z_1)} \frac{\mathrm{d}a'}{a' E(a')} \,. \tag{1.18}$$

(2) The *comoving distance* $D_{\mathrm{com}}$.

The comoving distance measures the distance between a source and an observer relative to comoving instead of physical coordinates. Therefore, the expansion of the Universe, parametrised by the scale factor $a$ has to be divided out yielding $\mathrm{d}D_{\mathrm{com}} = \mathrm{d}D_{\mathrm{prop}}/a = -c\,\mathrm{d}a/(a\dot{a})$ so that

$$D_{\mathrm{com}}(z_1, z_2) = -c \int_{a(z_1)}^{a(z_2)} \frac{\mathrm{d}a'}{a'\dot{a}'} = \frac{c}{H_0} \int_{a(z_2)}^{a(z_1)} \frac{\mathrm{d}a'}{a'^2 E(a')} \,. \tag{1.19}$$

(3) The *angular-diameter distance* $D_{\mathrm{ang}}$.

Measuring the solid angle $\omega$ under which an object of radius $R$ can be seen, the angular-diameter distance to that object is defined as $D_{\mathrm{ang}} = \sqrt{\pi R^2/\omega}$. In expanding and curved space-times, this expression can be written as

$$D_{\mathrm{ang}}(z_1, z_2) = \begin{cases} \dfrac{c}{H_0} \dfrac{a(z_2)}{\sqrt{\Omega_{\mathrm{K0}}}} \sinh\left[\dfrac{H_0}{c} \sqrt{\Omega_{\mathrm{K0}}} D_{\mathrm{com}}(z_1, z_2)\right] & (\Omega_{\mathrm{K0}} > 0) \\ a(z_2) D_{\mathrm{com}}(z_1, z_2) & (\Omega_{\mathrm{K0}} = 0) \\ \dfrac{c}{H_0} \dfrac{a(z_2)}{\sqrt{-\Omega_{\mathrm{K0}}}} \sin\left[\dfrac{H_0}{c} \sqrt{-\Omega_{\mathrm{K0}}} D_{\mathrm{com}}(z_1, z_2)\right] & (\Omega_{\mathrm{K0}} < 0) \end{cases} \tag{1.20}$$

(see Schneider, 2006, p. 157 for a derivation and cf. also Eq. 1.6).

(4) The *luminosity distance* $D_{\mathrm{lum}}$.

Given the luminosity $L$ and the flux $S$ of source, the luminosity distance to that object is defined

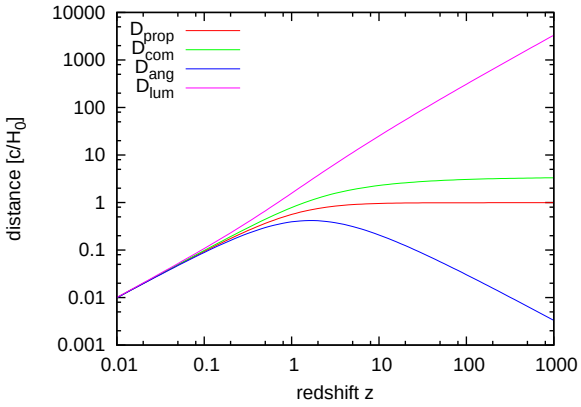


**Figure 1.5:** Dependence of the cosmological distances on redshift for a flat ΛCDM model with $\Omega_{m0} = 0.272$ and $\Omega_{\Lambda 0} = 0.728$.

as $D_{\rm lum} = \sqrt{L/(4\pi S)}$ and can be expressed via the *Etherington relation* with the help of $D_{\rm ang}$ yielding

$$D_{\rm lum}(z_1, z_2) = \left[\frac{a(z_1)}{a(z_2)}\right]^2 D_{\rm ang}(z_1, z_2) \; . \tag{1.21}$$

We show the dependence of the distances on redshift in Fig. 1.5. For small redshifts, all four distances yield approximately the same result. For $z \gtrsim 0.2$, however, they start deviating from each other. While both the proper and the comoving distance reach finite values for $z \to \infty$, the luminosity distance increases monotonically, and the angular-diameter distance has a maximum at $z \approx 1.7$ and decreases again for higher redshifts. The latter behaviour implies that an object which is moved to very high redshifts becomes larger again.

The fact that the curves for both the proper and the comoving distance flatten for large redshifts indicates that there exists a *particle horizon* $r_{\rm hor}$, i.e. light could have travelled only a finite distance between the Big Bang and any point in time. As a consequence, every particle could have been influenced by only a finite region of space over the cosmic time.

# 2 Chapter 2
# Structure formation

In the previous chapter, we assumed that the matter is homogeneously distributed in the Universe, inspired by observations of the CMB and the distribution of galaxies over large scales. In this chapter, we allow deviations from homogeneity and isotropy to form the structures in the Universe that we can observe today. These structures occupy over 30 orders of magnitudes in scale, starting from meters for asteroids to Megaparsecs for galaxy clusters, superclusters, and filaments, which finally form the cosmic web. The latter is perforated by large empty voids reaching sizes of about 100 $h^{-1}$ Mpc. We are later especially interested in galaxy clusters, the largest gravitationally bound objects in the observable Universe, with a size of order 1 $h^{-1}$ Mpc. They are mainly found at the intersections of cosmic filaments and grow over cosmic time via continuous accretion of matter and mergers with other galaxy clusters.

According to the theory of structure formation, all these objects originated from small initial perturbations in the matter distribution that collapsed under the influence of gravity and started forming small structures which then merged to form larger objects. This growth of structure is illustrated in Fig. 2.1, where we show different snapshots of the *Millennium simulation* by Springel et al. (2005). The initial perturbations can be seen in the temperature distribution of the CMB, leading to the relative temperature fluctuations of about $10^{-5}$ that we have already mentioned before.

It is an essential part of the cosmological standard model that these small perturbations were created during a short period of accelerated expansion shortly after the Big Bang, called *inflation*. One of its key features is that perturbations of the quantum level were enormously inflated, leading to an almost perfect Gaussian distribution. Since the Gaussianity of the initial perturbations is essential for the next chapters, we will mention the main ideas and results of inflation very shortly in an own section. Additionally, we will introduce basic concepts of structure formation like the spherical-collapse model and mass functions.

## 2.1 Newtonian perturbation equations

Although in principle, General Relativity is the correct framework in which the following calculations should be carried out, it turns out that it is sufficient to use Newtonian theory to derive the perturbation dynamics and neglect relativistic effects like the finiteness of the speed of light or curvature of spacetime since the structures that we want to study ($\sim$1 $h^{-1}$ Mpc) are small compared to the Hubble radius $r_\mathrm{H} = c/H_0$ ($\sim$3,000 $h^{-1}$ Mpc). The latter is a good approximation for the particle horizon $r_\mathrm{hor}$. In the following, we will derive the evolution equations for perturbations in the cosmic fluid, which is basically a mixture of baryons and dark matter. Since we will only consider perturbations on scales that are sufficiently large enough not to be influenced in their evolution by radiation, we can neglect its contribution here. Furthermore, the energy density due to the cosmological constant with $w = -1$ cannot clump and hence does not form perturbations. As in the previous chapter, the cosmic fluid is considered to be an ideal fluid without any viscosity and friction.

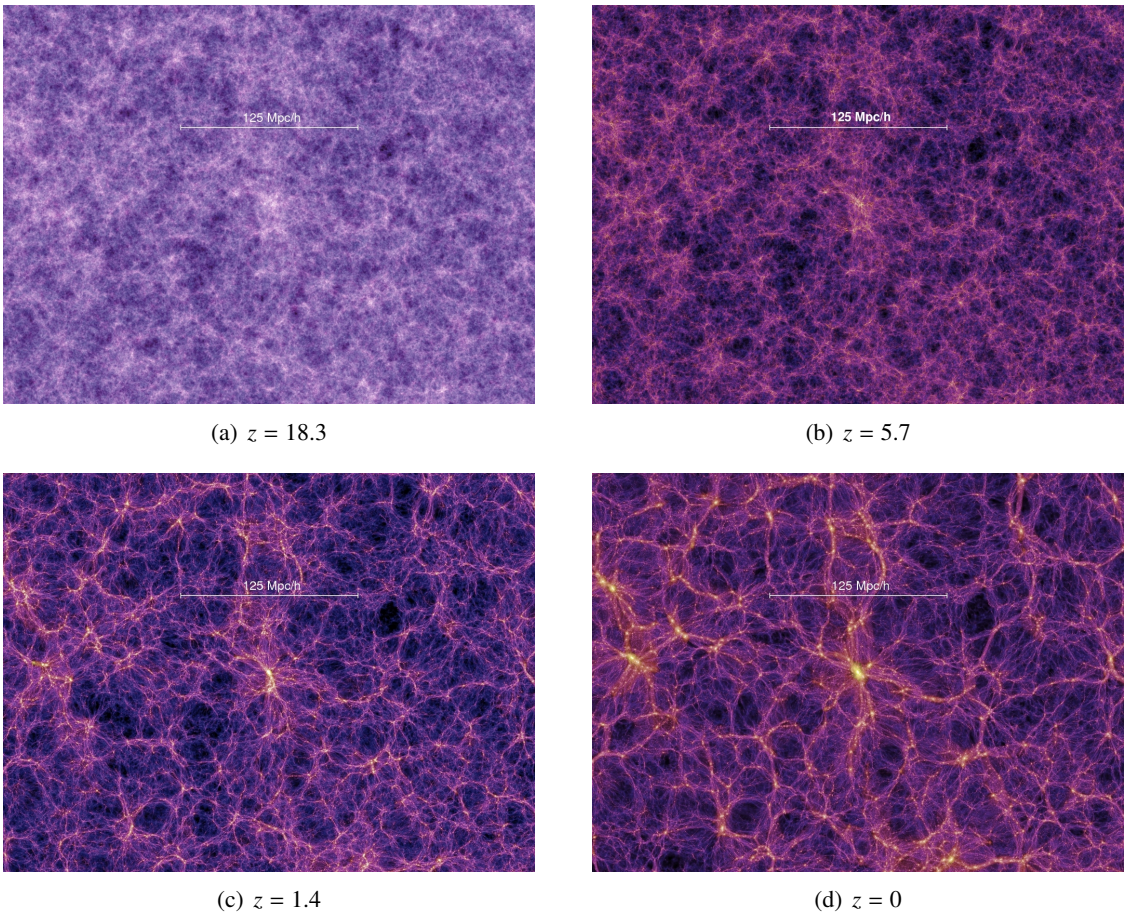


(a) $z = 18.3$ (b) $z = 5.7$

(c) $z = 1.4$ (d) $z = 0$

**Figure 2.1:** Snapshots of the Millennium simulation at four different redshifts. Note that the scale is given in comoving coordinates. In the centre, a large galaxy cluster forms due to accretion of material and mergers with smaller clumps.[6]

Since we deal with Newtonian gravity, the equation that relates the density $\rho$ with the gravitational field $\Phi$ is *Poisson's equation*

$$\Delta\Phi = 4\pi G\rho \,, \tag{2.1}$$

where $\Delta$ is the Laplacian defined as $\Delta \equiv \partial_x^2 + \partial_y^2 + \partial_z^2$ in physical coordinates. Two other important equations account for the conservation of mass and the conservation of momentum. The first one is the *continuity equation*,

$$\frac{\partial\rho}{\partial t} + \vec{\nabla}\cdot(\rho\vec{v}) = 0 \,, \tag{2.2}$$

the second one is *Euler's equation*,

$$\frac{\partial\vec{v}}{\partial t} + (\vec{v}\cdot\vec{\nabla})\vec{v} = -\frac{\vec{\nabla}p}{\rho} + \vec{\nabla}\Phi \,. \tag{2.3}$$

Note that from now on, all quantities depend on position $\vec{x}$ and time $t$ since we allow for deviations from homogeneity and isotropy! Consequently, the terms on the right-hand side of Eq. (2.3), which represent forces due to gradients in the pressure and the gravitational field, respectively, do not vanish.

We decompose all relevant quantities into a part that represents the background value and therefore only depends on time and another part that represents a small perturbation and hence depends on time

[6] http://www.mpa-garching.mpg.de/galform/millennium/

and position,

$$\rho(\vec{x}, t) = \rho_\mathrm{b}(t) + \delta\rho(\vec{x}, t) \,, \tag{2.4}$$

$$\vec{v}(\vec{x}, t) = \vec{v}_\mathrm{b}(t) + \delta\vec{v}(\vec{x}, t) \,, \tag{2.5}$$

where the first term on the right-hand side denotes the background value and the second term the perturbation. If we denote physical coordinates with $\vec{r}$ and comoving coordinates with $\vec{x}$, we can write the background velocity as $\vec{v}_\mathrm{b} = H_0\vec{r}$ and identify it with the *Hubble* or *recession velocity* originating from the expansion of the Universe, while the second term $\delta\vec{v} = a\dot{\vec{x}}$ takes into account the peculiar velocity of the perturbation, deviating from the mean cosmic flow. We introduce the same decomposition for the pressure and the gravitational field accordingly,

$$p(\vec{x}, t) = p_\mathrm{b}(t) + \delta p(\vec{x}, t) \,, \tag{2.6}$$

$$\Phi(\vec{x}, t) = \Phi_\mathrm{b}(t) + \delta\Phi(\vec{x}, t) \,. \tag{2.7}$$

Since a spatially constant background density is only mathematically consistent with both the Euler equation (2.3) and Poisson's equation (2.1) if $\rho_\mathrm{b} = 0$, we impose the *ad-hoc* assumption that Poisson's equation only relates the *perturbations* of the potential and the density with each other, set $\Phi_\mathrm{b} = 0$, and call the perturbation itself $\Phi(\vec{x}, t)$.[7]

Inserting the former definitions into Eqs. (2.2) and (2.3), we see that the gradients act only on the perturbation quantities since the background quantities do not depend on position. Additionally, we introduce the *comoving peculiar velocity* $\vec{u} \equiv \delta\vec{v}/a$ and the *density contrast* $\delta \equiv \delta\rho/\rho_\mathrm{b} = \rho/\rho_\mathrm{b} - 1$. A completely empty void, i.e. $\rho = 0$, therefore has a density contrast $\delta = -1$. The last step is to switch from physical to comoving coordinates, where have to take into account the respective transformation for the Laplacian and the time derivative as follows,

$$\Delta_x = a^2\Delta_r \,, \tag{2.8}$$

$$\left(\frac{\partial}{\partial t}\right)_x = \left[\left(\frac{\partial}{\partial t}\right)_r + H\vec{x}\cdot\vec{\nabla}_x\right] \,. \tag{2.9}$$

Since Eqs. (2.2) and (2.3) have to be fulfilled separately for the background and the perturbation quantities and taking into account only linear terms, the dynamics of the perturbations are described by the following three equations,

$$\Delta\Phi = 4\pi G\rho_\mathrm{b}a^2\delta \,, \tag{2.10}$$

$$\dot{\delta} + \vec{\nabla}\cdot\vec{u} = 0 \,, \tag{2.11}$$

$$\dot{\vec{u}} + H\vec{u} = -\frac{\vec{\nabla}(\delta p)}{a^2\rho_\mathrm{b}} + \frac{\vec{\nabla}\Phi}{a^2} \,, \tag{2.12}$$

where the first equation is based on the aforementioned assumption that only the perturbations of the potential and the density are related by Poisson's equation, written in comoving coordinates.

Since we have only three equations for four variables ($\delta$, $\vec{u}$, $\Phi$, $\delta p$), we need an additional constraint to have a closed system of equations. Introducing the sound speed $c_\mathrm{s}$, we can relate the pressure to the density contrast via

$$\delta p = c_\mathrm{s}^2\,\delta\rho = c_\mathrm{s}^2\,\rho_\mathrm{b}\delta \,. \tag{2.13}$$

## 2.2 Linear evolution of the density contrast

Equations (2.10–2.13) can be combined to yield one single equation for the density contrast $\delta$. First, we can combine the divergence of Eq. (2.12) with the time derivative of Eq. (2.11), and second, we

[7] This represents the "Jeans swindle", named after Sir James Jeans, cf. Binney & Tremaine (1987), pp. 287f.

can express $\delta p$ and $\Phi$ as a function of the density contrast using Eqs. (2.10) and (2.13). In this way, we arrive at a second-order differential equation for the density contrast,

$$\ddot{\delta} + 2H\dot{\delta} - 4\pi G\rho_\mathrm{b}\delta - \frac{c_\mathrm{s}^2}{a^2}\Delta\delta = 0\,. \tag{2.14}$$

The density contrast cannot be treated as a function of time only since Eq. (2.14) still has a spatial dependence via $\Delta\delta$ in the last term. The trick is to go from real space to Fourier space with the Fourier transformations

$$\delta(\vec{x},t) = \int_{-\infty}^{\infty} \frac{\mathrm{d}^3k}{(2\pi)^3}\,\hat{\delta}(\vec{k},t)\,\mathrm{e}^{-\mathrm{i}\vec{k}\cdot\vec{x}} \quad \text{and} \quad \hat{\delta}(\vec{k},t) = \int_{-\infty}^{\infty} \mathrm{d}^3x\,\delta(\vec{x},t)\,\mathrm{e}^{\mathrm{i}\vec{k}\cdot\vec{x}}\,. \tag{2.15}$$

Using additionally that $\Delta\delta(\vec{x},t) \rightarrow -\vec{k}^2\hat{\delta}(\vec{k},t)$ , Eq. (2.14) can be written in Fourier components as

$$\ddot{\hat{\delta}} + 2H\dot{\hat{\delta}} + \left(\frac{c_\mathrm{s}^2}{a^2}k^2 - 4\pi G\rho_\mathrm{b}\right)\hat{\delta} = 0\,. \tag{2.16}$$

Introducing $\omega \equiv \sqrt{c_\mathrm{s}^2k^2/a^2 - 4\pi G\rho_\mathrm{b}}$, the previous equation can be written as a damped oscillation equation with frequency $\omega$, which is real if $c_\mathrm{s}^2k^2/a^2 \geq 4\pi G\rho_\mathrm{b}$ and imaginary otherwise. The case $\omega = 0$ defines the *Jeans length*

$$\lambda_\mathrm{J} = \frac{2\pi}{k_\mathrm{J}} \equiv c_\mathrm{s}\sqrt{\frac{\pi}{G\rho_\mathrm{b}}}\,. \tag{2.17}$$

Perturbations of size $\lambda < \lambda_\mathrm{J}$ will experience a damped oscillation, perturbations with $\lambda > \lambda_\mathrm{J}$ will either grow or decay. Equation (2.16) can be further simplified for dark matter since we can treat it as a pressure-less fluid with $c_\mathrm{s} = 0$ yielding

$$\ddot{\hat{\delta}} + 2H\dot{\hat{\delta}} - 4\pi G\rho_\mathrm{b}\hat{\delta} = 0\,. \tag{2.18}$$

Since dark matter is the dominant matter component (cf. Tab. 1.1) providing the potential wells in which the baryonic matter can fall, the previous equation can be used to describe the linear cosmic structure formation on large and intermediate scales. On small scales, however, the pressure of the baryonic component and thus the existence of the Jeans length (2.17) cannot be neglected.

The solution of Eq. (2.18) includes one growing and one decaying mode. But since the decaying mode is not relevant for structure formation, we focus on the growing mode. Equation (2.18) does not depend on the wave number $k$ and hence, the solution can be expressed as

$$\delta(t) = \delta(t_0)D_+(t)\,, \tag{2.19}$$

defining the *linear growth factor* $D_+$. Thus, the time evolution of the linear density contrast is completely described by $D_+(t)$. Usually, it is normalised such that $D_+ = 1$ today and smaller in the past. But instead of expressing it as a function of time, we can also consider it as a function of the scale factor $a$. For an Einstein-de Sitter (EdS) cosmology with $\Omega_\mathrm{m} = 1$ and $\Omega_\Lambda = 0$, it can be easily shown that $D_+(a) = a$ so that the linear evolution of the density contrast is simply given by the scale factor. For more general cosmologies, $D_+$ deviates from this evolution, and Eq. (2.18) can be solved only numerically. The

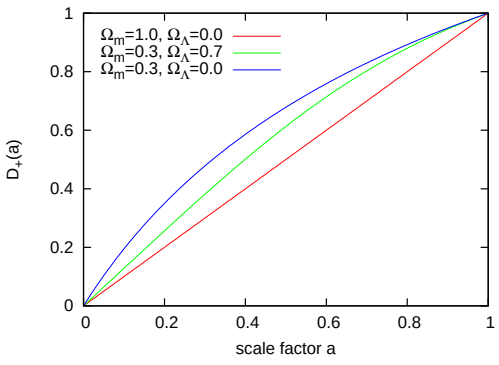


**Figure 2.2:** Evolution of the growth factor $D_+$ as a function of the scale factor for two flat and one open cosmological model.

solution for models involving only matter and a cosmological constant can be approximated by the following fitting formula of Carroll et al. (1992),

$$D_+(a) = \frac{5a}{2}\Omega_\mathrm{m}(a)\left\{\Omega_\mathrm{m}^{4/7}(a) - \Omega_\Lambda(a) + \left[1+\frac{1}{2}\Omega_\mathrm{m}(a)\right]\left[1+\frac{1}{70}\Omega_\Lambda(a)\right]\right\}^{-1} . \tag{2.20}$$

We show the dependence of $D_+$ on the scale factor for three different cosmologies in Fig. 2.2.

We want to note again that the previous results are only valid for small perturbations since we have neglected higher order terms in the derivation. At latest for $\delta \sim 1$, the linear treatment that we have followed so far breaks down and non-linearities become important. However, the non-linear evolution cannot be treated analytically in a simple way, one has to refer to other techniques like the Zel'dovich approximation for mildly non-linear regimes (Sect. 2.6) or the spherical-collapse model for spherical and homogeneous overdensities (Sect. 2.7). In order to follow in general the complete non-linear evolution, one usually has to rely on large cosmological $N$-body simulations, although semi-analytic models based on renormalised perturbation theory are currently being developed and refined (e.g. Crocce & Scoccimarro, 2006; Pietroni, 2008; Anselmi et al., 2010).

## 2.3 Statistical treatment

The density field can be modelled as a random field that has to obey the two fundamental assumptions of homogeneity and isotropy. Therefore, its statistical properties like e.g. variance and mean must not depend on position or direction. The random field can be described by $n$-point correlators,

$$\langle\delta(\vec{x}_1)\,\delta(\vec{x}_2)\ldots\delta(\vec{x}_n)\rangle , \tag{2.21}$$

quantifying the correlation between $n$ points in the sky. The easiest of them is the 2-point correlator which defines the *correlation function*

$$\xi(y) \equiv \langle\delta(\vec{x})\,\delta(\vec{x}+\vec{y})\rangle . \tag{2.22}$$

Note that it can only depend on the distance $y = |\vec{y}|$ due to homogeneity and isotropy. Instead of correlating the density contrast in real space, we can also correlate two Fourier modes, defining the *power spectrum* $P(k)$ by

$$\langle\delta(\vec{k})\,\delta(\vec{k}')\rangle \equiv (2\pi)^3 P(k)\,\delta_\mathrm{D}(\vec{k}-\vec{k}') , \tag{2.23}$$

where $\delta_\mathrm{D}$ is *Dirac's delta distribution*. The correlation function and the power spectrum are related to each other by a Fourier transformation. Also the power spectrum can only depend on the modulus of $\vec{k}$ due to the fundamental cosmological assumptions.

Higher order equivalents to the power spectrum exist (bispectrum, trispectrum, ...). However, we focus only on the lowest order here since we will show in Sect. 2.4.2 that the linear density contrast can be modelled by a Gaussian random field, which is fully described by the power spectrum. Its *spectral moments* are defined by

$$\sigma_j^2 \equiv \int_0^\infty \frac{\mathrm{d}k}{2\pi^2} P(k)\,k^{2j+2} , \tag{2.24}$$

where $\sigma_0^2 \equiv \sigma^2$ is the *variance* and $\sigma$ the *standard deviation*.

One often wants to filter the density contrast field on a certain scale $R$, e.g. to extract some information of objects with that size. This is done by a convolution with a window function $W_R$ of scale $R$ in real space or a multiplication with its Fourier transform $\hat{W}_R(k)$ in Fourier space,

$$\delta_R(\vec{x}) \equiv \int \mathrm{d}^3y\,\delta(\vec{y})W_R(|\vec{x}-\vec{y}|) \quad \text{and} \quad \hat{\delta}_R(k) = \hat{\delta}(k)\hat{W}_R(k) , \tag{2.25}$$

respectively. Combining Eqs. (2.19) and (2.23), the time-dependent variance of the filtered density contrast is given by

$$\sigma_R^2(a) = \int_0^\infty \frac{k^2\,\mathrm{d}k}{2\pi^2} D_+^2(a) P(k) \hat{W}_R^2(k)\ . \tag{2.26}$$

In most cases, a top-hat in real space is chosen as filter function, but also other choices like Gaussian smoothing are possible. The top-hat in real and Fourier space is given by

$$W_R(\vec{x}) = \frac{\theta_\mathrm{H}(R - |\vec{x}|)}{\frac{4\pi}{3}R^3} \quad \text{and} \quad \hat{W}_R(k) = \frac{3(\sin kR - kR\cos kR)}{k^3R^3}\ , \tag{2.27}$$

respectively, where $\theta_\mathrm{H}$ is *Heaviside's step function*. The square root of the density field's variance on a scale of 8 $h^{-1}$ Mpc today is $\sigma_8$ and contains information on the amplitude of the density fluctuations. The WMAP7+BAO+$H_0$ joint analysis yields $\sigma_8 = 0.809 \pm 0.024$ (Komatsu et al., 2011).

## 2.4 Initial perturbations from an inflationary phase

Originally introduced to solve two fundamental problems in cosmology, the theory of inflation provides an explanation for the origin of structures "for free". Before we will focus on the latter, we briefly sketch the reasons for the necessity of an inflationary epoch and its main properties.

### 2.4.1 Motivation and basic concepts

The standard model of cosmology presented in Chap. 1 is not complete yet. In fact, two key observations, namely the almost perfect isotropy of the CMB and the flatness of space cause severe problems from a theoretical point of view, named the *horizon problem* and the *flatness problem*, respectively.

(1) *Horizon problem.*

As already mentioned in Chap. 1, the temperature of the CMB is, independent of the direction, the same with tiny fluctuations of order $10^{-5}$. In order to achieve this enormous equality, the plasma of electrons and atomic nuclei must have been in thermal equilibrium when they finally combined and released the photons of the CMB at redshift $z \approx 1020$. However, at the end of Sect. 1.4, we have also argued that there exists a particle horizon, i.e. every particle can only be influenced by events inside his horizon. Calculating the size of these causally connected regions at the time of recombination yields patches with a diameter of $\sim 2°$ in the sky (Liddle, 1999). But how can regions for which it was not possible to have communicated with each other have (almost) identical temperatures?

(2) *Flatness problem.*

Dividing Friedmann's equation (1.4) by $H^2$ and leaving only the curvature term on the right-hand side yields

$$\Omega_\mathrm{tot} - 1 = \frac{Kc^2}{a^2H^2}\ , \tag{2.28}$$

where $\Omega_\mathrm{tot} = \Omega_\mathrm{m} + \Omega_\mathrm{r} + \Omega_\Lambda$. One can show, using again Friedmann's equation, that $a \propto t^{1/2}$ in the radiation-dominated era, and $a \propto t^{2/3}$ in the matter-dominated era. Together with the definition of the Hubble parameter $H = \dot{a}/a$ and $\dot{a} \propto n\,t^{n-1}$, where $n$ is either $1/2$ or $2/3$, we arrive at

$$\Omega_\mathrm{tot} - 1 \propto \begin{cases} t & \text{(radiation domination)} \\ t^{2/3} & \text{(matter domination)}\ . \end{cases} \tag{2.29}$$

Thus, any tiny deviation from unity for $\Omega_{\rm tot}$ shortly after the beginning of the Universe would lead to a large deviation now and therefore to a non-negligible curvature, which is in conflict with observations (see Tab. 1.1). This marks a fine-tuning problem, since at the electro-weak scale with $t \sim 10^{-11}$ s after the Big Bang, the deviation must have been $|\Omega_{\rm tot} - 1| < O(10^{-27})$ to be consistent with observations (Liddle, 1999).

In the standard picture without inflation, the comoving Hubble radius $c/(aH)$ increases with time since the Big Bang, until the cosmological constant finally takes over. If it was possible to find a mechanism that lets it decrease with time,

$$\frac{\mathrm{d}}{\mathrm{d}t}\left(\frac{c}{aH}\right) = \frac{\mathrm{d}}{\mathrm{d}t}\left(\frac{c}{\dot{a}}\right) < 0 \quad \Rightarrow \quad \ddot{a} > 0\,, \tag{2.30}$$

the total energy density $\Omega_{\rm tot}$ would have been driven towards unity according to Eq. (2.28). The second Friedmann equation (1.5) implies that this is the case if $p < -1/3\,\rho c^2$ and thus $w < -1/3$. If the inflationary period lasted long enough, the deviation of the total energy density from unity after inflation would be small enough not to deviate significantly from unity even today and thus, the flatness problem would be solved.

Additionally, an inflationary period would also solve the horizon problem, since a shrinking comoving Hubble radius would make it possible that distinct patches of the sky had been in causal contact before inflation started.

But how can we fulfill the condition that the pressure be negative enough ($w < -1/3$) to have an accelerated expansion? Although the cosmological constant $\Lambda$ has $w = -1$, its value is so small that it took over only recently. In the past, however, matter and radiation density were much larger so that another mechanism is needed. The easiest realisation can be constructed with a scalar field $\Psi$ rolling down its potential very slowly. This field is called the *inflaton field*, and from a particle-physics perspective, a spin-0 particle can be associated with it. Its pressure and energy density are given by

$$p = \frac{1}{2}\dot{\Psi}^2 - V(\Psi) \quad \text{and} \quad \rho c^2 = \frac{1}{2}\dot{\Psi}^2 + V(\Psi)\,, \tag{2.31}$$

respectively. If $V(\Psi) \gg \dot{\Psi}$, we have $w = p/(\rho c^2) \approx -1$, and inflation can last long enough to solve the horizon and flatness problems. Assuming that the inflaton field dominated the energy density of the early Universe, the right-hand side of Eq. (1.4) would be dominated by the potential term yielding

$$H^2 \approx \frac{8\pi G}{3c^2} V(\Psi)\,. \tag{2.32}$$

### 2.4.2 Origin of structures

An inflationary period shortly after the Big Bang not only solves the flatness and the horizon problem, but also yields an explanation for the tiny fluctuations that are imprinted on the CMB and finally led to the formation of structures. Like any other fields, the inflaton field experiences quantum fluctuations due to Heisenberg's uncertainty principle. However, since it satisfies the condition $V(\Psi) \gg \dot{\Psi}$, the Universe expands so rapidly that these quantum fluctuations are "frozen" and cannot evolve any further due to the sudden disruption of causality. The power spectrum of the corresponding fluctuations in the gravitational potential times $k^3$ is approximately constant over time since it obeys

$$k^3 P_\Phi = \left(\frac{H}{\dot{\Psi}}\right)^2 \left(\frac{H}{2\pi}\right)^2 \approx \text{const.} \tag{2.33}$$

(cf. Liddle & Lyth, 2000, p. 186 and also Eq. 2.32). Assuming that the inflaton field decays at the end of inflation into other particles so that the latter inherit the perturbations from the inflaton, and using the Fourier transform of Poisson's equation (2.10), we can relate the Fourier modes of the

perturbations in the gravitational potential with the ones of the density contrast by $-k^2\hat{\Phi} \propto \hat{\delta}$. But since then $k^4 P_\Phi \propto P_{\mathrm{ini}}$, where $P_{\mathrm{ini}}$ is the initial power spectrum of density fluctuations, we expect that $P_{\mathrm{ini}} \propto k^n$ with $n = 1$ due to Eq. (2.33).

However, as we have already mentioned, inflation has to stop at some time. Hence, $V(\Psi)$ and $\dot{\Psi}$ have to vary slowly to yield $\dot{\Psi} \sim V(\Psi)$, and the accelerated phase finally comes to an end. Since $k^3 P_\Phi$ therefore slightly deviates from being constant, we expect also a small deviation from $n = 1$. Indeed, the WMAP7+BAO+$H_0$ analysis yields $n = 0.963 \pm 0.012$ (Komatsu et al., 2011).

Another import conclusion from the theory of inflation, especially for this work, is the following. A single perturbation in the inflaton field can be understood as a linear superposition of frozen vacuum fluctuations, each represented by a Fourier mode that is independent from the others. According to the central limit theorem, the resulting inflaton is Gaussian distributed for any point $\vec{x}$ in space. Since the density field results from the decaying inflaton field, it also obeys Gaussian statistics so that the probability to find a density contrast between $\delta$ and $\delta + \mathrm{d}\delta$ at position $\vec{x}$ is given by

$$p[\delta(\vec{x})]\,\mathrm{d}\delta = \frac{1}{\sqrt{2\pi}\,\sigma} \exp\left(-\frac{\delta^2(\vec{x})}{2\sigma^2}\right) \mathrm{d}\delta\,, \tag{2.34}$$

where $\sigma^2$ is the variance of the density field defined by its power spectrum. Note that a small deviation from Gaussianity is expected due to the end of inflation after a finite time. These non-Gaussianities, however, are so small that we neglect them in the further considerations. Their effects on structure formation have been studied extensively, see e.g. Matarrese et al. (2000), Lo Verde et al. (2008), and Fedeli et al. (2009).

## 2.5 Shape of the power spectrum

Different Fourier modes of the density contrast reenter the horizon after inflation at different times. While for small-scale modes, this already happens at the radiation-dominated time, large-scale modes enter much later, when the Universe was dominated by matter. This has important consequences for the shape of the power spectrum.

While we have already seen that during matter domination, the density contrast evolves $\propto a$, Eq. (2.18) implies that for the radiation-dominated era, $\delta \propto a^2$. Modes that are still outside the horizon can grow without any inhibition, while modes that have entered the horizon feel the radiation pressure, which stops their growth almost completely. When the Universe becomes matter-dominated, the density modes starts growing again. Density modes, that are large enough not to enter the horizon before matter-radiation equality at $a_{\mathrm{eq}}$ hence do not feel this growth suppression. However, modes that entered before $a_{\mathrm{eq}}$ are suppressed by a factor $a_{\mathrm{enter}}^2/a_{\mathrm{eq}}^2$, where $a_{\mathrm{enter}}$ is the scale factor at horizon entry (see Fig. 2.3 for an illustration). Taking into account that the Hubble radius $r_{\mathrm{H}} = c/H$ scales $\propto a^2$ according to Eq. (1.17) during radiation domination, we can establish a relation between the wave vector $k$ and $a_{\mathrm{enter}}$. Density modes that enter the horizon have a physical wavelength

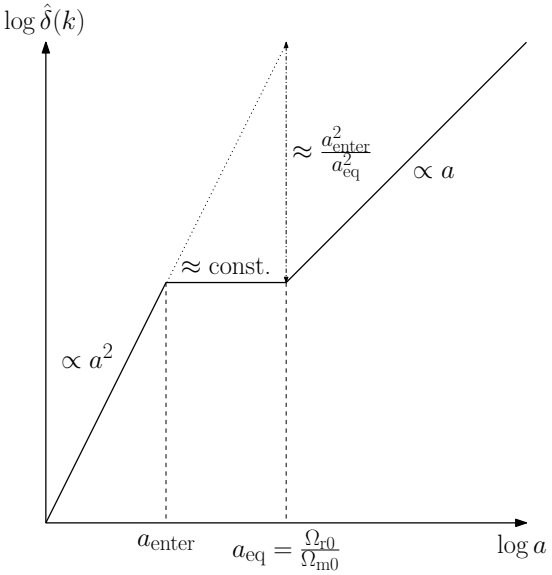


**Figure 2.3:** Growth of density modes and its suppression during the radiation-dominated era.

that is equal to the Hubble radius per definition so that

$$\begin{aligned} a_{\rm enter}\,\lambda = a_{\rm enter}\frac{2\pi}{k} &\propto a_{\rm enter}^2 \\ \Rightarrow \quad a_{\rm enter} &\propto k^{-1}\ . \end{aligned} \tag{2.35}$$

The suppression factor for a mode with wave vector $k$ that enters the horizon during radiation domination is therefore given by

$$f_{\rm sup} \equiv \frac{a_{\rm enter}^2}{a_{\rm eq}^2} = \frac{k_{\rm eq}^2}{k^2}\ , \tag{2.36}$$

where $k_{\rm eq}$ is the wave vector that enters the horizon at $a_{\rm eq}$. Since the power spectrum $P(k) \propto |\hat{\delta}|^2$, the suppression factor $f_{\rm sup}$ enters quadratically. In Sect. 2.4.2, we have shown that the initial power spectrum $P_{\rm ini}$ is expected to be $\propto k^n$ with $n \approx 1$. Including the suppression of modes that entered the horizon before matter-radiation equality, the power spectrum is expected to have a shape as follows,

$$P(k) \propto \begin{cases} P_{\rm ini}(k) \\ f_{\rm sup}^2\, P_{\rm ini}(k) \end{cases} \propto \begin{cases} k & (k \le k_{\rm eq}) \\ k^{-3} & (k > k_{\rm eq})\ . \end{cases} \tag{2.37}$$

Since the transition from the radiation-dominated to the matter-dominated phase is not as sharp as illustrated above, the shape of the power spectrum is a bit more complex. The conversion from an initial state of $\hat{\delta}$ at $a_{\rm ini}$ to a later state at $a_{\rm fin}$, excluding the growth expressed by the linear growth factor $D_+$, is given by the *transfer function*

$$T(k,a) \equiv \frac{D_+(a_{\rm ini})}{D_+(a_{\rm fin})}\frac{\hat{\delta}(k,a_{\rm fin})}{\hat{\delta}(k,a_{\rm ini})}\ . \tag{2.38}$$

For $z \lesssim 100$, the transfer function is independent of the scale factor since the influence of radiation on the growth of density perturbations becomes negligible. Taking the transfer function into account, the power spectrum at any scale factor is given by

$$P(k,a) = \frac{D_+^2(a)}{D_+^2(a_{\rm ini})}T^2(k,a)P_{\rm ini}(k)\ . \tag{2.39}$$

The following fitting function describes the transfer function for a universe dominated by cold dark matter and adiabatic initial conditions fairly well,

$$T(k) = \frac{\ln(1+2.34q)}{2.34q}[1+3.89q+(16.1q)^2+(5.46q)^3+(6.71q)^4]^{-1/4}\ , \tag{2.40}$$

where $q = k\,\sqrt{\theta}/(\Omega_{\rm m0}\,h^2\ {\rm Mpc}^{-1})$ and $\theta = \rho_{\rm r}/(1.68\rho_\nu)$ with the energy density of neutrinos $\rho_\nu$ (Bardeen et al., 1986). Hence, for three relativistic neutrinos $\theta = 1$.

Until now we have only considered the *linear* power spectrum based on the linearised perturbation equations (2.10–2.12). But with large cosmological $N$-body simulations, it is possible to quantify the effect of non-linear structure formation on the power spectrum and offer fitting formulae. The main effect is that power from large scales, i.e. small $k$ is shuffled to smaller scales, i.e. large $k$. An additional important effect of non-linear structure formation is that the probability to find a density contrast $\delta$ at position $\vec{x}$ becomes non-Gaussian, whereas it stays Gaussian in the linear regime. In Fig. 2.4, we show both the linear and the non-linear power spectrum for three different redshifts using the fitting formula by Smith et al. (2003) to compute the latter. Both spectra are computed for the best fit values of the WMAP7+BAO+$H_0$ joint analysis shown in Tab. 1.1. The figure illustrates very nicely that the non-linear region moves to smaller and smaller $k$, i.e. larger scales, with decreasing redshift.

An additional effect that we only want to mention here are small wiggles in the power spectrum, especially at large $k$, as a result from BAOs. But since this effect is negligible for the following chapters, we do not discuss it here and refer to Eisenstein & Hu (1998).

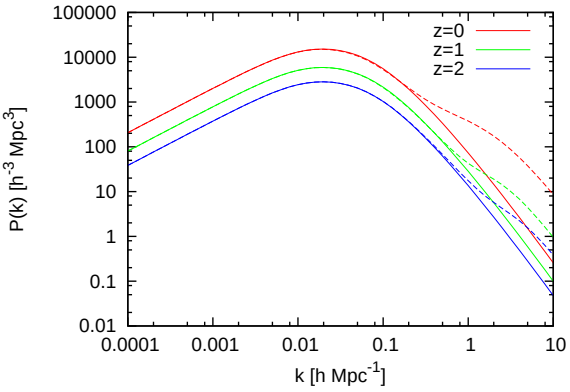


**Figure 2.4:** Linear (*solid curves*) and non-linear (*dashed curves*) power spectra for three different redshifts.

## 2.6 Zel'dovich approximation

As we have already mentioned, at the latest when $\delta \sim 1$, linear perturbation theory ultimately breaks down. However, it is possible to follow the evolution into the mildly non-linear regime with a model by Zel'dovich (1970). It starts with the decomposition of the cosmic fluid into individual particles whose trajectories can be written as

$$\vec{r} = \underbrace{a(t)\,\vec{x}}_{\text{expansion}} - \underbrace{f(t)\,\vec{s}(\vec{x})}_{\text{pec. velocity}} , \tag{2.41}$$

where $\vec{x}$ is the initial comoving coordinate of the particle, and $\vec{s}(\vec{x})$ is an irrotational *displacement field* with $\vec{s} = \vec{\nabla}\varphi(\vec{x})$. Again, $a(t)$ is the scale factor, and $f(t)$ is a function describing the time evolution of the displacement field. The derivatives $\partial r_i/\partial x_j$ can be written according to the previous equation as

$$\frac{\partial r_i}{\partial x_j} = a(t)\delta_{ij} - f(t)\frac{\partial^2\varphi}{\partial x_i\,\partial x_j} , \tag{2.42}$$

where $\partial^2\varphi/(\partial x_i\,\partial x_j)$ is the *deformation tensor* with eigenvalues $\lambda_i$ and $1 \le i \le 3$. If we transform to its eigensystem, the density at the scale factor $a$ can be written as

$$\rho(a) = \frac{\rho_{\mathrm{b}0}}{(a - f\lambda_1)(a - f\lambda_2)(a - f\lambda_3)} , \tag{2.43}$$

where $\rho_{\mathrm{b}0}$ is today's background density. The mean density at $a$, however, is given by $\rho_{\mathrm{b}}(a) = \rho_{\mathrm{b}0}a^{-3}$ so that the density contrast is

$$\delta = \frac{\rho}{\rho_{\mathrm{b}}} - 1 = \frac{1}{\left(1 - \frac{f}{a}\lambda_1\right)\left(1 - \frac{f}{a}\lambda_2\right)\left(1 - \frac{f}{a}\lambda_3\right)} - 1 \approx \frac{f}{a}(\lambda_1 + \lambda_2 + \lambda_3) = \frac{f}{a}\Delta\varphi , \tag{2.44}$$

where we have used that $(1+\epsilon)^n \approx 1 + n\,\epsilon$ for small $\epsilon$ and dropped all non-linear term in the following multiplication. Comparing the previous equation with Eq. (2.19) demands that $f/a = D_+(a)$ and $\Delta\varphi = \delta_0$ since $\Delta\varphi$ does not depend on time. Therefore, the trajectory of a particle is finally given by

$$\vec{r} = a\left[\vec{x} - D_+(a)\vec{s}\right] \tag{2.45}$$

and its derivative with respect to $a$ as

$$\frac{\mathrm{d}\vec{r}}{\mathrm{d}a} = \vec{x} - \left(1 + \frac{\mathrm{d}\ln D_+(a)}{\mathrm{d}\ln a}\right)D_+(a)\vec{s} . \tag{2.46}$$

Once the potential $\varphi \propto \Phi$ is given, where $\Phi$ is the gravitational potential, the displacement field $\vec{s} = \vec{\nabla}\varphi$ and thus the trajectories of the particles can be calculated. The Zel'dovich approximation finally breaks down when the particle trajectories start crossing each other since it neglects their gravitational interaction.

## 2.7 Spherical-collapse model

Another important analytic tool to study non-linear structure formation is the *spherical-collapse model* describing the collapse of a homogeneous and isotropic overdensity under its own gravity. Additionally, the structure is mathematically embedded in the expanding background, which is described by Eq. (1.17). A test particle with mass $m$ at the boundary of the overdensity $R$ feels the force

$$m\ddot{R} = -\frac{GMm}{R^2} + \frac{\Lambda}{3}mR \,, \tag{2.47}$$

where $M = (4\pi/3)\rho R^3$ is the total mass of the overdensity. The last term of the previous equation is the contribution from the cosmological constant, given by the last term on the right-hand side of Eq. (1.5). We scale all quantities at the time of turn-around (denoted by the subscript 'ta'), i.e. when the radius $R$ has its largest extent before the structure starts collapsing, and introduce

$$x \equiv \frac{a}{a_{\rm ta}} \,, \quad y \equiv \frac{R}{R_{\rm ta}} \,, \quad \tau \equiv H_{\rm ta} t \,, \quad \zeta \equiv \frac{\rho_{\rm ta}}{\rho_{\rm b,ta}} \,, \tag{2.48}$$

where $\rho_{\rm b,ta}$ is the background density at the time of turn-around. With these variables, Eqs. (1.17) and (2.47) can be written in a dimensionless form as

$$x' = \left[\frac{\Omega_{\rm m,ta}}{x} + \Omega_{\Lambda,\rm ta}\, x^2 + (1 - \Omega_{\rm m,ta} - \Omega_{\Lambda,\rm ta})\right]^{1/2} \,, \tag{2.49}$$

$$y'' = -\frac{\Omega_{\rm m,ta}\,\zeta}{2y^2} + \Omega_{\Lambda,\rm ta}\, y \,. \tag{2.50}$$

Here, prime denotes derivative with respect to $\tau$, and we have used that $\Omega_{\rm K,ta} = (1 - \Omega_{\rm m,ta} - \Omega_{\Lambda,\rm ta})$. A good choice for the boundary conditions of these differential equations is

$$y|_{x=0} = 0 \quad \text{and} \quad y'|_{x=1} = 0 \,, \tag{2.51}$$

claiming that the sphere starts with zero radius at $a = 0$ and reaches a maximal radius at turn-around. In Fig. 2.5, we show the evolution of the scales radius $y$ with scale factor $a$ for two overdensities that collapse at two different times. While for the first, $\zeta$ is chosen such that the collapse happens at $z_{\rm col} = 0$, the second collapses at $z_{\rm col} = 1$. Here and in the following, we denote quantities at the time of collapse with the subscript 'col'.

Most interestingly, the spherical-collapse model yields the possibility to relate the non-linear evolution directly to the linearised case so that the linear formulation can still be used for the formation of haloes through gravitational collapse, although the latter are highly non-linear objects. In the following, we will show how this can be done.

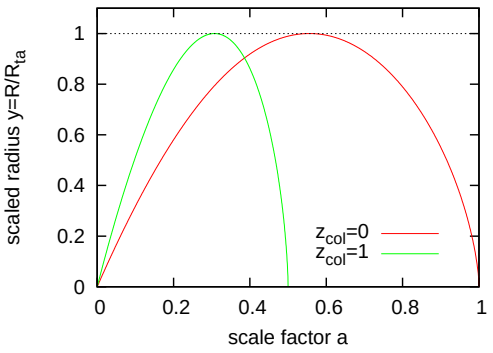


**Figure 2.5:** Evolution of the scaled radius $y$ with scale factor for two overdensities with different collapse redshifts $z_{\rm col}$.

Starting from the overdensity $\zeta$ at the time of collapse, the overdensity with respect to the background, $\Delta(a) \equiv \rho(a)/\rho_{\rm b}(a)$ can be calculated at any time using

$$\Delta = \left(\frac{x}{y}\right)^3 \zeta \,, \tag{2.52}$$

since $\rho_\mathrm{b} \propto x^{-3}$ and $\rho \propto y^{-3}$. Mathematically, the radius of the overdensity vanishes at collapse time and hence $\rho \to \infty$ for $z \to z_\mathrm{col}$. But this is an unphysical behaviour which should be avoided! Indeed, we expect that the sphere virialises at $z_\mathrm{col}$ instead of collapsing completely.

For bound objects, the total time-averaged kinetic and potential energies, $\langle E_\mathrm{kin}\rangle$ and $\langle E_\mathrm{pot}\rangle$, respectively, can be related to each other by the *virial theorem*. In the special case that the potential can be described by a power law with $V(r) \propto r^n$, it states that

$$\langle E_\mathrm{kin}\rangle = \frac{n}{2}\langle E_\mathrm{pot}\rangle \,. \tag{2.53}$$

According to Eq. (2.47), the gravitational force scales like $r^{-2}$, while the force induced by the cosmological constant scales like $r$. Consequently, the respective potentials scale like $r^n$ with $n = -1$ for gravity and $n = 2$ for the cosmological constant. Thus, in the ΛCDM model, the virialisation condition is

$$\langle E_\mathrm{kin}\rangle = -\frac{1}{2}\langle E_\mathrm{grav}\rangle + \langle E_\Lambda\rangle \,, \tag{2.54}$$

where $\langle E_\mathrm{grav}\rangle$ its average potential energy due to gravity, and $\langle E_\Lambda\rangle$ the average effective potential energy contributed by the cosmological constant. Using $\langle E_\mathrm{grav}\rangle = -3GM^2/(5R)$ and $\langle E_\Lambda\rangle = -\Lambda MR^2/10$ for the homogeneous sphere as well as energy conservation between turn-around and virialisation (subscript 'v'), one arrives at a cubic equation for $y_\mathrm{v} = R_\mathrm{v}/R_\mathrm{ta}$,

$$2\eta\, y_\mathrm{v}^3 - (2+\eta)\, y_\mathrm{v} + 1 = 0 \,, \tag{2.55}$$

with $\eta = \Lambda R_\mathrm{v}^3/(3GM)$ (Lahav et al., 1991). While for $\eta = 0$ (no cosmological constant) $y_\mathrm{v} = 0.5$, it is redshift-dependent for $\Lambda \neq 0$, with $y_\mathrm{v}$ slightly smaller than 0.5. Since Eq. (2.55) has to be solved numerically, it is faster to calculate $y_\mathrm{v}$ with a formula derived from a lowest-order Taylor expansion by Wang & Steinhardt (1998),

$$y_\mathrm{v} = \frac{1 - \frac{1}{2}\eta_\nu}{2 + \eta_t - \frac{3}{2}\eta_\nu} \quad \text{with} \quad \eta_\nu = \frac{2}{\zeta}\frac{\Omega_\Lambda(z_\mathrm{col})}{\Omega_\mathrm{m}(z_\mathrm{col})}\left(\frac{1+z_\mathrm{col}}{1+z_\mathrm{ta}}\right)^3 \quad \text{and} \quad \eta_t = \frac{2}{\zeta}\frac{\Omega_\Lambda(z_\mathrm{ta})}{\Omega_\mathrm{m}(z_\mathrm{ta})} \,. \tag{2.56}$$

The overdensity at the time of virialisation can be simply determined using Eq. (2.52),

$$\tilde{\Delta}_\mathrm{v} = \left(\frac{x_\mathrm{col}}{y_\mathrm{v}}\right)^3 \zeta \,. \tag{2.57}$$

While the former virial overdensity *with* the tilde is defined with respect to the *background density*, it is also possible to define it with respect to the *critical density* as usually done in the literature. We will denote the latter with $\Delta_\mathrm{v}$ *without* the tilde. Since $\tilde{\Delta}_\mathrm{v}\,\rho_\mathrm{b}(z_\mathrm{col}) = \Delta_\mathrm{v}\,\rho_\mathrm{c}(z_\mathrm{col})$ and $\rho_\mathrm{b}(z_\mathrm{col}) = \Omega_\mathrm{m}(z_\mathrm{col})\,\rho_\mathrm{c}(z_\mathrm{col})$, both quantities are related by

$$\Delta_\mathrm{v} = \tilde{\Delta}_\mathrm{v}\,\Omega_\mathrm{m}(z_\mathrm{col}) \,. \tag{2.58}$$

This non-linear overdensity that the spherical and homogeneous sphere has reached at virialisation can be related to a *critical linear overdensity* $\delta_\mathrm{c}$ that it would have reached in linear perturbation theory by extrapolating $\Delta(x)$ from very early times linearly to the time of virialisation via

$$\delta_\mathrm{c} \equiv \lim_{x\to 0}\left\{\frac{D_+(x_\mathrm{col})}{D_+(x)}[\Delta(x) - 1]\right\} \,. \tag{2.59}$$

Both $\delta_\mathrm{c}$ and $\Delta_\mathrm{v}$ are the key parameters of the spherical-collapse model which allow to relate non-linear and linear structure formation at least approximately.

In general, Eqs. (2.49) and (2.50) can only be solved using a numerical solver for differential equations. This, however, can introduce a non-negligible noise component to both $\delta_\mathrm{c}$ and $\Delta_\mathrm{v}$ since the radius approaches zero for both $x \to 0$ and $x \to x_\mathrm{col}$ which is difficult to handle numerically. Therefore,

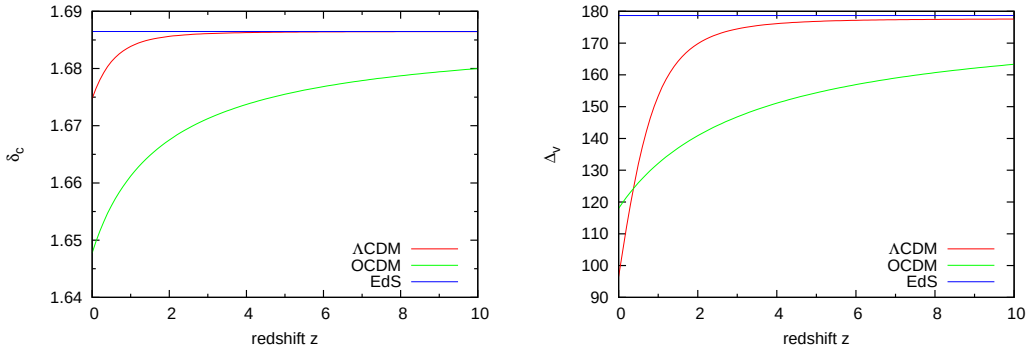


**Figure 2.6:** $\delta_c$ and $\Delta_v$ as a function of redshift for three cosmological models.

it is also possible to evaluate the two parameters for a given cosmological model using a combination of the linear perturbation equation (2.18) together with the related non-linear equation that can be derived if all non-linear terms in the derivation of Eqs. (2.10–2.12) are kept. This approach turns out to be numerically less sensitive for noise. For further reading, we refer to Padmanabhan (2002) or, for a more recent work, to Pace et al. (2010).

For the EdS universe with $\Omega_m = 1$ and $\Omega_\Lambda = 0$, Eqs. (2.49) and (2.50) simplify to

$$x' = x^{-1/2} \quad \text{and} \quad y'' = -\frac{\zeta}{2y^2} \,, \tag{2.60}$$

which can be solved analytically in parametric form yielding

$$y(\tau) = \frac{1}{2}(1 - \cos\theta) \,, \quad \tau = \frac{2}{3\pi}(\theta - \sin\theta) \,, \tag{2.61}$$

which lead to the redshift-independent parameters

$$\delta_c = \frac{3}{5}\left(\frac{3\pi}{2}\right)^{2/3} \approx 1.686 \quad \text{and} \quad \Delta_v = 18\pi^2 \approx 178 \,. \tag{2.62}$$

(compare Padmanabhan, 2002, pp. 330f). For more general cosmologies, however, both $\delta_c$ and $\Delta_v$ vary with redshift, which we show in Fig. 2.6 for three cosmologies: ΛCDM with the best-fit parameters from Tab. 1.1, OCDM with the same parameters as before but $\Omega_\Lambda = 0$, and EdS.

Since $\Delta_v = 178$ in an EdS universe, the size of a halo is often defined by the radius that encloses an averaged density of 178 times the critical density. The corresponding mass is then abbreviated as $M_{178}$. But also other definitions exist like $M_{200}$, $M_{500}$, .... The term "virial mass" usually denotes the mass that is inside the redshift-dependent virial radius of a halo, written as $M_v$. However, care has to be taken at this point since the overdensity and hence the mass is sometimes defined with respect to the background density instead of the critical density in the literature!

## 2.8 Halo profiles

Here, we want to shortly present two halo density profiles that can often be found in the literature and that we also need in the later chapters.

### 2.8.1 Singular isothermal sphere

The singular isothermal sphere is the density profile for a spherically symmetric density distribution with $T(r) = \text{const.}$ of an ideal gas. Although it is widely used in the literature, already the condition

of constant temperature is unphysical since the halo would evaporate at its outskirts. For *hydrostatic equilibrium*, i.e. the gravity force pointing inwards is balanced by the pressure pointing outwards, the pressure gradient is given by

$$\frac{\mathrm{d}p}{\mathrm{d}r} = -\frac{GM(r)}{r^2}\rho \,. \tag{2.63}$$

For an ideal gas, $p = \rho\, k_\mathrm{B} T/m$, where $m$ is the mass of a particle and $k_\mathrm{B}$ is Boltzmann's constant. Replacing the pressure by the density and writing the mass $M(r)$ as an integral over the sphere, we get

$$\frac{1}{\rho}\frac{\mathrm{d}\rho}{\mathrm{d}r} = -\frac{Gm}{k_\mathrm{B}T}\int_0^r \mathrm{d}r'\, 4\pi\rho(r')\, r'^2 \,. \tag{2.64}$$

Differentiating the previous equation with respect to $r$ finally yields the second-order equation for the density,

$$\frac{1}{r^2}\frac{\mathrm{d}}{\mathrm{d}r}\left(r^2\frac{\mathrm{d}\ln\rho}{\mathrm{d}r}\right) = -\frac{4\pi G m}{k_\mathrm{B}T}\rho \,, \tag{2.65}$$

for which an analytic solution exists,

$$\rho(r) = \frac{k_\mathrm{B}T}{2\pi G m}\frac{1}{r^2} \,. \tag{2.66}$$

This solution, however is both singular for the density in the centre, where $\rho \to \infty$, and for the mass since $M(r) \propto r$. Due to the singularity for the density in the centre, a system with the density profile (2.66) is called a *singular isothermal sphere*.

Besides Eq. (2.66), another solution for the differential equation (2.65) can be found by imposing the boundary conditions $\rho(r = 0) = \rho_0$ and $\mathrm{d}\rho/\mathrm{d}r\,(r = 0) = 0$ so that the density profile is flat in the centre and therefore non-singular at $r = 0$ by construction. For this case, Eq. (2.65) has to be solved numerically. The solution behaves like $\rho \propto r^{-2}$ for large radii and therefore $M(r) \propto r$ in this regime as for the singular isothermal sphere.

### 2.8.2 NFW profile

Navarro, Frenk, & White (1996) (NFW) found from $N$-body simulations that the density profiles of dark-matter haloes can be well described by the universal form

$$\rho(r) = \frac{\rho_\mathrm{s}}{\dfrac{r}{r_\mathrm{s}}\left(1+\dfrac{r}{r_\mathrm{s}}\right)^2} \,, \tag{2.67}$$

where $\rho_\mathrm{s}$ and $r_\mathrm{s}$ are two parameters that depend on the halo mass. In the inner part, where $r \ll r_\mathrm{s}$, the density scales like $\rho(r) \propto r^{-1}$, while in the outer part for $r \gg r_\mathrm{s}$, the density scales like $\rho(r) \propto r^{-3}$. Therefore, $r_\mathrm{s}$ denotes a scale at which the transition between the two different power laws takes place.

Denoting $r_{200}$ as the radius of the sphere whose average density is 200 times the critical density of the Universe, the *concentration parameter* $c$ is defined as

$$c \equiv \frac{r_\mathrm{s}}{r_{200}} \tag{2.68}$$

and is a function of both the halo mass and redshift and indirectly also of the cosmological parameters. Haloes that form earlier have a higher concentration parameter than haloes that form later. The parameter $\rho_\mathrm{s}$ is related to $c$ by the requirement that

$$\left(\frac{4\pi}{3}r_{200}^3\right)^{-1} 4\pi\int_0^{r_{200}} \mathrm{d}r\,\rho(r)r^2 \stackrel{!}{=} 200\rho_\mathrm{c} \tag{2.69}$$

with $\rho(r)$ from Eq. (2.67). The integral can be calculated analytically yielding the relation

$$\rho_\mathrm{s} = \frac{200\rho_\mathrm{c}}{3} \frac{c^3}{\ln(1+c) - \dfrac{c}{1+c}} \tag{2.70}$$

between $\rho_\mathrm{s}$ and $c$ and due to Eq. (2.68) also between $\rho_\mathrm{s}$ and $r_\mathrm{s}$.

Consequently, the NFW profile only depends on one parameter, namely the concentration parameter, and thus indirectly only on the halo mass given a cosmology and redshift. This makes the NFW profile be a universal density profile for dark-matter haloes. Its deeper physical origin, however, is still one of the subjects of current work.

## 2.9 Halo statistics

With the ingredients that we have introduced in this chapter so far, it is possible to derive the abundance of collapsed objects as a function of their mass. Although the resulting mass function is in good qualitative agreement with results from simulations, pronounced quantitative differences exist so that more recent mass functions are fits to numerical simulations. In the following, we will start with the classical approach by Press & Schechter (1974), which was then reformulated by Bond et al. (1991) considering halo formation as a random walk process. Lacey & Cole (1993) used this new formalism to make quantitative predictions of merger rates and occurrences. We will give a short overview over this *extended Press-Schechter formalism* before we finally present mass functions that are drawn from $N$-body simulations and do not rely on spherical collapse any more.

### 2.9.1 Classical Press-Schechter mass function

Based on Gaussian initial conditions and the spherical-collapse model, one can derive the number density of haloes as a function of their mass $M$ and redshift $z$ from linear theory of structure formation. We can assign a length scale to a halo by choosing a sphere of average background density $\rho_\mathrm{b} = \Omega_\mathrm{m}\rho_\mathrm{c}$ whose radius is chosen such that it contains a mass $M$,

$$M = \frac{4\pi}{3}\Omega_\mathrm{m}\rho_\mathrm{c}R^3 \quad \Rightarrow \quad R(M) = \left(\frac{3M}{4\pi\Omega_\mathrm{m}\rho_\mathrm{c}}\right)^{1/3} . \tag{2.71}$$

The Gaussian density field $\delta(\vec{x})$ is smoothed on that scale with a top-hat of size $R$ so that its variance is described by Eq. (2.26) with the filter function (2.27). Since the linear power spectrum scales with $D_+^2(z)$, the redshift dependence of $\sigma_R(z)$ is simply given by $\sigma_R(z) = D_+(z)\,\sigma_R$, where $\sigma_R$ is the square root of the linear power spectrum's variance filtered on scale $R$ *today*.

According to the spherical-collapse model, regions with $\delta \geq \delta_\mathrm{c}$ can be considered as collapsed. Thus, regions in which the scaled density contrast $\delta_R$ is equal or larger than the critical density should form haloes of mass $M$. The probability for this to happen is

$$P(\delta_R \geq \delta_\mathrm{c}) = \int_{\delta_\mathrm{c}(z)}^{\infty} \mathrm{d}\delta_R\, p(\delta_R) = \frac{1}{\sqrt{2\pi}\,\sigma_R(z)} \int_{\delta_\mathrm{c}(z)}^{\infty} \mathrm{d}\delta_\mathrm{R}\, \exp\left(-\frac{\delta_R^2}{2\sigma_R^2(z)}\right) = \frac{1}{2}\,\mathrm{erfc}\left(\frac{\delta_\mathrm{c}(a)}{\sqrt{2}\,\sigma_R(z)}\right) , \tag{2.72}$$

where $\mathrm{erfc}(x)$ is the complementary error function with $\mathrm{erfc}(x) \equiv 1 - \mathrm{erf}(x)$. Assuming that this probability is equal to the fraction of space $F$ filled with haloes of mass $M$, thus $P(\delta_R \geq \delta_\mathrm{c}) = F(M)$, the distribution of haloes with mass is

$$\frac{\partial F(M)}{\partial M}\,\mathrm{d}M = \frac{\partial P(\delta_R \geq \delta_\mathrm{c})}{\partial \sigma_R} \frac{\partial \sigma_R}{\partial R} \frac{\partial R}{\partial M}\,\mathrm{d}M . \tag{2.73}$$

It turns out, however, that the previous equation is not normalised correctly. Integrating $\partial F/\partial M$ over all masses yields 1/2 instead of 1. The reason is quite subtle and called the *cloud-in-cloud problem*. By smoothing the density on scale $R$, we do not account for haloes that form inside larger haloes since we only concentrate on that specific scale. In the next section, we will show that halo formation can be formulated as a random walk process and that in this case, the missing factor 2 is included correctly. Here, we will add the factor 2 by hand.

Dividing Eq. (2.73) by the typical volume $V_M$ of a halo with mass $M$, where $V_M = M/\rho_\mathrm{b}$, we finally arrive at the *Press-Schechter mass function* yielding the differential comoving number density of haloes with mass $M$ as a function of redshift,

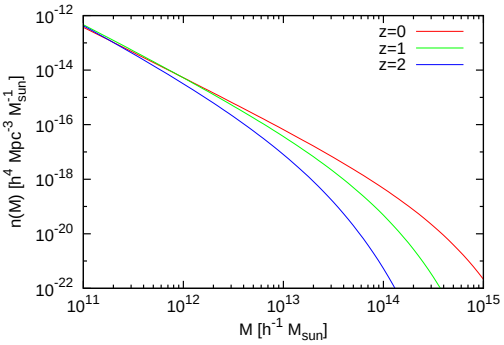


**Figure 2.7:** Press-Schechter mass function at three different redshifts for the concordance WMAP7 cosmology.

$$n(M,z) = \frac{\partial^2 N}{\partial M\,\partial V} = \sqrt{\frac{2}{\pi}}\frac{\rho_\mathrm{b}}{M}\frac{\delta_\mathrm{c}(z)}{D_+(z)\sigma_R}\left|\frac{\partial \ln \sigma_R}{\partial M}\right| \exp\left(-\frac{\delta_\mathrm{c}^2(z)}{2D_+^2(z)\sigma_R^2}\right) , \tag{2.74}$$

where $N$ is the total number of haloes. We show the redshift dependence of the mass function for three different redshifts in Fig. 2.7. The Press-Schechter mass function illustrates very well the *bottom-up scenario*, i.e. small objects form first at high redshift, whereas objects of larger scale form later.

### 2.9.2 Extended Press-Schechter formalism

Bond et al. (1991) formulated the process of halo formation as a random-walk problem. This does not only solve the problem of the missing factor 2 in the classical Press-Schechter mass function, but it has also the advantage that it is possible to generalise from spherical to ellipsoidal collapse in the derivation of the mass function (Sheth et al., 2001; Sheth & Tormen, 2002) and to calculate merger probabilities (Lacey & Cole, 1993).

We start with a filter function $W_R$ whose smoothing radius is set to a large value and then gradually shrunk. But instead of filtering with a top-hat in real space as in the sections before, we choose a top-hat in Fourier-space given by

$$\hat{W}_R(k) = \theta_\mathrm{H}(k_R - k) \quad \text{with} \quad k_R = \frac{2\pi}{R} . \tag{2.75}$$

When the density contrast at some position $\vec{x}$ is filtered using the previous filter function with $R \to \infty$, the filtered density contrast $\delta_R \to 0$ and also $\sigma_R^2 \to 0$. If then $R$ is gradually shrunk, $\sigma_R^2$ increases. Since the Fourier modes contributing to the perturbations are independent in this case, $\delta_R(\sigma_R^2)$ undergoes a Brownian motion, and the whole existing formalism can be applied. The threshold for collapse is included via a constant absorbing barrier at $\delta_R = \delta_\mathrm{c}$, for which the first-upcrossing distribution is calculated. The latter quantifies how often the barrier is hit at a given $\sigma_R^2$ for a large number of random-walk realisations, normalised to unity. We denote the first-upcrossing distribution with $f(\nu)\,\mathrm{d}\nu$, where $\nu \equiv \delta_\mathrm{c}^2/\sigma_R^2$. The relation to the mass function is given by

$$n(M) = \frac{\rho_\mathrm{b}}{M^2}\nu f(\nu)\frac{\mathrm{d}\ln\nu}{\mathrm{d}\ln M} . \tag{2.76}$$

The first-upcrossing distribution can be calculated from the probability of finding a filtered density contrast $\delta_R$. Without any barrier, this probability is simply the Gaussian distribution Eq. (2.34). But since for every trajectory that hits the barrier at $\delta_R = \delta_\mathrm{c}$ for a certain $\sigma_R^2$, there is an equal probability

due to the Brownian nature of the random-walk process to continue above or below the barrier, the probability distribution changes in the presence of the barrier. In other words, for every forbidden trajectory above the barrier, there is a mirror trajectory below the barrier, and the corresponding probability has to be subtracted from Eq. (2.34) since the trajectory has hit the barrier before. The mirror point to $\delta_R$ above the threshold is $\delta_c + (\delta_c - \delta_R) = 2\delta_c - \delta_R$, and thus, Eq. (2.34) has to be modified to

$$p_B(\delta_R) = \frac{1}{\sqrt{2\pi}\sigma_R}\left[\exp\left(-\frac{\delta_R^2}{2\sigma_R^2}\right) - \exp\left(-\frac{(2\delta_c - \delta_R)^2}{2\sigma_R^2}\right)\right] . \tag{2.77}$$

Since $p_B$ denotes the probability not to hit the barrier for *any* filter radius $R$,

$$1 - \int_{\delta_c}^{\infty} \mathrm{d}\delta_R \, p_B(\delta_R) = \mathrm{erfc}\left(\frac{\delta_c}{\sqrt{2}\sigma_R}\right) \tag{2.78}$$

is the probability to have a density contrast larger than $\delta_c$ at *any* scale. Note that this is equal to Eq. (2.72) but *without* the factor 1/2. Hence, the problem of the wrong normalisation can be solved by considering halo formation as a random-walk process.

The first-upcrossing distribution for the constant barrier at $\delta_c$ and the resulting probability distribution Eq. (2.77) can be calculated analytically by making use of the diffusion equation

$$\frac{\partial p_B(\delta_R)}{\partial S} = \frac{1}{2}\frac{\partial^2 p_B(\delta_R)}{\partial \delta_R^2} , \tag{2.79}$$

where $S \equiv \sigma_R^2$ serves as "time" variable. The result is

$$\nu f(\nu)\,\mathrm{d}\nu = \sqrt{\frac{\nu}{2\pi}}\exp\left(-\frac{\nu}{2}\right)\mathrm{d}\nu , \tag{2.80}$$

see Bond et al. (1991) for a detailed derivation. Inserting the previous expression into Eq. (2.76) yields again the Press-Schechter mass function (2.74).

### 2.9.3 Merger probabilities

Lacey & Cole (1993) extended the random-walk approach to make predictions of merger occurrences. Denoting the rescaled critical density contrast with $\omega \equiv \delta_c(t)/D_+(t)$, Eq. (2.80) can be rewritten as

$$f(S)\,\mathrm{d}S = \frac{\omega}{\sqrt{2\pi}S^{3/2}}\exp\left(-\frac{\omega^2}{2S}\right)\mathrm{d}S . \tag{2.81}$$

If we already start with a halo that has a variance $S_2$ at time $t_2$ with the corresponding scaled barrier $\omega_2$, and want to know the first-upcrossing distribution for $S_1 > S_2$ and corresponding scaled barrier $\omega_1 > \omega_2$ at time $t_1 < t_2$, we can simply replace $S \to S_1 - S_2$ and $\omega \to \omega_1 - \omega_2$, yielding the conditional probability

$$f(S_1, \omega_1|S_2, \omega_2)\,\mathrm{d}S_1 = \frac{\omega_1 - \omega_2}{\sqrt{2\pi}(S_1 - S_2)^{3/2}}\exp\left[-\frac{(\omega_1 - \omega_2)^2}{2(S_1 - S_2)}\right]\mathrm{d}S_1 . \tag{2.82}$$

Using Bayes' theorem $f(S_1, \omega_1|S_2, \omega_2)\, f(S_2, \omega_2) = f(S_2, \omega_2|S_1, \omega_1)\, f(S_1, \omega_1)$, we can infer the conditional probability for an upcrossing between $S_2$ and $S_2 + \mathrm{d}S_2$ with $\omega_2$ given $S_1$ and $\omega_1$ to be

$$f(S_2, \omega_2|S_1, \omega_1)\,\mathrm{d}S_2 = \frac{1}{\sqrt{2\pi}}\left[\frac{S_1}{S_2(S_1 - S_2)}\right]^{3/2}\frac{\omega_2(\omega_1 - \omega_2)}{\omega_1}\exp\left[-\frac{(\omega_2 S_1 - \omega_1 S_2)^2}{2S_1 S_2(S_1 - S_2)}\right]\mathrm{d}S_2 . \tag{2.83}$$

The previous equation can be used to calculate the probability that a halo of mass $M_1$ at time $t_1$ has formed a halo with a mass between $M_2$ and $M_2 + \mathrm{d}M_2$ at time $t_2 > t_1$ via mergers. Taking the limit $t_2 \to t_1$ and thus $\omega_2 \to \omega_1 \equiv \omega$ yields the *merger rate*

$$\frac{\mathrm{d}^2 N}{\mathrm{d}S_2\,\mathrm{d}\omega}\,\mathrm{d}S_2\,\mathrm{d}\omega = \frac{1}{\sqrt{2\pi}}\left[\frac{S_1}{S_2(S_1-S_2)}\right]^{3/2}\exp\left[-\frac{\omega^2(S_1-S_2)}{2S_1S_2}\right]\mathrm{d}S_2\,\mathrm{d}\omega \tag{2.84}$$

since in an infinitesimal interval $\mathrm{d}\omega$, the change $\mathrm{d}S_2$ can only be caused by a single merger event.

### 2.9.4 Mass functions calibrated by simulations

In the following, we present mass functions that we will need later and that are commonly used in the literature to describe the number density of dark-matter haloes as a function of mass and redshift.

**Sheth-Tormen mass function** The random-walk approach presented in Sect. 2.9.2 allows to study not only constant barriers, but also moving barriers, i.e. barriers $\delta_\mathrm{c}$ that are functions of $S$. The most prominent one is the one associated with ellipsoidal collapse presented by Sheth & Tormen (1999) and Sheth et al. (2001). They showed that $\delta_\mathrm{c}$ becomes dependent on the mass via the variance $S$ once the collapse is generalised to ellipsoidal dynamics, based on the ellipsoidal-collapse model by Bond & Myers (1996). The dependence on the mass can be well fitted by

$$\delta_{\mathrm{c,ell}}(S,z) = \delta_{\mathrm{c,sph}}(z)\left(1 + 0.47\nu^{-0.615}\right)\,, \tag{2.85}$$

where $\delta_{\mathrm{c,ell}}$ is the mass-dependent critical density contrast from the ellipsoidal-collapse model, $\delta_{\mathrm{c,sph}}$ is the corresponding quantity based on spherical dynamics, and again $\nu = \delta^2_{\mathrm{c,sph}}/S$. The first-upcrossing distribution of a moving barrier cannot be calculated analytically in general and hence, it has to be determined numerically via a large number of random-walk realisations. The resulting distribution can be fitted by a generalisation of Eq. (2.80),

$$\nu f(\nu)\,\mathrm{d}\nu = 2A\left(1 + \frac{1}{\nu^p}\right)\sqrt{\frac{\nu}{2\pi}}\exp\left(-\frac{\nu}{2}\right)\mathrm{d}\nu \tag{2.86}$$

with $p = 0.3$ and $A = 0.3222$, where $A$ is chosen such that $f(\nu)$ is normalised to unity. For $A = 0.5$ and $p = 0$, the distribution for the constant barrier (2.80) is recovered. The corresponding halo mass function can then again be calculated using Eq. (2.76). But in order to be consistent with numerical $N$-body simulations, the variable $\nu$ has to be rescaled by $\nu \to \nu' = 0.707\nu$. We compare the first-upcrossing distributions associated with the Sheth-Tormen and the Press-Schechter mass functions in Fig. 2.8.

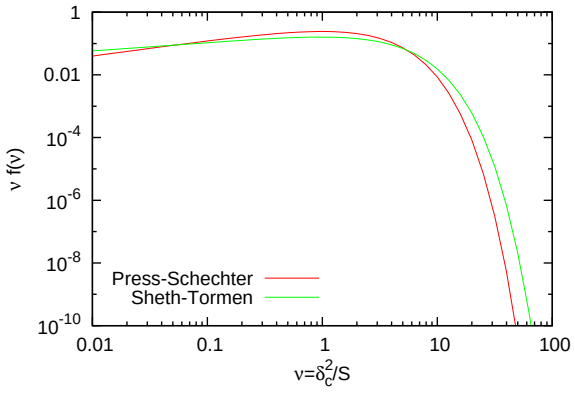


**Figure 2.8:** First-upcrossing distribution for the constant barrier (Press-Schechter) and the moving barrier (Sheth-Tormen). The transformation $\nu \to \nu' = 0.707\nu$ is already included for the latter.

**Jenkins et al. mass function** In contrast to the Sheth-Tormen mass function, Jenkins et al. (2001) directly fitted a function $f(\sigma)$ from data of numerical simulations *without* deriving the functional form from underlying collapse considerations and hence *without* including the parameter $\delta_c$. Their fit is

$$f\left(\ln\sigma^{-1}\right)\mathrm{d}\ln\sigma^{-1} = 0.315\exp\left(-\left|\ln\sigma^{-1}+0.61\right|^{3.8}\right)\mathrm{d}\ln\sigma^{-1}\,, \tag{2.87}$$

and the corresponding halo mass function can be calculated by

$$n(M) = \frac{\rho_\mathrm{b}}{M^2} f\left(\ln\sigma^{-1}\right)\frac{\mathrm{d}\ln\sigma^{-1}}{\mathrm{d}\ln M}\,. \tag{2.88}$$

**Tinker et al. mass function** While the previously presented mass functions do not depend on the overdensity $\Delta$ that is used for the mass definition (see the last paragraph of Sect. 2.7) and therefore are only valid for a single definition, usually $M_\mathrm{v}$ or $M_{200}$, this dependence was taken explicitly into account by Tinker et al. (2008). Their fitting formula is given by

$$f(\sigma)\,\mathrm{d}\ln\sigma^{-1} = A\left[\left(\frac{\sigma}{b}\right)^{-a}+1\right]\exp\left(-\frac{c}{\sigma^2}\right)\mathrm{d}\ln\sigma^{-1}\,, \tag{2.89}$$

where the fitting parameters $A$, $a$, $b$, and $c$ depend on both redshift $z$ and overdensity $\Delta$. The redshift dependence is given by

$$A(z) = A_0(1+z)^{-0.14}\,,\quad a(z) = a_0(1+z)^{-0.06}\,,\quad b(z) = b_0(1+z)^{-\alpha}\,,\quad \log\alpha(\Delta) = -\left[\frac{0.75}{\log\left(\frac{\Delta}{75}\right)}\right]^{1.2}\,, \tag{2.90}$$

where the subscript '0' indicates the corresponding parameter at $z = 0$. The parameter $c$ does not depend on redshift.

The dependence on the overdensity is given by the fitting functions

$$\begin{aligned} A_0 &= \begin{cases} -0.05 + 0.1\log\Delta & (\Delta < 1600) \\ 0.26 & (\Delta \geq 1600)\,, \end{cases} & a_0 &= 1.43 + (\log\Delta - 2.3)^{1.5}\,, \\ b_0 &= 1.0 + (\log\Delta - 1.6)^{-1.5}\,, & c_0 &= 1.2 + (\log\Delta - 2.35)^{1.6}\,. \end{aligned} \tag{2.91}$$

Note that the overdensity is defined with respect to the *background density* in this case. Instead of using the previous fitting formulae, one gets more accurate results if the parameters from Tab. 2.1 are interpolated for values of $\Delta$ in between using a cubic spline since they are determined individually from $N$-body simulations. In Chap. 5, we will choose the latter alternative.

In Fig. 2.9, we show the different mass functions presented in this section for the concordance WMAP7 cosmology. Besides the fact that the Press-Schechter mass function predicts more haloes of smaller mass, the overall shapes of the mass functions differ only at the high-mass end for $M > 10^{13}\,h^{-1}\,M_\odot$.

| $\Delta$ | $A_0$ | $a_0$ | $b_0$ | $c_0$ |
|---|---|---|---|---|
| 200 | 0.186 | 1.47 | 2.57 | 1.19 |
| 300 | 0.200 | 1.52 | 2.25 | 1.27 |
| 400 | 0.212 | 1.56 | 2.05 | 1.34 |
| 600 | 0.218 | 1.61 | 1.87 | 1.45 |
| 800 | 0.248 | 1.87 | 1.59 | 1.58 |
| 1200 | 0.255 | 2.13 | 1.51 | 1.80 |
| 1600 | 0.260 | 2.30 | 1.46 | 1.97 |
| 2400 | 0.260 | 2.53 | 1.44 | 2.24 |
| 3200 | 0.260 | 2.66 | 1.41 | 2.44 |

**Table 2.1:** Fitting parameters of the Tinker et al. mass function for various overdensities determined individually from numerical $N$-body simulations.

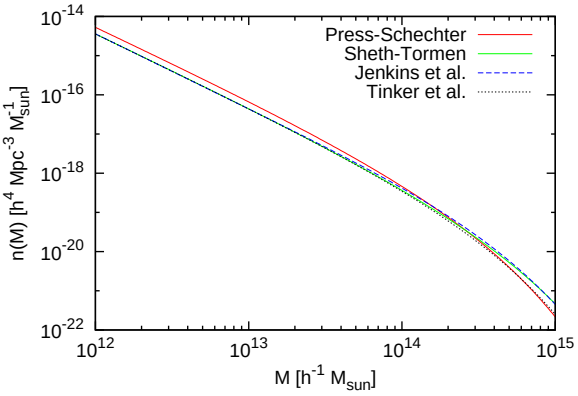


**Figure 2.9:** Mass functions presented in this section for the concordance WMAP7 cosmology at redshift $z = 0$. The overdensity for the Tinker et al. mass function was chosen to be $\Delta = \tilde{\Delta}_{\rm v}$.

Chapter 3

# 3 An X-ray temperature function without reference to mass

While the halo mass function is theoretically a very sensitive measure of cosmological models, masses of dark-matter haloes are poorly defined, global, and unobservable quantities. In the following chapter, we argue that local, observable quantities such as the X-ray temperatures of galaxy clusters can be directly compared to theoretical predictions without invoking masses. We derive the X-ray temperature function directly from the statistics of Gaussian random fluctuations in the gravitational potential constrained by the requirement that they belong to linearly collapsed structures. We then use the spherical-collapse model to relate linear to non-linear perturbations, and the virial theorem to convert potential depths to temperatures. Applying a proper high-pass filter that removes large enough modes from the gravitational potential, we derive an X-ray temperature function that agrees very well with the classical Press-Schechter approach on relevant temperature scales, but avoids the necessity of measuring masses.

The contents of this chapter is published in Angrick & Bartelmann (2009). Parts of this work were already discussed in Angrick (2007).

## 3.1 Introduction

Populating the far end of the halo mass function, galaxy clusters are in principle highly sensitive indicators of the cosmological parameters and non-linear structure growth. As shown in Sect. 2.9.1, combining Gaussian random density fields with linear structure growth and spherical collapse, the Press-Schechter mass function and its variants turn out to reproduce the halo mass function in fully non-linear cosmological simulations extremely well. If measurable, the abundance of haloes in the exponential tail of the mass function and its evolution on cosmic time scales allow precise constraints on both the density-fluctuation amplitude $\sigma_8$ today and during the second half of the cosmic age and on the matter-density parameter $\Omega_{\mathrm{m}0}$. The exponential dependence of the abundance of massive haloes on cosmological assumptions promises tight constraints (see Chap. 5).

A direct comparison between the theoretically predicted mass function of massive haloes and the observed distributions of galaxy clusters in various observable quantities, such as the flux and the temperature of their X-ray emission or the velocity dispersion of their member galaxies, requires observables to be translated into mass. While this conversion appears straightforward under the idealised assumptions of spherical symmetry, thermal, and hydrostatic equilibrium, in most cases, one has to work with empirical relations in reality since the cluster population as a whole shows all signs of being dynamically active. We will show the influence of mergers on the derived constraints for $\sigma_8$ and $\Omega_{\mathrm{m}0}$ in Chap. 5.

Even if clusters satisfied the idealising assumptions typically underlying their cosmological interpretation, their mass is not an observable. In fact, the mass of a dark-matter halo is a poorly defined,

derived quantity to which hardly any precise meaning can be given. It is common to operationally define halo masses as enclosed by spheres containing an average fixed overdensity. However, the many different choices of apparently appropriate overdensity values in the literature demonstrate that there is no uniquely defendable choice (cf. the last paragraph of Sect. 2.7). If the overdensity is chosen very high, the masses obtained are core masses rather than halo masses, and if it is chosen low, density profiles constrained near the core need to be extrapolated into regions where they are typically poorly measured or not at all.

Halo definitions in numerical simulations illustrate the same problem in a different way. There, haloes are typically identified by group finders connecting particles with neighbours closer than a certain linking length. Recipes exist for how the linking length should be chosen, but there is no objective criterion. The dependence on the linking length may be less relevant in practice because halo masses can again be defined as the masses of all particles in spheres containing a fixed overdensity. However, this refers back to the largely arbitrary overdensity threshold and creates the additional problem that several different plausible definitions of halo centres exist that often yield discrepant results.

Three main classes of observation are used to constrain cluster masses: (1) gravitational lensing, (2) X-ray flux and temperature, and (3) galaxy kinematics. None of them measures cluster masses. Gravitational lensing measures the curvature of the projected gravitational potential. X-ray observables are primarily determined by the gas density and temperature, which respond to the depth of the gravitational potential and its gradient, as do galaxy kinematics. Thus, cluster observables constrain the gravitational potential rather than any kind of mass. The conversion of the potential into a mass is hampered by the fact that mass is a non-local quantity, requiring an integration over potential derivatives. We raise the question whether cosmological conclusions can be drawn directly from cluster observables without the detour through problematic definitions of cluster masses.

As one step towards a possible answer, we derive here the X-ray temperature function from a locally defined quantity, namely the aforementioned gravitational potential. To this purpose, we first derive a function predicting the number density of potential minima having a certain depth. We include the non-linear evolution of the potential by considering the collapse of a spherical and homogeneous overdensity, and locally relate the non-linear potential depth to a temperature using the virial theorem. This direct relation of the temperature to the gravitational potential allows us to avoid introducing a global quantity such as the mass and the ambiguities in its definition.

Unless declared otherwise, we shall use the following cosmological models and parameters in this chapter: EdS: $\Omega_{\mathrm{m0}} = 1.0$, $\Omega_{\Lambda 0} = 0.0$, $\Omega_{\mathrm{b0}} = 0.04$, $h = 0.7$, $\sigma_8 = 0.52$. ΛCDM: $\Omega_{\mathrm{m0}} = 0.3$, $\Omega_{\Lambda 0} = 0.7$, $\Omega_{\mathrm{b0}} = 0.04$, $h = 0.7$, $\sigma_8 = 0.93$; OCDM: $\Omega_{\mathrm{m0}} = 0.3$, $\Omega_{\Lambda 0} = 0.0$, $\Omega_{\mathrm{b0}} = 0.04$, $h = 0.7$, $\sigma_8 = 0.87$. The different values for $\sigma_8$ reflect the normalisation of the power spectrum to reproduce the local abundance of galaxy clusters (Eke et al., 1996).

## 3.2 Gaussian random fields

As sketched in Sect. 2.4.2, simple models of inflation predict that the density contrast $\delta(\vec{r})$ should be a Gaussian random field right after inflation. Since the density contrast and the gravitational potential are linearly related via Poisson's equation (2.10), the latter is then also a Gaussian random field.

In this section, we shall follow the line of argument presented by Bardeen et al. (1986). For better comparison to their paper, we adopt $F(\vec{r})$ for the random field and $\vec{\eta}(\vec{r}) = \vec{\nabla} F(\vec{r})$ and $\zeta_{ij}(\vec{r}) = \partial_i \partial_j F(\vec{r})$ for its first and second derivatives, respectively.

### 3.2.1 Definition

An *n-dimensional random field* $F(\vec{r})$ assigns a set of random numbers to each point in $n$-dimensional space. A joint probability function can be declared for $m$ arbitrary points $\vec{r}_j$ as the probability that the

field $F$, considered at the points $\vec{r}_j$, has values between $F(\vec{r}_j)$ and $F(\vec{r}_j) + \mathrm{d}F(\vec{r}_j)$ with $1 \leq j \leq m$.

A *Gaussian random field* is a field whose joint probability functions are multivariate Gaussians. Let $y_i$ with $1 \leq i \leq p$ be a set of Gaussian random variables with means $\langle y_i \rangle$ and $\Delta y_i \equiv y_i - \langle y_i \rangle$. The *covariance matrix* $\mathsf{M}$ has the elements $M_{ij} \equiv \langle \Delta y_i \, \Delta y_j \rangle$, and the joint probability function of the Gaussian random variables is

$$p(y_1, \ldots, y_p) \, \mathrm{d}y_1 \cdots \mathrm{d}y_p = \frac{1}{\sqrt{(2\pi)^p \det \mathsf{M}}} \, \mathrm{e}^{-Q} \, \mathrm{d}y_1 \cdots \mathrm{d}y_p \tag{3.1}$$

with the quadratic form

$$Q \equiv \frac{1}{2} \sum_{i,j=1}^{p} \Delta y_i \left( \mathsf{M}^{-1} \right)_{ij} \Delta y_j \; . \tag{3.2}$$

A homogeneous Gaussian random field with zero mean is fully characterised by its two-point correlation function $\xi_F(\vec{r}_1, \vec{r}_2) = \xi_F(|\vec{r}_1 - \vec{r}_2|) \equiv \langle F(\vec{r}_1) \, F(\vec{r}_2) \rangle$ or equivalently its Fourier transform, the power spectrum $P_F(k)$ (for the power spectrum's definition, see Sect. 2.3).

### 3.2.2 The minimum constraint

An expression for the number density of field minima can be derived as follows. The joint probability function for a Gaussian random field in three-dimensional space with zero mean including first and second derivatives reads

$$p(F, \vec{\eta}, \zeta) \, \mathrm{d}F \, \mathrm{d}^3\eta \, \mathrm{d}^6\zeta = \frac{1}{\sqrt{(2\pi)^{10} \det \mathsf{M}}} \, \mathrm{e}^{-Q} \, \mathrm{d}F \, \mathrm{d}^3\eta \, \mathrm{d}^6\zeta \; , \tag{3.3}$$

with the quadratic form $Q$ given in Eq. (3.2) and $\vec{y} = (F, \eta_1, \eta_2, \eta_3, \zeta_{11}, \zeta_{22}, \zeta_{33}, \zeta_{12}, \zeta_{13}, \zeta_{23})$.

The matrix $\mathsf{M}$ contains all auto- and cross-correlations between these quantities, which read

$$\begin{aligned}
\langle F \, F \rangle &= \sigma_0^2 \, , & \langle \eta_i \, \eta_j \rangle &= \frac{\sigma_1^2}{3} \, \delta_{ij} \, , \\
\langle F \, \zeta_{ij} \rangle &= -\frac{\sigma_1^3}{3} \, \delta_{ij} \, , & \langle \zeta_{ij} \, \zeta_{kl} \rangle &= \frac{\sigma_2^2}{15} (\delta_{ij} \, \delta_{kl} + \delta_{ik} \, \delta_{jl} + \delta_{il} \, \delta_{jk}) \, , \\
\langle F \, \eta_i \rangle &= 0 \, , & \langle \eta_i \, \zeta_{jk} \rangle &= 0 \, ,
\end{aligned} \tag{3.4}$$

where the $\sigma_j$, $0 \leq j \leq 2$, are the *spectral moments* of the power spectrum $P_F(k)$ defined in Eq. (2.24), and the $\delta_{mn}$ are *Kronecker symbols*. The Fourier transform $\hat{W}_R(k)$ of the top-hat window function with the filter scale $R$ is given in Eq. (2.27).

Let $\vec{r}_0$ be a minimum of the field $F$ so that $\vec{\eta}(\vec{r}_0) = \vec{0}$. The eigenvalues $(\tilde{\zeta}_1, \tilde{\zeta}_2, \tilde{\zeta}_3)$ of the tensor $\zeta$ of second derivatives must be *positive*. Within an infinitesimal volume $\mathrm{d}^3r$ around $\vec{r} = \vec{0}$, we can approximate $\eta_i \approx \zeta_{ij} r_j$ and thus replace $\mathrm{d}^3\eta = |\det \zeta| \, \mathrm{d}^3r$ in Eq. (3.3). We also transform the volume element in the space of second derivatives, $\mathrm{d}^6\zeta$, into the space of eigenvalues,

$$\mathrm{d}^6\zeta = \frac{\pi^2}{3} \left| \left( \tilde{\zeta}_1 - \tilde{\zeta}_2 \right) \left( \tilde{\zeta}_2 - \tilde{\zeta}_3 \right) \left( \tilde{\zeta}_1 - \tilde{\zeta}_3 \right) \right| \mathrm{d}\tilde{\zeta}_1 \, \mathrm{d}\tilde{\zeta}_2 \, \mathrm{d}\tilde{\zeta}_3 \tag{3.5}$$

(Bardeen et al., 1986). Using $\det \zeta = \tilde{\zeta}_1 \, \tilde{\zeta}_2 \, \tilde{\zeta}_3$, we arrive at the final equation for the number density of minima,

$$n(F) = \frac{\pi^2}{3} \int_0^\infty \mathrm{d}\tilde{\zeta}_1 \int_0^\infty \mathrm{d}\tilde{\zeta}_2 \int_0^\infty \mathrm{d}\tilde{\zeta}_3 \, |\tilde{\zeta}_1 \, \tilde{\zeta}_2 \, \tilde{\zeta}_3| \left| \left( \tilde{\zeta}_1 - \tilde{\zeta}_2 \right) \left( \tilde{\zeta}_2 - \tilde{\zeta}_3 \right) \left( \tilde{\zeta}_1 - \tilde{\zeta}_3 \right) \right| \, p\left( F, \vec{\eta} = \vec{0}, \tilde{\zeta}_1, \tilde{\zeta}_2, \tilde{\zeta}_3 \right) \; . \tag{3.6}$$

### 3.2.3 Number density of potential minima

We now apply this formalism to the Gaussian random field of gravitational-potential fluctuations $\Phi$. We continue using $\vec{\eta}$ for the first derivative of the field and $\zeta$ for its tensor of second derivatives, but introduce new variables. Instead of the eigenvalues $\tilde{\zeta}_i$ with $1 \leq i \leq 3$, we switch to the linear combinations

$$\Delta\Phi \equiv \tilde{\zeta}_1 + \tilde{\zeta}_2 + \tilde{\zeta}_3 \,, \quad \tilde{x} \equiv \frac{\tilde{\zeta}_1 - \tilde{\zeta}_3}{2} \,, \quad \tilde{y} \equiv \frac{\tilde{\zeta}_1 - 2\tilde{\zeta}_2 + \tilde{\zeta}_3}{2} \,. \tag{3.7}$$

These choices simplify the correlation matrix $\mathsf{M}$, and we can later easily identify the Laplacian of the field. In these new variables, the non-vanishing correlations from Eq. (3.4) are

$$\begin{aligned} \langle \Phi\, \Delta\Phi \rangle &= -\sigma_1^2 \,, & \langle \tilde{x}\, \tilde{x} \rangle &= \frac{\sigma_2^2}{15} \,, \\ \langle \Delta\Phi\, \Delta\Phi \rangle &= \sigma_2^2 \,, & \langle \tilde{y}\, \tilde{y} \rangle &= \frac{\sigma_2^2}{5} \,. \end{aligned} \tag{3.8}$$

The determinant of the covariance matrix then becomes

$$\det \mathsf{M} = \frac{\sigma_1^6 \sigma_2^{10} \gamma}{6834375} \quad \text{with} \quad \gamma \equiv \sigma_0^2 \sigma_2^2 - \sigma_1^4 \,, \tag{3.9}$$

and the quadratic form, Eq. (3.2), turns into

$$Q = \frac{3\vec{\eta}\cdot\vec{\eta}}{2\sigma_1^2} + \frac{15\tilde{x}^2}{2\sigma_2^2} + \frac{5\tilde{y}^2}{2\sigma_2^2} + \frac{15(\zeta_{12}^2 + \zeta_{13}^2 + \zeta_{23}^2)}{2\sigma_2^2} + \frac{\sigma_0^2(\Delta\Phi)^2}{2\gamma} + \frac{2\sigma_1^2 \Phi\, \Delta\Phi}{2\gamma} + \frac{\sigma_2^2 \Phi^2}{2\gamma} \,. \tag{3.10}$$

In order to find the number density of potential minima, we have to invert the relations given in Eq. (3.7), considering that only the diagonal elements of the tensor $\zeta$ are non-zero after transforming to principal axes. After replacing $(\tilde{\zeta}_1, \tilde{\zeta}_2, \tilde{\zeta}_3)$ by $(\Delta\Phi, \tilde{x}, \tilde{y})$ and changing the integration boundaries accordingly, we integrate only over $\tilde{x}$ and $\tilde{y}$ because the Laplacian of the potential will become crucial in the following discussion, when another constraint on $\Delta\Phi$ will be introduced. We can now rewrite Eq. (3.6) as

$$\tilde{n}(\Phi, \Delta\Phi)\, \mathrm{d}\Phi\, \mathrm{d}(\Delta\Phi) = C(N_1 + N_2)\, \mathrm{d}\Phi\, \mathrm{d}(\Delta\Phi) \,, \tag{3.11}$$

with the integrals

$$N_1 = \int_{-\Delta\Phi/2}^{0} \mathrm{d}\tilde{x} \int_{-3\tilde{x}-\Delta\Phi}^{\Delta\Phi/2} \mathrm{d}\tilde{y} \left| \left(\tilde{x}^3 - \tilde{x}\tilde{y}^2\right) (\Delta\Phi - 2\tilde{y}) \, (\Delta\Phi - 3\tilde{x} + \tilde{y}) \right| |(\Delta\Phi + 3\tilde{x} + \tilde{y})|\, \mathrm{e}^{-\tilde{Q}} \,, \tag{3.12}$$

$$N_2 = \int_{0}^{\Delta\Phi/2} \mathrm{d}\tilde{x} \int_{3\tilde{x}-\Delta\Phi}^{\Delta\Phi/2} \mathrm{d}\tilde{y} \left| \left(\tilde{x}^3 - \tilde{x}\tilde{y}^2\right) (\Delta\Phi - 2\tilde{y}) \, (\Delta\Phi - 3\tilde{x} + \tilde{y}) \right| |(\Delta\Phi + 3\tilde{x} + \tilde{y})|\, \mathrm{e}^{-\tilde{Q}} \,, \tag{3.13}$$

the normalisation constant

$$C = \frac{25\sqrt{5}}{16\pi^3 \sigma_1^3 \sigma_2^5 \sqrt{3\gamma}} \,, \tag{3.14}$$

and the quadratic form

$$\tilde{Q} = \frac{1}{2}\left[ \frac{15\tilde{x}^2}{\sigma_2^2} + \frac{5\tilde{y}^2}{\sigma_2^2} + \frac{\sigma_0^2(\Delta\Phi)^2}{\gamma} + \frac{2\sigma_1^2 \Phi\Delta\Phi}{\gamma} + \frac{\sigma_2^2 \Phi^2}{\gamma} \right] . \tag{3.15}$$

Equations (3.12) and (3.13) can be integrated analytically, giving identical results. The final expression for $\tilde{n}(\Phi, \Delta\Phi)$ is

$$\tilde{n}(\Phi, \Delta\Phi) = \frac{1}{240\pi^3 \sigma_1^3 \sqrt{15\gamma}} (F_1 + F_2) \exp\left[ -\frac{\left(2\sigma_1^2 \Delta\Phi + \sigma_2^2 \Phi\right) \Phi}{2\gamma} \right] , \tag{3.16}$$

where $F_1$ and $F_2$ are functions depending only on the field's Laplacian but not on the field itself,

$$F_1 = 2\sigma_2\left(5\Delta\Phi^2 - 16\sigma_2^2\right)\exp\left[-\frac{\left(6\sigma_0^2\sigma_2^2 - 5\sigma_1^4\right)\Delta\Phi^2}{2\sigma_2^2\gamma}\right] + \sigma_2\left(155\Delta\Phi^2 + 32\sigma_2^2\right) \times \exp\left[-\frac{\left(9\sigma_0^2\sigma_2^2 - 5\sigma_1^4\right)\Delta\Phi^2}{8\sigma_2^2\gamma}\right], \tag{3.17}$$

$$F_2 = 5\sqrt{10\pi}\,\Delta\Phi\left(\Delta\Phi^2 - 3\sigma_2^2\right)\exp\left(-\frac{\sigma_0^2\,\Delta\Phi^2}{2\gamma}\right)\left[\mathrm{erf}\left(\frac{\sqrt{5}\,\Delta\Phi}{2\sqrt{2}\sigma_2}\right) + \mathrm{erf}\left(\frac{\sqrt{5}\,\Delta\Phi}{\sqrt{2}\sigma_2}\right)\right]. \tag{3.18}$$

We point out that Eqs. (3.16–3.18) are valid in this form only for $\Delta\Phi > 0$ and $\Phi < 0$ since the underlying integrations over $\tilde{x}$ and $\tilde{y}$ were carried out under these restrictions. Both assumptions are appropriate; the first because of Poisson's equation, and the second because we are only interested in gravitationally bound objects whose potentials must be negative.

For the further evaluation of Eqs. (3.16–3.18), we need the first three spectral moments, defined in Eq. (2.24), of the *potential* power spectrum including the additional weighting function $\hat{W}_R^2(k)$.

## 3.3 Linear and non-linear evolution of gravitational fluctuations

The potential power spectrum $P_\Phi(k)$ is related to the density power spectrum $P(k)$ through Poisson's equation. The power spectrum for the initially Gaussian density perturbations, however, only describes the linear evolution of fluctuations for which $\delta \lesssim 1$. Thus, we also need an *ansatz* for their non-linear evolution having higher amplitude. We shall use the *spherical-collapse model* to model non-linear effects. Along the way, we shall introduce a proper definition of a filter scale $R$.

### 3.3.1 Linear power spectrum

Poisson's equation in comoving coordinates (2.10) can be written in Fourier space as

$$-k^2\hat{\Phi} = 4\pi G\rho_\mathrm{b}a^2\hat{\delta}\,. \tag{3.19}$$

By the definition of the power spectrum, Eq. (2.23), and using $\rho_\mathrm{b} = (3H_0^2\Omega_\mathrm{m0})/(8\pi G a^3)$, the potential power spectrum is related to the density power spectrum by

$$P_\Phi(k) = \frac{9}{4}\frac{\Omega_\mathrm{m0}^2}{a^2}\frac{H_0^4}{k^4}P(k)\,. \tag{3.20}$$

Since $P(k) \propto k$ for $k \ll k_\mathrm{eq}$ and $P(k) \propto k^{-3}$ for $k \gg k_\mathrm{eq}$, where $k_\mathrm{eq}$ is again the comoving wave number of the perturbation mode entering the horizon at matter-radiation equality, we have $P_\Phi(k) \propto k^{-3}$ for $k \ll k_\mathrm{eq}$ and $P_\Phi(k) \propto k^{-7}$ for $k \gg k_\mathrm{eq}$.

Due to the steepness of the power spectrum, we have to introduce a cut-off wave number $k_\mathrm{min}$ when evaluating the spectral moments,

$$\sigma_j^2 = \int_{k_\mathrm{min}}^{\infty}\frac{k^2\mathrm{d}k}{2\pi^2}P_\Phi(k)\hat{W}_R^2(k)\,. \tag{3.21}$$

Thus, $k_\mathrm{min}$ defines a sharp high-pass filter in $k$-space. It has to be chosen properly to filter out large potential modes and therefore also large-scale potential gradients responsible for peculiar velocities of collapsed structures. In this way, this filter ensures that the gravitational potential of a structure is defined with respect to the large-scale potential value in its direct vicinity and that the constraint of a vanishing potential gradient is fulfilled for structures of all sizes. If they moved, they would not be

counted when searching for potential minima, and the number density derived in that way would be too small (see also App. A). We will discuss in Sect. 3.4.3 how to find the proper $k_{\min}$.

The evolution of the density power spectrum between the scale factors $a_1$ and $a_2$ is parametrised by the *linear growth factor* $D_+(a)$ and the *transfer function* $T(k, a)$ (see Eq. 2.39). Since $T(k, a)$ only changes for redshifts $z \gtrsim 100$, we do not need to take it into account for the evolution of the power spectrum at $z < 100$. Together with the additional factor of $a^{-2}$ of Eq. (3.20), the evolution of the potential power spectrum is thus given by

$$P_\Phi(k, a_2) = \left[\frac{G_+(a_2)}{G_+(a_1)}\right]^2 P_\Phi(k, a_1) \,, \tag{3.22}$$

where we have defined the *potential growth factor* $G_+(a) \equiv D_+(a)/a$.

We normalise $G_+$ such that $G_+(a = 1) = 1$. Since $D_+(a) = a$ in an EdS universe, the potential growth factor stays constant and thus, the potential power spectrum does not evolve with time in this case. This is not true for a ΛCDM and an OCDM model, yet the variation with time remains small. For cosmologies with $\Omega_\mathrm{m} \neq 1$, $\Omega_\Lambda \neq 0$ and negligible radiation density, the potential growth factor is accurately approximated by the right-hand side of Eq. (2.20) divided by $a$.

Figure 3.1 shows the evolution of $G_+$ with redshift. Obviously, the expression "growth factor" is somehow misleading because the potential power spectrum's amplitude is in fact *decreasing* with time.

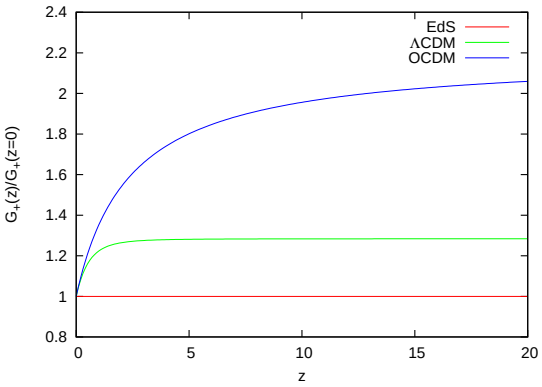


**Figure 3.1:** Potential growth factor for three different cosmologies.

### 3.3.2 Non-linear evolution

Aiming at the number density of potential minima including non-linear evolution, we have to relate the potential from linear theory used so far, $\Phi = \Phi_\mathrm{l}$, to the potential including non-linear evolution $\Phi_\mathrm{nl}$. We shall use the spherical-collapse model to estimate the ratio $\Phi_\mathrm{nl}/\Phi_\mathrm{l}$.

#### Gravitational potential in the centre of a homogeneous overdense sphere

A spherical and homogeneous overdensity with density contrast $\delta$ and radius $R$ has a gravitational potential given by Poisson's equation,

$$\frac{1}{r^2}\frac{\partial}{\partial r}\left(r^2 \frac{\partial}{\partial r}\Phi\right) = 4\pi G\bar{\rho}\,\theta_\mathrm{H}(R - r) \,, \tag{3.23}$$

where $\theta_\mathrm{H}$ is again *Heaviside's step function* and $\bar{\rho}$ is the density inside the sphere acting as the source of the gravitational field. This equation holds in physical coordinates, while Eq. (2.10) uses comoving coordinates. Integrating twice with the boundary conditions $(\partial\Phi/\partial r) \to 0$ for $r \to 0$ and $\Phi \to 0$ for $r \to \infty$ yields

$$\Phi(r) = \begin{cases} -2\pi G\bar{\rho}R^2\left(1 - \dfrac{r^2}{3R^2}\right) & \text{for } r \leq R \,, \\ -\dfrac{4\pi G}{3}\bar{\rho}\dfrac{R^3}{r} & \text{else} \,, \end{cases} \tag{3.24}$$

showing that the potential at the centre, $\Phi_0 \equiv \Phi(r = 0)$, is

$$\Phi_0 = -2\pi G\bar{\rho}R^2 \,. \tag{3.25}$$

Since the potential $\Phi(r) \propto 1 - r^2/(3R^2)$ inside a homogeneous sphere, it may appear appropriate to construct the low-pass filter from the window function

$$W_R(r) = \left(1 - \frac{r^2}{3R^2}\right)\left(\frac{16}{15}\pi R^3\right)^{-1} \tag{3.26}$$

instead of a top-hat. Its Fourier transform is given by

$$\hat{W}_R(k) = \frac{5\left[3\sin u - u\left(3+u^2\right)\cos u\right]}{2u^5} \quad \text{with} \quad u = kR\,. \tag{3.27}$$

Since this window function is more compact in real space than the top-hat, its Fourier transform is slightly broader in $k$-space and thus includes more Fourier modes.

The window function (3.27) does not (and should not) reproduce the potential outside an isolated, homogeneous sphere, which drops $\propto r^{-1}$. This is no surprise because it drops to the potential of the homogeneous background within a finite radius, and the presence of a background potential signals the breakdown of Newtonian gravity in the cosmological context.

#### Filter radius

The preceding consideration also provides a proper definition for the filter radius of the window function $\hat{W}_R$ used for the calculation of the spectral moments (3.21). Poisson's equation for the perturbations in physical coordinates (subscript '$r$') reads

$$\Delta_r\Phi = 4\pi G\bar{\rho}\,, \tag{3.28}$$

with $\bar{\rho} = \rho_\mathrm{b}\delta$. Combining Eqs. (3.25) and (3.28), we see that the central potential is $\Phi_0 = -\frac{1}{2}\Delta_r\Phi\, R_r^2$. We can use this relation to define a filter radius in physical coordinates by

$$R_r \equiv \sqrt{\frac{-2\Phi}{\Delta_r\Phi}}\,. \tag{3.29}$$

This expression remains valid in comoving coordinates (subscript '$x$') if we replace the Laplacian in physical coordinates by the Laplacian in comoving coordinates,

$$R_x = \frac{R_r}{a} = \sqrt{\frac{-2\Phi}{a^2\Delta_r\Phi}} = \sqrt{\frac{-2\Phi}{\Delta_x\Phi}}\,. \tag{3.30}$$

### 3.3.3 Ratio of linearly and non-linearly evolved potential

We shall use the potential in the centre of a spherical and homogeneous overdensity (3.25) to relate the linear and non-linear potential depths. During the following calculation, we will again denote quantities at an initial scale factor $a_\mathrm{ini}$ with the subscript 'ini', quantities at the turn-around scale factor with 'ta', and quantities at the collapse scale factor $a_\mathrm{col}$ with the subscript 'col' and use the dimensionless quantities $x = a/a_\mathrm{at}$ and $y = R/R_\mathrm{ta}$ that we have already defined for the spherical-collapse model in Sect. 3.21.

The potentials at the initial time and at collapse are

$$\Phi_\mathrm{ini} = -2\pi G\bar{\rho}_\mathrm{ini}R_\mathrm{ta}^2 y_\mathrm{ini}^2\,, \quad \Phi_\mathrm{col} = -2\pi G\bar{\rho}_\mathrm{col}R_\mathrm{ta}^2 y_\mathrm{col}^2\,, \tag{3.31}$$

respectively. Their ratio is

$$\frac{\Phi_\mathrm{col}}{\Phi_\mathrm{ini}} = \frac{\tilde{\delta}_\mathrm{v}}{\delta_\mathrm{ini}}\left(\frac{y_\mathrm{col}}{x_\mathrm{col}}\right)^3\left(\frac{x_\mathrm{ini}}{y_\mathrm{ini}}\right)^3\frac{y_\mathrm{ini}}{y_\mathrm{col}}\,, \tag{3.32}$$

where $\tilde{\delta}_\mathrm{v} = \tilde{\Delta}_\mathrm{v} - 1$. We have used here that the densities at the initial time and at collapse time are $\bar{\rho}_\mathrm{ini} = \rho_\mathrm{b0} a_\mathrm{ini}^{-3} \delta_\mathrm{ini}$ and $\bar{\rho}_\mathrm{col} = \rho_\mathrm{b0} a_\mathrm{col}^{-3} \tilde{\delta}_\mathrm{v}$, respectively. Using Eq. (2.57), we can write $(y_\mathrm{c}/x_\mathrm{c})^3 = \zeta/\tilde{\Delta}_\mathrm{v}$ and $y_\mathrm{ini} \approx \zeta^{1/3} x_\mathrm{ini}$ since $\Delta_\mathrm{ini} \approx 1$ for early times. This yields

$$\frac{\Phi_\mathrm{col}}{\Phi_\mathrm{ini}} = \frac{\tilde{\delta}_\mathrm{v}}{\tilde{\Delta}_\mathrm{v}} \frac{\zeta^{1/3}}{y_\mathrm{col}} \frac{x_\mathrm{ini}}{\delta_\mathrm{ini}} \approx \frac{\zeta^{1/3}}{y_\mathrm{col}} \frac{x_\mathrm{ini}}{\delta_\mathrm{ini}} \,. \tag{3.33}$$

We have neglected the difference between $\tilde{\delta}_\mathrm{v}$ and $\tilde{\Delta}_\mathrm{v}$ in the last step, which is a good approximation since $\tilde{\Delta}_\mathrm{v} = O(10^2)$. The ratio $\delta_\mathrm{ini}/x_\mathrm{ini} \equiv C$ is given by

$$C = \frac{3}{5} \left[ \zeta^{1/3} \left( 1 + \frac{\Omega_{\Lambda,\mathrm{ta}}}{\zeta\, \Omega_{\mathrm{m,ta}}} \right) + \frac{1 - \Omega_{\mathrm{m,ta}} - \Omega_{\Lambda,\mathrm{ta}}}{\Omega_{\mathrm{m,ta}}} \right] \tag{3.34}$$

(Bartelmann et al., 2006). Since Eqs. (3.33) and (3.34) describe the non-linear evolution between scale factors $a_\mathrm{ini}$ and $a_\mathrm{col}$, the linear and non-linear potential depths are related by

$$\frac{\Phi_\mathrm{nl}}{\Phi_\mathrm{l}} = \frac{\Phi_\mathrm{col}}{\Phi_\mathrm{ini}} \frac{\Phi_\mathrm{ini}}{\Phi_\mathrm{l,col}} = \frac{\zeta^{1/3}}{y_\mathrm{col}} \frac{1}{C} \frac{G_+(a_\mathrm{ini})}{G_+(a_\mathrm{col})} \,, \tag{3.35}$$

where $\Phi_\mathrm{l,col}$ is the potential evolved linearly from $a_\mathrm{ini}$ to $a_\mathrm{col}$. For an EdS universe, we have $\Phi_\mathrm{nl}/\Phi_\mathrm{l} = \frac{10}{3}$, independent of the collapse redshift because the potential growth factor $G_+(a)$ is constant and $y_\mathrm{col} = \frac{1}{2}$. For more general cosmological models, however, it depends on the collapse redshift.

We show $\Phi_\mathrm{nl}/\Phi_\mathrm{l}$ for three different cosmological models in Fig. 3.2. We arbitrarily choose the initial scale factor to be five times the scale factor at matter-radiation equality because this is early enough for the potential not to have begun developing since we are in the matter-dominated era, and late enough for ignoring any evolution of the transfer function $T(k, a)$ with time. While the ratio (3.35) reaches the constant $\frac{10}{3}$ expected in an EdS model relatively quickly in the ΛCDM case as the redshift increases, its evolution is much slower for OCDM. We point out that the difference between the linear and the non-linear potential evolution in the centre is by far not as large as for the density contrast, where it is of order $10^{3\ldots4}$.

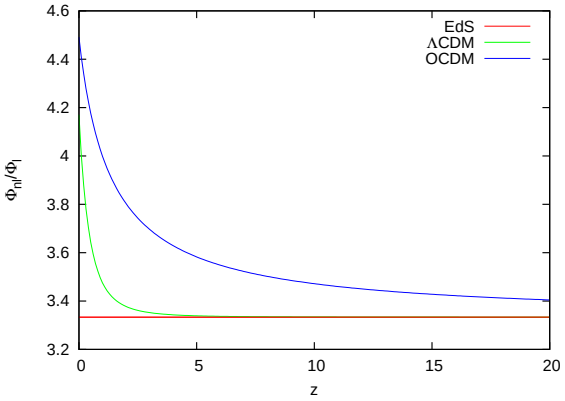


**Figure 3.2:** The ratio of the potential depth that is expected at collapse redshift $z_\mathrm{col}$ from linear theory $\Phi_\mathrm{l}$ and the one inferred from the spherical-collapse model $\Phi_\mathrm{nl}$.

### 3.3.4 Counting only collapsed structures

Since we are only interested in collapsed structures forming haloes, we have to include this additional constraint in our calculations. Following Press & Schechter (1974), this can be done by only taking structures into account whose linear density contrast exceeds the critical value $\delta_\mathrm{c}$. In our case, this translates to the criterion that the Laplacian $\Delta\Phi$ exceed a certain threshold $\Delta\Phi_\mathrm{c}$, which is, according to Poisson's equation, given by

$$\Delta\Phi_\mathrm{c}(a) = \frac{3}{2} H_0^2 \Omega_\mathrm{m0} \frac{\delta_\mathrm{c}(a)}{a} \,. \tag{3.36}$$

In that way, we count only structures whose gravitational potential is "curved enough" so that the number density of potential minima belonging to collapsed structures is finally

$$n(\Phi) = \int_{\Delta\Phi_\mathrm{c}}^{\infty} \mathrm{d}(\Delta\Phi)\, \tilde{n}(\Phi, \Delta\Phi) \,, \tag{3.37}$$

with $\tilde{n}(\Phi, \Delta\Phi)$ given by Eqs. (3.16–3.18).

## 3.4 Construction of the X-ray temperature function

Combining the results of the previous sections, we are now able to derive a function describing the differential number density of structures as a function of their X-ray temperature based on the statistics of minima in the cosmic gravitational potential. In order to count them properly, a high-pass filter is introduced that removes disturbing large-scale modes. Assuming virial equilibrium, it is possible to relate the potential depths to X-ray temperatures using the virial theorem.

### 3.4.1 Virial theorem

We can relate the potential depth $\Phi_{\mathrm{nl}}$ to the X-ray temperature of a cluster using the virial theorem for Newtonian gravity, which relates the ensemble-averaged kinetic and potential energies, $\langle E_{\mathrm{kin}} \rangle$ and $\langle E_{\mathrm{grav}} \rangle$, respectively, by $\langle E_{\mathrm{kin}} \rangle = -\frac{1}{2}\langle E_{\mathrm{grav}} \rangle$. The kinetic energy is connected to a temperature $T$ by $\langle E_{\mathrm{kin}} \rangle = \frac{3}{2} k_{\mathrm{B}} T$, where $k_{\mathrm{B}}$ is Boltzmann's constant. The potential energy is $m\Phi$ with a proper mass $m$. Assuming that the intracluster medium has primordial composition with Helium abundance $Y = 0.24$, $m = \mu m_{\mathrm{p}}$ with $\mu = 0.59$. Particles near the cluster core feel the potential $\Phi(r) \approx \Phi_0$, thus the virial theorem reads[8]

$$-\mu m_{\mathrm{p}} \Phi_0 = 3 k_{\mathrm{B}} T \ . \tag{3.38}$$

Since $\Phi_0$ can be regarded as the non-linear depth of a potential minimum, we can replace $\Phi_{\mathrm{nl}}$ by $\Phi_0 = -3k_{\mathrm{B}}T/(\mu m_{\mathrm{p}})$. Given a particular X-ray temperature, we calculate the corresponding linear potential depth by relating the temperature to the non-linear potential using Eq. (3.38), and the latter to the linear potential using Eq. (3.35) so that

$$\Phi_{\mathrm{l}} = -\frac{3 y_{\mathrm{col}}}{\zeta^{1/3}} \frac{C}{\mu m_{\mathrm{p}}} \frac{G_+(z)}{G_+(z_{\mathrm{ini}})} k_{\mathrm{B}} T \ . \tag{3.39}$$

### 3.4.2 Evaluation steps

The X-ray temperature function is implicitly determined by Eqs. (3.16–3.18). Assuming a temperature $T$, the linear potential depth $\Phi_{\mathrm{l}}$ is found from Eq. (3.39). Then, Eq. (3.16) needs to be integrated over $\Delta\Phi$ from $\Delta\Phi_{\mathrm{c}}$ to infinity. Since the smoothing radius (3.30) depends on the integration variable $\Delta\Phi$, each step in the integration requires updating the spectral moments, cf. Eq. (3.21).

In practice, the temperature interval for which the X-ray temperature function is to be calculated is divided into a reasonable number of bins large enough that the shape of the temperature function can be inferred from interpolating between them. At first, each X-ray temperature $T_i$ corresponding to one particular bin has to be related to a linear potential depth $\Phi_{\mathrm{l},i}$ using Eq. (3.39). We also have to take care of the Jacobian determinant of the transformation since $n(T)\,\mathrm{d}T$ must be replaced by $n(\Phi_{\mathrm{l}})\,(\mathrm{d}T/\mathrm{d}\Phi_{\mathrm{l}})\,\mathrm{d}\Phi_{\mathrm{l}}$. Having related both quantities, it is possible to evaluate Eqs. (3.16–3.18).

In order to calculate the spectral moments $\sigma_0$, $\sigma_1$, and $\sigma_2$, we also have to choose a reasonable amount of bins for the Laplacian of the potential, which we will denote with $\Delta\Phi_j$, since the spectral moments are functions of both $\Phi_{\mathrm{l}}$ and $\Delta\Phi$ through the filter radius entering via the Fourier transform of the window function, Eq. (2.27) or (3.27). Additionally, the cut-off wave vector $k_{\mathrm{min}}$ defining a sharp high-pass filter in $k$-space is also a function of both quantities. A detailed discussion how to find the proper $k_{\mathrm{min}}$ for a given temperature and Laplacian of the gravitational potential is presented in the next section. Thus, we have to evaluate both the filter radius and $k_{\mathrm{min}}$ for each pair $(\Phi_{\mathrm{l},i}, \Delta\Phi_j)$ starting for a given $\Phi_{\mathrm{l},i}$ with $\Delta\Phi_0 = \Delta\Phi_{\mathrm{c}}$.

[8] Strictly speaking, this is only valid for a universe with $\Omega_\Lambda = 0$. Due to the presence of dark energy, an additional potential arises whose contribution is small (see Sect. 2.7 and Fig. 4.1, where the latter shows that the virial radius only changes about few percents) so that we neglect it in our further calculations.

Inserting the spectral moments into Eqs. (3.16–3.18) yields the number density of minima per potential interval $\mathrm{d}\Phi_\mathrm{l}$ and per interval of the Laplacian $\mathrm{d}(\Delta\Phi)$ for the specific parameter pair $(\Phi_{\mathrm{l},i}, \Delta\Phi_\mathrm{c})$. Since $\Delta\Phi_\mathrm{c} = O(10^4\ \mathrm{km^2\ s^{-2}}\ h^2\ \mathrm{Mpc^{-2}})$, we choose the next step to be $\Delta\Phi_1 = \Delta\Phi_\mathrm{c} + \delta(\Delta\Phi)$ with $\delta(\Delta\Phi) = 10^2\ \mathrm{km^2\ s^{-2}}\ h^2\ \mathrm{Mpc^{-2}}$ and calculate now $R$ and the spectral moments for the pair $(\Phi_{\mathrm{l},i}, \Delta\Phi_1)$. We continue with $\Delta\Phi_j = \Delta\Phi_{j-1} + \delta(\Delta\Phi)$ for a given $\Phi_{\mathrm{l},i}$ until we fulfill the following convergence criterion.

We approximate the integral in Eq. (3.37) by the trapezium rule. Hence, for a specific potential value $\Phi_{\mathrm{l},i}$, the number density $n(\Phi_{\mathrm{l},i})$ is evaluated numerically as

$$n(\Phi_{\mathrm{l},i}) \approx \frac{\delta(\Delta\Phi)}{2} \sum_{j=1}^{N} \left[\tilde{n}(\Phi_{\mathrm{l},i}, \Delta\Phi_{j-1}) + \tilde{n}(\Phi_{\mathrm{l},i}, \Delta\Phi_j)\right] . \tag{3.40}$$

This summation is stopped at an index $N$ chosen as the first index for which the relative contribution to $n(\Phi_{\mathrm{l},i})$ is smaller than $10^{-6}$. This is a proper break condition since $\tilde{n}(\Phi_\mathrm{l}, \Delta\Phi)$ tends rapidly towards zero for $\Delta\Phi \to \infty$.

Having evaluated $n(T_i)$ for each $i$, we have an appropriate approximation of the X-ray temperature function's shape in the chosen temperature interval.

### 3.4.3 High-pass filtering

As mentioned before, we need a proper high-pass filter in order to remove disturbing large-scale potential modes since we want the potential associated with a collapsed structure to be defined with respect to the large-scale potential level in its direct vicinity, and we want the structure to have no peculiar motion so that the constraint $\vec{\eta} = \vec{0}$ is applicable. The natural filter choice is a sharp cut-off in $k$-space since this will effectively remove both large-scale potential modes and potential gradients.

Let again $R$ be the filter radius of either the top-hat (2.27) or the potential-related filter Eq. (3.26), and $R_\mathrm{hp}$ the filter radius related to a sharp cut-off wave number $k_\mathrm{hp}$ in $k$-space by $k_\mathrm{hp} = 2\pi/R_\mathrm{hp}$. We denote the ratio of both quantities with $\alpha$ so that

$$\alpha \equiv \frac{R_\mathrm{hp}}{R} . \tag{3.41}$$

Since $R$ and $R_\mathrm{hp}$ define a low- and a high-pass filter, respectively, one can expect $\alpha > 1$.

It is now a legitimate question how $\alpha$ should be chosen for calculating the correct number density of objects having a particular potential depth. We argue that a natural choice exists. In Fig. 3.3, we plot $\tilde{n}(T, \Delta\Phi)$ as a function of $\alpha$. For each pair $(T_i, \Delta\Phi_j)$, the number density peaks at some value $\alpha_\mathrm{max}$, which is a function of both the temperature and the Laplacian of the potential. It increases with both increasing Laplacian and increasing temperature. For low temperatures, the maximum is rather sharp, but broadens as the temperature increases. This is most pronounced for the EdS universe. The overall behaviour can be understood as follows.

On the one hand, decreasing the radius of the high-pass filter starting from a value much larger than the typical size of the object excludes more and more modes on decreasing scales. In this way, potential *gradients* are removed which would cause a non-zero peculiar velocity and thus a deviation from the constraint $\vec{\eta} = \vec{0}$. Since more and more objects are put to rest, the number density of objects with vanishing potential gradient increases. Figure 3.3 shows that the increase of the number density is less steep for large (or hot) than for small (or cool) objects. This reflects the fact that massive, hot objects, e.g. with $T = 10$ keV, are more likely located at potential minima, thus removing large-scale modes has less effect on their number counts.

On the other hand, increasing the radius of the high-pass filter starting from a value much smaller than the typical size of the relevant object adds more and more modes. While the window between low- and high-pass filtering is too small, modes relevant for the structures considered are filtered out

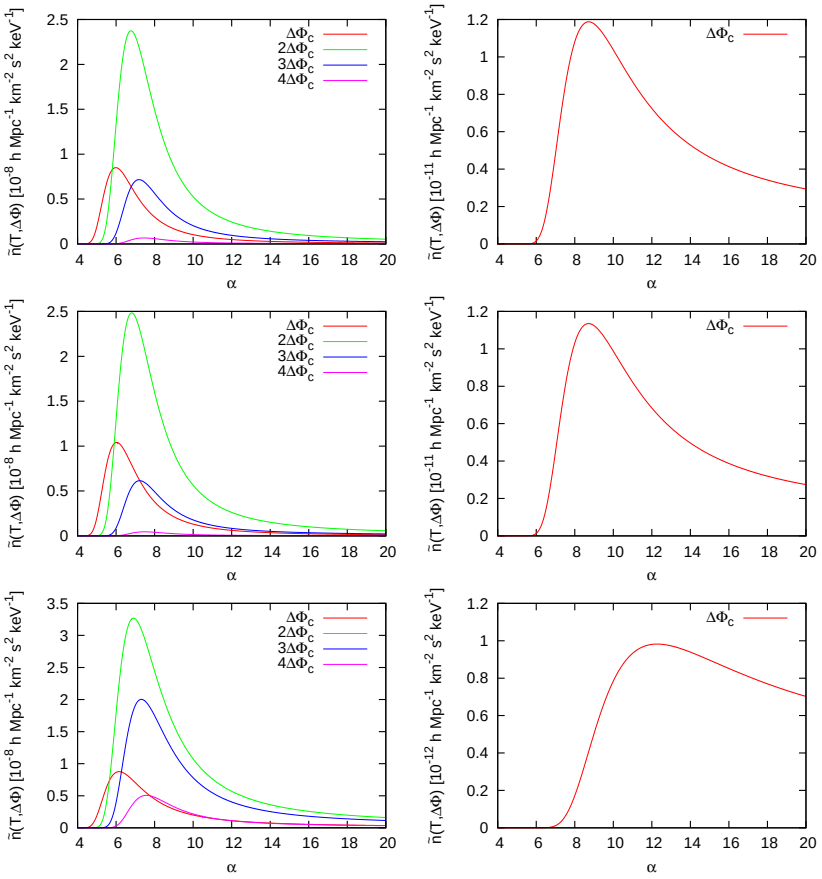


**Figure 3.3:** Differential number density $\tilde{n}(T, \Delta\Phi)$ as function of the parameter $\alpha$ for three different cosmologies and two temperatures at $z = 0$. *Upper row:* ΛCDM. *Central row:* OCDM. *Lower row:* EdS. *Left panels:* $T = 1$ keV. *Right panels:* $T = 10$ keV. The values for $\Delta\Phi$ were chosen to be multiples of the critical Laplacian $\Delta\Phi_c$ and are given in the plots. For $T = 10$ keV, we only plot the number density for $\Delta\Phi = \Delta\Phi_c$ since it is a very steep function of $\Delta\Phi$ and it is too small for larger multiples of $\Delta\Phi_c$ to be seen.

and the halo number density remains approximately zero. Once modes are included that compose the structures, the halo number density steeply rises as $\alpha$ is increased.

At a certain $\alpha_{\max}$, the number density of objects reaches a maximum, where both effects are balanced. Then, all modes relevant for structures of size $R = \sqrt{-2\Phi_i/\Delta\Phi_j}$ are included, but larger modes are excluded which would create a non-vanishing potential gradient. Thus, $\alpha_{\max}$ can be used to define $k_{\min}$ for each pair $(T_i, \Delta\Phi_j)$ individually by

$$k_{\min} = \frac{2\pi}{\alpha_{\max} R} \,. \tag{3.42}$$

This definition of $k_{\min}$ has to be used when evaluating the spectral moments (3.21).

In App. A, we present an alternative way to define a physically reasonable cut-off wave vector for the evaluation of the spectral moments. It turns out, however, that the number density of objects with a low X-ray temperature function is highly underestimated in this way.

### 3.4.4 Inferring the temperature function from the Press-Schechter mass function

In order to compare the X-ray temperature function that we have derived from the statistics of gravitational potential perturbations to the classical Press-Schechter theory, we need a proper, albeit idealised, and consistent mass-temperature relation. Since we used the virial theorem (3.38) to relate the temperature to the potential, we will start at the same point to relate the temperature to a mass. Note that this

has nothing to do with an assumption on real clusters, but merely serves the purpose of a theoretical cross-comparison between the mass-based Press-Schechter approach and our direct derivation of the temperature function.

We saw earlier that for a spherical and homogeneous overdensity, the potential depth in the centre is $\Phi_0 = -2\pi G\bar{\rho}R^2$, where $\bar{\rho} = \tilde{\delta}_\mathrm{v}\rho_\mathrm{b}$ is the constant density inside the *perturbation*. Nonetheless, we shall replace $\tilde{\delta}_\mathrm{v}$ by the virial overdensity $\tilde{\Delta}_\mathrm{v}$, which is a good approximation because $\tilde{\delta}_\mathrm{v} = \tilde{\Delta}_\mathrm{v} - 1$ and $\tilde{\Delta}_\mathrm{v} = O(10^2)$.

The mass of the overdensity is $M = \frac{4}{3}\pi\rho R^3$, where $\rho$ is the total density inside the sphere. It is related to the background density by $\rho = \tilde{\Delta}_\mathrm{v}\rho_\mathrm{b}$. According to the previous statements, we can identify $\bar{\rho}$ with $\rho$ since $\bar{\rho} \approx \rho$. Combining the equations for the potential and the mass, and using the virial theorem yields the temperature-mass relation

$$k_\mathrm{B}T = \left(\frac{\pi\rho}{6}\right)^{1/3} G\mu m_\mathrm{p} M^{2/3} \,. \tag{3.43}$$

The density $\rho$ inside the cluster is related to the background density by $\rho(z) = \rho_\mathrm{cr0}\Omega_\mathrm{m0}\tilde{\Delta}_\mathrm{v}(z)(1+z)^3$. In our further calculations, however, we will use the virial overdensity $\Delta_\mathrm{v}$, which was defined with respect to the *critical* density instead of the *background* density (see Eq. 2.58), yielding

$$\rho(z) = \rho_\mathrm{cr0}\frac{\Omega_\mathrm{m0}}{\Omega_\mathrm{m}(z)}\Delta_\mathrm{v}(z)(1+z)^3 \,. \tag{3.44}$$

Inserting the previous equation into Eq. (3.43), normalising to $M = 10^{15} M_\odot$ and $\Delta_\mathrm{v} = 178$, and combining all other quantities including $H_0 = 100\,h$ km s$^{-1}$ Mpc$^{-1}$ into one normalisation factor, we find

$$k_\mathrm{B}T = 7.83\ \mathrm{keV}\left(\frac{\Omega_\mathrm{m0}}{\Omega_\mathrm{m}(z)}\frac{\Delta_\mathrm{v}(z)}{178}\right)^{1/3}\left(\frac{M}{10^{15}\,h^{-1}\,M_\odot}\right)^{2/3}(1+z) \,. \tag{3.45}$$

This is almost the same relation as given by Eke et al. (1996). The only difference is the normalisation factor. While we used a spherical and homogeneous overdensity for the calculation in order to be consistent with the derivation of the potential function, they derived a mass temperature-relation for an isothermal sphere (see Sect. 2.8.1), which results in a different normalisation.

We shall use this relation to convert the classical Press-Schechter mass function into a temperature function. Again, we must not forget to account for the Jacobian when transforming from mass to temperature. In contrast to the transformation of the potential to the temperature, the Jacobian of the mass-temperature transformation depends on temperature since both quantities are related non-linearly.

Finally, we also use Eq. (3.45) to convert the mass functions derived by Sheth & Tormen (1999) and Jenkins et al. (2001) and introduced in Sect. 2.9.4, to X-ray temperature functions, knowing that these are fits to numerical simulations which include effects of ellipsoidal collapse, while the derivation of our mass-temperature relation is based on spherical collapse. Yet, it should yield qualitative information on the importance of ellipsoidal collapse in our potential approach, having in mind that structures in the potential field are smoother than structures in the density field.

## 3.5 Results

In this section, we present the X-ray temperature functions for the ΛCDM, OCDM, and EdS cosmologies calculated from the statistics of gravitational potential perturbations and compare them to temperature functions derived from three well-known mass functions. The results are shown in Fig. 3.4, where we compare the X-ray temperature function inferred from the potential using Eq. (3.39) to the X-ray temperature function calculated from the Press-Schechter, the Sheth-Tormen and the Jenkins et al. mass functions using Eq. (3.45) for our three cosmological models and three redshifts.

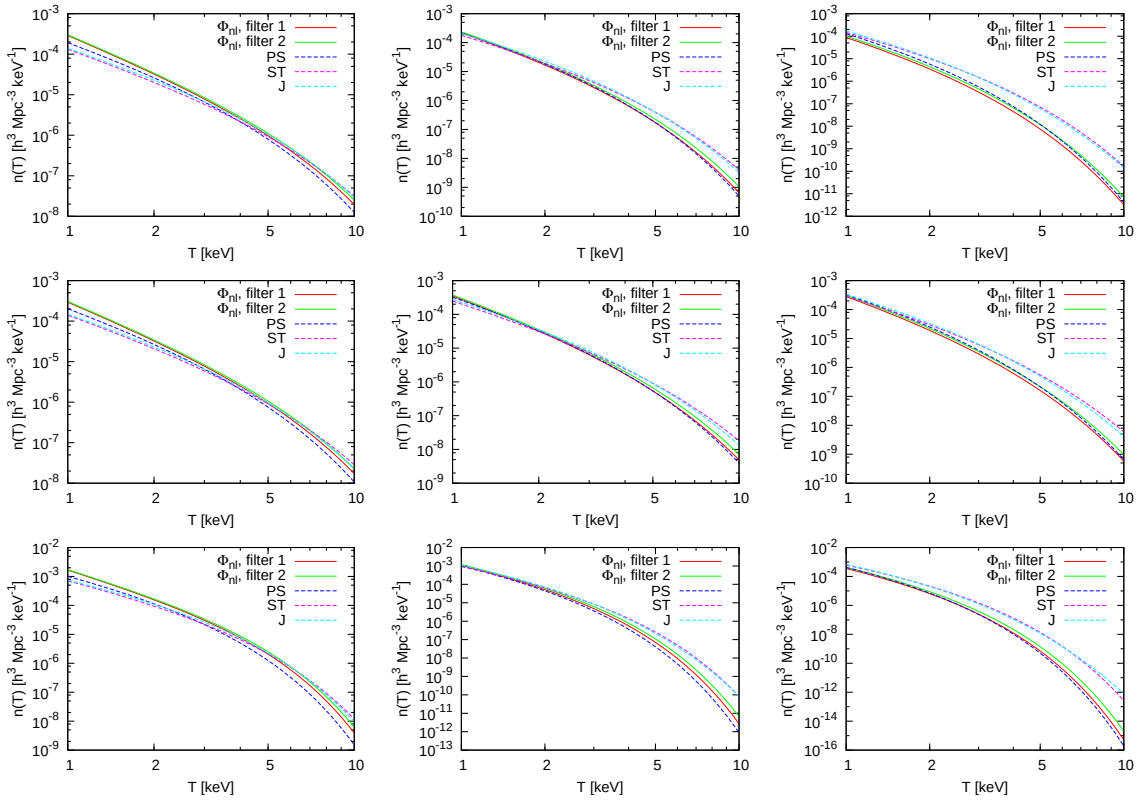


**Figure 3.4:** Comparison of the X-ray temperature functions derived from the statistics of gravitational potential perturbations ($\Phi_{\rm nl}$) and the mass functions by Press & Schechter (PS), Sheth & Tormen (ST), and Jenkins et al. (J) for three different cosmologies and three redshifts. The filters 1 and 2 are defined by Eqs. (2.27) and (3.27), respectively. *Upper row:* ΛCDM. *Central row:* OCDM. *Lower row:* EdS. *Left panels:* $z = 0$. *Central panels:* $z = 1$. *Right panels:* $z = 2$. Note that the $y$-axes are not scaled equally in order to compare the temperature functions more appropriately.

The X-ray temperature function inferred from the statistics of fluctuations in the gravitational potential matches the temperature function inferred from the Press-Schechter mass function quite well for all three cosmological models and redshifts shown. As expected, the filter modelled after the internal potential profile of a homogeneous sphere (filter 2) yields slightly larger number densities especially at the high-temperature end since it is wider in $k$-space than the top-hat filter (filter 1). The temperature function based on our novel approach is in good agreement with the classical Press-Schechter approach with an only slightly different amplitude depending on redshift. These differences, however, may be irrelevant because of the idealising assumptions entering both approaches.

A comparison with temperature functions inferred from mass functions including elliptical collapse like the Sheth-Tormen mass function shows that the deviations increase substantially with redshift. This suggests that ellipsoidal collapse should also explicitly be included in the potential approach. However, we emphasise again that this comparison is only qualitative since the mass-temperature relation used is based on spherical and homogeneous objects so that the actual difference between the different approaches may be even smaller.

## 3.6 Conclusions

In this chapter, we have developed a novel approach to a theoretical derivation of an X-ray temperature function that does not depend on global, unobservable cluster quantities, but merely on the depth of the gravitational potential, which is a locally defined quantity directly related to observables. Using the

statistical properties of a Gaussian random field, we were able to derive a distribution for the minima in the cosmic gravitational potential. Counting only those potential minima which are "curved enough", in the sense that their Laplacian exceeds a critical value, it was possible to compute semi-analytically a potential function belonging to collapsed structures. The critical Laplacian, needed to distinguish collapsed structures from non-collapsed structures, could be related to the critical density contrast $\delta_c$ of the spherical-collapse model, which also plays an important role in the Press-Schechter formalism.

We have also managed to calculate the influence of non-linear structure formation on the potential by referring again to the spherical-collapse model, which allows the ratio of the linearly and non-linearly evolved potential depths to be computed. Both the linear and the non-linear evolution of the potential are much slower compared to the evolution of the matter density. The ratio between the non-linearly and linearly evolved potential depths, for example, is ∼30 times smaller than the ratio $\Delta_v/\delta_c$.

One crucial ingredient to our approach is a proper high-pass filter that removes large-scale potential modes and gradients resulting from them. We have found that choosing the filter scale such as to maximise the number density of objects yields good agreement between the Press-Schechter approach based on an idealised mass-temperature relation, and our direct derivation of the temperature function. This criterion thus provides the foundation for using number counts of galaxy clusters in cosmology without invoking global quantities like cluster masses. Although we have only presented results for ΛCDM, OCDM, and EdS, it would be generally straightforward to extend our computation of the X-ray temperature function to more elaborate cosmological models including e.g. quintessence.

Suggested by Fig. 3.4, we should achieve a better compatibility to results from $N$-body simulations if ellipsoidal-collapse dynamics are included in the derivation. This is not as obvious as for density perturbations since potential fluctuations are much less asymmetric, and their non-linear evolution is much less pronounced. We will examine in Sects. 5.2 and 5.3 the effect of ellipsoidal-collapse dynamics on our potential-based temperature function. Therefore, we will develop a consistent ellipsoidal-collapse model in the next chapter. As we will see in Chap. 5, the inclusion of ellipsoidal-collapse dynamics in the derivation of the potential-based X-ray temperature function leads to a function with a different shape compared to the temperature functions derived from the Sheth-Tormen and Jenkins et al. mass functions, but yet is in good agreement with a temperature function inferred from a numerical simulation.

In the following chapters, we will use the filter (3.27) when calculating the spectral moments for the potential-based X-ray temperature function since it better reflects the profile of a halo's gravitational potential.

# 4 Chapter 4

# Triaxial collapse and virialisation of dark-matter haloes

In this chapter, we reconsider the ellipsoidal-collapse model by Bond & Myers (1996) and extend it in two ways: We modify the treatment of the external gravitational shear field, introducing a hybrid model in between linear and non-linear evolution, and we present a virialisation criterion derived from the tensor virial theorem to replace an *ad-hoc* criterion employed so far in the literature. We compute the collapse parameters $\delta_c$ and $\Delta_v$ and find that they increase with ellipticity $e$ and decrease with prolaticity $p$. We marginalise them over the appropriate distribution of $e$ and $p$ and show the results as functions of halo mass and virialisation redshift. While the hybrid model for the external shear gives results very similar to those obtained from the non-linear model, ellipsoidal collapse changes the collapse parameters typically by $(20\ldots50)\%$, in a way increasing with decreasing halo mass and decreasing virialisation redshift. We qualitatively confirm the dependence on mass and virialisation redshift expressed by a fitting formula for $\delta_c$, but find noticeable quantitative differences in particular at low mass and high redshift. A derived mass function is in good agreement with mass functions recently proposed in the literature.

The contents of this chapter is published in Angrick & Bartelmann (2010).

## 4.1 Introduction

The spherical-collapse model, introduced in Sect. 2.7, is a fundamental ingredient in the theory of cosmic structure formation (see e.g. Wang & Steinhardt 1998; Engineer et al. 2000 or more recent works by Mota & van de Bruck 2004; Bartelmann et al. 2006; Schäfer & Koyama 2008). Following the collapse of a slightly overdense, homogeneous sphere, it allows the derivation of two essential parameters; (1) the overdensity of a virialised halo compared to the mean ($\tilde{\Delta}_v$) or the critical cosmic density ($\Delta_v$), and (2) the critical linear density contrast $\delta_c$. The former is important since it allows relating sizes to masses of virialised structures, and the latter because it establishes a link between linear structure formation and the population statistics of collapsed haloes as for the Press-Schechter mass function (see Sect. 2.9.1). Despite fundamental doubts as to the validity of such a simplified model for accurate cosmological predictions, the parameters derived from the spherical-collapse model or variants thereof allow surprisingly far-reaching predictions such as the halo mass function or the correlation properties of haloes, which are confirmed by numerical simulations.

The statistics of a Gaussian random field implies that spherical collapse should not occur. In fact, the probability distribution for the eigenvalues $\lambda_i$ of the Zel'dovich deformation tensor (Doroshkevich, 1970, see also Sect. 2.6) shows that spherical collapse has a vanishing probability,

$$p(\lambda_1,\lambda_2,\lambda_3) = \frac{15^3}{8\pi\sqrt{5}\sigma_R^6}\exp\left(-\frac{3\delta^2}{\sigma_R^2}+\frac{15I}{2\sigma_R^2}\right)(\lambda_1-\lambda_2)(\lambda_2-\lambda_3)(\lambda_1-\lambda_3)\,, \tag{4.1}$$

since it requires $\lambda_1 = \lambda_2 = \lambda_3$. In this equation, $\delta \equiv \lambda_1 + \lambda_2 + \lambda_3$, $I \equiv \lambda_1\lambda_2 + \lambda_2\lambda_3 + \lambda_1\lambda_3$, and $\sigma_R^2$ denotes again the variance of the matter power spectrum smoothed on a scale $R$ that corresponds to a halo mass $M$, (see Eqs. 2.26 and 2.71). Modifications of the original Press-Schechter mass function motivated by ellipsoidal collapse (the Sheth-Tormen mass function, see Sect. 2.9.4) substantially improve the agreement of analytic predictions on the halo population with numerical simulations (e.g. the *Millennium simulation* by Springel et al., 2005).

Ellipsoidal collapse was analysed many times before (Bartelmann et al., 1993; Eisenstein & Loeb, 1995; Bond & Myers, 1996). Several authors have worked with the model by Bond & Myers (1996), generalising it for different cosmologies and introducing the scale factor $a$ as a time variable (Monaco, 1995, 1997, 1998; Sheth et al., 2001; Sheth & Tormen, 2002; Ohta et al., 2004). We are reconsidering it here for two reasons.

First, we want to analyse how different assumptions on the treatment of the environment of a halo impact on the parameters $\Delta_\mathrm{v}$ and $\delta_\mathrm{c}$. Previous assumptions have been that the principal-axis system of the homogeneous ellipsoid is either identical with that of the external gravitational shear field, or that the two eigensystems do not coincide, introducing rotation and a deviation from the homogeneous mass profile. We introduce another assumption here, letting the eigensystems of the collapsing ellipsoid and its surrounding shear field follow each other until turn-around of the major principal axis and then decoupling both.

Second, we want to stop the collapse along any of the principal axes according to a physically motivated virialisation condition. Virialisation must be invoked to prevent the axes from collapsing to zero, and thus to be able to follow the entire collapse of an ellipsoid, i.e. the collapse of its three principal axes. Conventionally, the collapse of each axis is stopped when $a_i(a) = 0.177\,a$, where $a_i$ is the scale factor of the $i$-th axis and $a$ is the background scale factor (Bond & Myers, 1996; Sheth et al., 2001). In this way, $\Delta = a^3/(a_1a_2a_3) = 178$ for spherical collapse in an EdS universe at the time when the third axis virialises. However, the value 0.177 has no fundamental physical motivation, and there is no guarantee for it not to be different for ellipsoidal rather than spherical collapse, or when cosmologies other than EdS are to be considered. We present a general virialisation condition based on the *tensor virial theorem* that avoids introducing such an uncalibrated factor. We find substantial changes on both $\Delta_\mathrm{v}$ and $\delta_\mathrm{c}$ from both modifications and point out several discrepancies of our results with earlier studies.

## 4.2 The model

In this section, we shall briefly review the ellipsoidal-collapse model of Bond & Myers (1996) for cosmologies with a cosmological constant introducing the scale factor $a$ as time variable. Furthermore, we shall present a physically motivated virialisation condition to stop the collapse of each axis, and show how to find the proper initial ellipticity and prolaticity as a function of mass and virialisation redshift.

### 4.2.1 The evolution equations

Let $a_i = R_i/R_\mathrm{pk}$ be the dimensionless principal axes of the ellipsoid, where $R_i$ with $1 \le i \le 3$ are its dimensional semi-major axes, and $R_\mathrm{pk}$ the size of a spherical top-hat corresponding to a mass $M$ via Eq. (2.71). The evolution of the three principal axes $a_i$ with time $t$ in a cosmology with a cosmological constant $\Lambda = (8\pi G/c^2)\,\rho_\Lambda$ is given by

$$\frac{\mathrm{d}^2a_i}{\mathrm{d}t^2} = \frac{8}{3}\pi G\rho_\Lambda a_i - 4\pi G\rho_\mathrm{b}a_i\left(\frac{1}{3} + \frac{\delta}{3} + \frac{b_i}{2}\delta + \lambda_{\mathrm{ext},i}\right) \tag{4.2}$$

(Bond & Myers, 1996), where $G$ is the gravitational constant and $c$ the speed of light. The density contrast of the ellipsoid with respect to the background density is $\delta = (\rho - \rho_\mathrm{b})/\rho_\mathrm{b} = a^3/(a_1a_2a_3) - 1$.

The parameters $b_i$ and $\lambda_{\mathrm{ext},i}$ denote the internal and external contributions to the gravitational tidal shear which occur due to the deviation from sphericity. Generally, the total tidal field is described by the *tidal field tensor* $\mathsf{T}$ with the elements $T_{ij} = \partial^2\varphi/(\partial x_i\,\partial x_j) = T_{\mathrm{int},ij} + T_{\mathrm{ext},ij}$, where $\varphi$ denotes a scaled version of the gravitational potential (cf. Sect. 2.6), and $T_{\mathrm{int},ij}$ and $T_{\mathrm{ext},ij}$ are the internal and external contributions to the shear, respectively. After a transformation into the ellipsoid's eigensystem, which is the same as the eigensystem of $\mathsf{T}$ in this model, the internal shear can be evaluated as

$$b_i(t) = a_1(t)\,a_2(t)\,a_3(t)\int_0^\infty \frac{\mathrm{d}\tau}{[a_i^2(t)+1]\prod_{k=1}^3[a_k^2(t)+1]^{1/2}} - \frac{2}{3}\,, \tag{4.3}$$

while the external shear can be approximated by

$$\lambda_{\mathrm{ext},i}(t) \equiv \begin{cases} \dfrac{D_+(t)}{D_+(t_\mathrm{ini})}\left[\lambda_i(t_\mathrm{ini}) - \dfrac{\delta(t_\mathrm{ini})}{3}\right] & \text{(linear approx.)}\,, \\ \dfrac{5}{4}b_i(t) & \text{(non-linear approx.)}\,, \end{cases} \tag{4.4}$$

where $D_+$ is the linear growth factor introduced in Eq. (2.19), and the $\lambda_i$ are the eigenvalues of the Zel'dovich deformation tensor. See the first appendix of Bond & Myers (1996) for details of the calculation. Here and in the following, the index 'ini' refers to initial values.

In linear approximation, the environment into which the ellipsoid is embedded evolves completely independently of it, whereas in the non-linear approximation, it is tightly coupled to the ellipsoid. In Sect. 4.3.1 we shall introduce the *hybrid model* as a third approximation for the external shear.

We can rewrite Eq. (4.2) by using the scale factor $a$ as time variable and Friedmann's equation (1.17), yielding

$$\frac{\mathrm{d}^2a_i}{\mathrm{d}a^2} + \left[\frac{1}{a} + \frac{E'(a)}{E(a)}\right]\frac{\mathrm{d}a_i}{\mathrm{d}a} + \left[\frac{3\Omega_{\mathrm{m}0}}{2a^5E^2(a)}C_i(a) - \frac{\Omega_{\Lambda0}}{a^2E^2(a)}\right]a_i = 0\,, \tag{4.5}$$

where a prime denotes differentiation with respect to $a$, and $C_i \equiv (1+\delta)/3 + b_i/2 + \lambda_{\mathrm{ext},i}$. Equation (4.5) defines a set of three coupled second-order differential equations, for which we need six independent initial conditions compatible with the Zel'dovich approximation, Eqs. (2.45) and (2.46), for early times. These are provided by

$$a_i(a_\mathrm{ini}) = a_\mathrm{ini}[1 - \lambda_i(a_\mathrm{ini})]\,, \tag{4.6}$$

$$\frac{\mathrm{d}a_i}{\mathrm{d}a}(a_\mathrm{ini}) = 1 - \left(1 + \frac{\mathrm{d}\ln D_+(a_\mathrm{ini})}{\mathrm{d}\ln a}\right)\lambda_i(a_\mathrm{ini}) \approx 1 - 2\lambda_i(a_\mathrm{ini})\,, \tag{4.7}$$

since $D_+(a) \approx a$ for $a \ll 1$. Choosing $a_\mathrm{ini} = 2\times10^{-5}$, this is comfortably fulfilled. In App. B, we compare Eqs. (4.5–4.7) with the results presented by Monaco (1997) and see that they differ.

In the following, we shall assume that the eigenvalues $\lambda_i$ of the Zel'dovich tensor are ordered as $\lambda_1 \geq \lambda_2 \geq \lambda_3$, which implies that the ellipsoid collapses along the direction 1, i.e. $a_1 \to 0$, first. At that time $\delta \to \infty$, and the collapse of the remaining two axes can no longer be followed so that we have to add a virialisation condition for each axis preventing its collapse to zero.

### 4.2.2 The virialisation condition

We want to replace the unphysical virialisation condition $a_i(a) = 0.177\,a$, inspired by considerations of the ellipsoidal-collapse model in the EdS cosmology (see Sect. 4.1), by following a different approach. We present a physically well-motivated virialisation condition to stop the collapse of each axis individually, starting from the *tensor virial theorem* (see Binney & Tremaine, 1987, pp. 213, 280),

$$\frac{1}{2}\frac{\mathrm{d}^2I_{ij}}{\mathrm{d}t^2} = 2K_{ij} + \Pi_{ij} + W_{ij} + V_{ij}\,, \tag{4.8}$$

where $\mathsf{I}$ is the *moment of inertia tensor*, $\mathsf{K}$ and $\Pi$ are the contributions to the *kinetic energy tensor* coming from ordered and random motions, respectively, $\mathsf{W}$ is the *potential energy tensor*, and $\mathsf{V}$ is the *external potential energy tensor*. Their elements are generally defined as

$$\begin{aligned} I_{ij} &\equiv \int_{\mathcal{V}} \mathrm{d}^3x\,\rho\, x_i x_j\,, \qquad W_{ij} \equiv -\int_{\mathcal{V}} \mathrm{d}^3x\,\rho\, x_i \frac{\partial \Phi_{\mathrm{int}}}{\partial x_j}\,, \\ K_{ij} &\equiv \frac{1}{2}\int_{\mathcal{V}} \mathrm{d}^3x\,\rho\, \overline{v}_i \overline{v}_j\,, \quad \Pi_{ij} \equiv \int_{\mathcal{V}} \mathrm{d}^3x\,\rho\, \sigma_{ij}^2\,, \end{aligned} \tag{4.9}$$

and

$$V_{ij} \equiv -\frac{1}{2}\int_{\mathcal{V}} \mathrm{d}^3x\,\rho \left( x_i \frac{\partial \Phi_{\mathrm{ext}}}{\partial x_j} + x_j \frac{\partial \Phi_{\mathrm{ext}}}{\partial x_i} \right), \tag{4.10}$$

where $\rho$ is the density of the fluid, $\Phi_{\mathrm{int}}$ and $\Phi_{\mathrm{ext}}$ are the gravitational potentials of the ellipsoid itself and its surroundings, respectively, $\mathcal{V}$ is the volume which is integrated over, $\sigma_{ij}^2 \equiv \overline{v_i v_j} - \overline{v}_i \overline{v}_j$ are the velocity dispersions, and the bar indicates averaging over $\mathcal{V}$.

We now specialise to the case of a homogeneous ellipsoid. For a stable mass configuration, the left-hand side of Eq. (4.8) has to vanish for each component of the inertial tensor individually. Since the ellipsoid is assumed to be at rest and the ellipsoid's eigensystem is chosen as a reference frame, $\overline{v}_i = 0$ so that $K_{ij} = 0$ and $\Pi_{ij} = \int_{\mathcal{V}} \mathrm{d}^3x\,\rho\,\langle v_i^2\rangle\,\delta_{ij}$ with the *Kronecker symbol* $\delta_{ij}$. Note again that in this framework, the eigensystems of the overdense ellipsoid and the gravitational tidal field are identical. For a homogeneous ellipsoid, $v_i(x_i) = (\dot{a}_i/a_i)x_i$, thus

$$\Pi_{ij} = \frac{1}{5}\dot{a}_i^2 M \delta_{ij}\,, \tag{4.11}$$

with the mass $M$ of the ellipsoid. The sum $W_{ij} + V_{ij}$ can be evaluated using $-\vec{\nabla}(\Phi + \Phi_{\mathrm{ext}}) = \ddot{\vec{x}}$ and Eq. (4.2) to be

$$W_{ij} + V_{ij} = \int_{\mathcal{V}} \mathrm{d}^3x\,\rho \frac{\mathrm{d}^2 a_i}{\mathrm{d}t^2}\frac{x_i}{a_i} = \frac{1}{5}a_i^2 M \left( \frac{8\pi G}{3}\rho_\Lambda - 4\pi G \rho_{\mathrm{b}} C_i \right)\delta_{ij}\,. \tag{4.12}$$

Requiring that Eq. (4.8) is fulfilled for each axis separately and introducing again the scale factor $a$ as time variable yields the *virialisation conditions* for the three axes $a_i$,

$$\left(\frac{a_i'}{a_i}\right)^2 = \frac{1}{a^2 E^2(a)}\left( \frac{3\Omega_{\mathrm{m0}}}{2a^3} C_i - \Omega_{\Lambda 0} \right). \tag{4.13}$$

When this condition is fulfilled for an axis together with $\dot{a}_i < 0$, its collapse is stopped and its size is frozen in.

We emphasise that the former equation is consistent with the virialisation condition for spherical collapse in the EdS universe, where $R_{\mathrm{v}}/R_{\mathrm{ta}} = 0.5$ (see Sect. 2.7). In this cosmology, Eq. (4.13) becomes

$$R = \frac{GM}{\dot{R}^2}\,, \tag{4.14}$$

with $a_1 = a_2 = a_3 \equiv R$. Using the parametric solution

$$R = \frac{R_{\mathrm{ini}}}{2\delta_{\mathrm{ini}}}(1 - \cos\theta)\,, \qquad t = \frac{3t_{\mathrm{ini}}}{4\delta_{\mathrm{ini}}^{3/2}}(\theta - \sin\theta) \tag{4.15}$$

(Engineer et al., 2000, compare also Eq. 2.61) together with the relations $R_{\mathrm{ini}}/\delta_{\mathrm{ini}} = R_{\mathrm{ta}}$ and $R_{\mathrm{ini}}^3 = 9GMt_{\mathrm{ini}}^2/2$ indeed gives the expected result that Eq. (4.14) is satisfied when $R = R_{\mathrm{ta}}/2$.

For the ΛCDM model, the additional potential from the cosmological potential has to be taken into account leading to Eq. (2.55) for the ratio of the radii at virialisation and collapse. The relevant solution of this equation agrees precisely with the condition derived from the tensor virial theorem, Eq. (4.13), as Fig. 4.1 shows. The small deviation occurs since we choose the time of virialisation rather than collapse as a reference ($z = z_{\mathrm{v}}$) when using the tensor virial theorem. If we use the collapse time ($z = z_{\mathrm{col}}$) instead, both conditions yield identical results.

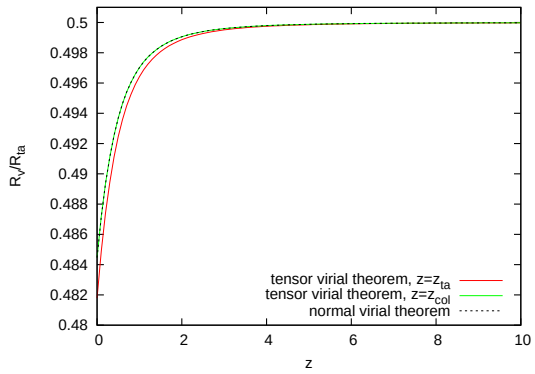


**Figure 4.1:** Comparison of the virialisation conditions from the scalar and tensor virial theorems.

### 4.2.3 The initial ellipticity and prolaticity

Equations (4.6) and (4.7) demand choosing initial values for the Zel'dovich deformation tensor to define the initial deviation of the principal axes and their time derivatives from the background. We shall show how they are chosen appropriately so that they comply with the assumed Gaussian nature of the Universe's initial conditions and represent a statistical average of haloes with the same mass $M$ and virialisation redshift $z_\mathrm{v}$ but different shapes.

Starting from the probability distribution for the eigenvalues of the Zel'dovich deformation tensor (4.1), the conditional probability distribution for the *ellipticity* $e \geq 0$ and the *prolaticity* $-e \leq p \leq e$, defined as $e \equiv (\lambda_1 - \lambda_3)/(2\delta)$ and $p \equiv (\lambda_1 - 2\lambda_2 + \lambda_3)/(2\delta)$, respectively, was derived by Sheth et al. (2001) to be

$$g(e,p|\delta) = \frac{1125}{\sqrt{10\pi}}\, e\,(e^2-p^2)\left(\frac{\delta}{\sigma}\right)^5 \exp\left[-\frac{5}{2}\left(\frac{\delta}{\sigma}\right)^2 (3e^2+p^2)\right]. \tag{4.16}$$

To compute a statistical average of any quantity $h(e,p)$ for a given halo that depends on $e$ and $p$, one should marginalise over the distribution $g(e,p)$,

$$\langle h\rangle = \int_0^\infty \mathrm{d}e \int_{-e}^{e} \mathrm{d}p\, h(e,p)\, g(e,p)\,. \tag{4.17}$$

However, a Taylor expansion of $\langle h\rangle$ up to second order in $e$ and $p$ around their mean values $\langle e\rangle$ and $\langle p\rangle$ under the distribution $g(e,p)$ gives

$$\langle h\rangle = h\left(\langle e\rangle,\langle p\rangle\right) + \frac{1}{2}\left.\frac{\partial^2 h}{\partial e^2}\right|_{\langle e\rangle,\langle p\rangle} \sigma_e^2 + \frac{1}{2}\left.\frac{\partial^2 h}{\partial p^2}\right|_{\langle e\rangle,\langle p\rangle} \sigma_p^2\,, \tag{4.18}$$

where $\sigma_e^2$ and $\sigma_p^2$ are the variances for $e$ and $p$ according to the distribution $g$. Up to first order, $\langle h\rangle = h\left(\langle e\rangle,\langle p\rangle\right)$. Deviations occur only at second order. The expectation values for $e$ and $p$ as well as their variances are given by

$$\begin{aligned} \langle e\rangle &= \frac{3\sigma}{\sqrt{10\pi}\,\delta}\,, & \langle p\rangle &= 0\,,\\ \sigma_e^2 &= \frac{(19\pi-54)\sigma^2}{60\pi\,\delta^2}\,, & \sigma_p^2 &= \frac{\sigma^2}{20\delta^2}\,. \end{aligned} \tag{4.19}$$

Since the variances are $\propto (\sigma/\delta)^2$, and $\sigma/\delta < 1$, using the approximation $\langle f\rangle \approx f\left(\langle e\rangle,\langle p\rangle\right)$ introduces only a small error, which is ~1% for $\delta_\mathrm{c}$ and ~3% for $\Delta_\mathrm{v}$ for ΛCDM and OCDM. For EdS, the error is larger and ~3% for $\delta_\mathrm{c}$ and ~10% for $\Delta_\mathrm{v}$. But since the latter cosmology is scientifically only of low relevance and usually serves as a reference model only, the usage of the former approximation is well justified. Instead of sampling $f(e,p)$ at several points for $e$ and $p$, one only has to evaluate it once for $\langle e\rangle$ and $\langle p\rangle = 0$.

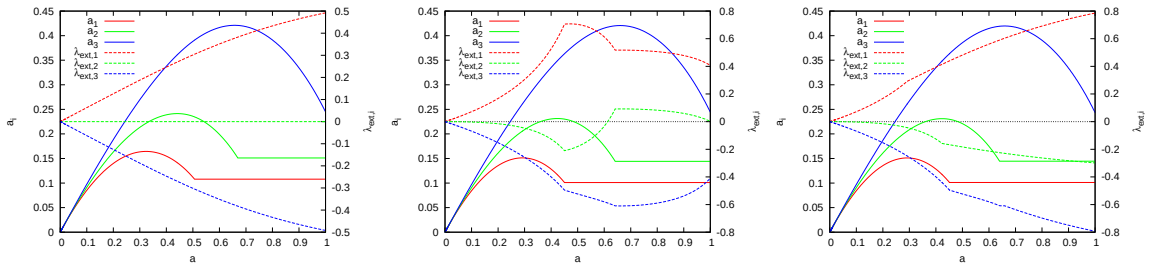

**Figure 4.2:** Evolution of the principal axes and the external shear for a $10^{14}\ h^{-1}\ M_\odot$ dark-matter halo with $e = \langle e \rangle$ and $p = 0$ in the reference ΛCDM model. *Left panel:* Linear approximation. *Central panel:* Non-linear approximation. *Right panel:* Hybrid approximation.

Generally, the eigenvalues $\lambda_i$ are related to $e$ and $p$ by

$$\lambda_1 = \frac{\delta}{3}(1 + 3e + p) = \frac{\delta}{3} + \frac{\sigma}{\sqrt{10\pi}}\,, \tag{4.20}$$

$$\lambda_2 = \frac{\delta}{3}(1 - 2p) = \frac{\delta}{3}\,, \tag{4.21}$$

$$\lambda_3 = \frac{\delta}{3}(1 - 3e + p) = \frac{\delta}{3} - \frac{\sigma}{\sqrt{10\pi}} \tag{4.22}$$

(see e.g. Bond & Myers, 1996; Bardeen et al., 1986), where we have set $e = \langle e \rangle$ and $p = 0$ in the last step.

## 4.3 Results

In this section, we show the results of the ellipsoidal-collapse model for the parameters $\delta_c$ and $\Delta_v$ for three different cosmologies and discuss how they are affected by the choice of the external-shear model.

### 4.3.1 Influence of the external shear

Figure 4.2 shows the evolution of the three principal axes and the eigenvalues of the external shear for a reference ΛCDM model with $\Omega_{m0} = 0.3$, $\Omega_{\Lambda 0} = 0.7$, and $\sigma_8 = 0.8$ for three different models of the external shear and $e = \langle e \rangle$, $p = 0$. The shear in the *linear approximation* evolves completely smoothly over the entire collapse time. Since the evolution of each eigenvalue is given by $D_+(a)$ (see Eq. 4.4), Eqs. (4.20–4.22) imply that $\lambda_{\mathrm{ext},1} > 0$, $\lambda_{\mathrm{ext},2} = 0$, and $\lambda_{\mathrm{ext},3} = -\lambda_{\mathrm{ext},1} < 0$ at all times.

This is different in the *non-linear approximation*: At early times, the evolution of the $\lambda_{\mathrm{ext},i}$ is the same, but soon thereafter, they start evolving non-linearly and $\lambda_{\mathrm{ext},2}$ becomes slightly negative. Noticeably, there are steps in the evolution of the external shear whenever an axis virialises since $\lambda_{\mathrm{ext},i} \propto a_1 a_2 a_3$, and the evolution of this volume factor changes after virialisation of each axis. In the right panel, we introduce the *hybrid approximation*: Initially, the evolution of $\lambda_{\mathrm{ext},i}$ is described by the non-linear model. When one of the axes turns around, however, the corresponding eigenvalue of the external shear continues evolving linearly, i.e. its value at turn-around is then scaled by $D_+(a)/D_+(a_{\mathrm{ta}})$.

We believe that the hybrid model is the preferred model for the evolution of the external shear since it takes into account that the evolution of the ellipsoid itself and its vicinity should be tightly coupled in the beginning. At turn-around, however, they are definitely decoupled so that choosing this moment to switch from non-linear to linear evolution seems appropriate. Hence, we will use the hybrid model for the evolution of the external shear in the following.

The influence of the external-shear model on the parameters $\delta_c$ and $\Delta_v$ is shown in Fig. 4.3. For a given mass and a given virialisation redshift $z_v$, the initial overdensity is chosen such that the third

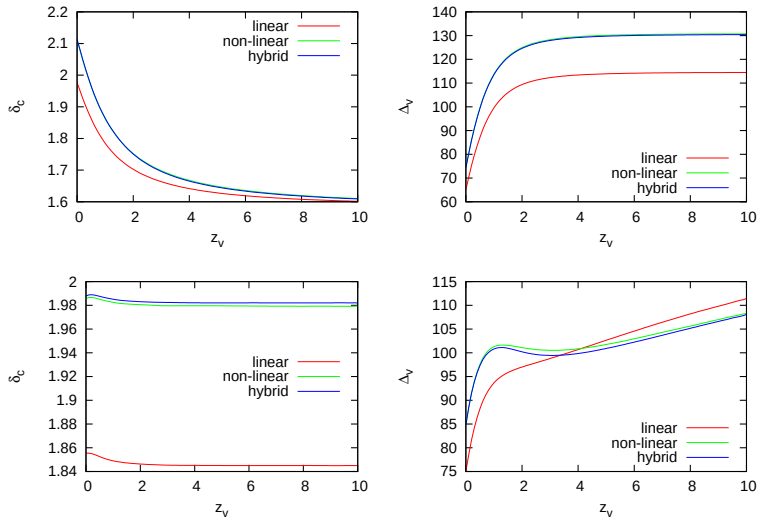


**Figure 4.3:** $\delta_c$ (*left panels*) and $\Delta_v$ (*right panels*) for three different models of the external shear. Both quantities were calculated for a $10^{14}\ h^{-1}\ M_\odot$ dark-matter halo in the reference ΛCDM model. *Top panels:* $e = \langle e \rangle$ as a function of virialisation redshift $z_v$. *Bottom panels:* $e = 0.2$ for all $z_v$. In both cases, $p = 0$.

axis of the ellipsoid finally virialises at $z_v$. Both parameters can then be calculated by

$$\delta_c = \frac{D_+(a_v)}{D_+(a_{ini})} \sum_{i=1}^{3} \lambda_i(a_{ini})\,, \qquad \Delta_v = \frac{\Omega_m(a_v)\, a_v^3}{a_1(a_v)\, a_2(a_v)\, a_3(a_v)}\,. \tag{4.23}$$

In this case, $\Delta_v$ is defined with respect to the *critical density* as it can be primarily found in the literature. For the definition with respect to the *background density*, $\tilde{\Delta}_v$, one simply has to omit $\Omega_m(a_v)$.

Using $\langle e \rangle$ as a function of virialisation redshift and $p = 0$ (top panels of Fig. 4.3), the dependence of $\delta_c$ and $\Delta_v$ on $z_v$ is almost the same for the non-linear and the hybrid models. However, both differ from the linear model, showing that the external shear is most important at the beginning of the ellipsoid's evolution. At that time, the non-linear and the hybrid models agree. While $\delta_c(z_v)$ is always smaller in the linear compared to the other two models, the curves for $\Delta_v(z_v)$ cross. This reflects the circumstance that the initial overdensity in the linear model is different from that in the two other models, leading to a different initial ellipticity and therefore to a completely different evolution history. This can be seen in the bottom panels of Fig. 4.3, for which we have chosen $e = 0.2$ independently of $z_v$. They also clearly show that a varying initial ellipticity drives primarily the evolution of $\delta_c$ with redshift, whereas $\Delta_v$ also strongly varies for fixed $e$. In this case, both $\delta_c$ and $\Delta_v$ are smaller in the linear-shear model compared to the non-linear and the hybrid models.

### 4.3.2 Parameters as function of mass and redshift

Before we present general results for the parameters $\delta_c$ and $\Delta_v$, we should comment on a subtle but very important issue: Whenever we want to compare our results with the ordinary spherical-collapse model, we have to keep in mind that we calculate all quantities at the time when the third axis *virialises*. Thus, we also have to compare these quantities to those from the spherical-collapse model that are also calculated at the time of virialisation and not of collapse, i.e. when $R = R_{ta}/2$ and not $R = 0$ for EdS. This leads to slightly lower reference values of $\delta_c$ and $\Delta_v$ since $z_{col} < z_v$. Using the parametric solutions of Ohta et al. (2004) for the linear and the non-linear overdensity,

$$\delta_l = \frac{3}{5}\left[\frac{3}{4}(\theta - \sin\theta)\right]^{2/3}, \qquad \Delta_{nl} = \frac{9}{2}\frac{(\theta - \sin\theta)^2}{(1 - \cos\theta)^3}\,, \tag{4.24}$$

respectively, and $\theta = 3\pi/2$ at virialisation, we find that $\delta_c = 1.583$ and $\Delta_v = 147$ for the EdS universe when $R = R_v$ independent of $z_v$. Recently, Lee & Ng (2010) also pointed out the difference between the parameter values at the times of collapse and virialisation and arrived at the same values.

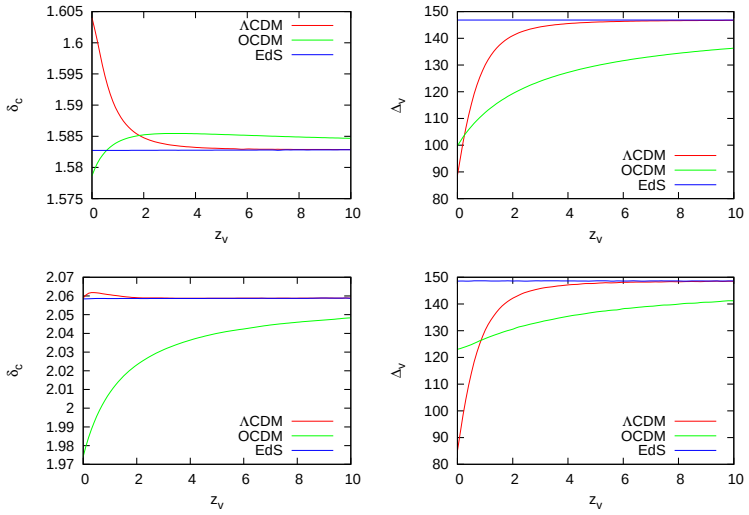


**Figure 4.4:** $\delta_c$ (*left panels*) and $\Delta_v$ (*right panels*) for three different cosmological models and fixed initial $e$ and $p$. *Top panels:* Spherical case ($e = p = 0$). *Bottom panels:* Triaxial case with $e = 0.2$ and $p = -0.1$.

The top panels of Fig. 4.4 show $\delta_c$ and $\Delta_v$ for three different cosmologies for $e = p = 0$, i.e. spherical systems. The OCDM cosmology is the same as our reference ΛCDM model except that $\Omega_\Lambda = 0$. For the EdS model, we set $\Omega_m = 1$ and $\Omega_\Lambda = 0$. Indeed, for the EdS universe, the constant values derived analytically are also reproduced by solving Eq. (4.5) numerically. This demonstrates again that Eqs. (4.5) and (4.13) are fully consistent with the well-known spherical-collapse model. Note that the qualitative behaviour of $\Delta_v(z_v)$ is the same as $\Delta_v(z_{col})$ (compare e.g. with Bartelmann et al., 2006). However, there is a difference for the critical linear overdensity $\delta_c$ whose shape as a function of $z_v$ differs substantially from the shape as a function of $z_{col}$. This should illustrate that the time chosen in the model when virialisation actually occurs ($z_v$ or $z_{col}$) can already have substantial impact on the qualitative behaviour of relevant quantities as a function of redshift, hence it is not necessarily a consequence of ellipsoidal collapse alone.

The bottom panels of Fig. 4.4 show $\delta_c$ and $\Delta_v$ for a triaxial halo with $e = 0.2$ and $p = -0.1$. Also in this case, both parameters are independent of $z_v$ for the EdS universe, although $\delta_c$ changes from 1.583 to 2.058, while $\Delta_v$ stays almost the same, 148 instead of 147. Interestingly, the most drastic changes in the shapes of both parameters occur for the OCDM model, for which the total density is only approximately a third of the critical density at $z = 0$, while for the ΛCDM model their changes are small.

The influence of the halo mass $M$ and the virialisation redshift $z_v$ on both $\delta_c$ and $\Delta_v$ are illustrated in Fig. 4.5. While for both decreasing mass and decreasing redshift, $\delta_c$ is a monotonically decreasing function, approaching the reference values from the spherical-collapse model in the EdS universe for large masses and high virialisation redshifts, the situation for $\Delta_v$ is much more complicated. For all three models, it has a minimum at redshifts 4–5 and at a mass of $\sim 10^{16}\ h^{-1}\ M_\odot$. For smaller values of mass and redshift, it is a monotonically decreasing function of both $M$ and $z_v$ for the OCDM and EdS models. It is also monotonically decreasing as a function of $M$ in the ΛCDM model, but reaches a maximum at $z_v \sim 1$. This is a direct result of the definition of $\Delta_v$ with respect to the *critical density*. If it was defined with respect to the *background density*, the factor $\Omega_m(a_v)$ would not appear in Eq. (4.23), and all three curves would increase with decreasing $z_v$.

In Fig. 4.5, one can clearly see that the intervals that are covered for both $\delta_c$ and $\Delta_v$ are the largest for the EdS model while the differences between their values in the framework of the ΛCDM and the OCDM model are not as large, indicating that the dependence of the ellipsoid's evolution on the total amount of matter in the Universe is stronger than on the value of the cosmological constant if varying initial ellipticities are taken into account.

For either $M \to \infty$ or $z_v \to \infty$, both $\delta_c$ and $\Delta_v$ must reach the reference values for spherical collapse in the EdS universe since the initial ellipticity $\langle e \rangle \propto \sigma/\delta$ and $\sigma$ both decrease with increasing mass,

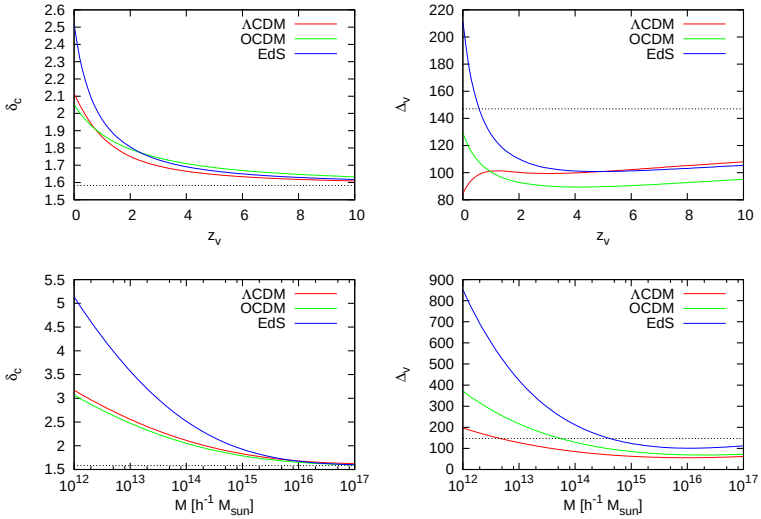


**Figure 4.5:** $\delta_c$ (*left panels*) and $\Delta_v$ (*right panels*) as a function of halo mass and virialisation redshift for three different cosmologies marginalised over $e$ and $p$. *Top panels:* Dependence on virialisation redshift $z_v$ for a halo with $M = 10^{14}\ h^{-1}\ M_\odot$. *Bottom panels:* Dependence on mass $M$ for a halo with $z_v = 0$. Thin dashed lines show the reference values from spherical collapse in the EdS universe, $\delta_c = 1.583$ and $\Delta_v = 147$.

and $\delta$ has to be the higher the earlier the structure is required to collapse. This expected behaviour can be clearly seen for $\delta_c$, whereas for $\Delta_v$ this happens finally for *very* large $M$ and $z_v$. We should stress again in this context that a crucial portion of the dependence on mass and virialisation redshift is driven by the change in the initial ellipticity, comparing Figs. 4.4 and 4.5.

We compare in Fig. 4.6 the results of this chapter for $\delta_c$ as a function of mass and redshift with the fitting formula (2.85) of Sheth et al. (2001). The left panel shows that the dependence on mass is similar for both. However, the fit by Sheth et al. (2001) is less steep as a function of mass resulting from the differences of their underlying work to ours: First, they use the linear-shear model instead of the hybrid model, leading to a smaller $\delta_c$ for all redshifts as shown in Fig. 4.3. Second, the collapse of each axis is stopped using the artificial condition $a_i = 0.177\,a$, leading to $\delta_c = 1.686$ as a reference value at high mass. Thus, the fitting formula provides a larger value for large masses, while our approach leads to a $\delta_c = 1.583$ for $M \to \infty$ due to the virialisation condition that we apply. Third, for a given initial overdensity $\delta$, Sheth et al. (2001) use the most probable value $e_{\rm mp} = (\sigma/\delta)/\sqrt{5}$ instead of the expectation value $\langle e \rangle$ given by Eq. (4.19), which leads to initial ellipticities that are slightly too low so that the asymptotic limit for high redshifts is reached earlier than in our case.

The right panel of Fig. 4.6 shows a similar behaviour for $\delta_c$ as a function of redshift. The differences between the fitting formula and the result of our work again occur due to the different virialisation time and condition, and the difference between the most probable and the expectation value of $e$.

For applications, fitting formulae for both $\delta_c$ and $\Delta_v$ may be useful. We provide expressions here, which are inspired by Eq. (2.85). For $\delta_c(M, z)$, we suggest

$$\delta_c(M,z) = \delta_{c,\rm sph}(z_v)\left\{1 + b\left[\frac{\sigma^2(M,z_v)}{\delta^2_{c,\rm sph}(z_v)}\right]^c\right\}, \tag{4.25}$$

where $b = 0.6536$, $c = 0.6387$, and both $\delta_{c,\rm sph}$ and $\sigma^2$ are cosmology-dependent quantities. Note again

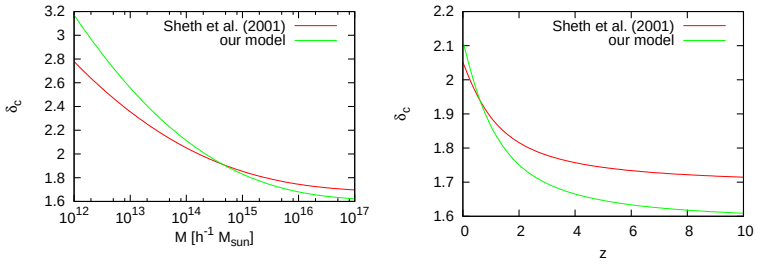


**Figure 4.6:** Comparison of the fitting formula (2.85) for $\delta_c(M, z)$ with the results of our refined model for the reference ΛCDM model. *Left panel:* $\delta_c$ as a function of mass and $z = 0$. *Right panel:* $\delta_c$ as a function of redshift and $M = 10^{14}\ h^{-1}\ M_\odot$.

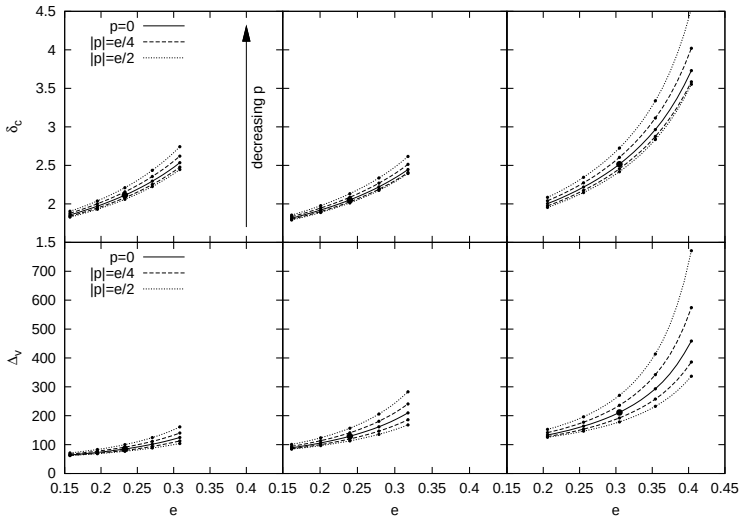


**Figure 4.7:** Influence of the initial ellipticity $e$ and prolaticity $p$ on the parameters $\delta_c$ (*top panels*) and $\Delta_v$ (*bottom panels*) for three different cosmological models at $z = 0$. *Left panels:* ΛCDM. *Central panels:* OCDM. *Right panels:* EdS. The large circle in each figure indicates the value of the respective parameter for $e = \langle e \rangle$ and $p = 0$. The small circles indicate values for a combination of $e \in [\langle e \rangle \pm \sigma_e/2,\ \langle e \rangle \pm \sigma_e]$ and $p \in [\pm e/4,\ \pm e/2]$ (see Eq. 4.19). For a fixed $e$, both $\delta_c$ and $\Delta_v$ grow for decreasing $p$.

that in our case, the redshift of virialisation $z_v$ has to be chosen as reference for $z$ for both $\delta_{c,sph}$ and $\sigma^2$. For a spatially-flat ΛCDM model with $\Omega_m \in [0.2, 0.4]$, $M \in [10^{11}, 10^{15}]\ h^{-1}\ M_\odot$, and $z \in [0, 10]$, the maximal error is ∼1.8% with a mean error of ∼0.4%.

A similar functional dependence can be found for $\Delta_v(M, z)$. Only a small correction term has to be added to arrive at a satisfactory accuracy. We find

$$\Delta_v(M, z) = \Delta_{v,sph}(z_v) \left[ a + b\,\sigma^{2c}(M, z_v) + d\,(1 + z_v)^{2/5}\,\log^{9/4}(M) \right] \tag{4.26}$$

with $a = 0.3819$, $b = 0.5379$, $c = 0.7589$, and $d = 3.456 \times 10^{-4}$. In the same range as above, the maximal error is ∼5% with a mean error of ∼1%.

### 4.3.3 Influence of initial ellipticity and prolaticity

In Fig. 4.7, we plot both $\delta_c$ and $\Delta_v$ as a function of the initial ellipticity $e$ and prolaticity $p$ centered around their expectation values given by Eq. (4.19) for three different cosmologies at $z = 0$. For increasing $e$ and decreasing $p$, both parameters grow qualitatively in the same way as already reported by Sheth et al. (2001) (cf. their Fig. 1). Quantitative deviations arise from the differences in the applied algorithm as discussed in Sect. 4.3.2. For a given mass and virialisation redshift, the initial overdensity for the EdS universe is larger compared to both ΛCDM and OCDM due to a shorter physical time interval that corresponds to the same redshift interval, resulting in a larger $\langle e \rangle$ and $\sigma_e$, but also in larger curvatures of $\delta_c$ and $\Delta_v$ with respect to $e$ and $p$. The latter are the sources of the larger error in the approximation $\langle h \rangle \approx h(\langle e \rangle, \langle p \rangle)$ discussed in Sect. 4.2.3. Since the redshift-time relation is not very different between ΛCDM and OCDM, the dependences of $\delta_c$ and $\Delta_v$ on $e$ and $p$ are comparable.

### 4.3.4 Mass function

Using Eq. (4.25), we are able to construct the mass function of dark-matter haloes using the extended Press-Schechter formalism developed by Bond et al. (1991) and Lacey & Cole (1993), as introduced in Sect. 2.9.2, which is based on the first-upcrossing distribution of the density contrast $\delta$ as a function of the "time" variable $S = \sigma^2(M)$. We shall proceed similarly to Sheth & Tormen (1999, 2002) and Sect. 2.9.2 and use the scaled variable $\nu \equiv \delta^2_{c,sph}/S$ to derive the mass function for our standard ΛCDM cosmology.

As Sheth & Tormen (2002) pointed out, expressing the first-upcrossing distribution $f$ as a function of $\nu$ has the advantage that it is only necessary to calculate $f(\nu)$ for a barrier of height $B(\nu, z)$ at one arbitrary redshift to infer the mass function $n(M)$ at any other redshift by a simple rescaling. For a

given first-upcrossing distribution $f(\nu)$, the differential mass function can be calculated using relation (2.76).

First, we want to find an accurate fit to the first-upcrossing distribution of a moving barrier which is given by the mass-dependent linear overdensity parameter of the ellipsoidal collapse,

$$B(\nu) = \delta_{\mathrm{c,sph}} \left(1 + 0.6536\, \nu^{-0.6387}\right) \tag{4.27}$$

(see Eq. 4.25). The parameter $\delta_{\mathrm{c,sph}}$ is evaluated at $z_{\mathrm{v}} = 0$. We ran one million random walks and recorded the first-upcrossing values for $\nu \in [0.01, 20]$ in 100 equidistant bins in logarithmic space. The resulting distribution $\nu f(\nu)$ is nicely expressed by the function

$$\nu f(\nu) = A \left[1 + (a\nu)^{-p}\right] \sqrt{\frac{a\nu}{2\pi}} \exp\left(-\frac{a\nu}{2} \frac{B(\nu)}{\delta_{\mathrm{c,sph}}}\right) . \tag{4.28}$$

Thus, our suggested fitting formula is a slight modification of the functional form (2.86) proposed by Sheth & Tormen (1999, 2002) with the additional factor $B(\nu)/\delta_{\mathrm{c,sph}}$ in the exponential and the scaling variable $a$ compared to Eq. (2.86). The best-fit parameters are $A = 0.357$, $p = 0.212$ and $a = 1.171$. The result is shown in Fig. 4.8.

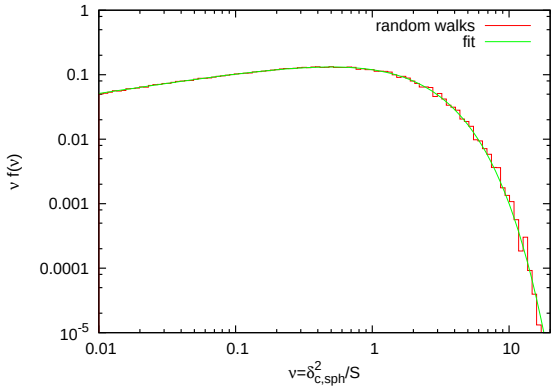


**Figure 4.8:** Comparison between the first-upcrossing distribution of the moving barrier (4.27), inferred from an ensemble of one million random walks, and the fitting formula (4.28).

Second, to find a viable mass function from the first-upcrossing distribution, we proceed in the same way as Sheth & Tormen (1999) and Sheth et al. (2001), normalise $f(\nu)$ to unity and rescale the variable $a$ such that we are in agreement with the standard Sheth-Tormen mass function and a mass function based on $N$-body simulations proposed by Courtin et al. (2011). The latter is based on a first-upcrossing distribution that has the same functional form as that proposed by Sheth & Tormen (1999), but slightly different best-fit parameters,

$$\nu f(\nu) = \tilde{A} \left[1 + (\tilde{a}\nu)^{-\tilde{p}}\right] \sqrt{\frac{\tilde{a}\nu}{2\pi}} \exp\left(-\frac{\tilde{a}\nu}{2}\right) , \tag{4.29}$$

with $\tilde{A} = 0.348$, $\tilde{a} = 0.695$, and $\tilde{p} = 0.1$. Note that in their definition of $\nu$, the linear density contrast $\delta_{\mathrm{c,sph}}$ has to be taken at *collapse*. Normalising the first-upcrossing distribution based on the moving barrier of our ellipsoidal-collapse model to unity yields a rescaled parameter $A \to A' = 1.364\, A$.

We compare the resulting mass function with those by Sheth & Tormen (1999) and Courtin et al. (2011) for three different redshifts in Fig. 4.9. The parameter $a$ was rescaled by $a \to a' = 0.625\, a$. Deviations from the Sheth-Tormen mass function at high masses occur at high redshifts which is compatible with the Courtin et al. mass function. Overall, our proposed mass function lies in between these two, suggesting that differences between $N$-body simulations and the Sheth-Tormen mass function might be due to an imprecise treatment of the ellipsoidal-collapse dynamics.

## 4.4 Conclusions

We have reconsidered the collapse of a homogeneous, triaxial ellipsoid in an expanding background universe and extended the treatment of Bond & Myers (1996) in two ways:

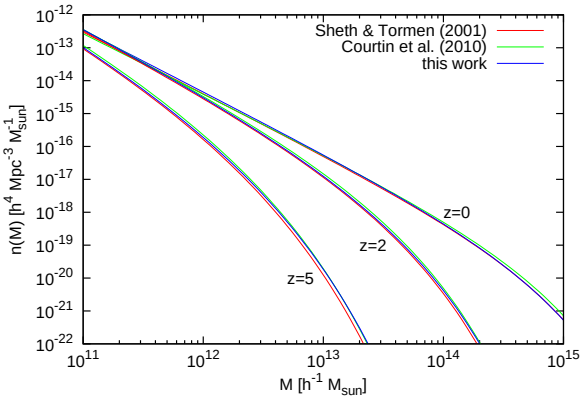


**Figure 4.9:** Comparison of the Sheth-Tormen and the Courtin et al. mass functions with the mass function derived from the rescaled upcrossing distribution (4.28), based on our treatment of the ellipsoidal-collapse dynamics.

- We have introduced a physically motivated criterion for the onset of virialisation along each principal axis of a collapsing ellipsoid. We have derived this criterion from the tensor virial theorem, demanding that the inertial tensor stabilises and its second time derivative vanishes. This approach is a generalisation of the usual virialisation condition for the spherical-collapse scenario and thus fully consistent with it. It replaces the conventional requirement that virialisation of an ellipsoid's dimensionless semi-major axis $a_i$ occurs when $a_i(a) = 0.177\,a$ is fulfilled.

- We have introduced a hybrid model for the influence of the external gravitational shear field acting on the ellipsoid, supplementing the two different models of Bond & Myers (1996). The principal axes of the shear field evolve with those of the halo before it turns around and decouples from the background expansion, and then continues evolving linearly while the halo evolves non-linearly and collapses. We have shown that the differences between the hybrid and the non-linear model are relatively small.

For a given initial ellipticity $e$ and prolaticity $p$, and for a specified virialisation redshift $z_\mathrm{v}$, the ellipsoidal-collapse model then gives a unique answer for the linear density contrast $\delta_\mathrm{c}$ at virialisation, as well as for the overdensity $\Delta_\mathrm{v}$ at that time. The probability distribution for $e$ and $p$, conditional on the density contrast $\delta$, is determined by the probability distribution of the eigenvalues of the Zel'dovich deformation tensor, as shown by Sheth et al. (2001). It is characterised by the variance of the matter-density fluctuations on a scale fixed by the halo mass required. We have shown that the marginalisation over $e$ and $p$ can be simplified by evaluating the ellipsoidal collapse at their mean values $\langle e\rangle$ and $\langle p\rangle = 0$.

Our main results are as follows:

- The collapse parameters $\delta_\mathrm{c}$ and $\Delta_\mathrm{v}$ depend only weakly on the model for the external gravitational shear. The hybrid model and the non-linear model by Bond & Myers (1996) give approximately the same results.

- When supplied with our virialisation condition derived from the tensor virial theorem, the ellipsoidal-collapse model returns values $\delta_\mathrm{c}$ and $\Delta_\mathrm{v}$ that differ substantially from those obtained with the spherical-collapse model. Depending on halo mass and redshift, deviations of order $(20\ldots50)\%$ are common. After marginalisation over $e$ and $p$, $\delta_\mathrm{c}$ and $\Delta_\mathrm{v}$ increase with decreasing halo mass and with decreasing virialisation redshift.

- Both parameters increase with increasing initial ellipticity $e$ and decrease with increasing prolaticity $p$, as already suggested by Sheth et al. (2001).

- Our results for $\delta_\mathrm{c}$ qualitatively confirm the dependence on halo mass and virialisation redshift given by a fitting formula by Sheth et al. (2001). Deviations in particular at low mass and high

redshift occur due to the differences in the virialisation condition, the model for the external shear, and the marginalisation over $e$.

- The mass function based on our refined treatment of the ellipsoidal-collapse model is in good agreement with those proposed by Sheth & Tormen (1999) for low redshifts and Courtin et al. (2011) for high redshifts. This suggests that differences between the Sheth-Tormen mass function and results from $N$-body simulations at large redshifts may occur due to an imprecise treatment of the ellipsoidal-collapse dynamics.

In the next chapter, we will incorporate the ellipsoidal-collapse model as presented here into the approach for the X-ray temperature function without reference to mass presented in Chap. 3.

# 5 Chapter 5

# The influence of mergers on the cluster temperature function and cosmological parameters derived from it

In this chapter, we develop a parameter-free analytic model to include the effects of mergers into the theoretical modelling of the X-ray temperature function of galaxy clusters. We include this description into the model for the cluster population based on fluctuations of the gravitational potential introduced in Chap. 3. Comparisons with a numerical simulation reveal that the theoretical model is in good agreement with the simulation results. We show that building the model on the dynamics of spherical rather than ellipsoidal collapse yields better results if emission-weighted temperatures are used, while ellipsoidal collapse yields good agreement between model and simulation for mass-weighted temperatures. Analysing two different samples of X-ray clusters, we quantify the influence of mergers and a conversion between different temperature definitions on the joint determination of $\Omega_{\mathrm{m0}}$ and $\sigma_8$. If effects from mergers are included, temperature functions based on cluster masses and on the gravitational potential are in good agreement with other cosmological probes, whereas the conversion to spectroscopic-like temperatures does not seem to be necessary.

The results of this chapter are published in Angrick & Bartelmann (2011).

## 5.1 Introduction

Galaxy clusters are a potentially very powerful probe of non-linear cosmological structure formation since their abundance and its evolution depends sensitively on the matter density $\Omega_{\mathrm{m0}}$, the normalisation of density fluctuations $\sigma_8$ and the cosmological constant term $\Omega_{\Lambda 0}$.[9] Conventionally, theoretical predictions of the cluster population parameterise clusters by mass (see Sect. 2.9). As already pointed out in Sect. 3.1, this is potentially problematic since mass is strictly not observable and an integral quantity which, for irregularly shaped bodies without well-defined boundary, is hard to define unambiguously. Calibration relations are needed between the mass and observable quantities such as X-ray temperature and luminosity, which are themselves prone to systematic and random uncertainties.

We have proposed a different approach avoiding any reference to mass in Chap. 3, where we have shown that the X-ray temperature function of the cluster population, i.e. their number-density distribution with X-ray temperature, can be theoretically predicted based on the statistics of gravitational-potential fluctuations. This procedure has several advantages. First, it parameterises the cluster population directly by their temperature, which is a locally defined observable tightly related to the potential

[9] We restrict ourselves to the ΛCDM model here, a generalisation towards more exotic forms of energy densities with a negative equation-of-state parameter sufficiently negative to yield the observed acceleration of the Universe, e.g. quintessence, could be easily done.

depth. Unambiguities caused by the integral definition of the mass are thus avoided. Second, calibration relations for the mass are circumvented, thus removing their scatter from the uncertainty of any inferences (see also Lau, 2010). Third, the gravitational potential evolves much less than the matter density, extending the range of validity of linear structure evolution.

We have shown in Chap. 3 under which conditions this potential-based temperature function reproduces the theoretical predictions based on matter density and mass. Here, we address two subsequent questions. First, we compare the potential-based temperature function to a gas-dynamical, numerical simulation. While we find agreement at low redshift, there is increasing disagreement towards moderate and higher redshifts. This brings us to the development of an analytic model for the effect of cluster mergers on the X-ray temperature function, which leads to a very good agreement of our theoretical predictions based on potential statistics with the numerical results. Our analytic model could be considered as providing an analytic complement to the numerical study by Randall et al. (2002).

Second, we use the potential-based temperature function including the merger model to infer the cosmological parameters $\Omega_{\mathrm{m0}}$ and $\sigma_8$ from two different samples of galaxy clusters. The results are not conclusive yet, mainly because of tensions between the different samples, but we find reasonable values for both parameters provided we use a definition of X-ray temperature that is adapted to the comparison with the gravitational potential.

## 5.2 Generalising the temperature function towards ellipsoidal collapse

In the following, we use the X-ray temperature function introduced in Chap. 3 and an extension thereof based on the generalisation from spherical to ellipsoidal collapse. We will use the results of the ellipsoidal-collapse model presented in Chap. 4 and implement it in our formalism for the X-ray temperature function where results from the spherical collapse were used.

We have to modify Eq. (3.37) since in the ellipsoidal-collapse case, the critical Laplacian $\Delta\Phi_{\mathrm{c}}$ is now a function of the variable $\Delta\Phi$, which one has to integrate over, through $R = \sqrt{-2\Phi_{\mathrm{l}}/\Delta\Phi}$ (see the last paragraph of Sect. 3.3.2), where $\Phi_{\mathrm{l}}$ is again the *linearly* evolved gravitational potential. Equation (3.37) becomes

$$n(\Phi_{\mathrm{l}})\,\mathrm{d}\Phi_{\mathrm{l}} = \int_0^\infty \mathrm{d}(\Delta\Phi)\,\tilde{n}(\Phi_{\mathrm{l}},\Delta\Phi)\,\theta_{\mathrm{H}}[\Delta\Phi - \Delta\Phi_{\mathrm{c}}(\Phi_{\mathrm{l}},\Delta\Phi)]\,\mathrm{d}\Phi_{\mathrm{l}}\,, \tag{5.1}$$

with *Heaviside's step function* $\theta_{\mathrm{H}}$. Note that it is still a good approximation to smooth the density field with an isotropic top-hat of size $R$ and not to introduce an anisotropic smoothing function at the initial time, when using the ellipsoidal- instead of the spherical-collapse model, since we are well within the linear regime, and the deviation from sphericity is of order a few times $10^{-5}$.

The potential in the centre of an ellipsoid with $a_i = R_i/R_{\mathrm{pk}}$ is given by

$$\Phi_0 = -\pi G\,\bar{\rho}\,a_1 a_2 a_3\,R_{\mathrm{pk}}^2 \int_0^\infty \frac{\mathrm{d}\tau}{\sqrt{(a_1^2+\tau)(a_2^2+\tau)(a_3^2+\tau)}} \tag{5.2}$$

(Binney & Tremaine, 1987, p. 57), where $\bar{\rho} = \rho_{\mathrm{b}}\delta$ is the density responsible for the gravitational potential. For a sphere, $a_1 = a_2 = a_3 \equiv \tilde{a}$, and the integral can be solved analytically, yielding $2/\tilde{a}$, hence the result for the sphere (3.25) with $R = \tilde{a}R_{\mathrm{pk}}$ is reproduced. We proceed exactly in the same way as in Sect. 3.3.3, calculating the ratio between linear and non-linear potential at the time of collapse. Again, quantities at a small initial scale factor $a_{\mathrm{ini}}$ are labelled with the index 'ini' and quantities at the time of collapse with 'col'. Using the approximations $a_{1,\mathrm{ini}} \approx a_{2,\mathrm{ini}} \approx a_{3,\mathrm{ini}} \approx a_{\mathrm{ini}}$, and

$\Delta_{\rm ini} \approx 1$, we arrive at

$$\frac{\Phi_{\rm nl}}{\Phi_{\rm l}} = \frac{a_{\rm col}}{2\delta_{\rm ini}} \frac{D_+(a_{\rm ini})}{D_+(a_{\rm col})} \int_0^\infty \frac{{\rm d}\tau}{\sqrt{(a_{1,\rm col}^2+\tau)(a_{2,\rm col}^2+\tau)(a_{3,\rm col}^2+\tau)}} \,, \tag{5.3}$$

where we have again used the fact that for the virial overdensity, we can approximate $\tilde{\delta}_{\rm v} = \tilde{\Delta}_{\rm v} - 1 \approx \tilde{\Delta}_{\rm v}$ since $\tilde{\Delta}_{\rm v}$ is of order 100. All quantities that are necessary to evaluate Eq. (5.3) can be calculated using the ellipsoidal-collapse model presented in Chap. 4. Note that in the ellipsoidal case, the ratio of non-linear and linear potential becomes dependent on both $\Phi_{\rm l}$ and $\Delta\Phi$ via the $a_{i,\rm col}$.

To infer an averaged linear potential for a given non-linear one, we marginalise over the dependence on $\Delta\Phi$ weighted by $\tilde{n}(\Phi_{\rm l}, \Delta\Phi)$ so that

$$\langle\Phi_{\rm l}\rangle_{\Delta\Phi}(\Phi_{\rm nl}) = \frac{\int_0^\infty {\rm d}(\Delta\Phi)\, \Phi_{\rm l}\, \tilde{n}(\Phi_{\rm l}, \Delta\Phi)\, \theta_{\rm H}[\Delta\Phi - \Delta\Phi_{\rm c}(\Phi_{\rm l}, \Delta\Phi)]}{\int_0^\infty {\rm d}(\Delta\Phi)\, \tilde{n}(\Phi_{\rm l}, \Delta\Phi)\, \theta_{\rm H}[\Delta\Phi - \Delta\Phi_{\rm c}(\Phi_{\rm l}, \Delta\Phi)]} \,, \tag{5.4}$$

where $\Phi_{\rm l} = \Phi_{\rm l}(\Phi_{\rm nl}, \Delta\Phi)$ via Eq. (5.3).

## 5.3 Confronting theory with results from a simulation

We now compare the analytic results for both X-ray temperature functions, using either spherical- or ellipsoidal-collapse dynamics, to a hydrodynamical simulation by Borgani et al. (2004) for a flat concordance ΛCDM model with $\Omega_{\rm m0} = 0.3$, $\Omega_{\rm bar0} = 0.04$, $h = 0.7$, and $\sigma_8 = 0.8$ in a box of side-length $192\,h^{-1}$ Mpc, starting at redshift $z_{\rm start} \simeq 46$. The gas physics was implemented using GADGET-2, a massively parallel $N$-body/SPH tree code with fully adaptive time-resolution (Springel, 2005). The density field was sampled with $480^3$ dark matter and an equal amount of gas particles with masses $M_{\rm DM} = 6.6 \times 10^9\ {\rm M}_\odot$ and $M_{\rm gas} = 9.9 \times 10^8\ {\rm M}_\odot$, respectively. During the time evolution, the number of gas particles decreases due to their conversion into star particles, which have slightly lower mass than the gas particles.

The simulation includes radiative cooling processes following Katz et al. (1996), and a photo-ionising background expected from quasars which ionise the Universe at $z \simeq 6$. Star formation is modelled using the hybrid multiphase model for the interstellar medium by Springel & Hernquist (2003). The simulation code also includes a method to follow the production of metals. However, the effects of metals on the cooling function are not taken into account. This only affects the analysis of simulated galaxy clusters with temperatures $T \lesssim 1$ keV. For the evaluation of the X-ray temperature function, cluster catalogues at the five redshifts 0, 0.2, 0.5, 0.7, and 1 are available.

In numerical simulations, the temperature of a cluster is defined as

$$T \equiv \frac{\int_{\mathcal{V}} {\rm d}V\, W\, T_{\rm gas}}{\int_{\mathcal{V}} {\rm d}V\, W} \,, \tag{5.5}$$

where $T_{\rm gas}$ is the temperature of a gas particle and $W$ is a weight function (Mazzotta et al., 2004). The integral covers a specified volume $\mathcal{V}$, e.g. the sphere defined by the virial radius. Depending on the choice of the weight function, mainly three different temperatures are used in the literature:

(1) the *mass-weighted* temperature $T_{\rm mw}$ with $W = m_{\rm gas}$, where $m_{\rm gas}$ is the mass of the gas element,

(2) the *emission-weighted* temperature $T_{\rm ew}$ with $W = \Lambda(T_{\rm gas})\, n^2$, where $\Lambda(T_{\rm gas}) \propto \sqrt{T_{\rm gas}}$ is the cooling function and $n$ the gas density, and

(3) the *spectroscopic-like* temperature $T_{\rm sl}$ with $W = n^2 / T_{\rm gas}^{3/4}$.

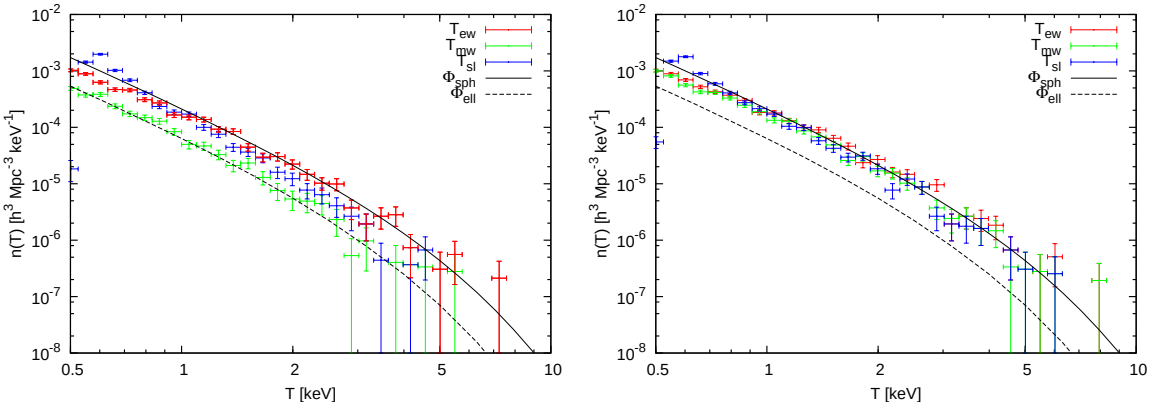


**Figure 5.1:** Comparison of the X-ray temperature function inferred from the simulation at $z = 0$ using different temperature definitions with the theoretically predicted temperature functions including either spherical- ($\Phi_{\rm sph}$) or ellipsoidal-collapse ($\Phi_{\rm ell}$) dynamics. *Left panel:* Temperatures evaluated inside $R_{\rm vir}$. *Right panel:* Temperatures evaluated inside $R_{2500}$.

$T_{\rm mw}$ is easy to calculate, but physically not well motivated. Hence, $T_{\rm ew}$ was used to relate temperatures from simulations with spectroscopically derived temperatures. But since disagreements remained, $T_{\rm sl}$ was introduced to match the spectroscopic temperatures of clusters in *Chandra* and *XMM-Newton* surveys better. For $z = 0$, the catalogue includes three differently defined temperatures averaged over various radii. The same is true for the higher redshifts, besides that $T_{\rm sl}$ is missing.

Also based on the simulation by Borgani et al. (2004), Rasia et al. (2005) provide a fitting formula relating the spectroscopic-like to the emission-weighted temperature for clusters with $T_{\rm ew} \gtrsim 2$ keV at $z = 0$,

$$T_{\rm sl} = (0.70 \pm 0.01) T_{\rm ew} + (0.29 \pm 0.05) \; . \tag{5.6}$$

We will use that relation in Sects. 5.5 and 5.6 later.

In Fig. 5.1, we compare the differential number density of clusters inferred from the simulation for $z = 0$ using all three different temperature definitions, where the theoretical prediction includes either spherical- or ellipsoidal-collapse dynamics. The predicted temperature function based on ellipsoidal collapse is in better agreement with the simulation for $T \gtrsim 1$ keV if the mass-weighted temperature within the virial radius $R_{\rm vir}$ is used (left panel), while spherical collapse suffices if emission-weighted temperatures are used instead.

The reason for this discrepancy might be that $T_{\rm ew}$ is weighted by $n^2$ and therefore pronounces the cluster cores, whereas $T_{\rm mw}$ is weighted by $n$, hence outer parts become more important instead. Therefore, the deviation from sphericity seems important only in the outskirts of clusters, while the number density of clusters based on the core temperatures can be well modelled using spherical-collapse dynamics. The temperature function based on $T_{\rm sl}$ lies between the two predictions and is hence not well-described by either of the two models.

Interestingly, when considering the temperature functions inferred within $R_{2500}$ (right panel), i.e. restricting the point of view to the very inner part of the halo per definition, the three functions approach each other and are more or less well described by the theoretical description based on the spherical-collapse model, where again the temperature function based on $T_{\rm ew}$ fits the prediction best. This behaviour seems to confirm the former statement that the inner parts of clusters are well described by spherical-collapse dynamics. In addition, the virial theorem was used to relate the non-linear potential to a temperature in the centre of clusters so that the prediction should be valid primarily when based on the temperatures in the central region.

Since the mass-weighted temperature is not well motivated, we concentrate on the temperature function based on $T_{\rm ew}$ within $R_{2500}$ from now on, also because the theoretical prediction invoking the spherical-collapse dynamics is much less time-consuming. Figure 5.2 compares the result from the

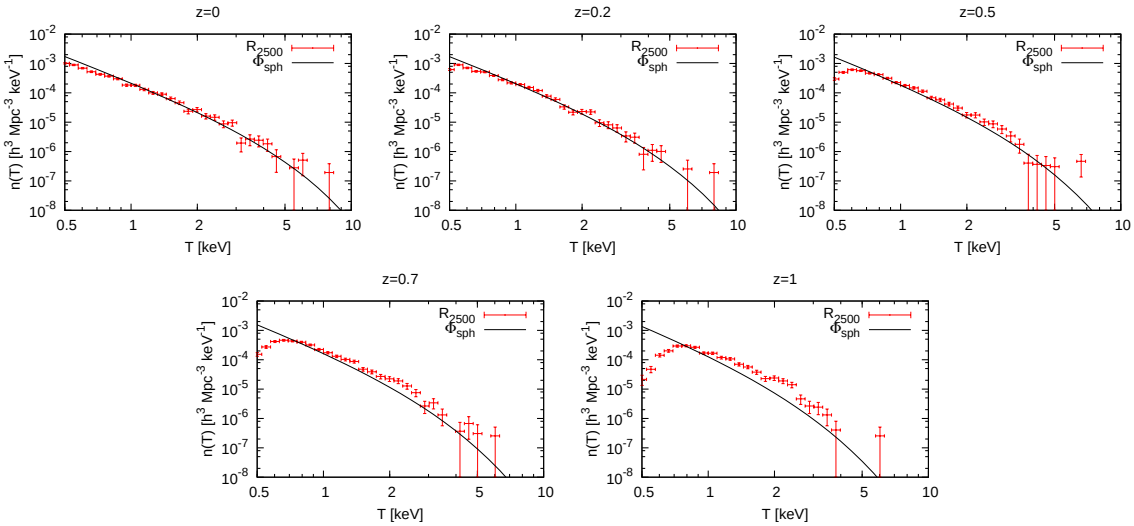


**Figure 5.2:** Comparison of the X-ray temperature function from the simulation based on $T_{\mathrm{ew}}$ within $R_{2500}$ with the theoretical prediction including the spherical-collapse model.

simulation using the spherical model also for redshifts $z > 0$. One can clearly see that the higher the redshift, the more the results of the simulation disagree from the theoretical prediction. The simulation data systematically fall above the prediction for $z \geq 0.5$. In the following section, we speculate that this effect is due to cluster mergers, which are much more numerous in the past than now, and develop a model for taking them into account in the construction of the cluster temperature function. Since in the definition of $T_{\mathrm{ew}}$, the temperature of each gas particle is weighted by the square of the gas density, not only the centre of the galaxy cluster is pronounced, but also infalling subclumps due to mergers contribute significantly.

## 5.4 Modelling merger effects

Randall et al. (2002) have shown with numerical simulations that mergers do have a strong impact on the X-ray temperature and luminosity functions of haloes and thus, cosmological parameters inferred from them without including this additional effect are biased. Since clusters that are undergoing mergers are shifted from lower to higher temperatures and due to the exponential cut-off at the high-temperature end, especially this part of the temperature function is enhanced. Consequently, Randall et al. (2002) find that the inferred $\sigma_8$ is biased towards higher values, whereas $\Omega_{\mathrm{m0}}$ is biased towards lower values. Both parameters change by ∼15–20%.

We choose a different approach here, trying to incorporate the essential physical effect of mergers in a simple analytic model based on the extended Press-Schechter formalism by Lacey & Cole (1993) introduced in Sect. 2.9.3. We see there that the conditional probability for a halo with mass $M_1$ at time $t_1$ to have mass $M_2 + \mathrm{d}M_2$ at $t_2$ can be calculated using Eq. (2.83). Changing variables to $M \equiv M_1$, $\Delta M \equiv M_2 - M_1$ and $z \equiv z(\omega_2)$, $\Delta z \equiv z(\omega_1) - z(\omega_2)$ yields

$$p(M, \Delta M, z, \Delta z)\,\mathrm{d}(\Delta M) \equiv p[S(M + \Delta M), \omega(z) | S(M), \omega(z - \Delta z)] \left| \frac{\mathrm{d}S(M + \Delta M)}{\mathrm{d}(\Delta M)} \right| \mathrm{d}(\Delta M)\,, \qquad (5.7)$$

where $\omega(z)$ is again the critical linear density contrast scaled by the growth factor, $\omega(z) = \delta_{\mathrm{c}}(z)/D_+(z)$, and $S(M) = \sigma^2(M)$ is the variance of the matter power spectrum (2.26) using the top-hat filter function in real space (2.27) with the scale $R$ as a function of mass given by Eq. (2.71).

Assume now that the temperature increase $\Delta T(M, \Delta M)$ due to a merger of a mass $M$ with another mass $\Delta M < M$ originates from the kinetic energy of the gas transported with the infalling clump,

which is completely transformed to thermal energy. The gain of energy is therefore

$$\Delta E = \frac{1}{2} f_\mathrm{b}\, \Delta M\, (\Delta v)^2 \stackrel{!}{=} \frac{3}{2} N k_\mathrm{B}\, \Delta T\ , \tag{5.8}$$

where $f_\mathrm{b}\,\Delta M$ is the baryon fraction of the lower-mass halo, $\Delta v$ is the relative velocity of the components, and $N = f_\mathrm{b} M/(\mu m_\mathrm{p})$ is the total number of gas particles in the halo of mass $M$. Note that in this ideal case, the factor $f_\mathrm{b}$ cancels exactly. To guess $\Delta v$, assume that the larger component is at rest, while the halo of mass $\Delta M$ approaches from infinity. In this case, the velocity can be easily calculated by equating potential and kinetic energy, so that

$$(\Delta v)^2 = \frac{2GM}{R} \qquad \text{with} \qquad R = \left(\frac{3M}{4\pi\rho_\mathrm{c}\Delta_\mathrm{v}}\right)^{1/3}\ . \tag{5.9}$$

Combining Eq. (5.8) with the first equation of (5.9) yields

$$k_\mathrm{B}\Delta T = \frac{2}{3}\frac{G\mu m_\mathrm{p}\,\Delta M}{R(M)}\ , \tag{5.10}$$

where $R(M)$ is given by the second equation of (5.9). We assume that the time scale for the temperature increase is set by the *sound-crossing time*

$$t_\mathrm{sc} = \frac{R}{c_\mathrm{s}} \qquad \text{with} \qquad c_\mathrm{s} = \sqrt{\frac{5}{3}\frac{k_\mathrm{B}T}{\mu m_\mathrm{p}}} \tag{5.11}$$

(Randall et al., 2002), where $c_\mathrm{s}$ is the sound speed.

As illustrated in Fig. 5.3, we thus model the temperature boost in an idealised, abrupt way: The halo of mass $M$ has a temperature $T_{\mathrm{vir},1}(M)$ before the merger, which increases instantaneously to $T_{\mathrm{vir},1}(M) + \Delta T(M, \Delta M)$ for the time period $t_\mathrm{sc}$ and then drops again instantaneously to $T_{\mathrm{vir},2}(M + \Delta M)$, assuming that a virialised halo of mass $M + \Delta M$ has finally formed. When inferring cosmological parameters in the next section, we will either use the theoretically motivated mass-temperature relation (3.45) for virialised objects, derived for spherical and homogeneous objects, or an empirical relation to relate temperatures and masses.

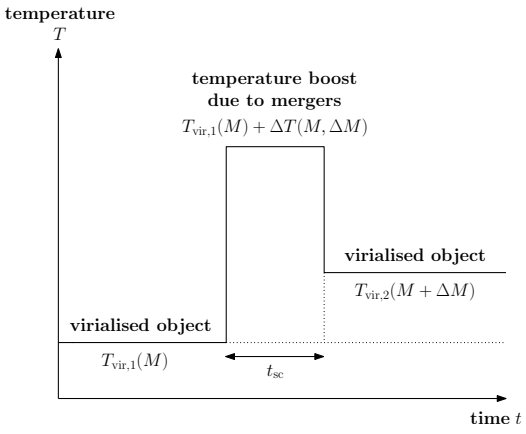


**Figure 5.3:** Illustration of a cluster's temperature curve due to a merger as assumed in our model.

Starting from the number density of virialised galaxy clusters $n(T)$, which can be calculated as explained in Chap. 3, we calculate two correction terms. The first is the number density of clusters that reach a temperature $T$ only due to mergers,

$$n_+(T) \equiv \int_0^\infty \mathrm{d}(\Delta M) \int_0^\infty \mathrm{d}M\, n[T_\mathrm{vir}(M)]\, p(M, \Delta M, z, \Delta z)\, \delta_\mathrm{D}[T - T_\mathrm{vir}(M) - \Delta T(M, \Delta M)]\, \theta_\mathrm{H}(M - \Delta M)\ , \tag{5.12}$$

where we ensure via *Dirac's delta function* $\delta_\mathrm{D}$ and *Heaviside's step function* $\theta_\mathrm{H}$ that only combinations of $\Delta M$ and $M$ contribute to the integral for which $T_\mathrm{vir}(M) + \Delta T(M, \Delta M) = T$ and $\Delta M < M$ are fulfilled. The redshift interval $\Delta z$ is set by the *sound-crossing time* (5.11) since in our simple model, one should be able to see all mergers at redshift $z$ that have happened in the redshift interval $\Delta z$ before. Starting

from Eq. (1.17), changing variable from $a$ to $z$ and integrating over the time period at which the temperature boost due to the merger occurs, leads to a relation between $\Delta z$ and $t_{\rm sc}$,

$$t_{\rm sc} = \frac{1}{H_0} \int_{z}^{z+\Delta z} \frac{{\rm d}z'}{E(z')\,(1+z')} \,. \tag{5.13}$$

Two assumptions where implicitly made during the derivation: First, the number density $n(T)$ is assumed not to change significantly during $\Delta z$, and second, the increase by $\Delta M$ is only due to a *single* merger event, ignoring multiple simultaneous merger events and smooth accretion. It turns out, however, that $\Delta z$ is short enough for these assumptions not to result in a significant error contribution.

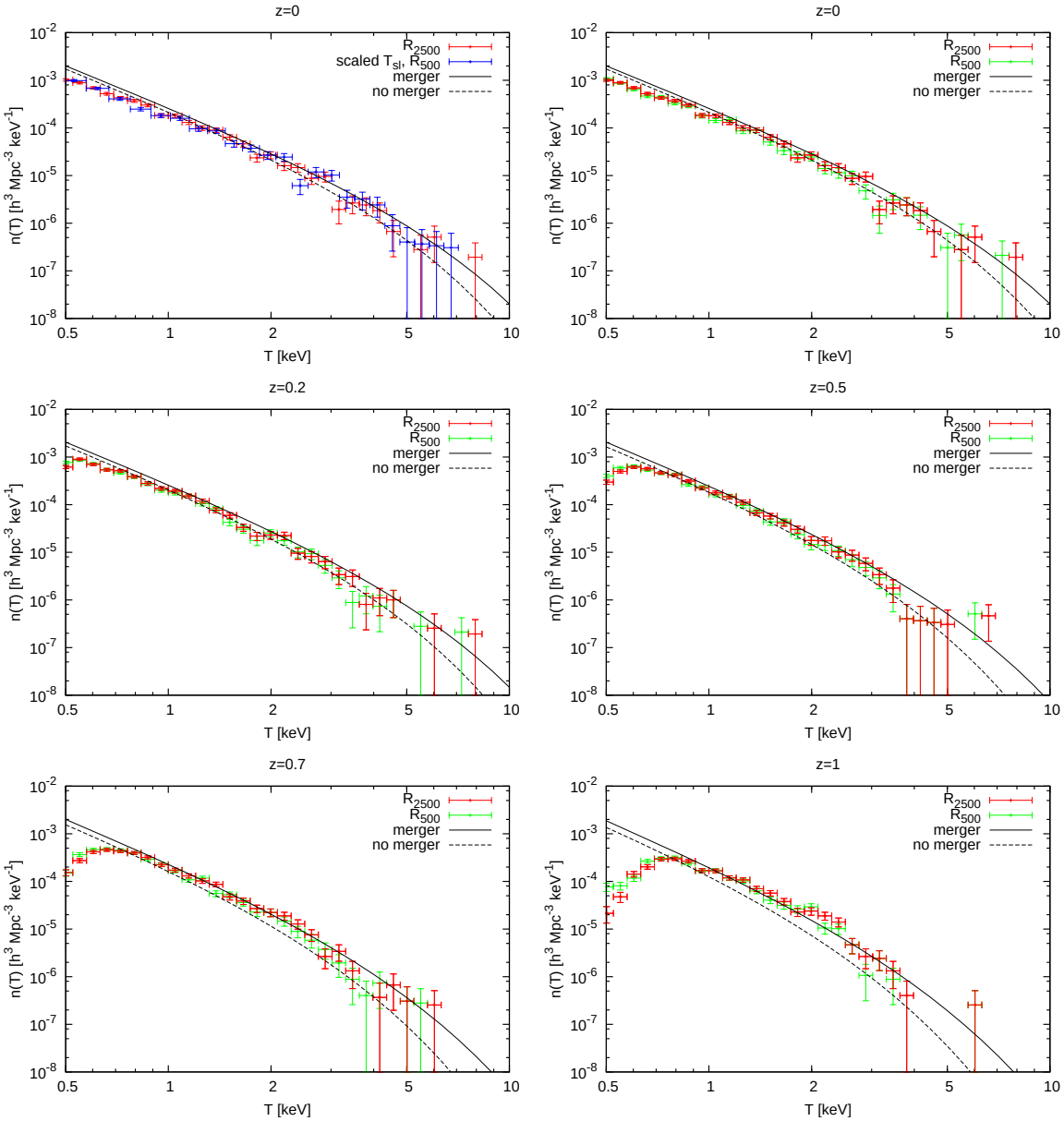


**Figure 5.4:** Comparison of the result from the simulation with the theoretical prediction both including (*solid line*) and excluding (*dashed line*) the effect of mergers on the temperature function. We compare with the *emission-weighted* temperature $T_{\rm ew}$ calculated inside $R_{2500}$ (*red data points*) and $R_{500}$ (*green data points*) except the upper left plot, where we also compare with the scaled spectroscopic-like temperature $T_{\rm sl}$ inside $R_{500}$ using Eq. (5.6).

The second correction term arises due to clusters that would have a temperature $T$ if they were virialised, but have a temperature higher than $T$ due to mergers,

$$n_{-}(T) \equiv \int_{0}^{M(T)} \mathrm{d}(\Delta M)\, n(T)\, p[M(T), \Delta M, z, \Delta z] \; . \tag{5.14}$$

Here, we use again Eq. (3.45) to assign a mass $M$ to the temperature $T$. The total number density of clusters is then given by

$$n_{\mathrm{ges}}(T) = n(T) + n_{+}(T) - n_{-}(T) \; . \tag{5.15}$$

In Fig. 5.4, we compare the prediction of our X-ray temperature function both with and without the enhancement by mergers with the results from the simulation by Borgani et al. (2004). The shape of the temperature function influenced by mergers is in qualitative agreement with Randall et al. (2002). The relative change of the number density increases with temperature and redshift. Using our simple model for the effects of mergers, the temperature function based on the emission-weighted temperature within $R_{2500}$ from the simulation is now in good agreement with the theoretical prediction for $T \gtrsim 1$ keV, the temperature range for which the results from the simulation can be trusted (see Sect. 5.3). For $R_{500}$, however, the result from the simulation is always slightly below the theoretical prediction, especially for low redshifts. But since we always use the *central* temperature in the theoretical derivation of the temperature function, small deviations are expected in this case.

Using Eq. (5.6) to scale $T_{\mathrm{sl}}$ inside $R_{500}$ and comparing the resulting temperature function to the prediction including mergers in the top left plot shows a better agreement with the theoretical prediction for $z = 0$. The reason is that the temperature function based on the scaled spectroscopic-like temperature (blue data points) seems to lie systematically slightly above the one based on $T_{\mathrm{ew}}$ (red data points) at the high-temperature end so that Eq. (5.6) does not seem to map both temperatures onto each other precisely. Unfortunately, the spectroscopic-like temperatures for the individual clusters from the simulation are not available for higher redshifts so that we cannot compare the two for this regime.

## 5.5 Inferring cosmological parameters

In this section, we want to infer the cosmological parameters $\Omega_{\mathrm{m0}}$ and $\sigma_8$ from two different samples by Ikebe et al. (2002) and Vikhlinin et al. (2009a) using our theoretical model for the X-ray temperature function both with and without the effect of mergers to quantify their influence on the final outcome. Additionally, we compare the results of our approach using the statistics of minima in the cosmic gravitational potential to the traditional method invoking mass functions and an empirical $M$-$T$ relation to see if any of the two gives tighter constraints.

### 5.5.1 The samples

The first flux-limited sample by Ikebe et al. (2002) consists of 61 clusters and is based on *ASCA* and *ROSAT* data with a median redshift of $z = 0.046$ in the temperature range $1.4\ \mathrm{keV} < T < 10.55\ \mathrm{keV}$. It covers 8.14 steradians, and the flux limit is $1.99 \times 10^{-11}$ ergs $\mathrm{s}^{-1}$ $\mathrm{cm}^{-2}$ in the 0.1–2.4 keV band. The maximal search volume $V_{\mathrm{max}}$ for each cluster is calculated and listed for an open model with $\Omega_{\mathrm{m0}} = 0.2$ and $\Omega_{\Lambda 0} = 0.0$ and for a flat model with $\Omega_{\mathrm{m0}} = 0.2$ and $\Omega_{\Lambda 0} = 0.8$. Although $V_{\mathrm{max}}$ itself depends on the cosmological parameters, it changes only very slightly with them. Neglecting this effect in the following analysis therefore does not induce a significant error.

The second sample encompasses two subsamples by Vikhlinin et al. (2009a), one at high and one at low redshift, based on *ROSAT* PSPC All-Sky (RASS) and 400 $\mathrm{deg}^2$ data. The *low-redshift sample* consists of 49 clusters with flux $S > 1.3 \times 10^{-11}$ erg $\mathrm{s}^{-1}$ $\mathrm{cm}^{-2}$ in the 0.5–2 keV band from several samples of RASS with a total area of 8.14 steradians. The redshift coverage is $0.025 < z < 0.25$ with $\langle z \rangle \approx 0.05$, and temperatures are in the range $2.61\ \mathrm{keV} < T < 14.72\ \mathrm{keV}$.

The *high-redshift sample* consists of 36 clusters from the *ROSAT* 400 deg$^2$ survey (Burenin et al., 2007) in the redshift range $0.35 < z < 0.9$ with $\langle z \rangle \approx 0.5$ and a redshift-dependent flux limit in the 0.5–2 keV band. For $z > 0.473$, the limiting flux is $1.4 \times 10^{-13}$ erg s$^{-1}$ cm$^{-2}$, whereas for $z < 0.473$, the flux limit corresponds to a minimal X-ray luminosity of $L_{\mathrm{X,min}} = 4.8 \times 10^{43}(1+z)^{1.8}$ erg s$^{-1}$. The cluster temperatures are in the range 2.13 keV $< T <$ 11.08 keV.

For both subsamples, the effective differential search volume $\mathrm{d}V/\mathrm{d}z$ as a function of mass $M$ and cosmological parameters $\Omega_{\mathrm{m0}}$, $\Omega_{\Lambda 0}$ and $h = 0.72$ for both subsamples was made available in electronic form on a grid by A. Vikhlinin. To convert it to a function of temperature, we used the best-fit values of the mass-temperature relation of Vikhlinin et al. (2009a),

$$M_{500} = M_0 \left( \frac{T}{5\ \mathrm{keV}} \right)^{\alpha} E^{-1}(z)\ , \tag{5.16}$$

where $M_0 = (3.02 \pm 0.11) \times 10^{14}\ h^{-1}\ M_\odot$, $\alpha = 1.53 \pm 0.08$, and $E(z)$ is again the expansion function of a Friedmann model.

### 5.5.2 The fitting procedure

Since the errors on the cluster number counts are Poissonian, we use the *C statistic* of Cash (1979) for unbinned data to find the best-fit values for $\Omega_{\mathrm{m0}}$ and $\sigma_8$, assuming a spatially flat universe, hence $\Omega_{\Lambda 0} = 1 - \Omega_{\mathrm{m0}}$. The $C$ statistic is defined as

$$C \equiv 2 \left( N - \sum_i \ln n_i \right)\ , \tag{5.17}$$

where $N$ is the total number of objects expected from the sample assuming a theoretical model and $n_i$ is the theoretically expected differential number density of the $i$-th cluster in the sample with temperature $T_i$ and redshift $z_i$. The sum extends over all sample members.

In total, we fit six different theoretical models to the two subsamples of Vikhlinin et al. (2009a):

(1) mass function by Tinker et al. (2008) (see Sect. 2.9.4),

(2) the same including merger effects,

(3) temperature function based on the gravitational potential (see Chap. 3) assuming that the measured temperature is equal to $T_{\mathrm{ew}}$,

(4) the same including mergers effects,

(5) temperature function based on the gravitational potential assuming that the measured temperature is equal to $T_{\mathrm{sl}}$ with rescaling according to Eq. (5.6),

(6) the same including merger effects.

In the first two cases, we assume the mass-temperature relation (5.16) whenever we have to relate a mass to a temperature or vice versa, thus also when applying our analytical merger model. To properly take the scatter into account, we convolve with a log-normal distribution,

$$p_M(T|M)\,\mathrm{d}T = \frac{1}{\sqrt{2\pi}\,\sigma_{\ln T} T} \exp\left( -\frac{[\ln T - \ln T_{\mathrm{exp}}(M)]^2}{2\sigma^2_{\ln T}} \right) \mathrm{d}T \tag{5.18}$$

where the expected temperature $T_{\mathrm{exp}}(M)$ is given by Eq. (5.16) using the best-fit values. The standard deviation is mass-dependent and set to

$$\sigma_{\ln T} = 0.03 + 0.04\,|\ln[ME(z)] - \ln M_0| \tag{5.19}$$

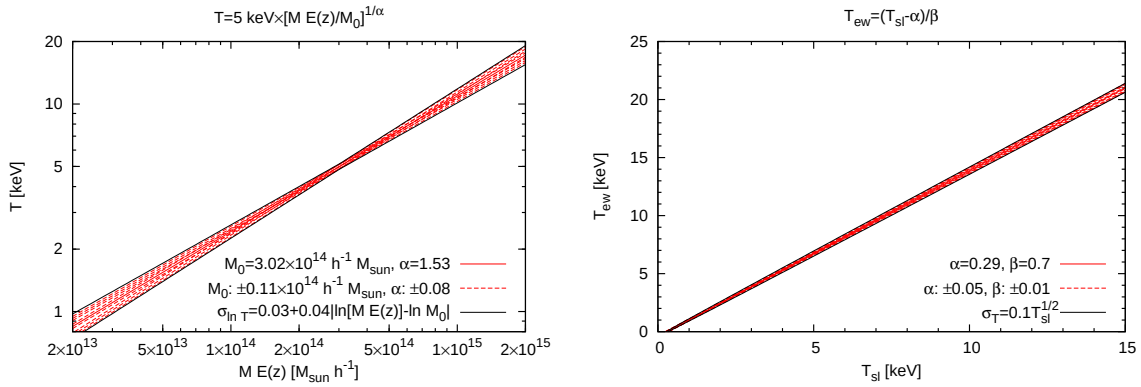


**Figure 5.5:** Uncertainties in the mass-temperature relation (*left panel*) and the $T_{\rm sl}$-$T_{\rm ew}$ relation (*right panel*), modelled by varying standard deviations of a log-normal ($\sigma_{\ln T}$) and a normal distribution ($\sigma_T$), respectively.

due to the uncertainty of $M_0$ and $\alpha$; see the left panel of Fig. 5.5. In the last four cases, we convolve with a normal distribution of the form

$$p_{T_{\rm sl}}(T|T_{\rm sl})\,{\rm d}T = \frac{1}{\sqrt{2\pi}\,\sigma_T}\exp\left(-\frac{[T-T_{\rm ew}(T_{\rm sl})]^2}{2\sigma_T^2}\right){\rm d}T\ , \tag{5.20}$$

where $T_{\rm ew} = (T_{\rm sl} - 0.29)/0.7$ (cf. Eq. 5.6). To take the scatter in the relation into account, the standard deviation is set to $\sigma_T = 0.1\,\sqrt{T_{\rm sl}}$; see the right panel of Fig. 5.5. We also use Eq. (5.20) to account for an error contribution in cases 3 and 4 by simply setting $T_{\rm ew} = T_{\rm sl}$.

Taking these uncertainties into account, the expected number of objects of each subsample is given by

$$N_{\rm low|high} = \int_{z_1}^{z_2}{\rm d}z \int_{T_1}^{T_2}{\rm d}T\,\frac{{\rm d}V_{\rm low|high}}{{\rm d}z}(T,z)\int{\rm d}x\,n(x)p_x(T|x)\ , \tag{5.21}$$

where $x$ can be either mass $M$ or spectroscopic-like temperature $T_{\rm sl}$ depending on the theoretical model used to fit the data (mass function or temperature function). The integral boundaries depend on the subsample and are given in Sect. 5.5.1 for $z$ and $T$. The integration over $x$ has to be done over the whole valid range of $p_x$. Finally, the expected differential number density of the $i$-th cluster is simply given by the convolution

$$n_{{\rm low|high},i} = \frac{{\rm d}V_{\rm low|high}}{{\rm d}z}(T_i,z_i)\int{\rm d}x\,n(x)p_x(T_i|x)\ . \tag{5.22}$$

To jointly fit both the low and the high-redshift cluster samples of Vikhlinin et al. (2009a), we have to add the two contributions, finding

$$C = 2\left(N_{\rm low} - \sum_i \ln n_{{\rm low},i} + N_{\rm high} - \sum_j \ln n_{{\rm high},j}\right)\ . \tag{5.23}$$

For the sample by Ikebe et al. (2002), we proceed analogously, but the situation is much easier since we only deal with one single sample that covers only a small redshift interval. The latter implies that we do not introduce a significant error if we ignore the redshift evolution of the mass or temperature function, respectively, in the analysis. Instead, we compute the theoretical functions at the sample's median redshift of $z = 0.046$ in the same way as Ikebe et al. (2002) did so that we only have to integrate

over the temperature when calculating the total expected number of objects from the sample. Hence, the $C$ statistic is given by

$$C = 2\left(N - \sum_i \ln n_i\right) \tag{5.24}$$

with

$$N = \int_{T_1}^{T_2} \mathrm{d}T\, V_{\max}(T) \int \mathrm{d}x\, n(x) p_x(T|x) \quad \text{and} \quad n_i = V_{\max}(T_i) \int \mathrm{d}x\, n(x) p_x(T_i|x)\ . \tag{5.25}$$

The conditional probability $p_x(T|x)$ is again given by either Eq. (5.18) or Eq. (5.20), respectively, thus assuming the same errors on the relations as for the Vikhlinin et al. (2009a) data. To better compare with the results by Ikebe et al. (2002), we shall also use the classical Press-Schechter mass function (2.74) instead of the one by Tinker et al. (2008) and relate mass and temperature via Eq. (3.45).

We search for minima of the $C$ statistic as a function of the two cosmological parameters $\Omega_{\mathrm{m0}}$ and $\sigma_8$, which enter both via $n(x)$ and the volume factors $\mathrm{d}V/\mathrm{d}z$ and $V_{\max}$. Only because the latter is very insensitive to changes in these two parameters, its dependence on $\Omega_{\mathrm{m0}}$ and $\sigma_8$ can be neglected. Cash (1979) showed that one can create confidence intervals for the $C$ statistic in the same way as it can be done for a $\chi^2$ fit using properties of the $\chi^2$ distribution. Following Lampton et al. (1976), intervals with confidence $y$ are implicitly given solving

$$y = \int_0^t \mathrm{d}\chi^2\, q(\chi^2) \tag{5.26}$$

for $t$, where $q$ is the density of the $\chi^2_p$ distribution with $p$ degrees of freedom determined by the number of parameters. For 95% confidence and $p = 2$, it follows that $t = 5.991$. Using the minimum of the $C$ statistic $C_{\min}$, we can simply calculate the 95% confidence contours by searching for points in the parameter space for which $C = C_{\min} + 5.991$.

## 5.6 Results

In Fig. 5.6, we present the 95% confidence contours for the samples by both Ikebe et al. (2002) and Vikhlinin et al. (2009a). Comparing the left and right panel, one can see that the results from both data sets are compatible with each other, although pronounced differences exist. However, for the Vikhlinin et al. (2009a) data, the confidence contours are smaller due to the additional information on the temperature function's redshift evolution.

The mass-based temperature functions (red contours) and the potential-based temperature functions without conversion from $T_{\mathrm{sl}}$ to $T_{\mathrm{ew}}$ (blue contours) give similar and compatible results, i.e. the confidence contours are in agreement with each other and have approximately the same size. When redshift evolution information is added (right panel), it seems that the direction of degeneracy is slightly changed for the potential-based temperature functions so that $\sigma_8$ can be constrained more tightly compared to the left panel. For the mass-based temperature function, there is no such effect. Overall, the potential-based functions yield slightly smaller best-fit values for $\sigma_8$ compared to their mass-based counterparts.

If merger effects are taken into account, $\sigma_8$ is significantly lowered while $\Omega_{\mathrm{m0}}$ is increased for all temperature functions. Consequently, the confidence contours of the results including and excluding mergers do not overlap. This result is in good agreement with the work by Randall et al. (2002), who also found using numerical simulations that mergers do have a drastic impact on the results for those two parameters.

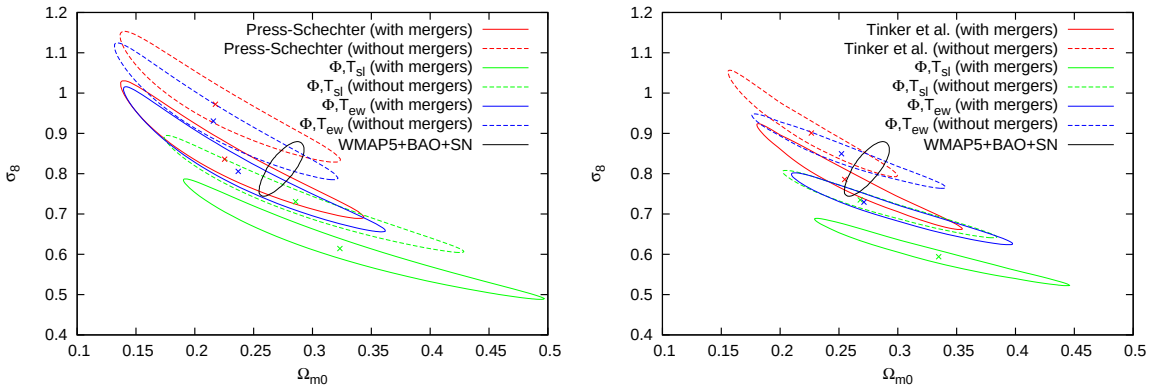


**Figure 5.6:** 95% confidence contours for the various theoretical models presented in Sect. 5.5.2. The results for the potential-based temperature function assuming that the measured temperature corresponds to either $T_{\rm sl}$ or $T_{\rm ew}$ are labeled $\Phi, T_{\rm sl}$ and $\Phi, T_{\rm ew}$, respectively. The crosses mark the respective best-fit values. Parameter constraints from a joint analysis of WMAP5, BAO, and SN data inferred from Komatsu et al. (2009) are indicated by the black solid contour. *Left panel:* Ikebe et al. (2002) data. *Right panel:* Vikhlinin et al. (2009a) data.

Assuming that the measured temperature is equal to $T_{\rm sl}$ and thus converting it to $T_{\rm ew}$ before comparing it to the theoretical potential-based temperature function (green contours) has a similar effect as mergers: $\sigma_8$ is decreased while $\Omega_{\rm m0}$ is increased. Interestingly, equating the measured temperature with $T_{\rm ew}$ and directly using it as input for the theoretical temperature function including the effect of mergers (blue solid contours) and transforming the measured temperature from $T_{\rm sl}$ to $T_{\rm ew}$ *without* including merger effects (green dashed contours) give almost identical (as for Vikhlinin et al., 2009a) or at least similar (for Ikebe et al., 2002) confidence contours. Hence, these two described processes are highly degenerate. Additionally, merger boosts increase the uncertainty on $\Omega_{\rm m0}$ since the confidence contours become more elongated in this direction.

All confidence contours are in agreement with a joint analysis of the five-year data release of the *Wilkinson Microwave Anisotropy Probe* (WMAP5) and data from both baryonic acoustic oscillations (BAO) and and type-Ia supernovae (SN) by Komatsu et al. (2009) (black solid contour) except one: if both the temperature conversion from $T_{\rm sl}$ to $T_{\rm ew}$ and merger effects are included in the calculation of the X-ray temperature function (green solid contour), the resulting confidence contour no longer overlaps with the one by Komatsu et al. (2009). This may imply that one either has to identify the measured temperature directly with the temperature that is used in the theoretical model and to include additional merger effects, or one has to convert the measured temperature using Eq. (5.6) to a theoretical temperature which is then used in the model. However, in the latter case it seems that one has to exclude merger effects since including both corrections results in values for $\sigma_8$ and $\Omega_{\rm m0}$ that are inconsistent with other cosmological probes.

We feel that the first approach is correct since in the theoretical derivation of the pure X-ray temperature function, we explicitly assume virial equilibrium, which only relaxed clusters should have reached. Combining the results of Randall et al. (2002), who also found that mergers do have a significant impact on the inferred values for $\Omega_{\rm m0}$ and $\sigma_8$, with the results of Sect. 5.4, we believe that correcting for merger effects should be a necessary step. Note additionally that the scaling relation (5.6) between both temperatures was established for clusters at $z = 0$ and hence, it is not known how this relation evolves with redshift.

In the preceding discussion, however, we should keep in mind that measurements of $\sigma_8$ from CMB data are degenerate with the optical depth due to reionisation. Breaking this degeneracy requires polarisation data, e.g. the $T$-$E$ cross-power spectrum. Thus, its value is sensitive to uncertainties in particular in the reionisation parameters and has changed significantly several times with subsequent

data releases. Additional information from BAO and SN do not directly constrain $\sigma_8$ either, but rather tighten constraints on the matter density $\Omega_{\rm m0}\,h^2$ through information on the cosmological constant at fixed spatial curvature. We thus hesitate to accept $\sigma_8$ as derived from WMAP data as a firm reference. Weak-lensing data, that are in principle capable of constraining $\sigma_8$ more directly, still yield a fairly broad range of results, $\sigma_8 \sim 0.6-0.9$; cf. the compilation in Bartelmann (2010b). Some tension between expectations and data are also reflected in the literature. For example, while Evrard et al. (2008) prefer a high normalisation of the power spectrum to be consistent with numerical simulations, Reiprich (2006) concludes that data from the *HIFLUCS* sample prefer a low $\sigma_8$.

Vikhlinin et al. (2009a) take merger effects into account by dividing the clusters of their samples into relaxed and unrelaxed due to their respective X-ray morphology. If a cluster is classified as unrelaxed, the mass estimate from Eq. (5.16) is multiplied by a factor of 1.17, assuming that the $M$-$T$ relations for these two classes of clusters evolve separately but similarly. This approach is inspired by results of a numerical simulation by Kravtsov et al. (2006). We think that this rigorous classification of clusters into relaxed and unrelaxed objects is problematic and should be avoided if possible. This can be done using our model of merger effects from Sect. 5.4. The resulting solid red contour in the lower panel of Fig. 5.6 is in good agreement with Vikhlinin et al. (2009b) (see their Fig. 3), where the rigorous classification was made. This and the compatibility with other cosmological probes indicate that our merger model can improve the determination of cosmological parameters from X-ray data without having to decide individually if a cluster is relaxed or not, at least if mass functions and an empirical $M$-$T$ relation are used to model an X-ray temperature function.

## 5.7 Conclusions

In the first part of this chapter, we have refined the theoretical X-ray temperature function derived in Chap. 3 in two different ways: First, we have used the ellipsoidal-collapse model of Chap. 4 to account for effects of the dynamics of ellipsoidal rather than spherical collapse and second, we have developed a simple analytic and parameter-free model that takes into account the net effect of temporary X-ray temperature boosts of galaxy clusters that previously underwent mergers on the temperature function. Comparing these two modifications to an $N$-body simulation by Borgani et al. (2004), we have found the following results:

- Taking into account ellipsoidal-collapse dynamics is only important when comparing the theoretical model to temperature functions of numerical simulations that are based on mass-weighted temperatures averaged over a large volume (e.g. inside the virial radius). Temperatures from real observations, however, are similar to the emission-weighted or the spectroscopic-like temperature, $T_{\rm ew}$ or $T_{\rm sl}$, respectively. We have shown that temperature functions based on $T_{\rm ew}$ are in good agreement with the theoretical model only for spherical-collapse dynamics.

- Especially for $z \gtrsim 0.5$, the effects of mergers cannot be excluded since the higher the redshift, the more clusters are unrelaxed and therefore deviate from virial equilibrium. Our simple analytic and parameter-free model based on the merger probability derived by Lacey & Cole (1993) can account for these effects. Including it in our theoretical modelling leads to a substantially improved agreement with the simulation for redshifts $0 \leq z \leq 1$.

In the second part, we have used both mass-based and potential-based X-ray temperature functions together with samples of Ikebe et al. (2002) and Vikhlinin et al. (2009a) to constrain the cosmological parameters $\Omega_{\rm m0}$ and $\sigma_8$. We have analysed the influence of merger effects on the inferred values of both parameters by using our analytical model. In addition, we have tested whether it is necessary to convert the measured temperatures to $T_{\rm ew}$ or if it is possible to compare them to the theoretical prediction directly. The main results are the following:

- Our potential-based temperature function leads to confidence contours in the $\Omega_{m0}$-$\sigma_8$ plane that are compatible to those inferred from classical mass-based temperature functions. The best-fit values might be shifted by a few percent. However, the formalism does not refer to cluster masses whose relation to observables have to be calibrated.

- Different temperature definitions give different results. Identifying the measured temperature directly with the temperature that is used in the theoretical model and additionally including merger effects, or converting the measured temperature using Eq. (5.6) before comparing to the model and disregarding merger effects give similar results for $\Omega_{m0}$ and $\sigma_8$. Since the comparison to the simulation and the results from the mass-based temperature functions indicate that merger effects lead to biases, we believe that the direct comparison between measured and theoretical temperatures is the correct choice when using our potential-based X-ray temperature function.

- Almost all of our results are compatible with constraints from a joint analysis by Komatsu et al. (2009) using WMAP5+BAO+SN data. Only if both the temperature conversion from $T_{sl}$ to $T_{ew}$ and merger effects are taken into account, the resulting confidence contours disagree with the latter. Since merger effects do have a significant impact on the determination of $\Omega_{m0}$ and $\sigma_8$ (one of the main results of Randall et al., 2002), a temperature conversion does not seem to be necessary in the context of the potential-based temperature function.

- The combination of the mass function by Tinker et al. (2008) with our simple analytic merger model yields similar results as the technique by Vikhlinin et al. (2009a,b), i.e. rigorously classifying galaxy clusters into relaxed and unrelaxed objects. However, we believe that our model is physically better justified since we take merger effects into account statistically.

- Although the results for the samples by Ikebe et al. (2002) and Vikhlinin et al. (2009a) are in agreement with each other, pronounced differences exist, implying that the final confidence regions from our analysis of the data might still be biased from systematics in the X-ray analysis and therefore, even better agreement with other cosmological probes could be achieved.

# 6 Chapter 6
# Basics of weak gravitational lensing

When light passes through the gravitational potential of an object (the lens), it is deflected so that another object (the source) behind the lens appears at a position on the sky different from the location that it would have without the lens. Additionally, the image of the source is distorted. Dependent on the local strength of the gravitational potential, the resulting effects are different so that one basically differentiates three regimes:

(1) **Strong lensing**

The most impressive features like giant arcs and luminous circles, the so-called *Einstein rings*, can be seen in the strong-lensing regime, where the source lies either directly behind the lens or very close to its centre. In the first case, an Einstein ring can be observed while in the second case, highly distorted images of the background source form arcs. Since a very deep gravitational potential is needed to produce these spectacular events, galaxy clusters usually serve as lenses, while the source is often a single galaxy in the background.

(2) **Weak lensing**

In this regime, the effects of gravitational lensing are much less spectacular and only lead to small image distortions since the local gravitational potential that the light ray passes is not as deep as in the strong-lensing regime. A spherical galaxy, for example, would appear elliptical to an observer. But since galaxies carry intrinsic ellipticities which are not known a priori, but which should average out if averaged over a sufficiently large amount of galaxies, the weak-lensing regime has to be treated statistically. We will present its basic formalism in this chapter. We recommend the review by Bartelmann & Schneider (2001) for further reading.

(3) **Microlensing**

This regime encompasses gravitational-lensing effects that are caused by the passage of a star or planet in front of another star inside the Milky Way resulting in a magnification of the background star's light curve. Using this effect, 12 exoplanets have been found until now.[10] Although the exoplanet itself cannot be seen directly, it adds a second but much smaller maximum as a characteristic fingerprint to the light curve of the background star.

We illustrate characteristic examples for the different lensing regimes in Fig. 6.1. For a detailed discussion of gravitational lensing as a whole, we recommend the review by Bartelmann (2010b).

## 6.1 Lens equation

Since the distances between observer and lens as well as lens and source are much larger compared to the extent of both the lens and the source, one usually works in the framework of the *thin-lens*

[10] http://exoplanet.eu/catalog-microlensing.php, last update on February 5th, 2011

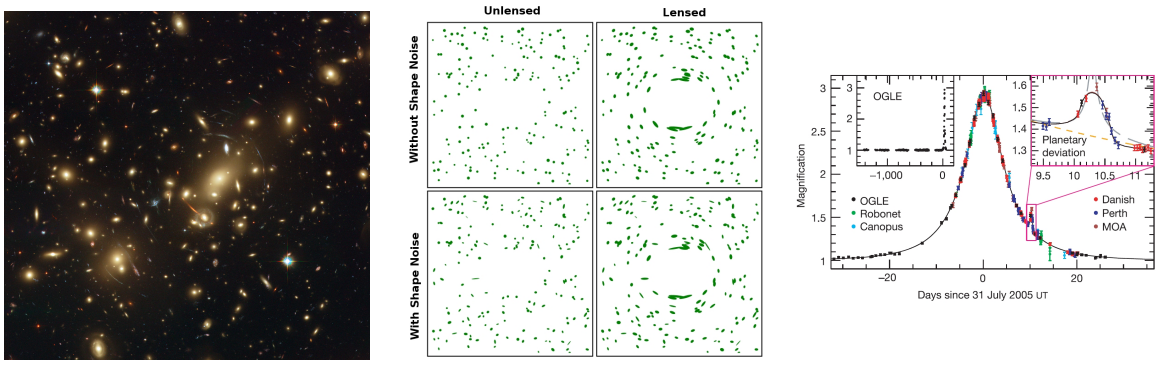


(a) Strong lensing (b) Weak lensing (c) Microlensing

**Figure 6.1:** Typical examples for the different lensing regimes. (a) Galaxy cluster Abell 2218 with numerous arcs.[11] (b) Illustration of the weak-lensing effect for spherical and elliptical galaxies.[12] (c) Light curve of the OGLE-2005-BLG-390 microlensing event. The second smaller maximum on the right is due to the magnification caused by an exoplanet.[13]

*approximation*, thus projecting the mass and the gravitational potential of the lens along the line-of-sight onto a plane perpendicular to it at distance $D_\mathrm{d}$ from the observer. This is the so-called *lens plane*, where the light deflection is assumed to take place. The corresponding plane at the distance $D_\mathrm{s}$ from the observer and at distance $D_\mathrm{ds}$ from the lens plane is the *source plane*. For large cosmological distances, $D_\mathrm{ds} \neq D_\mathrm{s} - D_\mathrm{d}$ due to the non-additive behaviour of the angular-diameter distance discussed in Sect. 1.4. A typical lens system is sketched in Fig. 6.2. Since all the following quantities are defined on two-dimensional planes, we write them as vectors in the form $\boldsymbol{x} = (x_1, x_2)$.

A light beam from a source at position $\boldsymbol{\eta}$ intersects the lens plane at position $\boldsymbol{\xi}$, where both positions are defined perpendicular to the line-of-sight that goes through the centre of the lens. The two points enclose the angles $\boldsymbol{\beta}$ and $\boldsymbol{\theta}$ with the optical axis, respectively. The light is deflected by an angle $\hat{\boldsymbol{\alpha}}$ which depends on $\boldsymbol{\xi}$ due to the position-depending gravitational potential. With the definitions above, the angles $\boldsymbol{\beta}$ and $\boldsymbol{\theta}$ can be written as

$$\boldsymbol{\beta} = \frac{\boldsymbol{\eta}}{D_\mathrm{s}} \quad \text{and} \quad \boldsymbol{\theta} = \frac{\boldsymbol{\xi}}{D_\mathrm{d}} \,. \tag{6.1}$$

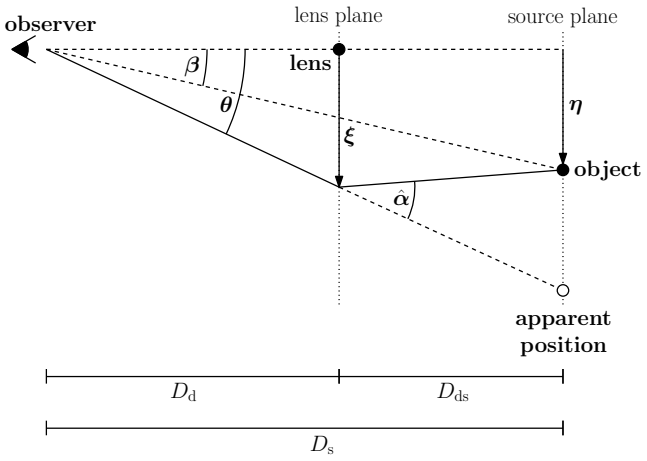


**Figure 6.2:** Geometry of a typical lens system.

From the intercept theorem for the lens situation shown in Fig. 6.2, one can deduce that the light ray reaching us under the angle $\boldsymbol{\theta}$ has to fulfill

$$\boldsymbol{\eta} + D_\mathrm{ds}\,\hat{\boldsymbol{\alpha}} = \frac{D_\mathrm{s}}{D_\mathrm{d}}\boldsymbol{\xi} \,, \tag{6.2}$$

which can be expressed for the angles $\boldsymbol{\beta}$ and $\boldsymbol{\theta}$ instead of the positions $\boldsymbol{\eta}$ and $\boldsymbol{\xi}$ by using Eq. (6.1). This yields

$$\boldsymbol{\beta} = \boldsymbol{\theta} - \boldsymbol{\alpha}(\boldsymbol{\theta}) \,, \tag{6.3}$$

[11] http://www.spacetelescope.org/images/heic0814a/
[12] http://commons.wikimedia.org/wiki/File:Shapenoise.svg
[13] Reprinted by permission from Macmillian Publishers Ltd: Nature, Beaulieu et al. (2006), copyright 2006.

with the *reduced deflection angle* $\boldsymbol{\alpha}(\boldsymbol{\theta}) \equiv (D_{\mathrm{ds}}/D_{\mathrm{s}})\,\hat{\boldsymbol{\alpha}}(D_{\mathrm{d}}\boldsymbol{\theta})$.

## 6.2 Lensing potential

For $|\boldsymbol{\xi}| \gg R_{\mathrm{S}}$, where $R_{\mathrm{S}}$ is the Schwarzschild radius of a point mass $M$, it can be concluded from the linearised field equations of General Relativity that the modulus of the deflection angle is given by $|\hat{\boldsymbol{\alpha}}| = (4GM)/(c^2|\boldsymbol{\xi}|)$, which is twice the value that is expected from Newtonian theory. Taking into account that the deflection angle is always pointed towards the mass, it can be written in vectorial form as

$$\hat{\boldsymbol{\alpha}} = \frac{4GM}{c^2}\frac{\boldsymbol{\xi}}{|\boldsymbol{\xi}|^2}\,. \tag{6.4}$$

Consider a three-dimensional mass distribution with density $\rho(\vec{r})$, where $\vec{r} = (\xi_1, \xi_2, r_3)$, so that $r_3$ is perpendicular to the lens plane. Approximating the mass distribution as a sum of point masses with mass $\mathrm{d}M = \rho(\vec{r})\,\mathrm{d}V$, we can write the total reduced deflection angle as[14]

$$\hat{\boldsymbol{\alpha}}(\boldsymbol{\xi}) = \frac{4G}{c^2}\int \mathrm{d}^3r'\,\rho(\vec{r'})\frac{\boldsymbol{\xi}-\boldsymbol{\xi}'}{|\boldsymbol{\xi}-\boldsymbol{\xi}'|^2} = \frac{4G}{c^2}\int \mathrm{d}^2\xi'\,\Sigma(\boldsymbol{\xi}')\frac{\boldsymbol{\xi}-\boldsymbol{\xi}'}{|\boldsymbol{\xi}-\boldsymbol{\xi}'|^2}\,, \tag{6.5}$$

where we have introduced the *surface mass density* $\Sigma = \int \mathrm{d}r_3'\,\rho$.

Switching from the deflection angle to the *reduced* deflection angle and from the distances to the angles introduces an additional factor $D_{\mathrm{d}}D_{\mathrm{ds}}/D_{\mathrm{s}}$, which can be absorbed into the definition of the *critical mass density*

$$\Sigma_{\mathrm{cr}} \equiv \frac{c^2}{4\pi G}\frac{D_{\mathrm{s}}}{D_{\mathrm{d}}D_{\mathrm{ds}}}\,. \tag{6.6}$$

Thus, the surface mass density can be written in a dimensionless form, defining the *convergence*

$$\kappa(\boldsymbol{\theta}) \equiv \frac{\Sigma(D_{\mathrm{d}}\boldsymbol{\theta})}{\Sigma_{\mathrm{cr}}}\,. \tag{6.7}$$

The critical mass density and thus the convergence are typical measures to distinguish between weak and strong lenses. While in typical weak-lensing situations $\kappa \ll 1$, strong lenses, producing multiple images of the source in form of arcs, usually have $\kappa \geq 1$.

Using Eqs. (6.1) and (6.7), we can rewrite Eq. (6.5) as

$$\boldsymbol{\alpha}(\boldsymbol{\theta}) = \frac{1}{\pi}\int \mathrm{d}^2\theta'\,\kappa(\boldsymbol{\theta}')\frac{\boldsymbol{\theta}-\boldsymbol{\theta}'}{|\boldsymbol{\theta}-\boldsymbol{\theta}'|^2}\,. \tag{6.8}$$

Since $\boldsymbol{\nabla}_{\boldsymbol{x}}\ln|\boldsymbol{x}| = \boldsymbol{x}/|\boldsymbol{x}|^2$, we can write the reduced deflection angle as the gradient of a *lens potential* $\psi$,

$$\boldsymbol{\alpha}(\boldsymbol{\theta}) = \boldsymbol{\nabla}\psi \quad \text{with} \quad \psi \equiv \frac{1}{\pi}\int \mathrm{d}^2\theta'\kappa(\boldsymbol{\theta}')\ln|\boldsymbol{\theta}-\boldsymbol{\theta}'|\,, \tag{6.9}$$

which satisfies Poisson's equation $\Delta\psi = 2\kappa$ in two dimensions and is a weighted projection of the three-dimensional Newtonian potential $\Phi$,

$$\psi(\boldsymbol{\theta}) = \frac{2}{c^2}\frac{D_{\mathrm{ds}}}{D_{\mathrm{d}}D_{\mathrm{s}}}\int \mathrm{d}r_3\,\Phi(D_{\mathrm{d}}\boldsymbol{\theta}, r_3)\,. \tag{6.10}$$

[14] Since the deflection angle is very small, we are in the weak-field regime, where Einstein's field equations (1.2) can be linearised, and the total mass can be regarded as the sum of small point masses. Furthermore, we can use the *Born approximation* so that the light beam can be approximated as a straight line in the vicinity of every single infinitesimal point mass.

## 6.3 Magnification and distortion

Since a light bundle that is emitted from the source is subject to differential deflection (remember that the deflection angle depends on the position $\boldsymbol{\xi}$), an image of the source is distorted and either magnified or dimmed. Let $\omega_\mathrm{I}$ be the solid angle that the lensed object covers on the sky and $\omega_\mathrm{S}$ the solid angle that it would cover if no lens was present. The magnification $\mu$ is simply determined by $\mu = \omega_\mathrm{I}/\omega_\mathrm{S} = S_\mathrm{I}/S_\mathrm{S}$, where $S_\mathrm{I}$ and $S_\mathrm{S}$ are the fluxes of the lens image and the source without the influence of the lens, respectively. Since no photons are absorbed or emitted by the lensing process, the surface brightness is conserved and $I_\mathrm{I}(\boldsymbol{\theta}) = I_\mathrm{S}[\boldsymbol{\beta}(\boldsymbol{\theta})]$, where $I_\mathrm{I}$ and $I_\mathrm{S}$ are the surface brightnesses of the image and the source, respectively. Thus, the magnification $\mu$ is solely a geometric effect. It depends on the two-dimensional mapping $\boldsymbol{\beta} \mapsto \boldsymbol{\theta}$, which can be locally linearised due to the smallness of the source compared to the lens to

$$\boldsymbol{\beta} = \boldsymbol{\beta}_0 + \mathsf{A}(\boldsymbol{\theta} - \boldsymbol{\theta}_0) \,, \tag{6.11}$$

where $\mathsf{A}$ is the local Jacobian and $\boldsymbol{\beta}_0$ and $\boldsymbol{\theta}_0$ are the angles between the line-of-sight and the centres of the source and the image, respectively. They are related through the lens equation (6.3). Hence, the magnification is given by

$$\mu = |\det \mathsf{A}|^{-1} \equiv \left| \det \left( \frac{\partial \beta_i}{\partial \theta_j} \right) \right|^{-1} \,. \tag{6.12}$$

The Jacobian can be written in terms of the lensing potential as

$$\mathsf{A}(\boldsymbol{\theta}) = \left( \delta_{ij} - \frac{\partial^2 \psi}{\partial \theta_i \, \partial \theta_j} \right) \equiv \begin{pmatrix} 1 - \kappa - \gamma_1 & -\gamma_2 \\ -\gamma_2 & 1 - \kappa + \gamma_1 \end{pmatrix} \,, \tag{6.13}$$

where we have introduced the *complex shear* $\gamma \equiv \gamma_1 + \mathrm{i}\gamma_2$. Its components together with the convergence are given by

$$\gamma_1 = \frac{1}{2} \left( \frac{\partial^2 \psi}{\partial \theta_1^2} - \frac{\partial^2 \psi}{\partial \theta_2^2} \right) \,, \quad \gamma_2 = \frac{\partial^2 \psi}{\partial \theta_1 \, \partial \theta_2} \,, \quad \kappa = \frac{1}{2} \left( \frac{\partial^2 \psi}{\partial \theta_1^2} + \frac{\partial^2 \psi}{\partial \theta_2^2} \right) \,. \tag{6.14}$$

From Eq. (6.13), the magnification can be written in terms of the convergence and shear as

$$\mu = \frac{1}{(1 - \kappa)^2 - |\gamma|^2} \,. \tag{6.15}$$

We want to note that generally also higher-order derivatives of the lensing potential $\psi$ are involved if the relation between $\boldsymbol{\beta}$ and $\boldsymbol{\theta}$ is not linearised as in Eq. (6.11), but also following non-linear terms are included. The next order lensing quantities based on third derivatives of the lensing potential are the *F*- and *G-flexion*. See Bartelmann (2010b) for further information.

In Fig. 6.3, we show the effects of the convergence $\kappa$ and the two shear components $\gamma_1$ and $\gamma_2$ on a circular source.

The image distortion, however, is generally neither caused by the convergence nor the shear alone, but by a combination of both. This can be seen if we write the Jacobian as

$$\mathsf{A}(\boldsymbol{\theta}) = (1 - \kappa) \begin{pmatrix} 1 - g_1 & -g_2 \\ -g_2 & 1 + g_1 \end{pmatrix} \,, \tag{6.16}$$

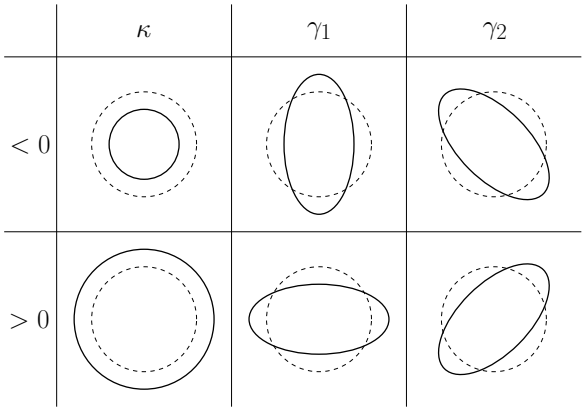


**Figure 6.3:** Influence of the individual weak-lensing quantities on the distortion of a circular source. The dotted circles indicate the source without lensing effects.

where the $g_i \equiv \gamma_i/(1-\kappa)$ are the components of the *reduced shear*. The term $(1-\kappa)$ induces a *homogeneous* distortion and hence only changes the size of an object but does not alter its shape. The latter is distorted by the reduced shear $g$, which is a combination of convergence and shear. Thus, only the combined quantity $g$ can be determined by measurements of galaxy ellipticities. But since in the majority of weak-lensing situations, $\kappa \ll 1$ and therefore $g \approx \gamma$, the reduced shear is a good proxy for the "real" shear.

## 6.4 Relation between ellipticity and shear

The question how to determine the ellipticity of an irregularly shaped galaxy could fill a thesis on her own since it is a non-trivial task to do, especially in the presence of noise (which is always the case in real observations). We will only sketch the main idea here and refer to recent works on this issue by Melchior et al. (2011) and Viola et al. (2011).

We start with the second moments of the brightness distribution defined as

$$Q_{ij} \equiv \frac{\int \mathrm{d}^2\theta\, I_\mathrm{I}(\boldsymbol{\theta})\, W(I_\mathrm{I})\, (\theta_i - \theta_{0,i})(\theta_j - \theta_{0,j})}{\int \mathrm{d}^2\theta\, I_\mathrm{I}(\boldsymbol{\theta})\, W(I_\mathrm{I})}\,, \tag{6.17}$$

where $W(I_\mathrm{I})$ is a proper weighting function depending on the light distribution, and $\boldsymbol{\theta}_0$ is the centre of the image, which also depends on $W(I_\mathrm{I})$ via

$$\boldsymbol{\theta}_0 \equiv \frac{\int \mathrm{d}^2\theta\, I_\mathrm{I}(\boldsymbol{\theta})\, W(I_\mathrm{I})\, \boldsymbol{\theta}}{\int \mathrm{d}^2\theta\, I_\mathrm{I}(\boldsymbol{\theta})\, W(I_\mathrm{I})}\,. \tag{6.18}$$

We define the *complex ellipticity* as

$$\epsilon \equiv \frac{Q_{11} - Q_{22} + 2\mathrm{i}Q_{12}}{Q_{11} + Q_{12} + 2\sqrt{Q_{11}Q_{12} - Q_{12}^2}}\,. \tag{6.19}$$

Note that also other ellipticity definitions exist in the literature, see e.g. Bonnet & Mellier (1995). Defining the intrinsic ellipticity of the source $\epsilon_\mathrm{S}$ analogously and using $\mathsf{Q}_\mathrm{S} = \mathsf{A}\,\mathsf{Q}\,\mathsf{A}^\mathrm{T}$, the ellipticity of the lensed object for $|g| \leq 1$ is given by

$$\epsilon = \frac{\epsilon_\mathrm{S} + g}{1 + g^*\epsilon_\mathrm{S}} \tag{6.20}$$

(Seitz & Schneider, 1997), where the asterisk denotes complex conjugation. Since in typical weak-lensing situations $|g| \ll 1$ and $g \approx \gamma$, the previous equation becomes $\epsilon \approx \epsilon_\mathrm{S} + \gamma$ so that to first order, the observed ellipticity is the sum of the intrinsic ellipticity and the shear. Assuming that the intrinsic ellipticities are randomly oriented, they average to zero for a large number of galaxies, so that $\langle\epsilon\rangle \approx \langle\gamma\rangle$. Note, however, that for high-precision cosmological weak-lensing surveys, the previous approximations induce a non-negligible error, so that the full description has to be used.

## 6.5 Weak-lensing power spectra

Not only single objects can deflect the light from a source, but also the large-scale density field $\delta$ (cf. Chap. 2) in total bends the light on the way to us. Since the gravitational field caused by the large-scale structure is much less strong than the one of collapsed objects like galaxy clusters, we can safely work in the weak-lensing regime, and quantities like shear and convergence can be analogously defined.

So far, we have seen that the convergence is related to the lens potential, which itself is a weighted projection of the three-dimensional Newtonian potential (see Eq. 6.10), by $\kappa = \Delta\psi/2$. Combining these two equations yields

$$\kappa(\boldsymbol{\theta}) = \frac{1}{c^2}\,\Delta\left[\int \mathrm{d}r_3\, \frac{D_\mathrm{ds}}{D_\mathrm{d} D_\mathrm{s}}\,\Phi(D_\mathrm{d}\boldsymbol{\theta}, r_3)\right] \quad \text{with} \quad \Delta = \frac{\partial^2}{\partial\theta_1^2} + \frac{\partial^2}{\partial\theta_2^2}\,. \tag{6.21}$$

A similar expression can be found for the case of light deflection by the large-scale density field to yield an *effective convergence*

$$\kappa_{\rm eff}(\boldsymbol{\theta},\chi) = \frac{1}{c^2}\int_0^\chi {\rm d}\chi' \, \frac{r(\chi-\chi')\,r(\chi')}{r(\chi)}\,\Delta\Phi[r(\chi')\boldsymbol{\theta},\chi'] \quad \text{with} \quad \Delta = \frac{\partial^2}{\partial x_1^2}+\frac{\partial^2}{\partial x_2^2}+\frac{\partial^2}{\partial x_3^2}\,, \tag{6.22}$$

where $\chi$ is the comoving distance, and $r(\chi)$ was defined in Eq. (1.6) (see Bartelmann & Schneider, 2001, for a detailed derivation). Note, however, that the Laplacian in Eq. (6.21) is defined in two dimensions, whereas the Laplacian in Eq. (6.22) is the three-dimensional one. Using Poisson's equation (2.10) with $\rho = \Omega_{\rm m0}\,\rho_{\rm c0}\,a^{-3}$, we can directly relate the effective convergence to the density field $\delta$,

$$\kappa_{\rm eff}(\boldsymbol{\theta},\chi) = \frac{3H_0^2\Omega_{\rm m0}}{2c^2}\int_0^\chi {\rm d}\chi' \, \frac{r(\chi-\chi')\,r(\chi')}{r(\chi)}\,\frac{\delta[r(\chi')\boldsymbol{\theta},\chi']}{a(\chi')}\,. \tag{6.23}$$

We have assumed so far that the sources are distributed at a fixed comoving distance $\chi$. If this is not the case, $\kappa_{\rm eff}$ has to be averaged over the line-of-sight using a normalised source distribution function $G(\chi)$ so that

$$\bar\kappa_{\rm eff}(\boldsymbol{\theta}) = \int_0^{\chi_{\rm H}} {\rm d}\chi\, G(\chi)\,\kappa_{\rm eff}(\boldsymbol{\theta},\chi)\,, \tag{6.24}$$

where $\chi_{\rm H}$ is the comoving distance to the horizon.

Instead of integrating over $\chi$ from 0 to $\chi_{\rm H}$ and $\chi'$ from 0 to $\chi$, we can also integrate over $\chi'$ from 0 to $\chi_{\rm H}$ and over $\chi$ from $\chi'$ to $\chi_{\rm H}$ (see Fig. 6.4). Interchanging $\chi$ and $\chi'$ afterwards again leads to

$$\bar\kappa_{\rm eff}(\boldsymbol{\theta}) = \int_0^{\chi_{\rm H}} {\rm d}\chi\, q(\chi)\,\delta[r(\chi)\boldsymbol{\theta},\chi] \tag{6.25}$$

with

$$q(\chi) = \frac{3H_0^2\Omega_{\rm m0}}{2c^2}\,\frac{r(\chi)}{a(\chi)}\int_\chi^{\chi_{\rm H}} {\rm d}\chi'\, G(\chi')\,\frac{r(\chi'-\chi)}{r(\chi')}\,. \tag{6.26}$$

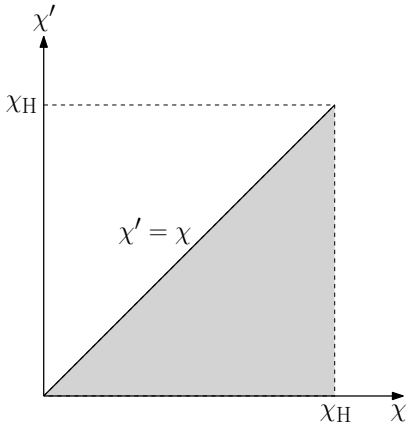


**Figure 6.4:** Area that is integrated over for the effective convergence $\bar\kappa_{\rm eff}(\boldsymbol{\theta})$.

Since the relation between $\bar\kappa_{\rm eff}$ and the three-dimensional density contrast $\delta$ has the form (6.25) and $\delta$ varies on much smaller scales than the window function $q(\chi)$, we can use *Limber's equation* (Limber, 1953) to calculate the convergence correlation function from the correlation function of the density contrast, or, equivalently, the convergence power spectrum $P_\kappa(l)$ from the density power spectrum $P(k,z)$ (Kaiser, 1992, 1998),

$$P_\kappa(l) = \int_0^{\chi_{\rm H}} {\rm d}\chi\,\frac{q^2(\chi)}{r^2(\chi)}\,P\left[\frac{l}{r(\chi)},z(\chi)\right]\,, \tag{6.27}$$

with $q(\chi)$ from Eq. (6.26) and $P(k,z) = D_+^2(z)P(k,z=0)$.

According to Eq. (6.14), the Fourier components of the shear and convergence are related to the Fourier components of the lensing spectrum by

$$\hat\gamma_1 = -\frac{1}{2}(l_1^2-l_2^2)\hat\psi\,, \quad \hat\gamma_2 = -l_1l_2\hat\psi\,, \quad \hat\kappa = -\frac{1}{2}(l_1^2+l_2^2)\hat\psi\,, \tag{6.28}$$

so that

$$\langle|\hat\gamma|^2\rangle = \langle|\hat\gamma_1|^2\rangle + \langle|\hat\gamma_2|^2\rangle = \left[\frac{1}{4}(l_1^2-l_2^2)^2 + l_1^2l_2^2\right]|\hat\psi|^2 = \left[\frac{1}{4}(l_1^2+l_2^2)^2\right]|\hat\psi|^2 = \langle|\hat\kappa|^2\rangle \tag{6.29}$$

and hence $P_\gamma(l) = P_\kappa(l)$.

Chapter 7

# 7 An analytic approach to number counts of weak-lensing peak detections

In this chapter, we develop and apply an analytic method to predict peak counts in weak-lensing surveys. It is based on the theory of Gaussian random fields, that we have presented in Sect. 3.2, and suitable to quantify the level of detections caused by chance projections of large-scale structures as well as the shape and shot noise contributed by the background galaxies. A simple analytical recipe is given to compute the signal-to-noise distribution of those detections. We compare our method to peak counts obtained from numerical ray-tracing simulations and find good agreement at the expected level. The number of peak detections depends substantially on the shape and size of the filter applied to the gravitational shear field. We confirm that weak-lensing peak counts are dominated by spurious detections up to signal-to-noise ratios of 3–5 and that most filters yield only a few detections per square degree above this level, while a filter optimised for suppressing large-scale structure noise returns up to an order of magnitude more. Galaxy shape noise and noise from large-scale structures cannot be treated as two independent components since the two contributions add in a non-trivial way.

The contents of this chapter is published in Maturi et al. (2010).

## 7.1 Introduction

Wide-area surveys for weak gravitational lensing can be and have been used for counting peaks in the shear signal, which are commonly interpreted as the signature of sufficiently massive dark-matter haloes. However, such detections are clearly contaminated by spurious detections caused by the chance superposition of large-scale structures, and also by the shape- and shot-noise contributions from the background galaxies used to sample the foreground shear field. As a function of the peak height, what is the contribution of genuine haloes to these detections, and how much do large-scale structures and other sources of noise contribute? In addition, the number of peaks produced by large-scale structures constitute a cosmological signal which can be used as a cosmological probe together with cluster counts. Can we predict this number without expensive numerical simulations?

Given the power of lensing-peak number counts as a cosmological probe (Marian et al., 2009; Kratochvil et al., 2010; Dietrich & Hartlap, 2010), we address this question here after applying a suitable analytic approach based on peak counts in Gaussian random fields as laid out by Bardeen et al. (1986). This extends van Waerbeke (2000), who studied the background galaxy noise component alone. With respect to the latter work, we give a detection definition more suitable for comparison with observations and include the non-negligible contribution of large-scale structures. It is reasonable to do so even though at least the high peaks are caused by haloes in the non-Gaussian tail of the density fluctuations since the noise and large-scale structure contributions to the filtered weak-lensing maps remain Gaussian, and thus at least their contribution to the counts can be well described analytically.

Peaks with the highest signal-to-noise ratios are expected to be more abundant than predicted based on Gaussian random fields.

Weak-lensing data are filtered to derive peak counts from them. Several linear filters have been proposed and used in the literature. They can all be seen as convolutions of the measured shear field with filter functions of different shapes. Many shapes have been proposed for different purposes (Schneider et al., 1998; Schirmer et al., 2004; Maturi et al., 2005). One filter function, called the *optimal filter* later on, was designed specifically to suppress the contribution from large-scale structures by maximising the signal-to-noise ratio of halo detections against the shear field caused by large-scales structures. We study three such filters here with the optimal filter among them. Results will differ substantially, arguing for a careful filter choice if halo detections are the main goal of the application. We compare our analytic results to a numerical simulation and show that both agree at the expected level.

In App. C, we show predictions of peak counts and the noise levels in them for several planned and ongoing weak-lensing surveys.

## 7.2 Measuring weak gravitational lensing

Here, we present the techniques that are applied to measure the shear $\gamma$ from weak gravitational lensing in apertures using appropriate filters and derive their relation to the convergence $\kappa$.

### 7.2.1 Weak-lensing estimates

In absence of intrinsic alignments between background galaxies due to possible tidal interactions (Heavens & Peacock, 1988; Schneider & Bridle, 2010), the intrinsic source ellipticities in Eq. (6.20) average to zero in a sufficiently large source sample. An appropriate and convenient measure for the lensing signal on circular apertures is the *aperture mass*, which is the weighted average over the tangential component of the shear $\gamma_\mathrm{t}$ relative to the position $\boldsymbol{\theta}$ on the sky,

$$\tilde{\Gamma}(\boldsymbol{\theta}) \equiv \int \mathrm{d}^2\theta' \gamma_\mathrm{t}(\boldsymbol{\theta}', \boldsymbol{\theta})\, Q(|\boldsymbol{\theta}' - \boldsymbol{\theta}|)\, W(\boldsymbol{\theta}') \,. \tag{7.1}$$

While the filter function $Q$ determines the statistical properties of the quantity $\tilde{\Gamma}$, $W$ describes the survey geometry. We shall consider three filter functions here, which will be described in Sect. 7.2.

Introducing polar coordinates with $\theta_1' = |\boldsymbol{\theta}'| \cos\varphi$ and $\theta_2' = |\boldsymbol{\theta}'| \sin\varphi$, the tangential shear can be written as

$$\gamma_\mathrm{t}(\boldsymbol{\theta}', \boldsymbol{\theta}) = -[\gamma_1(\boldsymbol{\theta}', \boldsymbol{\theta}) \cos(2\varphi) + \gamma_2(\boldsymbol{\theta}', \boldsymbol{\theta}) \sin(2\varphi)] \,. \tag{7.2}$$

Data on gravitational lensing due to a mass concentration can be modelled by a signal $s(\boldsymbol{\theta}) = \Gamma\tau(\boldsymbol{\theta})$ described by its amplitude $\Gamma$ and its radial profile $\tau$, and a noise component $n(\boldsymbol{\theta})$ with zero mean, i.e.

$$\gamma_\mathrm{t}(\boldsymbol{\theta}) = \Gamma\tau(\boldsymbol{\theta}) + n(\boldsymbol{\theta}) \tag{7.3}$$

for the tangential shear. The variance of $\tilde{\Gamma}$ (Eq. 7.1) is

$$\sigma^2_{\tilde{\Gamma}} = \int \frac{l\,\mathrm{d}l}{2\pi} \tilde{P}_\mathrm{g}(l)\, \hat{Q}^2(l) \,, \tag{7.4}$$

where $\hat{Q}(l)$ is the Fourier transform of the filter $Q$ and $\tilde{P}_\mathrm{g}(l) = P_\mathrm{g}(l)\, \hat{W}^2(l)$ is the effective power spectrum of the noise component, i.e. the intrinsic noise power spectrum convolved with a window function representing the *frequency response* of the survey. Note that the contribution from cosmic variance is not included in this definition since it is negligibly small. In our application, the latter is a band-pass filter accounting for the finite field of view of the survey (high-pass component) and the average galaxy separation (low-pass component). See Sect. 7.4.2 for its explicit expression. For

complex sky coverage and especially for too small fields of view the adopted approximation would not hold and a general treatment accounting for the full geometry $\hat{W}(\boldsymbol{l})$ must be considered (see for e.g. Hivon et al., 2002).

Here and in the following, we make use of the *flat-sky approximation*, i.e. we can still use the Fourier transform for a two-dimensional flat space instead of the one for the surface of a sphere, which would invoke spherical harmonics, since the field of view is only a small fraction of the whole sky.

In practical applications, $\tilde{\Gamma}$ is approximated by

$$\tilde{\Gamma}(\boldsymbol{\theta}) = \frac{1}{n} \sum_i \epsilon_{\mathrm{t},i}(\boldsymbol{\theta}) Q(|\boldsymbol{\theta_i} - \boldsymbol{\theta}|) \;, \tag{7.5}$$

where $\epsilon_{\mathrm{t},i}(\boldsymbol{\theta})$ is the tangential ellipticity with respect to $\boldsymbol{\theta}$ of a galaxy located at the position $\boldsymbol{\theta}_i$, providing an estimate for $\gamma_\mathrm{t}$. Note that in our application, we consider linear structures only and therefore, the weak-lensing approximation is always satisfied, i.e. $g \approx \gamma$.

### 7.2.2 Weak-lensing filters

Different filter profiles have been proposed in the literature depending on their specific application in weak lensing. We adopt three of them here, which have been used so far to identify halo candidates through weak lensing.

(1) The polynomial filter described by Schneider et al. (1998),

$$Q_\mathrm{poly}(x) \equiv \frac{6x^2}{\pi\theta_\mathrm{s}^2} \left(1 - x^2\right) \theta_\mathrm{H}\,(1 - x) \;, \tag{7.6}$$

where the projected angular distance from the filter centre, $x \equiv \theta/\theta_\mathrm{s}$, is expressed in units of the filter scale radius $\theta_\mathrm{s}$, and $\theta_\mathrm{H}$ is *Heaviside's step function* again. This filter was originally proposed for cosmic-shear analysis, but several authors have used it also for dark-matter halo searches (see e.g. Erben et al., 2000; Schirmer et al., 2004).

(2) A filter optimised for haloes with an NFW density profile (see Sect. 2.8.2), approximating their shear signal with a hyperbolic tangent (Schirmer et al., 2004),

$$Q_\mathrm{tanh}(x) \equiv \left(1 + \mathrm{e}^{a-bx} + \mathrm{e}^{cx-d}\right)^{-1} \tanh\left(x/x_\mathrm{c}\right) \;, \tag{7.7}$$

where the two exponentials in parentheses are cut-offs imposed at small and large radii (with $a = 6$, $b = 150$, $c = 50$, and $d = 47$), and $x_\mathrm{c}$ is a parameter defining the filter-profile slope. A good choice is $x_\mathrm{c} = 0.1$ as empirically shown by Hetterscheidt et al. (2005).

(3) The optimal linear filter introduced by Maturi et al. (2005) which, together with the optimisation with respect to the expected halo-lensing signal, optimally suppresses the contamination due to the line-of-sight projection of large-scale structures (LSS),

$$\hat{Q}_\mathrm{opt}(l) \equiv \alpha \frac{\tau(l)}{P_\mathrm{f}(l)} \quad \text{with} \quad \alpha^{-1} \equiv 2\pi \int \mathrm{d}l\, l\, \frac{|\hat{\tau}(l)|^2}{P_\mathrm{f}(l)} \;. \tag{7.8}$$

Here, $\hat{\tau}(l)$ is the Fourier transform of the expected shear profile of the halo and $P_\mathrm{f}(l) = P_\mathrm{g} + P_\gamma(l)$ is the complete noise power spectrum. It includes the linearly evolved LSS through the shear power spectrum $P_\gamma$, which is equal to the convergence power spectrum $P_\kappa$ (6.27) (see also the last paragraph of Sect. 6.5) as well as the noise contributions from the intrinsic source ellipticities and the shot noise by

$$P_\mathrm{g} = \frac{\sigma_\epsilon^2}{2n_\mathrm{g}} \;, \tag{7.9}$$

given their angular number density $n_g$ and the intrinsic ellipticity dispersion $\sigma_\epsilon$. We want to stress again that for the filter construction, we use the linear convergence power spectrum instead of the non-linear one. This is a kind of an implicit definition of a halo since we assume that the difference between linear and non-linear power spectrum is completely due to their formation. The optimal filter depends on parameters determined by physical quantities such as the halo mass and redshift, the galaxy number density and the intrinsic ellipticity dispersion and not on an arbitrarily chosen scale which has to be determined empirically through costly numerical simulations (e.g. Hennawi & Spergel, 2005). An application of this filter to the GaBoDS survey (Schirmer et al., 2003) was presented in Maturi et al. (2007), while a detailed comparison of all the three filters was performed by Pace et al. (2007) by means of numerical ray-tracing simulations. They found that the optimal linear filter defined by Eq. (7.8) returns the halo sample with the largest completeness (100% for masses $M \geq 3 \times 10^{14}\ h^{-1}\ M_\odot$ and ~50% for masses $M \sim 2 \times 10^{14}\ h^{-1}\ M_\odot$ for sources at $z_s = 1$) and the lowest number of spurious detections caused by the LSS ($\leq 10\%$ for a signal-to-noise threshold of S/N ~ 5).

### 7.2.3 Weak-lensing estimates and convergence

In order to simplify comparisons with numerical simulations, we convert the quantity $\tilde{\Gamma}$ from Eq. (7.1) to a quantity involving the convergence,

$$\tilde{\Gamma}(\boldsymbol{\theta}) = \int \mathrm{d}^2\theta' \kappa(\boldsymbol{\theta}')\, U(|\boldsymbol{\theta}' - \boldsymbol{\theta}|)\, W(\boldsymbol{\theta}')\ , \tag{7.10}$$

where $U$ is related to $Q$ by

$$Q(\theta) = \frac{2}{\theta^2} \int_0^\theta \mathrm{d}\theta' \theta' U(\theta') - U(\theta) \tag{7.11}$$

(Schneider, 1996) if the weight function $U(\theta)$ is defined to be compensated, i.e.

$$\int_0^{\theta_{\max}} \mathrm{d}\theta\, \theta\, U(\theta) = 0\ , \tag{7.12}$$

where $\theta_{\max}$ is the maximal extent of the filter, implying $Q(\theta) = U(\theta) = 0$ for $\theta > \theta_{\max}$.

Equation (7.11) has the form of a *Volterra integral equation of the second kind*, which can be solved for $U$ once $Q$ is specified. If $\lim_{x\to 0} Q(x)/x$ is finite, the solution is

$$U(\theta) = -Q(\theta) - \int_0^\theta \mathrm{d}\theta' \frac{2}{\theta'} Q(\theta')\ , \tag{7.13}$$

(Polyanin & Manzhirov, 1998), which can be solved analytically for the polynomial filter, yielding

$$U_{\mathrm{poly}}(x) = \frac{9}{\pi\theta_s^2}\left(1 - x^2\right)\left(\frac{1}{3} - x^2\right)\Theta_{\mathrm{H}}(1 - x)\ , \tag{7.14}$$

and numerically for the hyperbolic-tangent filter of Eq. (7.7) with an efficient recursive scheme over the desired radii $\theta$. If $\lim_{x\to 0} Q(x)/x = \infty$ as in the case of the optimal filter, Eq. (7.13) can be solved by introducing an exponential cut-off at small radii to avoid the divergence. The correct solution is obtained if the cut-off scale is close to the mean separation between the background galaxies so that no information is lost.

Another way is to solve Eq. (7.11) iteratively with respect to $Q$ by

$$U_0(\theta) = -Q(\theta)\ , \quad U_n(\theta) = -Q(\theta) + \frac{2}{\theta^2} \int_0^\theta \mathrm{d}\theta' \theta' U_{n-1}(\theta')\ . \tag{7.15}$$

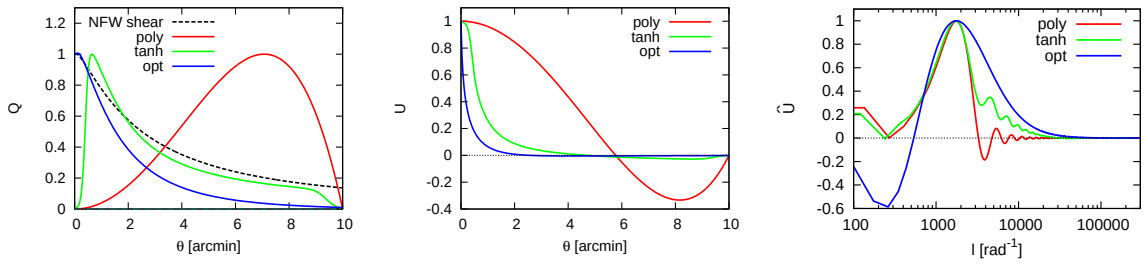


**Figure 7.1:** Overview of different weak-lensing filters. The *left panel* shows the three filters adopted here to be used on shear catalogues, while the *central* and *right panels* show the corresponding filters to be used on convergence fields both in real and Fourier space, respectively. For illustration only, the spatial frequencies in the right panel are rescaled such that the main filter peaks coincide.

The iterative procedure is stopped once the difference $U_n(\theta) - U_{n-1}(\theta)$ is sufficiently small. After $U(\theta)$ has been found, an appropriate constant $C$ has to be added in order to satisfy the compensation requirement (7.12). It is given by

$$C = -\frac{2}{\theta_{\rm max}^2} \int_0^{\theta_{\rm max}} {\rm d}\theta\, \theta\, U(\theta) \,. \tag{7.16}$$

We show in Fig. 7.1 the resulting filter profiles to be used on shear catalogues through Eq. (7.1) and their corresponding variants to be used on convergence fields with Eq. (7.10), the latter both in real and in Fourier space. In the right panel, one can clearly see that all of them are band-pass filters and the two of them designed for halo searches (tanh, opt) have larger amplitudes at higher frequencies compared to the polynomial filter (poly) by Schneider et al. (1998), where the halo signal is most significant. This feature is particularly prominent for the optimal filter, which is additionally negative at low frequencies, where the LSS signal dominates. These two features ensure the minimisation of the LSS contamination in halo searches.

## 7.3 Predicting weak-lensing peak counts

Our analytic predictions for the number counts of weak-lensing detections as a function of their signal-to-noise ratio are based on modelling the analysed and filtered lensing data, resulting from Eq. (7.10), as an isotropic and homogeneous Gaussian random field. We refer to Sect. 3.2 for its definition and properties. This is an extremely good approximation for the noise and the LSS components, but not necessarily for the non-linear structures such as sufficiently massive haloes, as we shall discuss in Sect. 7.4.3.

In our case, the relevant power spectrum that fully describes the Gaussian random field is a combination of the convergence power spectrum and the power spectrum of the observational noise caused by the galaxies.

Since we are interested in gravitational-lensing quantities such as the convergence $\kappa$, we here consider two-dimensional Gaussian random fields only with $\boldsymbol{r} \equiv \boldsymbol{\theta}$. We adopt the formalism of Sect. 3.2 here and modify it according to our weak-lensing purposes so that $F = \kappa$, $\eta_i = \partial_i F$ and $\zeta_{ij} = \partial_i \partial_j F$ denote the convergence field and its first and second derivatives, respectively.

### 7.3.1 Definition of detections: a new upcrossing criterion

We define as *detection* any contiguous area of the field $\kappa$ which exceeds a given threshold $\kappa_{\rm th} = {\rm S/N} \cdot \sigma_{\tilde{\Gamma}}$, determined by the required signal-to-noise ratio S/N and the variance $\sigma_{\tilde{\Gamma}}$ of the quantity $\tilde{\Gamma}$ (see Eq. 7.4).

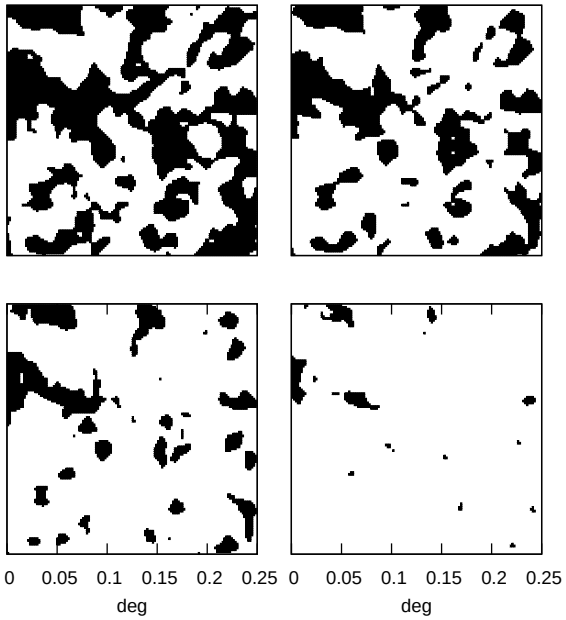


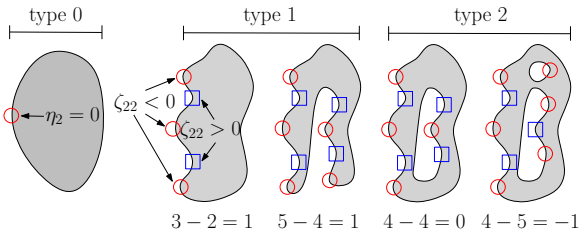


**Figure 7.2:** Weak lensing detection maps. The four plots *on the left* show the segmentation of a realistic weak-lensing S/N map for increasing thresholds: 0.1, 0.5, 1, and 2, respectively. The illustration *on the top* sketches the three discussed detection types together with the points identified by the standard and the modified upcrossing criteria. *Red circles* and *blue squares* correspond to upcrossing points for which the second field derivatives are $\zeta_{22} < 0$ and $\zeta_{22} > 0$, respectively.

This definition is widely used in surveys for galaxy clusters or peak counts in weak-lensing surveys and can be easily applied both to real data and Gaussian random fields.

Each detection is delimited by its contour at the threshold level $\kappa_{\rm th}$. If this contour is convex, it has a single point $\boldsymbol{\theta}_{\rm up}$, called *upcrossing point*, where the field is rising along the $x$-axis direction only, i.e. where the field gradient has one vanishing and one positive component (see the sketch for type-0 detections in the top panel of Fig. 7.2),

$$\kappa(\boldsymbol{\theta}_{\rm up}) = \kappa_{\rm th} \,, \quad \eta_1(\boldsymbol{\theta}_{\rm up}) > 0 \,, \quad \eta_2(\boldsymbol{\theta}_{\rm up}) = 0 \,. \tag{7.17}$$

Since we assume $\kappa$ to be a homogeneous and isotropic random field, the orientation of the coordinate frame is arbitrary and irrelevant. The conditions expressed by Eq. (7.17) define the so-called *upcrossing criterion* which allows to identify the detections and to derive their statistical properties, such as their number counts, by associating their definition to the Gaussian random field variables $\kappa$, $\eta_1$ and $\eta_2$.

However, this criterion is prone to fail for low thresholds, where detections tend to merge and the isocontours tend to deviate from the assumed convex shape. This causes detection numbers to be overestimated at low cut-offs because each "peninsula" and "bay" of their contour (see type-1 in Fig. 7.2) would be counted as one detection. We solve this problem by dividing the upcrossing points into those with negative (red circles) and those with positive (blue squares) curvature, $\zeta_{22} < 0$ and $\zeta_{22} > 0$ respectively. In fact, for each detection their difference is one (type-1), providing the correct number count. The only exception is for those detections containing one or more "lagoons" (type-2) since each of them decreases the detection count by one. But since this is not a frequent case and occurs only at very low cut-off levels, we do not consider this case here.

### 7.3.2 The number density of detections

Once the relation between the detections and the Gaussian random variables $\vec{y} = (\kappa, \eta_1, \eta_2, \zeta_{22})$ together with their constraints from Eq. (7.17) and $\zeta_{22} < 0$ or $\zeta_{22} > 0$ are defined, we can describe their statistical properties through the multivariate Gaussian probability distribution (3.1) with the covari-

ance matrix

$$\mathsf{M} = \begin{pmatrix} \sigma_0^2 & 0 & 0 & -\sigma_1^2/2 \\ 0 & \sigma_1^2/2 & 0 & 0 \\ 0 & 0 & \sigma_1^2/2 & 0 \\ -\sigma_1^2/2 & 0 & 0 & 3\sigma_2^2/8 \end{pmatrix}, \tag{7.18}$$

as given by van Waerbeke (2000). Here, the $\sigma_j$ are the spectral moments of the power spectrum,

$$\sigma_j^2 = \int \frac{\mathrm{d}l}{2\pi} \tilde{P}(l)\, \hat{U}^2(l)\, l^{2j+1}\,, \tag{7.19}$$

where $\tilde{P}(l)$ is an effective power spectrum which is a combination of the *non-linear* power spectrum $P_{\rm LSS}(l)$ of matter fluctuations (the non-linear counterpart to $P_\kappa$, Peacock & Dodds, 1996) combined with the noise contribution by the background galaxies and the survey frequency response (see Sect. 7.4.2 for its explicit expression). $\hat{U}(l)$ is the Fourier transform of the filter adopted for the weak-lensing analysis (see Sect. 7.2). We will explain in Sect. 7.4.3 why we choose the non-linear convergence power spectrum instead of the linear one here.

The determinant of $\mathsf{M}$ is $(3\sigma_0^2\sigma_1^4\sigma_2^2 - 2\sigma_1^8)/32$, and the quadratic form (3.2) can be written explicitly as

$$Q = \frac{1}{2}\left(\frac{2\boldsymbol{\eta}\cdot\boldsymbol{\eta}}{\sigma_1^2} + \frac{8\zeta_{22}^2\sigma_0^2 + 8\zeta_{22}\,\kappa\,\sigma_1^2 + 3\kappa^2\sigma_2^2}{3\sigma_0^2\sigma_2^2 - 2\sigma_1^4}\right). \tag{7.20}$$

Both $\kappa$ and $\eta_2$ can be expanded into Taylor series around the points $\boldsymbol{\theta}_{\rm up}$ where the upcrossing conditions are fulfilled,

$$\kappa(\boldsymbol{\theta}) \approx \kappa_{\rm th} + \sum_{i=1}^{2} \eta_i(\boldsymbol{\theta} - \boldsymbol{\theta}_{\rm up})_i\,, \quad \eta_1(\boldsymbol{\theta}) \approx \sum_{i=1}^{2} \zeta_{2i}(\boldsymbol{\theta} - \boldsymbol{\theta}_{\rm up})_i\,, \tag{7.21}$$

so that the infinitesimal volume element $\mathrm{d}\kappa\,\mathrm{d}\eta_2$ can be written as $\mathrm{d}\kappa\,\mathrm{d}\eta_2 = |\det \mathsf{J}|\,\mathrm{d}^2\theta$, where $\mathsf{J}$ is the *Jacobian*,

$$\mathsf{J} = \begin{pmatrix} \partial\kappa/\partial x_1 & \partial\kappa/\partial x_2 \\ \partial\eta_2/\partial x_1 & \partial\eta_2/\partial x_2 \end{pmatrix} = \begin{pmatrix} \eta_1 & \eta_2 \\ \zeta_{21} & \zeta_{22} \end{pmatrix} \tag{7.22}$$

and $|\det \mathsf{J}| = |\eta_1\zeta_{22}|$ since $\eta_2 = 0$. The number density of upcrossing points at the threshold $\kappa_{\rm th}$ with $\zeta_{22} < 0$, and $\zeta_{22} > 0$, $n^-$ and $n^+$ respectively, can thus be evaluated as

$$n^{\mp}(\kappa_{\rm th}) = \mp \int_0^{\infty} \mathrm{d}\eta_1 \int_0^{\pm\infty} \mathrm{d}\zeta_{22}\, |\eta_1\zeta_{22}|\, p\,(\kappa = \kappa_{\rm th}, \eta_1, \eta_2 = 0, \zeta_{22})\,, \tag{7.23}$$

where $p(\kappa, \eta_1, \eta_2, \zeta_{22})$ is the multivariate Gaussian defined by Eq. (3.1) with $p = 4$, the correlation matrix (7.18), and the quadratic form (7.20). Both expressions can be integrated analytically, and their difference, $n_{\rm det}(\kappa_{\rm th}) \equiv n^-(\kappa_{\rm th}) - n^+(\kappa_{\rm th})$ as explained in Sect. 7.3.1, returns the number density of detections $n_{\rm det}$ above the threshold $\kappa_{\rm th}$,

$$n_{\rm det}(\kappa_{\rm th}) = \frac{1}{4\sqrt{2}\,\pi^{3/2}} \left(\frac{\sigma_1}{\sigma_0}\right)^2 \frac{\kappa_{\rm th}}{\sigma_0} \exp\left(-\frac{\kappa_{\rm th}^2}{2\sigma_0^2}\right). \tag{7.24}$$

Note how the dependence on $\sigma_2$ drops out of the difference $n^- - n^+$, leading to a very simple result. This equation is much less complex than Eqs. (41) and (42) of van Waerbeke (2000). It returns the number of detection contours rather than the number of peaks.

For completeness, we report the number density estimate also for the classical upcrossing criterion (7.17) only, where the constraint on the second derivative of the field $\zeta_{22}$ is not used,

$$n_{\rm up}(\kappa_{\rm th}) = \frac{1}{4\sqrt{2}\,\pi^{3/2}} \left(\frac{\sigma_1}{\sigma_0}\right)^2 \frac{\kappa_{\rm th}}{\sigma_0} \exp\left(-\frac{\kappa_{\rm th}^2}{2\sigma_0^2}\right)\left[\mathrm{erf}\left(\frac{\kappa_{\rm th}\sigma_1^2}{\sigma_0\gamma}\right) + \frac{\sigma_0\gamma}{\sigma_1^2\sqrt{\pi}\,\kappa_{\rm th}} \exp\left(-\frac{\kappa_{\rm th}^2\sigma_1^4}{\sigma_0^2\gamma^2}\right)\right], \tag{7.25}$$

with $\gamma \equiv \sqrt{3\sigma_0^2\sigma_2^2 - 2\sigma_1^4}$. This number density converges to the correct value $n_{\rm det}$ for $\kappa_{\rm th} \to \infty$, i.e. large thresholds, because $\mathrm{erf}(x) \to 1$ and $\exp(-x^2)/x \to 0$ for $x \to \infty$. This reflects the fact that for large thresholds, the detection shapes become fully convex and any issues with more complex shapes disappear.

## 7.4 Analytic predictions vs. numerical simulations

We now compare the number counts of detections predicted by our analytic approach with those resulting form the analysis of synthetic galaxy catalogues produced with numerical ray-tracing simulations.

### 7.4.1 Numerical simulations

We use the same hydrodynamical, numerical $N$-body simulation carried out by Borgani et al. (2004) that we have already presented in Sect. 5.3 (see there for the simulation details). Due to the relatively high mass resolution of both gas and dark-matter particles, haloes of mass $10^{13}\ h^{-1}\ M_\odot$ are resolved into several thousands of particles.

This simulation is used to construct backward light cones by stacking the output snapshots from $z = 1$ to $z = 0$. Since the snapshots contain the same cosmic structures at different evolutionary stages, they are randomly shifted and rotated to avoid repetitions of the same cosmic structures along one line-of-sight. The light cone is then sliced into thick planes, whose particles are subsequently projected with a triangular-shaped-cloud scheme (TSC, Hockney & Eastwood, 1988) on lens planes perpendicular to the line-of-sight. We trace a bundle of $2048 \times 2048$ light rays through one light cone which start propagating at the observer into directions on a regular grid of 4.9 degrees on each side. The effective resolution of this ray-tracing simulation is of the order of $1'$ (for further detail, see Pace et al., 2007).

The effective convergence and shear maps obtained from the ray-tracing simulations are used to lens a background source population according to Eq. (6.20). Galaxies are randomly distributed on the source plane at $z = 1$ with a number density of $n_{\rm g} = 30$ arcmin$^{-2}$ and have intrinsic random ellipticities drawn from the distribution

$$p(\epsilon_{\rm s}) = \frac{\exp\left[(1-\epsilon_{\rm s}^2)/\sigma_\epsilon^2\right]}{\pi\sigma_\epsilon^2\left[\exp(1/\sigma_\epsilon^2) - 1\right]}\,, \tag{7.26}$$

where $\sigma_\epsilon = 0.25$ (for further details, see Pace et al., 2007).

Synthetic galaxy catalogues produced in this way are finally analysed with the aperture mass, Eq. (7.1), evaluated on a regular grid of $512 \times 512$ positions covering the entire field-of-view of the light cone. All three filters presented in Sect. 7.2 were used with three different scales: the polynomial filter with $\theta_{\rm s} = 2\farcm75,\ 5\farcm5$, and $11'$, the hyperbolic-tangent filter with $\theta_{\rm s} = 5',\ 10'$, and $20'$, and the optimal filter with scale radii of the cluster model set to $\theta_{\rm s} = 1',\ 2'$, and $4'$. These scales are chosen to sample angular scales typically used in literature.

For a statistical analysis of the weak-lensing detections and their relation to the numerical simulations structures, see Pace et al. (2007).

### 7.4.2 Accounting for the geometry of surveys: the window function

Our analytic predictions for the number density of detections accounts for the survey frequency response $\hat{W}(l)$ discussed in Sect. 7.2.1. As already stated, this is a simplified approach and the adopted full geometry $\hat{W}(\boldsymbol{l})$ should be considered (see for e.g. Hivon et al., 2002) in case of complex sky masking, especially if involving small fields of view. Thus, in our approach, we consider only an effective

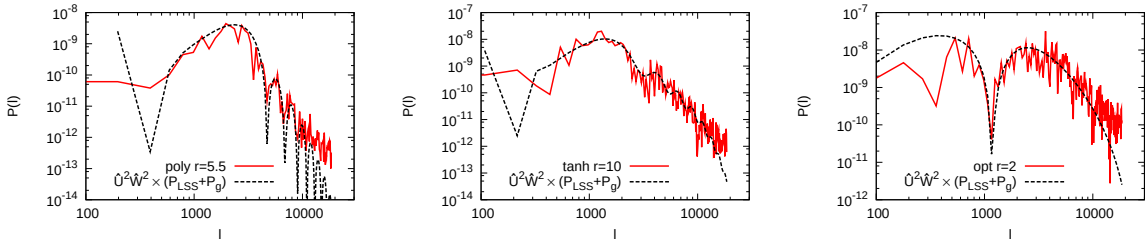


**Figure 7.3:** Comparison of the predicted power spectra based on the expected combined large-scale structure and noise power spectra and convolved with the weak-lensing filter and the frequency response of the survey with the one measured from a simulation. For clarity, we only show the results for the intermediate scales.

power spectrum $\tilde{P}(l) = P(l)\hat{W}^2(l)$, where the frequency response $\hat{W}(l)$ is the product of a high-pass filter suppressing the scales larger than the light cone's side length $L_\mathrm{f} = 2\pi/l_\mathrm{f} = 4.9$ deg,

$$\hat{W}^2_\mathrm{f}(l) = \exp\left(-\frac{l^2_\mathrm{f}}{l^2}\right) \tag{7.27}$$

(note that $l$ is in the denominator here), a low-pass filter imposed by the average separation $d = 2\pi/l_\mathrm{g} = n_\mathrm{g}^{-1/2} = 0.'18$ between the galaxies,

$$\hat{W}^2_\mathrm{g}(l) = \exp\left(-\frac{l^2}{l^2_\mathrm{g}}\right) , \tag{7.28}$$

and a low-pass filter related to the resolution $d_\mathrm{pix} = 0.'57$ used to sample the sky with the quantity $\tilde{\Gamma}$ of Eq. (7.5),

$$\hat{W}_\mathrm{pix}(l) = \frac{2\sqrt{\pi}}{l\,d_\mathrm{pix}}\,\mathrm{J}_1\left(\frac{l\,d_\mathrm{pix}}{\sqrt{\pi}}\right) , \tag{7.29}$$

where $\mathrm{J}_1(x)$ is the *cylindrical Bessel function of order one*. The latter function is a circular step function covering the same area as a square-shaped pixel of size $d_\mathrm{pix}$. The square shapes of the field-of-view and the pixels could be better represented by the product of two step functions in both the $x$- and $y$-direction, but the low gain in accuracy does not justify the higher computational cost.

Finally, for the comparison with our numerical ray-tracing simulation, we have to account for its resolution properties which act on the large-scale power spectrum only by including a low-pass filter

$$\hat{W}^2_\mathrm{sim}(l) = \exp\left(-\frac{l^2}{l^2_\mathrm{sim}}\right) , \tag{7.30}$$

where $l_\mathrm{sim} = 2\pi/(1\text{ arcmin})$ as discussed in Sect. 7.4.1.

The agreement of this simple recipe with the numerical simulation is shown in Fig. 7.3, where we compare $\tilde{P}(l)\,\hat{U}^2(l)$, the expected effective power spectrum multiplied with the weak-lensing filter as used in Eq. (7.19), with those measured from the synthetic galaxy catalogues and convolved with the three adopted filters $\hat{U}(l)$, respectively. For clarity, we show the results for the intermediate filter scales only since the others are equivalent. All main features are well reproduced. Only at high frequencies, the assumed power spectra drop slightly more steeply than measured in the numerical simulations. This might be one reason for the small deviations between the numerical measurements and the analytical predictions in the next section. The other one is sample variance.

Note that when relating the detection threshold to the signal-to-noise ratio S/N according to the variance (7.4) and $\kappa_\mathrm{th} = \mathrm{S/N} \cdot \sigma_{\tilde{\Gamma}}$, all window functions are used except Eq. (7.29), which, of course, does not affect the variance.

### 7.4.3 Comparison with numerical simulations

Our analytic approach approximates the data as Gaussian random fields, representing very well both noise and LSS contributions to the weak-lensing signal-to-noise ratio maps. In fact, even if shear and convergence of LSS show non-Gaussianities (Jain et al., 2000), weak-lensing data are convolved with filters broad enough to make their signal Gaussian. On the other hand, this is not the case for highly non-linear objects such as galaxy clusters whose non-Gaussianity remains after the filtering process. Thus, particular care has to be taken when comparing the predicted number counts with real or simulated data by modelling the non-linear structures, which is difficult and uncertain, or by avoiding their contribution in the first place.

We follow the latter approach by counting the *negative* instead of the positive peaks found in the filtered convergence maps derived from galaxy catalogues. In fact, massive haloes contribute only positive detections in contrast to the LSS and other sources of noise, which equally produce positive and negative detections with the same statistical properties. Both, negative and positive peak counts, contain cosmologically relevant information. Apart from noise, the negative peak counts are caused by mainly linearly evolved LSS, while the difference between positive and negative counts is due to highly non-linear structures. The mean density of negative peak counts can also be used to statistically correct positive peak counts by the level of spurious detections.

Since the formation of haloes, leading to an enhancement of positive with respect to negative peaks, also slightly influences the statistics of negative peak counts, we use $P_{\rm LSS}(l)$ instead of $P_\kappa(l)$ and thus, implicitly due to the definition of $P_{\rm LSS}(l)$, the *non-linear* matter power spectrum for the negative-peak prediction. In this way, we properly take into account non-linear effects also in the negative tail of the probability distribution function (PDF) although its shape still remains Gaussian.

To verify these considerations, we tested if the resulting weak-lensing maps below the zero level behave as Gaussian random fields, i.e. if the negative wing of their PDF is compatible with a Gaussian. The result is shown in Fig. 7.4 for all adopted filters and scales. On the one hand, the left side of the PDF is fitted by a Gaussian whose mean is compatible with zero. On the other hand, the largest PDF values show a slightly extended tail caused by the non-linear objects present in the numerical simulation.

A comparison of the original upcrossing criterion with the new blended upcrossing criterion presented here is shown in Fig. 7.5 together with the number counts of negative peaks obtained from the numerical simulations. Only the result for the optimal filter with $\theta_{\rm s} = 1'$ is shown for clarity. As expected, the two criteria agree very well for high signal-to-noise ratios since the detections are mostly of type-0, i.e. with a convex contour, as shown in the top panel of Fig. 7.2, while the merging of detections at lower signal-to-noise ratios is correctly taken into account only by our new criterion.

Our analytic predictions of the number counts for all filters and both positive and negative detection counts resulting from the synthetic galaxy catalogue are shown in Fig. 7.6. The high signal-to-noise

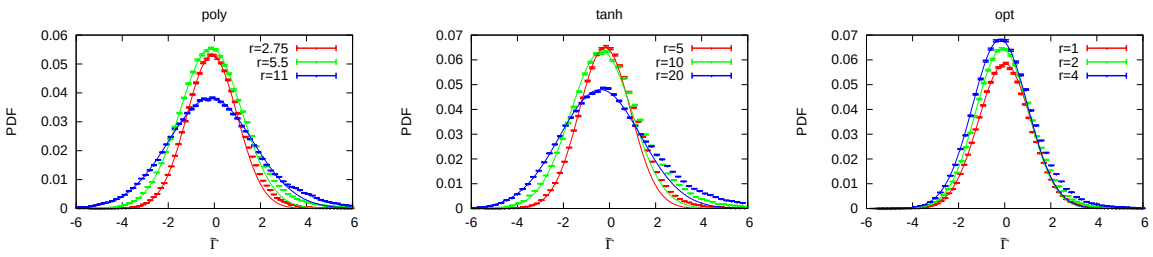


**Figure 7.4:** Probability distribution function (PDF) measured from the synthetic galaxy catalogue, which covers 24.4 square degrees, analysed with all adopted filters and scales. The negative part of the PDF is well described by a Gaussian (*solid lines*). The 3-$\sigma$ error bars related to the Poissonian uncertainty are shown.

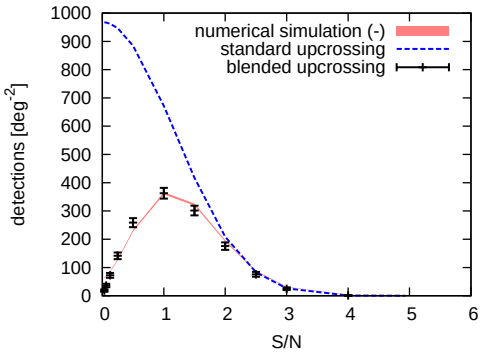


**Figure 7.5:** Number of negative peaks detected in the numerical simulation (*shaded area*) compared to our prediction. For the latter, both the original upcrossing criterion (*dashed line*) and the new blended upcrossing criterion (*points with error bars*) were used. Error bars represent the Poisson noise of the number counts of a one square degree survey, while the shaded area shows the Poisson noise in our numerical simulation covering 24.4 square degrees.

ratio tail caused by the nonlinear structures is present only in the positive detection counts, as expected. The agreement with the negative detections is within the 1-$\sigma$ error bars (representing the Poissonian uncertainties for a one square degree survey) except for the Schirmer et al. (2004) filter (tanh) and the Maturi et al. (2005) filter (opt), with a scale of $5'$ and $4'$ respectively, which are compatible only at a $2-3$-$\sigma$ level for $S/N \sim 1$. It is plausible that these deviations are caused by the small amount of non-Gaussianities still present in the data and the small deviations between the adopted and the actual signal power spectra (see Fig. 7.3).

We finally compare the contribution of the LSS and the noise to the total signal by treating them separately. Their number counts are plotted with dashed and dot-dashed lines in Fig. 7.6. All filters show an unsurprisingly large number of detections caused by the noise up to signal-to-noise ratios of 3 while the number of detections caused by the LSS increases with the filter scale except for the optimal filter, which always suppresses their contribution to a negligible level. Thus, the LSS contaminates halo catalogues selected by weak lensing up to signal-to-noise ratios of 4–5 if its contribution is ignored in the filter definition. Note that the total number of detections can be obtained only by counting the peaks from the total signal, i.e. LSS plus noise, and not by adding the peaks found in the two components separately, because the blending of peaks is different for the two cases.

To additionally confirm the assumption that the contributions from both LSS and noise from the background galaxies can be described by a Gaussian random field after the filtering process, the positive peak counts were modelled as a combination of the peak statistics described in this work (used for the negative peaks) and the halo mass function for the contribution of highly non-linearly evolved haloes that should be responsible for the high signal-to-noise part and that are not taken into account by the Gaussian field statistics. The analytical prediction in this case also shows good agreement with the results from the simulation. More detailed information on the method and results for a study on non-Gaussianity can be found in Maturi et al. (2011).

## 7.5 Conclusions

We have applied an analytic method for predicting peak counts in weak-lensing surveys, based on the theory of Gaussian random fields presented in Sect. 3.2. Peaks are typically detected in shear fields after convolving them with filters of different shapes and widths. We have taken these into account by first filtering the assumed Gaussian random field appropriately and then searching for suitably defined peaks. On the way, we have argued for a refinement of the upcrossing criterion for peak detection which avoids biased counts of detections with a low signal-to-noise ratio, and implemented it in the analytic peak-count prediction. Peaks in the non-linear tail of the shear distribution are underrepresented in this approach since they are highly non-Gaussian, but our method is well applicable to the prediction of spurious counts, and therefore to the quantification of the background in attempts to measure number densities of dark-matter haloes. We have compared our analytic prediction to peak counts in numerically simulated, synthetic shear catalogues and found agreement at the expected level.

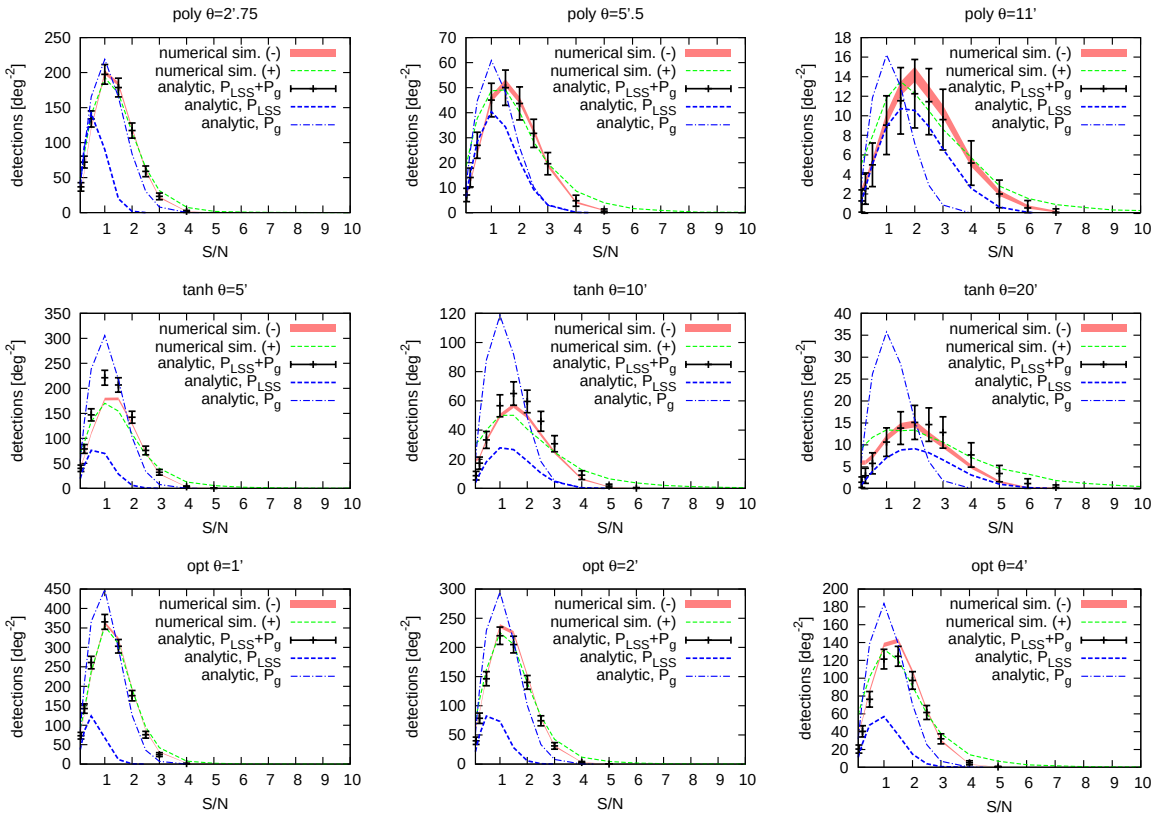


**Figure 7.6:** Number of weak-lensing peaks, shown as a function of the signal-to-noise ratio and predicted with our proposed analytic method for the Schneider et al. (1998) (poly), the Schirmer et al. (2004) (tanh), and the Maturi et al. (2005) (opt) filters from top to bottom, and increasing filter radii from left to right as labeled in each panel. The number counts generated by the intrinsic galaxy noise alone ($P_\mathrm{g}$) and the LSS alone ($P_\mathrm{LSS}$) are also shown. The results are compared with the number counts of positive (labeled with +) as well as negative (labeled with -) peaks detected, based on the synthetic galaxy catalogues from the numerical simulation. Thus, all numbers refer to a survey of one square degree with a galaxy number density of $n_\mathrm{g} = 30$ arcmin$^{-1}$ and an intrinsic shear dispersion of $\sigma_\epsilon = 0.25$. Error bars have the same meaning as in Fig. 7.5.

Our main results can be summarised as follows:

- The shapes and sizes of the filters applied to the shear field have a large influence on the contamination by spurious detections. For the optimal filter, the contribution from large-scale structures is low on all filter scales, while they typically contribute substantially for other filters. This confirms previous results with a different approach (Maturi et al., 2005; Dietrich et al., 2007; Pace et al., 2007).

- Taken together, large-scale structures and galaxy noise contribute the majority of detections up to signal-to-noise ratios between 3 and 5. Only above this level, detections due to real dark-matter haloes begin dominating.

- Shape and shot noise due to the background galaxies cannot be predicted separately from the large-scale structure since both affect another in a complex way.

- The optimal filter allows the detection of ∼30–40 haloes per square degree at signal-to-noise ratios high enough for suppressing all noise contributions. For the other filters, this number is lower by almost an order of magnitude.

Our conclusions are thus surprisingly drastic: peak counts in weak-lensing surveys are almost exclusively caused by chance projections in the large-scale structure and by galaxy shape and shot noise unless only peaks with high signal-to-noise ratios are counted. With typical filters, only a few detections per square degree can be expected at that level, while the optimal filter returns up to an order of magnitude more. Nevertheless, the contamination level of the cluster number counts can be predicted and, after all, it is a quantity containing valuable cosmological information which can be used to tighten cosmological constraints as well.

# Summary and conclusions

In this thesis, we have presented a novel approach for the derivation of the cluster temperature function from the statistics of Gaussian random fields applied to the cosmic gravitational potential. The Gaussian nature of the potential field arises naturally from simple theories of inflation and is conserved during its linear evolution. No reference to mass has been made during the derivation as for the classical approaches that can be found in the literature. We have thus avoided the inclusion of this problematic global quantity, invoking a volume integral over the density distribution and the necessity of introducing a sharp boundary which, in practice, cannot be chosen unambiguously. Consequently, we could also get around empirical relations which are needed to relate the mass to observables like the temperature or the luminosity, but which also induce an additional scatter.

Our analytic approach is based on predicting the number density of minima in the gravitational potential, where a minimum could be easily related to the X-ray temperature in the centre of a cluster by the virial theorem. Both the constraint that only collapsed structures be counted, and the relation between linear and non-linear evolution of the potential could be included using the spherical-collapse model. Another crucial ingredient to our formalism was a proper high-pass filter that filters out large potential modes and also modes of potential gradients, where the filter radius could be defined naturally by maximising the number density of objects for a given temperature and Laplacian of the potential and hence, it is not an arbitrary parameter.

Since a comparison of our approach to different mass functions using a theoretically motivated mass-temperature relation has shown on the one hand that the results were in good agreement with the Press-Schechter mass function and has suggested on the other hand that including ellipsoidal collapse might remove discrepancies to mass functions calibrated by numerical simulations and including ellipsoidal-collapse dynamics like the Sheth-Tormen mass function, we have decided to include ellipsoidal-collapse dynamics also in our approach. As a consequence, we have refined the ellipsoidal-collapse model by Bond & Myers (1996) in different ways. First, we have introduced initial conditions for the ellipticity and prolaticity that are consistent with a marginalisation over the distribution for the eigenvalues of the Zel'dovich deformation tensor. Second, we have combined the linear and the non-linear model for the external gravitational shear to the hybrid model, in which a shear component first evolves non-linearly until the corresponding axis has its turn-around. Then, the evolution of the shear and the axis decouple from each other, and the external-shear field continuous evolving linearly. Last, we have derived proper virialisation conditions from the tensor virial theorem to stop the collapse of each axis individually and hence were able to remove an ad-hoc criterion that had been used so far. Comparably to Sheth et al. (2001), we were able to derive a mass function from the first-upcrossing distribution of the moving barrier associated with ellipsoidal collapse, which is in good agreement with other results from the literature.

Using the results of our ellipsoidal-collapse study, we have replaced spherical- by ellipsoidal-collapse dynamics in the derivation of the cluster temperature function, but compared both alternatives to temperature functions from a numerical simulation based on different temperature definitions. We have found that for low redshifts, the theoretical temperature function including ellipsoidal collapse is consistent with one from the simulation based on the mass-weighted temperature within the virial radius, while the temperature function including spherical collapse is consistent with a temperature function based on the emission-weighted temperature. On the whole, we could show that a restriction to the inner parts of a halo leads to a good agreement with the theoretical temperature function accounting for spherical collapse, whereas ellipsoidal collapse seems to become important if outer parts of the cluster are weighted more strongly in the temperature definition.

Since increasing discrepancies have occurred between the theoretical prediction and the results from the numerical simulation for increasing redshift, which we have attributed to the influence of more and more frequent merger events, we have developed an analytic model based on the merger statistics derived by Lacey & Cole (1993) that describes the temperature boosts resulting from merger events and thus quantifies the influence of mergers on the cluster temperature function. Including this model in our theoretical description, we have found a good agreement between model and simulation for all redshifts. Furthermore, we have studied the influence of mergers on the joint determination of the cosmological parameters $\Omega_{\mathrm{m0}}$ and $\sigma_8$. Our study has confirmed the results of Randall et al. (2002) that the best-fit values for both parameters are significantly shifted if mergers are not taken into account in the analysis. Including the effects of mergers on the potential-based X-ray temperature function, a conversion from spectroscopic-like to emission-weighted temperature, often used in the literature, was not necessary to be compatible with classical mass-based temperature functions.

Inspired by the results for the X-ray temperature function, we have also used the statistics of Gaussian random fields to develop an analytic model to predict the influence of cosmic large-scale structures and shot noise on weak-lensing number counts. Refining the classical upcrossing criterion originally introduced by Bardeen et al. (1986), we were able to predict the number density of spurious detections as a function of signal-to-noise ratio for various weak-lensing filters used in the literature and have found agreement with results from a numerical simulation at the expected level. We could furthermore show that the optimal filter developed by Maturi et al. (2005) performs best in suppressing the unwanted contribution from large-scale structures and shot noise.

Overall, this thesis has demonstrated that in some cases, the statistics of Gaussian random fields can be applied even in the non-linear regime when either it is possible to establish a relation between linear and non-linear growth of a quantity, as it can be done with the spherical- or the ellipsoidal-collapse model for the X-ray temperature function, or a field obeying non-Gaussian statistics due to non-linear growth is properly filtered so that after the filtering procedure, its probability distribution function can be well approximated by a Gaussian again. The latter situation was utilised for the predictions of detections in weak-lensing convergence maps. In this way, analytic models can be developed, which are based on rather simple physical concepts on the one hand, but on the other hand can compete with results from current numerical simulations. This has two main advantages: The most important one is that the deeper physical understanding, why things happen as they happen, is much better conserved compared to complex numerical simulations. There, one has to start with a set of initial conditions and physical assumptions. However, it is mostly not possible to simulate a large fraction of the Universe for a whole set of them since the simulation for one single element requires large clusters of CPUs and high-performance computing infrastructure so that the influence of individual components on the overall result can be inferred more easily with analytic models. Additionally, the aforementioned computational effort for large numerical simulations can be avoided in the first place.

Although we have shown how well the predictions of our simple analytic models are in agreement with the results from numerical simulations, there are certainly a few points that could be examined in more detail and some that could be further improved. It would be very interesting to study the virialisation process of haloes in more detail. We have seen in Chap. 4 that the results from the spherical-collapse model depend on the choice of the virialisation time, i.e. if either half of the turn-around radius is chosen as a reference or the time when the spherical overdensity collapses mathematically to a point. Also in our ellipsoidal model, the virialisation of each axis had to be included "by hand". A model that includes virialisation naturally and does not demand to include it artificially seems necessary at this point. Engineer et al. (2000) already go into this direction, but their model is still dependent on results from numerical simulations to fix a key parameter. Maybe a full derivation in the context of General Relativity would offer more insight to the complex process of virialisation.

Similar to Eisenstein & Loeb (1995), relaxing the assumption that the ellipsoid's eigensystem coincide with the one of the surrounding shear field and comparing the results to those from Chap. 4 would be an additionally possible extention of the work presented here. In this context, not only ho-

mogeneous ellipsoids could be examined, but also more complex density profiles could be taken into account. However, this would surely only be possible in a more numerical framework.

Regarding the virial theorem, which is used to relate the potential depth to the cluster's X-ray temperature, it would be interesting to quantify the deviation from virial equilibrium for clusters that underwent mergers in order to quantify the scatter around the assumed potential-temperature relation and to infer its influence on the joint determination of $\Omega_{\mathrm{m0}}$ and $\sigma_8$. So far, especially due to the ignorance of the true scatter, we have included the scatter from the conversion from spectroscopic-like to emission-weighted temperature in the derivation also for the case, where no conversion was necessary, in order to have a rough estimate.

The reason why temperature functions constructed from central temperatures of clusters in numerical simulations are in such a good agreement with predictions using the spherical-collapse model, whereas the ones based on temperature definitions that use information from large radii in addition can well be modelled accounting for ellipsoidal-collapse dynamics, is not understood. It seems that the deviation from sphericity becomes only important for data from cluster outskirts. Further work is therefore also needed in this respect.

Since one of the results of Chap. 5 shows that the conversion from spectroscopic-like temperature to emission-weighted temperature is not necessary in the context of the potential-based temperature function as long as the influence of mergers is properly taken into account, a more detailed study on the reasons for the conversion in previous studies should clearly be done. The degeneracy between the temperature conversion and influence of mergers in the joint determination of $\Omega_{\mathrm{m0}}$ and $\sigma_8$ is also surely an interesting feature which should be examined more closely, especially since other correction factors in the literature could maybe emerge from neglected merger effects.

Instead of predicting the spurious detections from large-scale structures and shot noise in weak-lensing number counts only or, in other words, taking into account the *negative* part of the probability distribution function, it is possible to extend the work presented in Chap. 7 to its *positive* part, including even more non-linear structures like collapsed and virialised dark-matter haloes. Maturi et al. (2011) have shown that this is possible by modelling the filtered convergence signal as a sum of Gaussian peak statistics using the modified upcrossing criterion as presented in this thesis and a projection of the halo mass function along the line-of-sight so that an analytic model for the full lensing signal at all signal-to-noise ratios is available. This formalism cannot only be used for non-Gaussianity studies as done in their work, but also for deriving cosmological parameters from weak-lensing convergence maps. Including also data for large signal-to-noise ratios modelled by the halo mass function promises tighter constraints than using Gaussian peak statistics alone since first, the whole available information is used and second, signals at high-signal-to noise ratios are caused by massive haloes in the exponential tail of the mass function, which is highly sensitive to cosmological parameters.

Although there are still some points that can be improved or should be examined more closely as mentioned above, we can conclude that it is possible to derive analytical models from the statistics of Gaussian random fields which provide an improved understanding of the physical mechanisms behind structure formation and which are additionally able to compete with results from numerical simulations, both for the cluster temperature function and for the analysis of weak-lensing convergence maps.

# A Appendix A

# An alternative way to determine the cut-off wave number

In this appendix, we present an alternative approach to determine a physically reasonable definition of $k_{\min}$. Although it does not give the correct number density for smaller objects with a low X-ray temperature, the definition presented here might be important for future work based on the statistics of potential perturbations.

## A.1 Definition

An alternative appropriate choice for $k_{\min}$ could be the redshift-dependent *particle horizon* $r_{\text{hor}}$, taking into account that light could have travelled only a finite comoving distance between the Big Bang and redshift $z$. Consequently, we must only consider modes of the gravitational potential already inside the horizon. Thus,

$$k_{\min}(z) = \frac{\pi}{r_{\text{hor}}(z)} = \frac{\pi H_0}{c}\left[\lim_{a_1\to 0}\int_{a_1}^{a(z)} \frac{\mathrm{d}a'}{a'^2 E(a')}\right]^{-1} , \tag{A.1}$$

where $E(a)$ is again the *expansion rate* of the Universe.

In principle, signal retardation should also be taken into account. Considering an arbitrary point $\vec{x}$ at time $t$, only modes lying inside its past light cone can have influenced it. However, retardation has to be included "by hand" when using Newtonian gravity. This gives rise to an additional factor when calculating the power spectrum's amplitude since we must evaluate the amplitude of a mode with wave length $\lambda$ not at time $t$, but at the earlier time $t - \Delta t = t - \lambda/(2c)$.

We can compute the corresponding scale factors at $t - \Delta t$ as follows. We must have $\lambda = 2\pi/k \overset{!}{=} 2D_{\text{com}}(z, z_k)$, where $z$ and $z_k$ are the redshifts corresponding to times $t$ and $t - \Delta t$, respectively, and $D_{\text{com}}(z, z_k)$ is the comoving distance between both redshifts. Thus, we have to find a scale factor $a_k = 1/(1 + z_k)$ for each mode $k$ such that

$$k = \frac{\pi}{D_{\text{com}}(a, a_k)} = \frac{\pi H_0}{c}\left[\int_{a_k(z_k)}^{a(z)} \frac{\mathrm{d}a'}{a'^2 E(a')}\right]^{-1} \tag{A.2}$$

holds. This is consistent with Eq. (A.1) because the wave number $k$ approaches $k_{\min}$ for $a_k \to 0$. The influence on the power spectrum's amplitude results in an additional factor $G_+^2(a_k)/G_+^2(a)$ entering Eq. (3.22). Since $P_\Phi$ does not evolve with time in an EdS universe, it has no effect in this case. Additionally, it turns out that its contribution is quite small for both the ΛCDM and the OCDM model, where it only affects the power spectrum's amplitude for a relatively small amount of wave numbers.

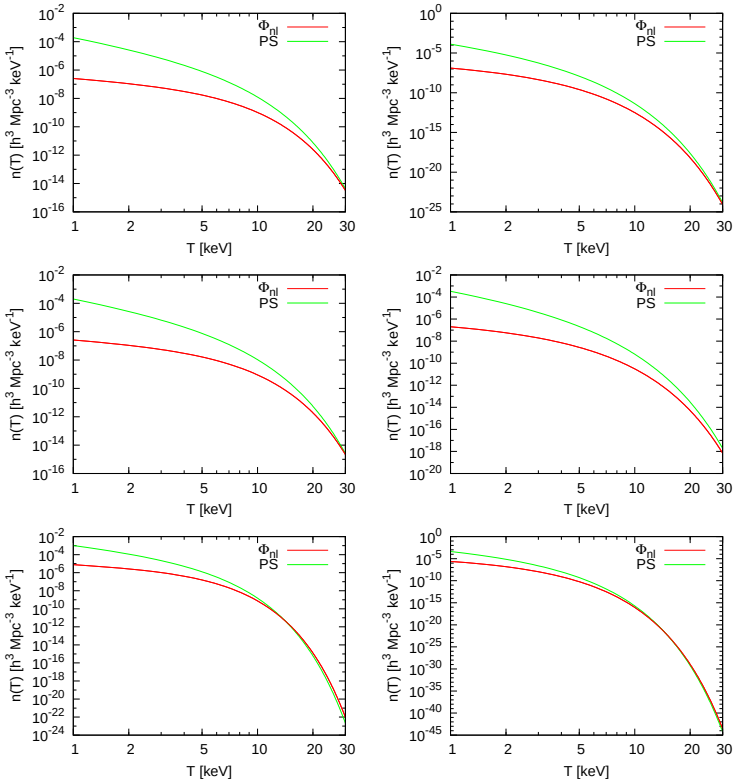


**Figure A.1:** Comparison of the X-ray temperature function derived from the statistics of gravitational potential perturbations ($\Phi_{\mathrm{nl}}$) using the alternative definition of $k_{\mathrm{min}}$ from Eq. (A.1) with the classical Press-Schechter approach (PS) for three cosmologies. *Upper row:* ΛCDM. *Central row:* OCDM. *Lower row:* EdS. *Left panels:* $z = 0$. *Right panels:* $z = 2$.

Hence, it only has a negligible effect on the computation of the spectral moments and can be usually ignored.

## A.2 Results for the X-ray temperature function

In Fig. A.1 we present the results for the X-ray temperature function from the statistics of gravitational potential perturbations using the alternative definition of $k_{\mathrm{min}}$ and compare it to the Press-Schechter approach for three different cosmologies and two redshifts for temperatures between 1 and 30 keV. We can see clearly that both functions match quite well for very high temperatures, especially in the EdS case. For all three models, the temperature function derived from the gravitational potential is much flatter for low temperatures than the temperature function inferred from the Press-Schechter mass function so that the number density of objects with temperatures of about 1 keV is too low by a factor of more than 100.

This discrepancy can be explained considering that we expect many more density maxima than potential minima for the same volume of space due to the following reason. The Gaussian random field of potential perturbations is much smoother and has much more power on large scales than the corresponding field for the density contrast due to the steepness of the potential power spectrum $P_\Phi$. Only large structures that have a high density contrast also correspond to a potential minimum, smaller structures only correspond to a maximum in the potential's Laplacian but not to a minimum in the potential itself. Since they are not located at a minimum of the potential, they have a non-vanishing potential gradient which corresponds to a non-zero peculiar velocity.

The definition presented in Eq. (3.42) does not involve these problems due to the fact that large-scale potential gradients are removed and therefore, the condition $\vec{\eta} = \vec{0}$ is also applicable for structures with a low X-ray temperature.

# B Appendix B

# Comparison with a previous ellipsoidal-collapse study

Here, we compare our results for the evolution equations of the collapsing ellipsoid with those presented by Monaco (1997) for a flat ΛCDM and an OCDM model.

Starting from Eq. (4.5), we can replace $E(a)$ and $E'(a)$ for a flat ΛCDM model using

$$E(a) = \sqrt{\Omega_{\mathrm{m0}} a^{-3} + (1 - \Omega_{\mathrm{m0}})} \quad \text{and} \quad E'(a) = -\frac{3\Omega_{\mathrm{m0}} a^{-4}}{2E(a)} \tag{B.1}$$

since $\Omega_{\Lambda 0} = 1 - \Omega_{\mathrm{m0}}$ and the curvature parameter $\Omega_{\mathrm{k}} = 0$. This yields

$$\frac{\mathrm{d}^2 a_i}{\mathrm{d}a^2} - \frac{1 - 2(\Omega_{\mathrm{m0}}^{-1} - 1)a^3}{2a\left[1 + (\Omega_{\mathrm{m0}}^{-1} - 1)a^3\right]} \frac{\mathrm{d}a_i}{\mathrm{d}a} + \frac{3C_i - 2a^3(\Omega_{\mathrm{m0}}^{-1} - 1)}{2a^2\left[1 + (\Omega_{\mathrm{m0}}^{-1} - 1)a^3\right]} a_i = 0\,. \tag{B.2}$$

This equation differs from Eq. (B11) of Monaco (1997) in the second and third term: A factor $a^2$ in the denominator of both terms was omitted. Additionally, the vacuum term $\propto \rho_\Lambda$ as well as a factor 3 were not included in the nominator of the third term.

For an OCDM model, we have

$$E(a) = \sqrt{\Omega_{\mathrm{m0}} a^{-3} + (1 - \Omega_{\mathrm{m0}}) a^{-2}} \quad \text{and} \quad E'(a) = -\frac{3\Omega_{\mathrm{m0}} a^{-4} + 2(1 - \Omega_{\mathrm{m0}}) a^{-3}}{2E(a)} \tag{B.3}$$

since $\Omega_{\Lambda 0} = 0$ and $\Omega_{\mathrm{k}} = (1 - \Omega_{\mathrm{m0}}) a^{-2}$. Inserting this again into Eq. (4.5) yields

$$\frac{\mathrm{d}^2 a_i}{\mathrm{d}a^2} - \left\{2a\left[1 + (\Omega_{\mathrm{m0}}^{-1} - 1)a\right]\right\}^{-1} \frac{\mathrm{d}a_i}{\mathrm{d}a} + 3\left\{2a^2\left[1 + (\Omega_{\mathrm{m0}}^{-1} - 1)a\right]\right\}^{-1} C_i a_i = 0\,. \tag{B.4}$$

Equation (B12) of Monaco (1997) is again slightly different: The factor 3 in the last term was omitted.

There is one last difference concerning the initial conditions: Comparing Eq. (B17) of Monaco (1997) with Eq. (4.6) of Chap. 4, one can find an additional factor $a_{\mathrm{ini}}$ in front of $\lambda_i(a_{\mathrm{ini}})$ which should be dropped.

# Appendix C

# Forecast for different weak-lensing surveys

For convenience, we evaluate here the expected number density of peak counts for signal-to-noise ratios 1, 3, and 5 and for a collection of present and future weak-lensing surveys with different intrinsic ellipticity dispersion $\sigma_\epsilon$ and galaxy number density $n_g$ per arcmin$^2$. To give typical values, we assumed for all of them a square-shaped field of view, a uniform galaxy number density and no gaps for two main reasons. First, their fields-of-view are typically very large and thus do not affect the frequencies relevant for our evaluation. Second, the masking of bright objects can be done in many different ways which cannot be considered in this paper in any detail. Finally, we fixed the sampling scale (7.29) to be 5 times smaller than the typical filter scale in order to avoid undersampling, i.e. such that the high frequency cut-off is imposed by the filters themselves. For each filter, we used two or three different scales, namely

- $Q_{\rm poly}$: scale-1 $\hat{=}$ 2.′75, scale-2 $\hat{=}$ 5.′5, scale-3 $\hat{=}$ 11′;
- $Q_{\rm tanh}$: scale-1 $\hat{=}$ 5′, scale-2 $\hat{=}$ 10′, scale-3 $\hat{=}$ 20′;
- $Q_{\rm opt}$: scale-1 $\hat{=}$ $10^{14}\ h^{-1}\ {\rm M}_\odot$, scale-2 $\hat{=}$ $5\times10^{14}\ h^{-1}\ {\rm M}_\odot$,
- $Q_{\rm gauss}$ (Gaussian FWHM): scale-1 $\hat{=}$ 1′, scale-2 $\hat{=}$ 2′, scale-3 $\hat{=}$ 5′.

The results are shown in Tab. C.1 together with the number counts obtained with a simple Gaussian filter, usually used together with the Kaiser & Squires shear inversion algorithm (Kaiser & Squires, 1993).

| **Pan-STARRS** | $Q_{\text{poly}}$ | | | $Q_{\tanh}$ | | | $Q_{\text{opt}}$ | | | $Q_{\text{gauss}}$ | | |
|---|---|---|---|---|---|---|---|---|---|---|---|---|
| $\sigma_\epsilon = 0.3, n_g = 5$ | 1 | 3 | 5 | 1 | 3 | 5 | 1 | 3 | 5 | 1 | 3 | 5 |
| scale-1 | 207.7 | 8.127 | 0.002 | 252.7 | 8.824 | 0.002 | 186.3 | 6.243 | 0.001 | 3125 | 131.1 | 0.042 |
| scale-2 | 51.49 | 2.82 | 0.001 | 61.8 | 3.214 | 0.002 | 62.69 | 3.576 | 0.002 | 989.6 | 38.93 | 0.011 |
| scale-3 | 12.45 | 1.258 | 0.002 | 14.02 | 1.518 | 0.003 | - | - | - | 173.2 | 7.82 | 0.003 |

| **DES** | $Q_{\text{poly}}$ | | | $Q_{\tanh}$ | | | $Q_{\text{opt}}$ | | | $Q_{\text{gauss}}$ | | |
|---|---|---|---|---|---|---|---|---|---|---|---|---|
| $\sigma_\epsilon = 0.3, n_g = 10$ | 1 | 3 | 5 | 1 | 3 | 5 | 1 | 3 | 5 | 1 | 3 | 5 |
| scale-1 | 206.6 | 9.55 | 0.004 | 248.9 | 10.98 | 0.004 | 288.8 | 12.72 | 0.005 | 3593 | 144.5 | 0.043 |
| scale-2 | 50.09 | 4.178 | 0.005 | 56.87 | 5.112 | 0.008 | 95.6 | 8.325 | 0.012 | 1047 | 41.67 | 0.012 |
| scale-3 | 11.67 | 2.339 | 0.0174 | 11.92 | 2.847 | 0.030 | - | - | - | 169.8 | 9.807 | 0.006 |

| **CFHTLS** | $Q_{\text{poly}}$ | | | $Q_{\tanh}$ | | | $Q_{\text{opt}}$ | | | $Q_{\text{gauss}}$ | | |
|---|---|---|---|---|---|---|---|---|---|---|---|---|
| $\sigma_\epsilon = 0.3, n_g = 20$ | 1 | 3 | 5 | 1 | 3 | 5 | 1 | 3 | 5 | 1 | 3 | 5 |
| scale-1 | 206.6 | 9.907 | 0.004 | 249.6 | 11.48 | 0.004 | 324 | 14.12 | 0.005 | 3971 | 151.6 | 0.041 |
| scale-2 | 49.76 | 4.545 | 0.007 | 55.86 | 5.61 | 0.010 | 104.5 | 9.519 | 0.015 | 1085 | 42.15 | 0.012 |
| scale-3 | 11.49 | 2.622 | 0.025 | 11.51 | 3.166 | 0.044 | - | - | - | 169.7 | 10.28 | 0.007 |

| **Subaru** | $Q_{\text{poly}}$ | | | $Q_{\tanh}$ | | | $Q_{\text{opt}}$ | | | $Q_{\text{gauss}}$ | | |
|---|---|---|---|---|---|---|---|---|---|---|---|---|
| $\sigma_\epsilon = 0.3, n_g = 30$ | 1 | 3 | 5 | 1 | 3 | 5 | 1 | 3 | 5 | 1 | 3 | 5 |
| scale-1 | 198.5 | 16.22 | 0.020 | 219.5 | 21.51 | 0.038 | 603.2 | 42.99 | 0.04045 | 4110 | 160.9 | 0.046 |
| scale-2 | 44.84 | 10.82 | 0.117 | 42.97 | 13.32 | 0.237 | 172.8 | 29.81 | 0.1642 | 1070 | 50.42 | 0.021 |
| scale-3 | 9.406 | 6.321 | 0.528 | 7.857 | 6.457 | 0.807 | - | - | - | 151.6 | 19.14 | 0.057 |

| **EUCLID** | $Q_{\text{poly}}$ | | | $Q_{\tanh}$ | | | $Q_{\text{opt}}$ | | | $Q_{\text{gauss}}$ | | |
|---|---|---|---|---|---|---|---|---|---|---|---|---|
| $\sigma_\epsilon = 0.3, n_g = 40$ | 1 | 3 | 5 | 1 | 3 | 5 | 1 | 3 | 5 | 1 | 3 | 5 |
| scale-1 | 194.3 | 20.01 | 0.039 | 206.3 | 27.29 | 0.088 | 730.9 | 58.61 | 0.070 | 4189 | 165.5 | 0.048 |
| scale-2 | 42.64 | 14.25 | 0.295 | 38.54 | 16.8 | 0.591 | 197.7 | 40.75 | 0.321 | 1062 | 54.99 | 0.027 |
| scale-3 | 8.653 | 7.642 | 1.104 | 6.873 | 7.282 | 1.514 | - | - | - | 143.6 | 24.19 | 0.127 |

| **LSST** | $Q_{\text{poly}}$ | | | $Q_{\tanh}$ | | | $Q_{\text{opt}}$ | | | $Q_{\text{gauss}}$ | | |
|---|---|---|---|---|---|---|---|---|---|---|---|---|
| $\sigma_\epsilon = 0.22, n_g = 50$ | 1 | 3 | 5 | 1 | 3 | 5 | 1 | 3 | 5 | 1 | 3 | 5 |
| scale-1 | 174.8 | 42.42 | 0.463 | 156.8 | 56.13 | 1.333 | 1206 | 138 | 0.334 | 4169 | 187.7 | 0.070 |
| scale-2 | 34.5 | 28.13 | 3.464 | 26.15 | 26.81 | 5.218 | 269.2 | 95.09 | 2.198 | 991.5 | 82 | 0.104 |
| scale-3 | 6.403 | 10.32 | 4.964 | 4.519 | 8.139 | 4.889 | - | - | - | 113.5 | 48.96 | 1.688 |

| **SNAP** | $Q_{\text{poly}}$ | | | $Q_{\tanh}$ | | | $Q_{\text{opt}}$ | | | $Q_{\text{gauss}}$ | | |
|---|---|---|---|---|---|---|---|---|---|---|---|---|
| $\sigma_\epsilon = 0.3, n_g = 100$ | 1 | 3 | 5 | 1 | 3 | 5 | 1 | 3 | 5 | 1 | 3 | 5 |
| scale-1 | 172.6 | 45.42 | 0.5824 | 152.5 | 59.33 | 1.664 | 1322 | 148.6 | 0.3481 | 4287 | 190.2 | 0.069 |
| scale-2 | 33.73 | 29.39 | 4.133 | 25.22 | 27.43 | 6.009 | 281.6 | 102.2 | 2.494 | 991.3 | 85.32 | 0.117 |
| scale-3 | 6.218 | 10.41 | 5.403 | 4.355 | 8.1 | 5.19 | - | - | - | 110.8 | 51.68 | 2.083 |

**Table C.1:** Expected number counts of peak detections per square degree for different weak-lensing surveys, filters, and signal-to-noise ratios.

# D Appendix D

# Units and constants

Here, we want to give the astronomical units and physical constants used in this thesis.

## D.1 Astronomical units

The *astronomical unit* (AU) is defined as the average distance of the Earth to the Sun, which is

$$1\ \mathrm{AU} = 1.4960 \times 10^{13}\ \mathrm{cm}\ . \tag{D.1}$$

One *light-year* (ly) is the distance that light travels in vacuum within one year. It is

$$1\ \mathrm{ly} = 9.4607 \times 10^{17}\ \mathrm{cm}\ . \tag{D.2}$$

At a distance of one *parsec* (pc), the parallax of an object on the sky due to Earth's motion around the Sun is 1″ (arcsecond). See Fig. D.1 for an illustration. The word "parsec" is an abbreviation for "*par*allax of one arc*sec*ond". It is

$$1\ \mathrm{pc} = 3.2616\ \mathrm{ly} = 3.0857 \times 10^{18}\ \mathrm{cm}\ . \tag{D.3}$$

One *Megaparsec* (Mpc) is therefore

$$1\ \mathrm{Mpc} = 3.0857 \times 10^{24}\ \mathrm{cm}\ . \tag{D.4}$$

The mass of the sun is

$$M_\odot = 1.9889 \times 10^{33}\ \mathrm{g}\ . \tag{D.5}$$

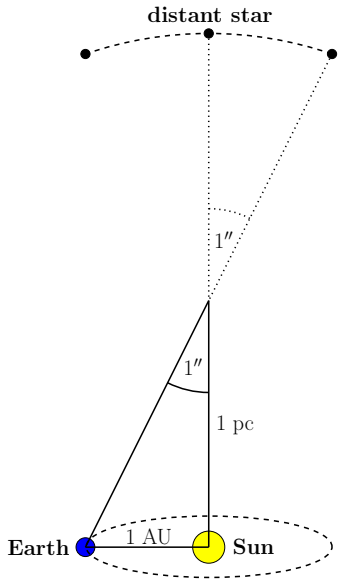


**Figure D.1:** Definition of a parsec (not to scale!).

## D.2 Physical constants

The *speed of light* is

$$c = 2.9979 \times 10^{10}\ \mathrm{cm\ s^{-1}}\ . \tag{D.6}$$

The *gravitational constant* is

$$G = 6.6720 \times 10^{-8}\ \mathrm{cm^3\ g^{-1}\ s^{-2}}\ . \tag{D.7}$$

Assuming that the intracluster medium has primordial composition, one particle of it has on average the mass $\mu m_\mathrm{p}$, where $\mu = 0.59$ and $m_\mathrm{p}$ is the *proton mass* given by

$$m_\mathrm{p} = 938.27\ c^{-2}\ \mathrm{MeV} = 1.6726 \times 10^{-24}\ \mathrm{g}\ . \tag{D.8}$$

The *Hubble constant*, quantifying today's expansion rate of the Universe, is

$$H_0 = 100\,h\ \mathrm{km\ s^{-1}\ Mpc^{-1}} = (9.7778)^{-1}\,h\ \mathrm{Gyr^{-1}} = 3.2408\times10^{-18}\,h\ \mathrm{s^{-1}}\ . \tag{D.9}$$

Together with the gravitational constant, the *critical density of the Universe* can be expressed as

$$\rho_\mathrm{c} \equiv \frac{3H_0^2}{8\pi G} = 2.7754\times10^{11}\,h^2\,M_\odot\,\mathrm{Mpc^{-3}} = 1.8788\times10^{-29}\,h^2\ \mathrm{g\ cm^{-3}}\ . \tag{D.10}$$

The *Hubble radius*, describing approximately the size of the visible Universe, is given by

$$r_\mathrm{H} \equiv \frac{c}{H_0} = 2997.9\,h^{-1}\ \mathrm{Mpc} = 9.2506\times10^{27}\,h^{-1}\ \mathrm{cm}\ . \tag{D.11}$$

# Bibliography


Anderhalden, D. & Diemand, J. (2011): *The Total Mass of Dark Matter Haloes*. MNRAS, accepted, arXiv:1102.5736.

Angrick, C.: *Statistics of Gravitational Potential Perturbations: A New Approach to derive the X-Ray Temperature Function*. Diploma Thesis, University of Heidelberg (2007).

Angrick, C. & Bartelmann, M. (2009): *Statistics of gravitational potential perturbations: A novel approach to deriving the X-ray temperature function*. A&A, **494**, 461.

Angrick, C. & Bartelmann, M. (2010): *Triaxial collapse and virialisation of dark-matter haloes*. A&A, **518**, A38+.

Angrick, C. & Bartelmann, M. (2011): *The influence of mergers on the cluster temperature function and cosmological parameters derived from it*. A&A, submitted, arXiv:1102.0458.

Anselmi, S., Matarrese, S., & Pietroni, M. (2010): *Next-to-leading resummations in cosmological perturbation theory*. arXiv:1011.4477.

Bardeen, J. M., Bond, J. R., Kaiser, N., & Szalay, A. S. (1986): *The statistics of peaks of Gaussian random fields*. ApJ, **304**, 15.

Bartelmann, M. (2010a): *The dark Universe*. Reviews of Modern Physics, **82**, 331.

Bartelmann, M. (2010b): *TOPICAL REVIEW Gravitational lensing*. Classical and Quantum Gravity, **27** (23), 233001.

Bartelmann, M., Doran, M., & Wetterich, C. (2006): *Non-linear structure formation in cosmologies with early dark energy*. A&A, **454**, 27.

Bartelmann, M., Ehlers, J., & Schneider, P. (1993): *Timescales of isotropic and anisotropic cluster collapse*. A&A, **280**, 351.

Bartelmann, M. & Schneider, P. (2001): *Weak gravitational lensing*. Phys. Rep., **340**, 291.

Beaulieu, J., Bennett, D. P., Fouqué, P., et al. (2006): *Discovery of a cool planet of 5.5 Earth masses through gravitational microlensing*. Nature, **439**, 437.

Binney, J. & Tremaine, S., *Galactic dynamics*. Princeton Series in Astrophysics (Princeton University Press, Princeton, NJ, 1987).

Bond, J. R., Cole, S., Efstathiou, G., & Kaiser, N. (1991): *Excursion set mass functions for hierarchical Gaussian fluctuations*. ApJ, **379**, 440.

Bond, J. R. & Myers, S. T. (1996): *The Peak-Patch Picture of Cosmic Catalogs. I. Algorithms*. ApJS, **103**, 1.

Bonnet, H. & Mellier, Y. (1995): *Statistical analysis of weak gravitational shear in the extended periphery of rich galaxy clusters.* A&A, **303**, 331.

Borgani, S., Murante, G., Springel, V., et al. (2004): *X-ray properties of galaxy clusters and groups from a cosmological hydrodynamical simulation*. MNRAS, **348**, 1078.

Burenin, R. A., Vikhlinin, A., Hornstrup, A., et al. (2007): *The 400 Square Degree ROSAT PSPC Galaxy Cluster Survey: Catalog and Statistical Calibration*. ApJS, **172**, 561.

Carroll, S. M., Press, W. H., & Turner, E. L. (1992): *The cosmological constant*. ARA&A, **30**, 499.

Cash, W. (1979): *Parameter estimation in astronomy through application of the likelihood ratio*. ApJ, **228**, 939.

Courtin, J., Rasera, Y., Alimi, J., et al. (2011): *Imprints of dark energy on cosmic structure formation - II. Non-universality of the halo mass function*. MNRAS, **410**, 1911.

Crocce, M. & Scoccimarro, R. (2006): *Renormalized cosmological perturbation theory*. Phys. Rev. D, **73** (6), 063519.

Dietrich, J. P., Erben, T., Lamer, G., et al. (2007): *BLOX: the Bonn lensing, optical, and X-ray selected galaxy clusters. I. Cluster catalog construction*. A&A, **470**, 821.

Dietrich, J. P. & Hartlap, J. (2010): *Cosmology with the shear-peak statistics*. MNRAS, **402**, 1049.

Doroshkevich, A. G. (1970): *Spatial structure of perturbations and origin of galactic rotation in fluctuation theory*. Astrophysics, **6**, 320.

Einstein, A. (1905): *Zur Elektrodynamik bewegter Körper*. Annalen der Physik, **322**, 891.

Einstein, A. (1915): *Die Feldgleichungen der Gravitation*. Sitzungsberichte der Königlich Preußischen Akademie der Wissenschaften (Berlin), 844–847.

Einstein, A. (1916): *Die Grundlage der allgemeinen Relativitätstheorie*. Annalen der Physik, **354**, 769.

Eisenstein, D. J. & Hu, W. (1998): *Baryonic Features in the Matter Transfer Function*. ApJ, **496**, 605.

Eisenstein, D. J. & Loeb, A. (1995): *An analytical model for the triaxial collapse of cosmological perturbations*. ApJ, **439**, 520.

Eke, V. R., Cole, S., & Frenk, C. S. (1996): *Cluster evolution as a diagnostic for Omega*. MNRAS, **282**, 263.

Engineer, S., Kanekar, N., & Padmanabhan, T. (2000): *Non-linear density evolution from an improved spherical collapse model*. MNRAS, **314**, 279.

Erben, T., van Waerbeke, L., Mellier, Y., et al. (2000): *Mass-detection of a matter concentration projected near the cluster Abell 1942: Dark clump or high-redshift cluster?* A&A, **355**, 23.

Evrard, A. E., Bialek, J., Busha, M., et al. (2008): *Virial Scaling of Massive Dark Matter Halos: Why Clusters Prefer a High Normalization Cosmology*. ApJ, **672**, 122.

Fedeli, C., Moscardini, L., & Matarrese, S. (2009): *The clustering of galaxy clusters in cosmological models with non-Gaussian initial conditions: predictions for future surveys*. MNRAS, **397**, 1125.

Friedmann, A. (1922): *Über die Krümmung des Raumes*. Zeitung für Physik, **10**, 377.

Friedmann, A. (1924): *Über die Möglichkeit einer Welt mit konstanter negativer Krümmung des Raumes*. Zeitung für Physik, **21**, 326.

Heavens, A. & Peacock, J. (1988): *Tidal torques and local density maxima*. MNRAS, **232**, 339.

Hennawi, J. F. & Spergel, D. N. (2005): *Shear-selected Cluster Cosmology: Tomography and Optimal Filtering*. ApJ, **624**, 59.

Hetterscheidt, M., Erben, T., Schneider, P., et al. (2005): *Searching for galaxy clusters using the aperture mass statistics in 50 VLT fields*. A&A, **442**, 43.

Hivon, E., Górski, K. M., Netterfield, C. B., et al. (2002): *MASTER of the Cosmic Microwave Background Anisotropy Power Spectrum: A Fast Method for Statistical Analysis of Large and Complex Cosmic Microwave Background Data Sets*. ApJ, **567**, 2.

Hockney, R. W. & Eastwood, J. W., *Computer simulation using particles* (Hilger, Bristol, 1988).

Ikebe, Y., Reiprich, T. H., Böhringer, H., Tanaka, Y., & Kitayama, T. (2002): *A new measurement of the X-ray temperature function of clusters of galaxies*. A&A, **383**, 773.

Jain, B., Seljak, U., & White, S. (2000): *Ray-tracing Simulations of Weak Lensing by Large-Scale Structure*. ApJ, **530**, 547.

Jenkins, A., Frenk, C. S., White, S. D. M., et al. (2001): *The mass function of dark matter haloes*. MNRAS, **321**, 372.

Kaiser, N. (1992): *Weak gravitational lensing of distant galaxies*. ApJ, **388**, 272.

Kaiser, N. (1998): *Weak Lensing and Cosmology*. ApJ, **498**, 26.

Kaiser, N. & Squires, G. (1993): *Mapping the dark matter with weak gravitational lensing*. ApJ, **404**, 441.

Katz, N., Weinberg, D. H., & Hernquist, L. (1996): *Cosmological Simulations with TreeSPH*. ApJS, **105**, 19.

Komatsu, E., Dunkley, J., Nolta, M. R., et al. (2009): *Five-Year Wilkinson Microwave Anisotropy Probe Observations: Cosmological Interpretation*. ApJS, **180**, 330.

Komatsu, E., Smith, K. M., Dunkley, J., et al. (2011): *Seven-year Wilkinson Microwave Anisotropy Probe (WMAP) Observations: Cosmological Interpretation*. ApJS, **192**, 18.

Kratochvil, J. M., Haiman, Z., & May, M. (2010): *Probing cosmology with weak lensing peak counts*. Phys. Rev. D, **81** (4), 043519.

Kravtsov, A. V., Vikhlinin, A., & Nagai, D. (2006): *A New Robust Low-Scatter X-Ray Mass Indicator for Clusters of Galaxies*. ApJ, **650**, 128.

Lacey, C. & Cole, S. (1993): *Merger rates in hierarchical models of galaxy formation*. MNRAS, **262**, 627.

Lahav, O., Lilje, P. B., Primack, J. R., & Rees, M. J. (1991): *Dynamical effects of the cosmological constant*. MNRAS, **251**, 128.

Lampton, M., Margon, B., & Bowyer, S. (1976): *Parameter estimation in X-ray astronomy*. ApJ, **208**, 177.

Lau, E. T. (2010): *Characterizing Galaxy Clusters with Gravitational Potential*. ApJ, submitted, arXiv:1009.2124.

Lee, S. & Ng, K. (2010): *Spherical collapse model with non-clustering dark energy*. J. Cosmology Astropart. Phys., **10**, 28.

Lemaître, G. (1927): *Un Univers homogène de masse constante et de rayon croissant rendant compte de la vitesse radiale des nébuleuses extra-galactiques*. Annales de la Societe Scientifique de Bruxelles, **47**, 49.

Liddle, A. R., *An Introduction to Cosmological Inflation*. In A. Masiero, G. Senjanovic, & A. Smirnov, ed., *High Energy Physics and Cosmology, 1998 Summer School*, 260–+ (1999).

Liddle, A. R. & Lyth, D. H., *Cosmological Inflation and Large-Scale Structure* (Cambridge University Press, Cambridge, UK, 2000).

Limber, D. N. (1953): *The Analysis of Counts of the Extragalactic Nebulae in Terms of a Fluctuating Density Field.* ApJ, **117**, 134.

Lo Verde, M., Miller, A., Shandera, S., & Verde, L. (2008): *Effects of scale-dependent non-Gaussianity on cosmological structures*. J. Cosmology Astropart. Phys., **4**, 14.

Marian, L., Smith, R. E., & Bernstein, G. M. (2009): *The Cosmology Dependence of Weak Lensing Cluster Counts*. ApJ, **698**, L33.

Matarrese, S., Verde, L., & Jimenez, R. (2000): *The Abundance of High-Redshift Objects as a Probe of Non-Gaussian Initial Conditions*. ApJ, **541**, 10.

Maturi, M., Angrick, C., Pace, F., & Bartelmann, M. (2010): *An analytic approach to number counts of weak-lensing peak detections*. A&A, **519**, A23+.

Maturi, M., Fedeli, C., & Moscardini, L. (2011): *Imprints of primordial non-Gaussianity on the number counts of cosmic shear peaks*. MNRAS, submitted, arXiv:1101.4175.

Maturi, M., Meneghetti, M., Bartelmann, M., Dolag, K., & Moscardini, L. (2005): *An optimal filter for the detection of galaxy clusters through weak lensing*. A&A, **442**, 851.

Maturi, M., Schirmer, M., Meneghetti, M., Bartelmann, M., & Moscardini, L. (2007): *Searching dark-matter halos in the GaBoDS survey*. A&A, **462**, 473.

Mazzotta, P., Rasia, E., Moscardini, L., & Tormen, G. (2004): *Comparing the temperatures of galaxy clusters from hydrodynamical N-body simulations to Chandra and XMM-Newton observations*. MNRAS, **354**, 10.

Melchior, P., Viola, M., Schäfer, B. M., & Bartelmann, M. (2011): *Weak gravitational lensing with DEIMOS*. MNRAS, **412**, 1552.

Monaco, P. (1995): *The Mass Function of Cosmic Structures with Nonspherical Collapse*. ApJ, **447**, 23.

Monaco, P. (1997): *A Lagrangian Dynamical Theory for the Mass Function of Cosmic Structures - I. Dynamics*. MNRAS, **287**, 753.

Monaco, P. (1998): *The Cosmological Mass Function*. Fundamentals of Cosmic Physics, **19**, 157.

More, S., Kravtsov, A., Dalal, N., & Gottlöber, S. (2011): *The overdensity and masses of the friends-of-friends halos and universality of the halo mass function*. ApJS, submitted, arXiv:1103.0005.

Mota, D. F. & van de Bruck, C. (2004): *On the spherical collapse model in dark energy cosmologies*. A&A, **421**, 71.

Navarro, J. F., Frenk, C. S., & White, S. D. M. (1996): *The Structure of Cold Dark Matter Halos*. ApJ, **462**, 563.

Ohta, Y., Kayo, I., & Taruya, A. (2004): *Cosmological Density Distribution Function from the Ellipsoidal Collapse Model in Real Space*. ApJ, **608**, 647.

Pace, F., Maturi, M., Meneghetti, M., et al. (2007): *Testing the reliability of weak lensing cluster detections*. A&A, **471**, 731.

Pace, F., Waizmann, J., & Bartelmann, M. (2010): *Spherical collapse model in dark-energy cosmologies*. MNRAS, **406**, 1865.

Padmanabhan, T., *Theoretical Astrophysics, Volume III: Galaxies and Cosmology* (Cambridge University Press, Cambridge, UK, 2002).

Peacock, J. A. & Dodds, S. J. (1996): *Non-linear evolution of cosmological power spectra*. MNRAS, **280**, L19.

Pietroni, M. (2008): *Flowing with time: a new approach to non-linear cosmological perturbations*. J. Cosmology Astropart. Phys., **10**, 36.

Polyanin, A. D. & Manzhirov, A. V., *Handbook of Integral Equations* (CRC Press, Boca Raton, 1998).

Press, W. H. & Schechter, P. (1974): *Formation of Galaxies and Clusters of Galaxies by Self-Similar Gravitational Condensation*. ApJ, **187**, 425.

Randall, S. W., Sarazin, C. L., & Ricker, P. M. (2002): *The Effect of Merger Boosts on the Luminosity, Temperature, and Inferred Mass Functions of Clusters of Galaxies*. ApJ, **577**, 579.

Rasia, E., Mazzotta, P., Borgani, S., et al. (2005): *Mismatch between X-Ray and Emission-weighted Temperatures in Galaxy Clusters: Cosmological Implications*. ApJ, **618**, L1.

Reiprich, T. H. (2006): *The galaxy cluster X-ray luminosity-gravitational mass relation in the light of the WMAP 3rd year data*. A&A, **453**, L39.

Robertson, H. P. (1935): *Kinematics and World-Structure*. ApJ, **82**, 284.

Schäfer, B. M. & Koyama, K. (2008): *Spherical collapse in modified gravity with the Birkhoff theorem*. MNRAS, **385**, 411.

Schirmer, M., Erben, T., Schneider, P., Wolf, C., & Meisenheimer, K. (2004): *GaBoDS: The Garching-Bonn Deep Survey. II. Confirmation of EIS cluster candidates by weak gravitational lensing*. A&A, **420**, 75.

Schirmer, M., Erben, T., Schneider, P., et al. (2003): *GaBoDS: The Garching-Bonn Deep Survey. I. Anatomy of galaxy clusters in the background of NGC 300*. A&A, **407**, 869.

Schneider, M. D. & Bridle, S. (2010): *A halo model for intrinsic alignments of galaxy ellipticities*. MNRAS, **402**, 2127.

Schneider, P. (1996): *Detection of (dark) matter concentrations via weak gravitational lensing*. MNRAS, **283**, 837.

Schneider, P., *Extragalactic Astronomy and Cosmology* (Springer, Berlin, 2006).

Schneider, P., van Waerbeke, L., Jain, B., & Kruse, G. (1998): *A new measure for cosmic shear*. MNRAS, **296**, 873.

Seitz, C. & Schneider, P. (1997): *Steps towards nonlinear cluster inversion through gravitational distortions. III. Including a redshift distribution of the sources.* A&A, **318**, 687.

Sheth, R. K., Mo, H. J., & Tormen, G. (2001): *Ellipsoidal collapse and an improved model for the number and spatial distribution of dark matter haloes*. MNRAS, **323**, 1.

Sheth, R. K. & Tormen, G. (1999): *Large-scale bias and the peak background split*. MNRAS, **308**, 119.

Sheth, R. K. & Tormen, G. (2002): *An excursion set model of hierarchical clustering: ellipsoidal collapse and the moving barrier*. MNRAS, **329**, 61.

Smith, R. E., Peacock, J. A., Jenkins, A., et al. (2003): *Stable clustering, the halo model and non-linear cosmological power spectra*. MNRAS, **341**, 1311.

Springel, V. (2005): *The cosmological simulation code GADGET-2*. MNRAS, **364**, 1105.

Springel, V. & Hernquist, L. (2003): *Cosmological smoothed particle hydrodynamics simulations: a hybrid multiphase model for star formation*. MNRAS, **339**, 289.

Springel, V., White, S. D. M., Jenkins, A., et al. (2005): *Simulations of the formation, evolution and clustering of galaxies and quasars*. Nature, **435**, 629.

Tinker, J., Kravtsov, A. V., Klypin, A., et al. (2008): *Toward a Halo Mass Function for Precision Cosmology: The Limits of Universality*. ApJ, **688**, 709.

van Waerbeke, L. (2000): *Noise properties of gravitational lens mass reconstruction*. MNRAS, **313**, 524.

Vikhlinin, A., Burenin, R. A., Ebeling, H., et al. (2009a): *Chandra Cluster Cosmology Project. II. Samples and X-Ray Data Reduction*. ApJ, **692**, 1033.

Vikhlinin, A., Kravtsov, A. V., Burenin, R. A., et al. (2009b): *Chandra Cluster Cosmology Project III: Cosmological Parameter Constraints*. ApJ, **692**, 1060.

Viola, M., Melchior, P., & Bartelmann, M. (2011): *Biases in, and corrections to, KSB shear measurements*. MNRAS, **410**, 2156.

Walker, A. G. (1935): *On Riemannian Spaces with Spherical Symmetrie about a Line, and the Conditions for Isotropy in General Relativity*. The Quarterly Journal of Mathematics, **os-6** (1), 81.

Wang, L. & Steinhardt, P. J. (1998): *Cluster Abundance Constraints for Cosmological Models with a Time-varying, Spatially Inhomogeneous Energy Component with Negative Pressure*. ApJ, **508**, 483.

Zel'dovich, Y. B. (1970): *Gravitational instability: An approximate theory for large density perturbations.* A&A, **5**, 84.

# Acknowledgements

At this stage, it's time to thank all the people that have supported me in writing this thesis in various aspects.

Matthias, you've been a great advisor over the last years. I especially appreciate that you gave me the opportunity to continue the project I've already started with my diploma thesis and that I can stay for an additional postdoc. On the one hand, you gave me a lot of scientific freedom to follow my own thoughts, but on the other hand, you were always there when I didn't know how to go on. But what was even more important to me was the fact that I knew I could count on you when my mother became severely ill, and it was no problem to go back to Northeim much more often than usual. A very big THANK YOU for all this!

I thank Luca Amendola to agree on being my second corrector as well as Eva Grebel and Christian Enss to take part in my PhD committee.

Another great thank you goes to the ITA-boys and -girls for the extraordinary working atmosphere in our group! It has always been a pleasure not only to discuss scientific issues but also to spend a lot of my spare time with you, for Friday evening beer(s) at Bar Centrale, wine tasting sessions, Bavarian breakfasts, etc. I know that my sense of "humour" is sometimes (or should I say often) a bit "heavy", but I know that's the way you like it! (yes, you too, Phillip! ;-) ) I'm proud to call a lot of you friends. A special thanks goes to my office mates in various combinations (Cosimo, Claudia, Stefan, Gero, and Alex) for the great time we've had (and hopefully will still have).

Sorry for the non-German speakers, but I have to switch to German for the last part.

Ich möchte mich ganz besonders bei meinen Eltern bedanken, die mich von klein auf immer das haben machen lassen, was mich interessiert hat und mir wirklich nie das Gefühl gegeben haben, dass ich irgendwie ihre Erwartungen erfüllen muss. Auch wenn Ihr die meiste Zeit nicht wirklich verstanden habt, was ich da eigentlich mache, habt ihr mich in jeglicher Hinsicht unterstützt. Ohne Euch hätte ich es nie geschafft, aus einer Nicht-Akademikerfamilie so weit zu kommen! Ich bin stolz auf Euch!

Nun zu Dir, Evi. Ich habe mir vorgenommen, hier nicht etwas total Kitschiges zu schreiben. Mal sehen, ob es mir gelingt. Vielen Dank, dass Du immer für mich da warst und mich unterstützt hast, wenn ich nicht mehr weiter wusste und einfach keine Lust mehr hatte. Ich weiß, dass ich immer auf Dich zählen kann. Ich freue mich auf ein Leben mit Dir mit vielen kleinen Maxls und Liesls, einem Pony, Meerschweinchen, Hunden, Katzen, Kühen, unserem eigenen Gemüsegarten…